ANALYTICAL MODELING OF BIFURCATIONS, CHAOS AND MULTIFRACTALS IN NONLINEAR DYNAMICS

BY

ALBERT CHAO JUN LUO

A THESIS

SUBMITTED TO THE FACULTY OF GRADUATE STUDIES OF THE UNIVERSITY OF MANITOBA

IN PARTIAL FULFILLMENT OF THE REQUIREMENTS FOR THE DEGREE OF

DOCTOR OF PHILOSOPHY

DEPARTMENT OF MECHANICAL AND INDUSTRIAL ENGINEERING

UNIVERSITY OF MANITOBA

WINNIPEG, MANITOBA, CANADA

ISBN 0-612-13322-2

Name _____

Dissertation Abstracts International is arranged by broad, general subject categories. Please select the one subject which most nearly describes the content of your dissertation. Enter the corresponding four-digit code in the spaces provided.

Applied Mechanics
SUBJECT TERM

0	3	4	6

SUBJECT CODE

U·M·I

Subject Categories

THE HUMANITIES AND SOCIAL SCIENCES

COMMUNICATIONS AND THE ARTS
Architecture 0729
Art History 0377
Cinema 0900
Dance 0378
Fine Arts 0357
Information Science 0723
Journalism 0391
Library Science 0399
Mass Communications 0708
Music 0413
Speech Communication 0459
Theater 0465

EDUCATION
General 0515
Administration 0514
Adult and Continuing 0516
Agricultural 0517
Art 0273
Bilingual and Multicultural 0282
Business 0688
Community College 0275
Curriculum and Instruction 0727
Early Childhood 0518
Elementary 0524
Finance 0277
Guidance and Counseling 0519
Health 0680
Higher 0745
History of 0520
Home Economics 0278
Industrial 0521
Language and Literature 0279
Mathematics 0280
Music 0522
Philosophy of 0998
Physical 0523
Psychology 0525
Reading 0535
Religious 0527
Sciences 0714
Secondary 0533
Social Sciences 0534
Sociology of 0340
Special 0529
Teacher Training 0530
Technology 0710
Tests and Measurements 0288
Vocational 0747

LANGUAGE, LITERATURE AND LINGUISTICS
Language
- General 0679
- Ancient 0289
- Linguistics 0290
- Modern 0291

Literature
- General 0401
- Classical 0294
- Comparative 0295
- Medieval 0297
- Modern 0298
- African 0316
- American 0591
- Asian 0305
- Canadian (English) 0352
- Canadian (French) 0355
- English 0593
- Germanic 0311
- Latin American 0312
- Middle Eastern 0315
- Romance 0313
- Slavic and East European 0314

PHILOSOPHY, RELIGION AND THEOLOGY
Philosophy 0422
Religion
- General 0318
- Biblical Studies 0321
- Clergy 0319
- History of 0320
- Philosophy of 0322

Theology 0469

SOCIAL SCIENCES
American Studies 0323
Anthropology
- Archaeology 0324
- Cultural 0326
- Physical 0327

Business Administration
- General 0310
- Accounting 0272
- Banking 0770
- Management 0454
- Marketing 0338

Canadian Studies 0385
Economics
- General 0501
- Agricultural 0503
- Commerce-Business 0505
- Finance 0508
- History 0509
- Labor 0510
- Theory 0511

Folklore 0358
Geography 0366
Gerontology 0351
History
- General 0578
- Ancient 0579
- Medieval 0581
- Modern 0582
- Black 0328
- African 0331
- Asia, Australia and Oceania 0332
- Canadian 0334
- European 0335
- Latin American 0336
- Middle Eastern 0333
- United States 0337

History of Science 0585
Law 0398
Political Science
- General 0615
- International Law and Relations 0616
- Public Administration 0617

Recreation 0814
Social Work 0452
Sociology
- General 0626
- Criminology and Penology ... 0627
- Demography 0938
- Ethnic and Racial Studies 0631
- Individual and Family Studies 0628
- Industrial and Labor Relations 0629
- Public and Social Welfare 0630
- Social Structure and Development 0700
- Theory and Methods 0344

Transportation 0709
Urban and Regional Planning 0999
Women's Studies 0453

THE SCIENCES AND ENGINEERING

BIOLOGICAL SCIENCES
Agriculture
- General 0473
- Agronomy 0285
- Animal Culture and Nutrition 0475
- Animal Pathology 0476
- Food Science and Technology 0359
- Forestry and Wildlife 0478
- Plant Culture 0479
- Plant Pathology 0480
- Plant Physiology 0817
- Range Management 0777
- Wood Technology 0746

Biology
- General 0306
- Anatomy 0287
- Biostatistics 0308
- Botany 0309
- Cell 0379
- Ecology 0329
- Entomology 0353
- Genetics 0369
- Limnology 0793
- Microbiology 0410
- Molecular 0307
- Neuroscience 0317
- Oceanography 0416
- Physiology 0433
- Radiation 0821
- Veterinary Science 0778
- Zoology 0472

Biophysics
- General 0786
- Medical 0760

EARTH SCIENCES
Biogeochemistry 0425
Geochemistry 0996
Geodesy 0370
Geology 0372
Geophysics 0373
Hydrology 0388
Mineralogy 0411
Paleobotany 0345
Paleoecology 0426
Paleontology 0418
Paleozoology 0985
Palynology 0427
Physical Geography 0368
Physical Oceanography 0415

HEALTH AND ENVIRONMENTAL SCIENCES
Environmental Sciences 0768
Health Sciences
- General 0566
- Audiology 0300
- Chemotherapy 0992
- Dentistry 0567
- Education 0350
- Hospital Management 0769
- Human Development 0758
- Immunology 0982
- Medicine and Surgery 0564
- Mental Health 0347
- Nursing 0569
- Nutrition 0570
- Obstetrics and Gynecology .. 0380
- Occupational Health and Therapy 0354
- Ophthalmology 0381
- Pathology 0571
- Pharmacology 0419
- Pharmacy 0572
- Physical Therapy 0382
- Public Health 0573
- Radiology 0574
- Recreation 0575
- Speech Pathology 0460
- Toxicology 0383

Home Economics 0386

PHYSICAL SCIENCES
Pure Sciences
Chemistry
- General 0485
- Agricultural 0749
- Analytical 0486
- Biochemistry 0487
- Inorganic 0488
- Nuclear 0738
- Organic 0490
- Pharmaceutical 0491
- Physical 0494
- Polymer 0495
- Radiation 0754

Mathematics 0405
Physics
- General 0605
- Acoustics 0986
- Astronomy and Astrophysics 0606
- Atmospheric Science 0608
- Atomic 0748
- Electronics and Electricity 0607
- Elementary Particles and High Energy 0798
- Fluid and Plasma 0759
- Molecular 0609
- Nuclear 0610
- Optics 0752
- Radiation 0756
- Solid State 0611

Statistics 0463

Applied Sciences
Applied Mechanics 0346
Computer Science 0984
Engineering
- General 0537
- Aerospace 0538
- Agricultural 0539
- Automotive 0540
- Biomedical 0541
- Chemical 0542
- Civil 0543
- Electronics and Electrical 0544
- Heat and Thermodynamics ... 0348
- Hydraulic 0545
- Industrial 0546
- Marine 0547
- Materials Science 0794
- Mechanical 0548
- Metallurgy 0743
- Mining 0551
- Nuclear 0552
- Packaging 0549
- Petroleum 0765
- Sanitary and Municipal 0554
- System Science 0790

Geotechnology 0428
Operations Research 0796
Plastics Technology 0795
Textile Technology 0994

PSYCHOLOGY
General 0621
Behavioral 0384
Clinical 0622
Developmental 0620
Experimental 0623
Industrial 0624
Personality 0625
Physiological 0989
Psychobiology 0349
Psychometrics 0632
Social 0451

Nom _____

Dissertation Abstracts International est organisé en catégories de sujets. Veuillez s.v.p. choisir le sujet qui décrit le mieux votre thèse et inscrivez le code numérique approprié dans l'espace réservé ci-dessous.

_____ ☐☐☐ U·M·I

SUJET — CODE DE SUJET

Catégories par sujets

HUMANITÉS ET SCIENCES SOCIALES

COMMUNICATIONS ET LES ARTS
Architecture 0729
Beaux-arts 0357
Bibliothéconomie 0399
Cinéma 0900
Communication verbale 0459
Communications 0708
Danse 0378
Histoire de l'art 0377
Journalisme 0391
Musique 0413
Sciences de l'information 0723
Théâtre 0465

ÉDUCATION
Généralités 515
Administration 0514
Art 0273
Collèges communautaires 0275
Commerce 0688
Économie domestique 0278
Éducation permanente 0516
Éducation préscolaire 0518
Éducation sanitaire 0680
Enseignement agricole 0517
Enseignement bilingue et multiculturel 0282
Enseignement industriel 0521
Enseignement primaire. 0524
Enseignement professionnel 0747
Enseignement religieux 0527
Enseignement secondaire 0533
Enseignement spécial 0529
Enseignement supérieur 0745
Évaluation 0288
Finances 0277
Formation des enseignants 0530
Histoire de l'éducation 0520
Langues et littérature 0279
Lecture 0535
Mathématiques 0280
Musique 0522
Orientation et consultation 0519
Philosophie de l'éducation 0998
Physique 0523
Programmes d'études et enseignement 0727
Psychologie 0525
Sciences 0714
Sciences sociales 0534
Sociologie de l'éducation 0340
Technologie 0710

LANGUE, LITTÉRATURE ET LINGUISTIQUE
Langues
- Généralités 0679
- Anciennes 0289
- Linguistique 0290
- Modernes 0291

Littérature
- Généralités 0401
- Anciennes 0294
- Comparée 0295
- Médiévale 0297
- Moderne 0298
- Africaine 0316
- Américaine 0591
- Anglaise 0593
- Asiatique 0305
- Canadienne (Anglaise) 0352
- Canadienne (Française) 0355
- Germanique 0311
- Latino-américaine 0312
- Moyen-orientale 0315
- Romane 0313
- Slave et est-européenne 0314

PHILOSOPHIE, RELIGION ET THÉOLOGIE
Philosophie 0422
Religion
- Généralités 0318
- Clergé 0319
- Études bibliques 0321
- Histoire des religions 0320
- Philosophie de la religion 0322

Théologie 0469

SCIENCES SOCIALES
Anthropologie
- Archéologie 0324
- Culturelle 0326
- Physique 0327

Droit 0398
Économie
- Généralités 0501
- Commerce-Affaires 0505
- Économie agricole 0503
- Économie du travail 0510
- Finances 0508
- Histoire 0509
- Théorie 0511

Études américaines 0323
Études canadiennes 0385
Études féministes 0453
Folklore 0358
Géographie 0366
Gérontologie 0351
Gestion des affaires
- Généralités 0310
- Administration 0454
- Banques 0770
- Comptabilité 0272
- Marketing 0338

Histoire
- Histoire générale 0578
- Ancienne 0579
- Médiévale 0581
- Moderne 0582
- Histoire des noirs 0328
- Africaine 0331
- Canadienne 0334
- États-Unis 0337
- Européenne 0335
- Moyen-orientale 0333
- Latino-américaine 0336
- Asie, Australie et Océanie 0332

Histoire des sciences 0585
Loisirs 0814
Planification urbaine et régionale 0999
Science politique
- Généralités 0615
- Administration publique 0617
- Droit et relations internationales 0616

Sociologie
- Généralités 0626
- Aide et bien-être social 0630
- Criminologie et établissements pénitentiaires 0627
- Démographie 0938
- Études de l' individu et de la famille 0628
- Études des relations interethniques et des relations raciales 0631
- Structure et développement social 0700
- Théorie et méthodes. 0344
- Travail et relations industrielles 0629

Transports 0709
Travail social 0452

SCIENCES ET INGÉNIERIE

SCIENCES BIOLOGIQUES
Agriculture
- Généralités 0473
- Agronomie. 0285
- Alimentation et technologie alimentaire 0359
- Culture 0479
- Élevage et alimentation 0475
- Exploitation des pâturages 0777
- Pathologie animale 0476
- Pathologie végétale 0480
- Physiologie végétale 0817
- Sylviculture et faune 0478
- Technologie du bois 0746

Biologie
- Généralités 0306
- Anatomie 0287
- Biologie (Statistiques) 0308
- Biologie moléculaire 0307
- Botanique 0309
- Cellule 0379
- Écologie 0329
- Entomologie 0353
- Génétique 0369
- Limnologie 0793
- Microbiologie 0410
- Neurologie 0317
- Océanographie 0416
- Physiologie 0433
- Radiation 0821
- Science vétérinaire 0778
- Zoologie 0472

Biophysique
- Généralités 0786
- Medicale 0760

SCIENCES DE LA TERRE
Biogéochimie 0425
Géochimie 0996
Géodésie 0370
Géographie physique 0368
Géologie 0372
Géophysique 0373
Hydrologie 0388
Minéralogie 0411
Océanographie physique 0415
Paléobotanique 0345
Paléoécologie 0426
Paléontologie 0418
Paléozoologie 0985
Palynologie 0427

SCIENCES DE LA SANTÉ ET DE L'ENVIRONNEMENT
Économie domestique 0386
Sciences de l'environnement 0768
Sciences de la santé
- Généralités 0566
- Administration des hôpitaux 0769
- Alimentation et nutrition 0570
- Audiologie 0300
- Chimiothérapie 0992
- Dentisterie 0567
- Développement humain 0758
- Enseignement 0350
- Immunologie 0982
- Loisirs 0575
- Médecine du travail et thérapie 0354
- Médecine et chirurgie 0564
- Obstétrique et gynécologie 0380
- Ophtalmologie 0381
- Orthophonie 0460
- Pathologie 0571
- Pharmacie 0572
- Pharmacologie 0419
- Physiothérapie 0382
- Radiologie 0574
- Santé mentale 0347
- Santé publique 0573
- Soins infirmiers 0569
- Toxicologie 0383

SCIENCES PHYSIQUES
Sciences Pures
Chimie
- Généralités 0485
- Biochimie 487
- Chimie agricole 0749
- Chimie analytique 0486
- Chimie minérale 0488
- Chimie nucléaire 0738
- Chimie organique 0490
- Chimie pharmaceutique 0491
- Physique 0494
- PolymÈres 0495
- Radiation 0754

Mathématiques 0405
Physique
- Généralités 0605
- Acoustique 0986
- Astronomie et astrophysique 0606
- Électronique et électricité 0607
- Fluides et plasma 0759
- Météorologie 0608
- Optique 0752
- Particules (Physique nucléaire) 0798
- Physique atomique 0748
- Physique de l'état solide 0611
- Physique moléculaire 0609
- Physique nucléaire 0610
- Radiation 0756

Statistiques 0463

Sciences Appliqués Et Technologie
Informatique 0984
Ingénierie
- Généralités 0537
- Agricole 0539
- Automobile 0540
- Biomédicale 0541
- Chaleur et thermodynamique 0348
- Conditionnement (Emballage) 0549
- Génie aérospatial 0538
- Génie chimique 0542
- Génie civil 0543
- Génie électronique et électrique 0544
- Génie industriel 0546
- Génie mécanique 0548
- Génie nucléaire 0552
- Ingénierie des systèmes 0790
- Mécanique navale 0547
- Métallurgie 0743
- Science des matériaux 0794
- Technique du pétrole 0765
- Technique minière 0551
- Techniques sanitaires et municipales 0554
- Technologie hydraulique 0545

Mécanique appliquée 0346
Géotechnologie 0428
Matières plastiques (Technologie) 0795
Recherche opérationnelle 0796
Textiles et tissus (Technologie) 0794

PSYCHOLOGIE
Généralités 0621
Personnalité 0625
Psychobiologie 0349
Psychologie clinique 0622
Psychologie du comportement 0384
Psychologie du développement 0620
Psychologie expérimentale 0623
Psychologie industrielle 0624
Psychologie physiologique 0989
Psychologie sociale 0451
Psychométrie 0632

ANALYTICAL MODELING OF BIFURCATIONS, CHAOS AND MULTIFRACTALS IN NONLINEAR DYNAMICS

BY

ALBERT CHAO JUN LUO

A Thesis submitted to the Faculty of Graduate Studies of the University of Manitoba in partial fulfillment of the requirements of the degree of

DOCTOR OF PHILOSOPHY

DEDICATION

To all scientists who contributed to science and technology for the benefit of mankind.

ABSTRACT

Several analytical models of bifurcations, chaos and multifractals are proposed in this thesis. To verify and access the performance of these models, comparisons with published solutions are made whenever possible, otherwise, the analytically generated results are compared with those obtained via numerical simulations. In all cases, good to excellent agreements are observed. The research is divided into three parts: *Part* I describes models for continuous systems, *Part* II characterizes models for discontinuous systems and *Part* III introduces multifractal models for chaotic dynamics.

To study a continuous system, the Duffing oscillator is employed. The Chirikov overlap criterion and the renormalization group technique are used to independently derive, for the first time, the chaotic condition near a subharmonic resonant orbit of the undamped Duffing oscillator. To analyze the stability and bifurcation of periodic solutions of the damped Duffing oscillator with strong nonlinearities, an improved harmonic balance method is proposed. The physical system studied is the buckling of a nonlinear rod and for this structure, four types of Duffing oscillator are identified. Chaos in the weakly damped Duffing oscillator is studied using the Melnikov method.

A new method based on the incremental energy approach is developed to model stochastic layers near the homoclinic and the heteroclinic orbits, and also, resonant layers in the vicinity of the resonant orbit. Analytical expressions for the strengths of these layers are derived. In the case of the stochastic layers, the outer and inner strengths for the Duffing and forced planar-pendulum oscillators are obtained, and for the resonant layers, the

appearance, disappearance and accumulated disappearance strengths for the Duffing oscillator are determined. Employing a Naive discretization of the differential equation of motion of the Duffing oscillator and the subsequent application of the cubic renormalization on its discrete mapping, the universal character of the oscillator is studied for the first time. The jump phenomenon and the strange attractor are clearly seen in the cascades of bifurcations.

To examine a discontinuous system, the impact oscillator is used. Based on the differential equation of motion of a ball bouncing on a massive vibrating table, the stability and bifurcation conditions are derived for the first time. Analyzing the mappings of the motion, three types of stable motion and two types of unstable motion are found. From the Poincare mappings of the unstable period-1 motion, the two saddles are shown to possess identical Smale horseshoe structures. However, this is not necessarily true for the higher periodic solutions. Another example of a discontinuous system is that of a horizontal impact pair. A theory for a system with discontinuities and applied to the impact analysis of a horizontal impact pair is developed. Mappings for four switch planes are defined and from these, five impact motions; Model I, Model II, Model III, Model IV and Model V are derived. One of the findings here is that period doubling bifurcations cannot occur for equispaced impacts of the Model I motion.

A highly accurate method for the analysis of period doubling bifurcations in 1-D iterative maps is proposed. The technique consists of constructing similar structures of the period doubling solutions and applying a renormalization procedure to evaluate the appropriate length scaling factors. An example is solved to demonstrate and assess the accuracy of the procedure. The weight parameter function, several generalized fractal dimensions, the scaling index and the fractal spectrum functions are derived.

To develop a theory for multifractals in chaotic dynamics, the m-D horseshoe map is adopted. The results for 1-D uniform and nonuniform Cantor sets are first derived, and

then extended to handle 2-D uniform and nonuniform Smale horseshoes. Fractal characteristics for the invariant sets generated via the Cantor sets and Smale horseshoes can be easily determined using this new theory.

One of the key features of the analytical models developed for the study of the various nonlinear dynamics phenomena is that bifurcations and the onset of chaos can be theoretically predicted by employing computed instead of prescribed input parameters in numerical simulations. This ability is very beneficial as it can significantly reduce the amount of numerical experimentations.

ACKNOWLEDGMENT

I would like to acknowledge the encouragement, advice and constructive suggestions from my supervisor Dr. RAY P.S. HAN. I would also like to thank the internal members of the advisory committee, Dr. D. RUTH and Dr. B. SOUTHERN, and the external examiner, DR. H.G. DAVIES of the University of New Brunswick, for their careful reading of my thesis which is not necessarily written in perfect English at all times.

I wish to thank my classmates, the faculty and staff in the Department of Mechanical and Industrial Engineering for their friendship and help throughout my study at the University of Manitoba. I would like to express my appreciation to Graduate Studies for its financial support in the form of the award of the Clarence Bogardus Scholarship and the University of Manitoba Fellowship.

Finally, most of all, I would like to thank my wonderful wife and our beautiful daughter for their patience and understanding during the period of my study. I would like to apologize to them for being away so much, working constantly in the computer lab.

LIST OF FIGURES

LIST OF TABLES

NOMENCLATURE

PART I CONTINUOUS SYSTEM: DUFFING OSCILLATOR

A	Cross-section area, response amplitude of vibration.
C^r	r-times differentiable.
ds	Differential arch-length.
dx	Differential element.
$Det(\cdot)$	Determinant of matrix.
E	Young's Modulus.
$E(k)$	Complete elliptic integral of the second kind.
H	Hamiltonian energy function.
H_0	Conservative energy.
H_1	External energy.
I	Moment of inertia.
k	Modulus of the Jacobian-elliptic function.
$K(k)$	Complete elliptic integral of the first kind.
l	Length of the nonlinear rod.
m	Modal number.
M	Bending moment of the nonlinear rod.
P	Axial load.
q_0	Static load.
Q_0	Excitation amplitude.
$q(t)$	Lateral load or phase orbits.
t	Time variable

T Period of vibration.

$Tr(\cdot)$ Trace of matrix.

$u(t)$ Coefficient in the method of harmonic balance.

$v(t)$ Coefficient in the method of harmonic balance.

w Lateral deflection of the nonlinear rod.

$X(t)$ Axial distributing load in the x-direction.

$Y(t)$ Axial distributing load in the y-direction.

α Coefficient for the forced planar-pendulum oscillator.

α_1 Linear stiffness of the Duffing oscillator.

α_2 Nonlinear coefficient in the Duffing oscillator.

δ Damping coefficient.

Σ Poincare mapping section.

ω Nonlinear frequency.

Ω Excitation frequency.

$\cap$ Intersection.

$\cup$ Contained in.

$\in$ A member of.

$\forall$ For all.

$\exists$ There is.

PART II DISCONTINUOUS SYSTEMS: IMPACT OSCILLATORS

A Amplitude of excitation.

d Gap.

$Det(\cdot)$ Determinant of matrix

$\mathbf{DP}$ Jacobian of the mapping $\mathbf{P}$.

e Coefficient of restitution.

E	External excitation.
f	Vector function.
g	Gravitational acceleration.
$\mathbf{I}$	Identity matrix.
m	Mass of the bouncing ball.
m_R	Impact number on the right-hand-side.
M	Mass of the vibrating table.
M_p	Primary mass.
M_s	Secondary mass.
n_L	Impact number on the left-hand-side.
$\mathbf{P}$	Poincare mapping.
T	Period of excitation.
t	Time variable.
t_i	Impact time at the ith impact.
TM	State space.
$Tr(\cdot)$	Trace of matrix.
$\mathbf{x}$	Element of switch plane Σ^+ or Σ^- or Σ.
x	Absolute displacement of impact ball.
x_i	Absolute displacement of impact ball at the ith impact.
y	Relative displacement of impact ball.
y_i	Relative displacement of impact ball at the ith impact.
Σ	Switch plane.
τ	Phase plane.
ω	Frequency of excitation.
ω_i	ith frequency of excitation.
$\in$	A member of.
$\cup$	Contained in.

PART III DISCONTINUOUS SYSTEMS: IMPACT OSCILLATORS

$\mathbf{D}$	Dimension, unit square.
D_0	Hausdorff dimension.
D_1	Information dimension.
D_2	Correlation dimension.
D_i	Dimension in the ith direction.
D_q	Fractal dimension.
f	Mapping function, fractal spectrum.
$f^{(k)}$	k-times mapping.
m	Number of dimensions.
M	Scaled number of the original object.
n	Number of dimension.
N	Number of nonempty objects.
p_i	Action probability.
q	Order q of moment.
r	Scaling ratio.
x	Variable.
y	Variable.
α	Scaling (fractal) index.
μ	Parameter.
$\prod$	Products.
τ	Weight (auxiliary) parameter.
$\in$	Member of.
$\cap$	Intersection.
$\cup$	Contained in.

TABLE OF CONTENTS

CHAPTER 1

INTRODUCTION

1.1 Literature Survey

The advent of powerful and affordable computers during the past two decades was the major impetus towards the rapid growth and development in nonlinear dynamics. This emergence created increased awareness which in turn, led to an expanding number of applications in engineering. Chaotic phenomena in completely deterministic systems arise from the nonlinearities present in the systems. These nonlinearities include the following: geometrical nonlinearities, material nonlinearities, dissipative nonlinearities (e.g., structural damping, fluid damping, dry friction), motion nonlinearities (e.g., impacts, clearance, backlash, play), boundary condition nonlinearities, coupled system nonlinearities (e.g., fluid-solid coupling, mechanical-electrical coupling), feedback control nonlinearities, (Moon (1987)). Since nonlinearities are unavoidable, engineers have come to recognize chaotic vibrations and accept that the ensuing stochastic motion can exist in deterministic systems. Therefore, it is the objective of engineering-based nonlinear dynamics not only to study and comprehend these complex phenomena, but also to learn how to control them. To achieve this, it is crucial that engineers keep abreast of the new developments and discoveries that are taking place with great vigor in this area. New concepts for modeling bifurcations and chaotic vibrations, modern techniques of chaos detection, quantification and characterization, and the evolution of highly sophisticated mathematical and numerical tools constitute the bulk of current research in nonlinear dynamics. Indeed, the use of computer simulations, coupled with powerful analysis methods meant that realistic

problems can now be adequately and accurately investigated.

One of the first persons to notice the dynamical instability arising from the sensitive dependency on initial conditions was Hadamard (1901), in his work on the geodesic flow on compact surfaces, towards the end of the 19th century. This feature was also observed by Poincare (1899) who around this time, formulated a theory for the perturbative analysis of planetary orbits. Unfortunately, these work slipped into obscurity for just over half a century later, until Lorenz (1963) employed a high-speed computer to model weather patterns via the Rayleigh-Benard convection equations. He not only re-confirmed the sensitivity of nonlinear systems to initial conditions (now popularly known as the *butterfly* effect), but also demonstrated the first *chaotic* solutions through numerical simulations. Henon and Heiles (1964) also used numerical techniques to study the motion in a two-dimensional potential well, as an example of a two-degree of freedom system. New analytical tools were also being introduced. Based on the conjecture of Kolmogorov (1954), Arnold (1963) proved that for an analytically perturbed Hamiltonian and also, Moser (1962) for a sufficient number of continuous derivatives, a very fundamental result concerning orbit stability which is now accorded the name KAM theorem in their honor. It states that when an integrable Hamiltonian system is given a small perturbation, invariant tori continue to exist. This implies that the stochastic motion near the separatrix of each resonance is still constrained by KAM curves and is valid only for sufficiently incommensurable orbits. For commensurate orbits, one can resort to the Poincare-Birkhoff fixed point theorem. Melnikov (1963) presented a criterion which predicts the onset of chaos near the separatrix of an integrable dissipative system. It can be used to investigate the bifurcation to subharmonic and homoclinic orbits. Morosov (1973) and Holmes (1979) applied the method to study the Duffing equation.

By the late 1960's, research in nonlinear dynamics had moved into high-gear and with even greater vigor. Smale (1967) described strange attractors in dynamical systems, but it was Ruelle and Takens (1971) who actually introduced the term, *strange attractor,* in

their work on flow turbulence. They suggested that the behavior of turbulent flow is due to a strange attractor regime in the Navier-Stokes equation. Feigenbaum (1978) discovered universality and scaling in sequences of period doubling bifurcations to chaos. Earlier on, May (1976) had demonstrated this route to chaos via a one-dimensional quadratic map for modeling population growth. One could generalize the results for a wider class of one-dimensional maps by employing the *renormalization* technique. This has been shown by Collet, Eckmann and Lanford (1980) using an *exact* renormalization theory, and by Helleman (1980) based on an approximate model. One could also utilize renormalization to deduce universality in global bifurcations. Luo and Han (1992a) constructed self-similar structures of the period doubling solutions and obtained multifractal results of very high precision using a renormalization procedure. Chirikov (1979) presented an improved overlap criterion, to study the transition to conservative global chaos. He observed that between the two lowest order resonances, chaos occurs when the distance between these resonances is greater than the sum of half the vertical distances of the two island separatrices formed by the resonances. In other words, when the two island separatrices overlap, chaos occurs, and when they are just touching, the last KAM torus is destroyed. For higher accuracy, it is necessary to include the width of the stochastic layer and the secondary resonances lying in-between the main ones.

Probabilistic methods for handling the stochastic motion are a logical development in chaos modeling. Hsu (1981) introduced the concept of cell-to-cell mapping by dividing the phase space into many cells, then applying probabilistic methods (for Markov processes) to analyze chaos. Symbolic dynamics is another area of current interest. Pioneering work was first carried out by Frechet (1938) and more recently, by Devaney (1986) and Hao (1989). The procedure involves not only discretizing the time domain, but also the state variables. With this approach, the state variables can take a finite set of values and this permits the use of symbols such as L, C, R to denote Left, Center and Right of the map for a given orbit. Kluiving, Capel and Pasmanter (1992a, b) applied the method to analyze fully developed chaos via a statistical technique. Recently, Benedicks (1994) presented a

survey of the more recent developments in the ergodic theory of chaos and strange attractors. His work focused on the non-uniformly hyperbolic dynamical systems.

With the proliferation of powerful and affordable computers, the analysis of actual observed chaotic time series data is now becoming increasingly important. An excellent review in this area is given in a recent publication of Babarbanel, Brown, Sidorowich and Tsimring (1993). Masri, Chassiakos and Caughey (1993) applied the method of neural networks for the identification of nonlinear dynamical systems, specifically, a damped Duffing oscillator. Through neural networks we can have parallel information processing of the immense chaos data and the benefit is obvious. Bressloff and Stark (1991) described the relationship between neural networks and *Iterated Function Systems* (IFS) which are basically, finite sets of mappings in some metric space. IFS has the distinct advantage of being able to describe an extremely complex image using a relatively small number of parameters and thus, when combined with neural networks, the method can be very useful and efficient for analyzing chaos and for generating fractal images. We are not aware of anyone working in this exciting area of research which combines neural networks with IFS for chaos modeling, and we feel there is great potential in doing so.

Although fractals have been known to mathematicians and artists for hundreds of years, it was only in the mid-seventies of this century that the concept was introduced to describe the nature by Mandelbrot (1977). Several books have since been published. For example, see Mandelbrot (1977, 1982) for a good and original introduction of the basic concepts; Feder (1988) and Falconer (1990) for a mathematical foundation of the fractal theory; Bunde and Havlin (1991) for a summary of papers on the use of fractals in disordered structures and random processes; and Schroeder (1991) for a discussion of fractal phenomena in nature. Naturally, there has been countless articles in this fast developing area. Among the interesting ones are, Herrmann (1991) for a description of fractals in modeling material fracture and crack growth; Gouyet, Rosso and Sapoval (1991) for the use of fractals in surface roughness modeling; Luo (1991) and, Leung and Luo (1992) for

the generation of multifractals via multigenerators; Olemskoi and Flat (1993) for the development of fractals in condensed matter; and, Meneveau et. al (1990) for the application of fractals in turbulence; and Borgas (1993) for a survey of multifractals in small-scale dynamics of turbulent flows.

With respect to fractals in chaotic dynamics, it is well known that chaotic dynamics possess characteristics of self-similar structures which is an essential property of fractals. Therefore, fractal dimension measurements can be used to describe strange attractors (see Moon (1987)). Statistical mechanics can be formulated completely in which a single-particle energy is the Lyapunov exponent for a given trajectory and the lattice configuration is identified as the symbolic sequence of the iterative map. Several researchers have applied ergodic theory and statistical thermodynamic approaches to determine chaotic behavior, see for instance, Eckman and Ruelle (1985); Szepfalusy and Tel (1989); and, Shigmatsa (1990). Others such as Mori et al. (1989) and Kobayashi et al. (1989) studied the statistical characteristics of chaotic phenomena; and Kluiving et al (1990) described the scaling structures of chaos and the use of phase transition methods. Specific developments of fractal theory in chaotic dynamics are summarized as follows. Renyi (1971) expressed the generalized Hausdorff dimension using concepts based on generalized entropies. Grassberger and Procaccia (1983a) employed these ideas to study the complexities of chaotic attractors (or strange attractors) since these attractors exhibit self-similarity. In their work on the singularities of strange attractors, Halsey et al. (1986) presented a generalization of multifractals via a scaling analogy of the phase transitions. They applied the multifractal theory to several simple cases of chaotic dynamics for 1-D problems. The variations of Lyapunov exponents with initial conditions generate multiscale fractals and based on this idea, McCauley (1990) presented a detailed introduction to multifractals in dynamical systems. Considering the fractality of chaotic structures in 1-D dynamical system, Bene and Szepfalusy (1988) and, Szepfalusy and Tel (1989) studied the multifractal properties of 1-D random field Ising models and 1-D maps. A highly accurate method to compute period doubling bifurcation solutions of a general 1-

D iterative map was presented by Luo and Han (1992a). For period doubling bifurcations leading to chaos, this approach yields very accurate multifractal results compared to say, the analytical technique of Halsey et al. (1986). This is evident by comparing with the experimental results reported by Glazier et al. (1986). Luo and Han (1992b) presented some ideas on the fractality of multi-dimensional horseshoe maps for chaotic dynamics. In another publication, Luo and Han (1995d) introduced a new definition for multidimensional fractals based on the 1-D multifractal theory for the analysis of horseshoe maps.

1.2 Continuous and Discrete Systems in Engineering

In the previous section, we presented development histories of bifurcations, chaos and fractals. Next, we consider continuous and discrete systems as modeled by the Duffing oscillator and an impact oscillator respectively.

1.2.1 Duffing oscillators

Consider the following damped Duffing oscillator subjected to a periodic forcing function:

$$\ddot{x} + \delta\dot{x} + x^3 = Q_0 \cos t, \tag{1.1}$$

where x is the displacement and the dot denotes time derivatives. The parameters δ and Q_0 represent the damping constant and excitation amplitude respectively. The behavior of the solutions for this nonlinear oscillator was first investigated by Duffing (1918) (hence its name). The generalized form of *Equation* (1.1), namely,

$$\ddot{x} + \delta\dot{x} + \alpha_1 x + \alpha_2 x^3 = f(t), \tag{1.2}$$

can be used to capture the nonlinear vibration of structural elements such as springs, beams, plates and shells. Note that α_1 and α_2 are appropriate system parameters.

Using traditional techniques, Hayashi (1964) employed the method of harmonic balance to determine its periodic solution and the amplitude-frequency curves. In addition, using the technique of Poincare mapping, he provided topological portraits in phase space for the strongly nonlinear and forced oscillations. Recently, Debnath and Chowdhury (1991), Wang et al. (1992) etc. studied the bifurcations for the periodic solution of the Duffing oscillator. Luo and Han (1995b) considered the stability and bifurcations for periodic solutions of the Duffing oscillator.

In the study of chaos, the behavior of undamped and damped systems is quite different. For an undamped Duffing oscillator, Reichl and Zhang (1984a, b) used Chirikov resonance overlap criteria to compute the width of the stochastic layer for the double-well problem near its homoclinic orbit. They verified their calculations of the width of the stochastic layer by using an alternative approach involving standard mappings. Han and Luo (1994) employed this technique to calculate critical conditions for the ensuing global stochasticity near the subharmonic resonant orbits. Luo, Han and Xiang (1995) determined the critical condition of an undamped Duffing oscillator via the renormalization technique. Applying the universality of the standard mapping, Luo(1993b, 1994) devised a prediction method for determining the minimum critical condition for the onset of global stochasticity near the subharmonic resonant orbits. For the damped oscillator, using a one-mode model of a buckled beam and the Melnikov method, Moon and Holmes (1979), Moon (1980), and Holmes and Moon (1983) presented an approximate analytic criterion for the onset of chaos. To further understand the chaotic characteristics, Luo and Han (1995d) employed an approximate renormalization approach to explore the universal behavior of a damped Duffing oscillator. Moon and Holmes (1979) and Moon (1980a, b) demonstrated chaos in a damped oscillator via experiments by studying the buckling of an elastic cantilevered beam in a magnetic field. Using numerical simulation of the Poincare mapping section, Ueda (1980a, b) demonstrated steady-state chaos and strange attractors. Other important numerical works were reported by Dowell (1982, 1984), Moon and Li (1985a, b), Dowell and Pezeshi (1986) in their

study of the double-well problem.

1.2.2 Impact Oscillators

Discontinuous systems are commonly encountered in engineering. Many physical systems have operational constraints in their dynamical behavior, and therefore, result in discontinuities or intermittencies in their motions. Examples include constrained vibrating beams, moored ships in rough sea states, the rattling of gears, and the bouncing of balls. *Impact* oscillators constitute an important class of non-smooth dynamical systems. A formal definition of an impact oscillator was recently forwarded by Bishop (1994) to represent a periodically driven system which also exhibits intermittence or a continuous sequence of contacts with motion limiting constraints. Impact oscillators not only produce typical characteristics associated with smooth nonlinear systems, for example, generic bifurcations, multiple solutions and chaos, but also displays new phenomena such as grazing bifurcations.

In mechanical vibrations, noise and wear are often attributed to impacts in machinery. The increase in impact forces due to clearances was evaluated by Johnson (1958); Dubowsky and Freudenstein (1971); Dubowsky and Moening (1978); Haines (1979). Rattling of gears was investigated using an impact model by Pfeiffer and Kunert (1990) and the action of print hammers was studied by Hendricks (1983). In the area of fluid-induced impacts, a moored ship undergoing repeated contacts with the fender was investigated by Lean (1971), wave forces on structures was studied by Thompson and Ghaffari (1982) and Paidoussis and Li (1992) researched on vibration of fluid-filled tubes. In earthquake engineering, Housner (1963) investigated the behavior of buildings under random excitations. Stability analysis of impact dampers have been investigated by many people, starting with Masri and Caughey (1966); Bapat, Popplewell and Mclachlan (1983); Bapat and Bapat (1988); Heiman, Bajaj and Sherman (1987); and Han, Luo and Deng (1994). Bifurcation and chaos in impact oscillators have been studied by Shaw and Holmes

(1983a, b); Shaw (1985a, b); Nordmark (1991); Foale and Bishop (1992) Peterka and Vacik (1992) and also, by Han, Luo and Deng (1995). A very interesting impact model was studied by Holmes (1982); Tufillaro and Albano (1986); Everson (1986); and Whiston (1992) using a bouncing ball. Further improvement of this model was introduced by Luo and Han (1994a). The impacts of a constrained driven pendulum was analyzed by Shaw and Shaw (1989). In experimental studies of impact oscillators, models subjected to random forcing were studied by Davies (1980); and Wood and Byrne (1981); and pendulum-type models by Moore and Shaw (1990); and Bayly and Virgin(1993).

1.3 Basic Theories in Bifurcation, Chaos and Fractals

To avoid cluttering this doctoral dissertation with unnecessary material, the basic theories in bifurcation, chaos and fractals are described in *Appendix* A. Since many of the materials covered are expressed in a form not readily found in books and other publications, I have presented a detailed report in an invited state-of-the-art-review in Han and Luo (1995c).

1.4 Thesis Objective and Scope of Study

The objective of this doctoral thesis research is to carry out analytical studies of bifurcations, chaos and multifractals for nonlinear dynamic problems arising from engineering applications. The work consists of research and development of theoretical models to study these phenomena, in order to achieve a better understanding of their mathematical and statistical structures. Numerical simulations are employed to verify and assess the performance of these models.

The scope of study includes the following areas:

- Investigation of stability and bifurcation of periodic solutions, and the development of chaotic conditions for a continuous system via the Duffing oscillator.
- Investigation of stability and bifurcation of periodic solutions for a discrete system

such as the horizontal impact pair and the bouncing ball. Work also includes research in the universality of the Duffing oscillator via a discrete mapping.

- Development of multifractal theories for 1-D and 2-D chaotic dynamics.

1.5 Organization of Thesis

The body of this thesis, not including *Introduction* and *Conclusion*, consists of three main parts distributed into 9 chapters. Part I, consisting of 5 chapters, describes the nonlinear dynamical behavior of continuous systems modeled by the Duffing equation; Part II, comprising 2 chapters, discusses similar nonlinear behavior but for the discrete systems modeled by impact oscillators; and finally, Part III, composing of 2 chapters, introduces fractals and their applications in chaotic dynamics. The details are as follows:

In *Chapter* 1, an introduction of the doctoral research by presenting a literature survey of the major recent developments in bifurcation, chaos and fractal modeling is presented. Additionally, the thesis objective and scope of study are discussed.

In *Chapter* 2, the stability and bifurcations of periodic solutions for a nonlinear rod modeled by the Duffing equation are studied. Analytical results are obtained using the method of harmonic balance. Verification of the analytical result is carried out via numerical experimentations.

In *Chapter* 3, the theoretical chaotic conditions for the Duffing oscillator are derived based on an energy approach. Four types of Duffing oscillators including both undamped and damped systems, are identified. For the undamped system, the Chirikov overlap criterion approach and the renormalization group technique are used. For the damped system, the Melnikov method is employed. As before, verification through numerical simulations are performed.

In *Chapter* 4, an incremental energy method is presented to determine the critical conditions for predicting stochastic layers in forced Hamiltonian systems near their homoclinic/heteroclinic orbits. Stochastic layers for an undamped Duffing oscillator and also, an undamped forced planar-pendulum oscillator are investigated. The former represents the computation of the stochastic layer for the homoclinic orbit and the latter, for the heteroclinic orbit. Both the appearance and disappearance strengths of the stochastic layer for these two oscillators are determined. Numerical simulations for the two models are carried out for the purpose of model verification.

In *Chapter* 5, resonant layers near the resonant orbits for the undamped Duffing oscillator are investigated. Approximate conditions for predicting the appearance and disappearance of these resonance layers are established by the use of an incremental energy method. Once again, four types of the undamped Duffing oscillator are investigated. The results are compared not only with similar results computed via the Chirikov overlap criterion and the renormalization group technique but also with numerical simulations.

In *Chapter* 6, a qualitative investigation of the universal character of the damped Duffing oscillator is presented. The onset of chaos via period-doubling bifurcation of the discretized Duffing oscillator is predicted. Applying cubic renormalization to the discrete mapping of the Duffing oscillator, self-similarity leading to whole sequences of period doubling bifurcations is demonstrated. Numerical investigations are also carried out to observe the chaotic attractors of the damped Duffing oscillator.

In *Chapter* 7, the dynamics of a bouncing ball is revisited by computing its exact periodic solutions, stability and bifurcation conditions. The basic mapping and its Poincare mapping sections are established to facilitate the study of the regular and chaotic motions of the ball. Numerical experimentation is performed not only for the purpose of comparison with analytical results but also, to observe the chaotic attractors. Finally, physical motion associated with both the periodic and the chaotic motion are also plotted.

In *Chapter* 8, the dynamics of a horizontal impact pair subjected to a periodic base excitation is investigated. Based on its motion characteristics, mappings for four switch-planes are defined. From these mappings, five possible impact motions, Model I to V, are developed. The most studied model is the Model I motion which includes both the equispaced and non-equispaced impacts. Numerical simulations are also presented.

In *Chapter* 9, a highly accurate method to compute the period doubling bifurcation of a general 1-D iterative map is presented. The technique consists of constructing similar structures of the period doubling solutions and then applying a renormalization procedure to evaluate the appropriate length scaling factors. For period doubling bifurcations leading to chaos, this approach yields multifractal results of very high precision compared with the traditional multifractal analysis alone.

In *Chapter* 10, a new fractal theory is developed via a 1-D multifractal model. Application to Smale horseshoe invariant sets in chaotic dynamics is also carried out. Multifractal characteristics of these invariant sets generated by 1-D and 2-D horseshoe maps in chaotic dynamics are easily and directly determined.

In *Chapter* 11, several important results and observations of this doctoral research are summarized. In addition, further research is suggested.

PART I

CONTINUOUS SYSTEMS: DUFFING OSCILLATOR

CHAPTER 2

STABILITY AND BIFURCATIONS OF PERIODIC SOLUTIONS

In this chapter, an analytical approach for the quantitative predictions of stability and bifurcation of periodic solutions for the Duffing oscillator are presented. Physically, the oscillator considered is a nonlinear rod which is subjected to strong nonlinearities. Several methods for handling this situation are available: Barkham and Soudack (1969), and Yuste and Bejarano (1989, 1990) proposed an extended KB method; Burton and Rahman (1986) developed a multi-scale procedure; Garcia-Margallo and Bejarano (1987) suggested a generalized harmonic balance approach; and Xu and Cheung (1994) used an averaging technique based on generalized harmonic functions. In the work here, I employed an improved harmonic balance method to treat the strong nonlinearity. Verification via numerical simulation is performed and good accuracy is obtained.

2.1 Formulation of the Nonlinear Rod Dynamics

The model considered is a rod undergoing large displacements but at small strains. A sketch of the rod is depicted in *Figure* 2.1(a). It will be shown that this geometric nonlinearity manifest itself in the form of the cubic term in the Duffing equation. Consider an initially straight, long slender rod under the action of a compressive force P, shown in *Figure* 2.1(a). The usual engineering beam assumption of the bending plane sections not only remaining plane but also being perpendicular to the middle surface during deformations is invoked. Due to the small strain assumption in the model, Hook's law is applicable. A differential element of the rod is shown in *Figure* 2.1(b) where N,

Q_s and M represent the normal force, the shear force and the bending moment, respectively. Only planar vibration is considered here. Adopting the exact curvature, we have

$$\sin\theta = \frac{w_x}{\sqrt{(1+u_x)^2 + w_x^2}} \text{ and } \cos\theta = \frac{1+u_x}{\sqrt{(1+u_x)^2 + w_x^2}}, \tag{2.1}$$

where u and w are the axial and lateral deformations, respectively. Also, the subscript x denotes partial derivative with respect to x.

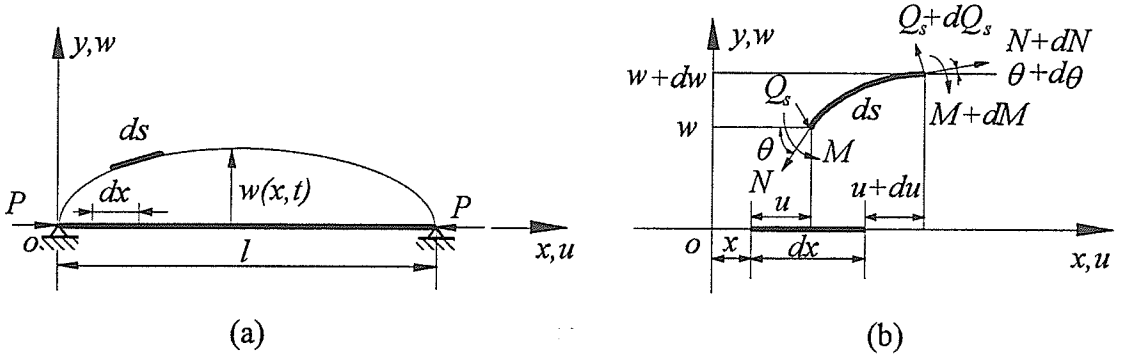

Figure 2.1 Nonlinear rod: (a) mechanical model and (b) differential element.

The bending moment M, based on exact curvature, is (Stoker (1968))

$$M = -EI\theta_s = -\frac{EI\theta_x}{\sqrt{(1+u_x)^2 + w_x^2}} = -\frac{EI\left[w_{xx}(1+u_x) - u_{xx}w_x\right]}{\left[\sqrt{(1+u_x)^2 + w_x^2}\right]^3}, \tag{2.2}$$

in which E, I, u and w are the Young's modulus, moment of inertia, respectively. The curve length $s = \int_0^x \sqrt{(1+u_x)^2 + w_x^2}\,dx$. The exact strain for the extensional nonlinearity is:

$$\varepsilon = \varepsilon_0 + \sqrt{(1+u_x)^2 + w_x^2} - 1, \tag{2.3}$$

where $\varepsilon_0 = -P/(EA)$ is an initial strain at the neutral axis of the beam. The instantaneous

force $N(x,t)$ is given by

$$N(x,t) = EA\varepsilon = -P + EA\left[\sqrt{(1+u_x)^2 + w_x^2} - 1\right]. \tag{2.4}$$

Note that A denotes the cross-sectional area. *Equation* (2.4) is identical to the expression given in Nayfeh and Mook (1979). As both bending and extensional nonlinearities are captured, the equations of motion for the planar vibration of the nonlinear rod based on the differential element shown in *Figure* 2.1(b) are

Axial component:

$$\rho A u_{tt} + \xi u_t - \frac{\partial}{\partial x}(N\cos\theta - Q_s \sin\theta) = X(t). \tag{2.5}$$

Transverse component:

$$\rho A w_{tt} + \xi w_t - \frac{\partial}{\partial x}(N\sin\theta + Q_s \cos\theta) = Y(t); \tag{2.6}$$

Rotational motion about the center of mass:

$$-\frac{\partial M}{\partial x} + Q_s\left[(1+u_x)\cos\theta + w_x \sin\theta\right] - N\left[w_x \cos\theta - (1+u_x)\sin\theta\right] = (1+u_x)\tilde{J}\theta_{tt}; \tag{2.7}$$

where ρ ξ, $\tilde{J}$, $X(t)$ and $Y(t)$ are the mass density, damping coefficient, mass moment of inertia per length of the rod, axial and lateral distributing loads in x and y directions, respectively. To simplify *Equation* (2.7), it is assumed that the rotational inertia is small and can be neglected. Thus we have from *Equation* (2.7),

$$Q_s = \frac{1}{\sqrt{(1+u_x)^2 + w_x^2}} \frac{\partial M}{\partial x}. \tag{2.8}$$

It is assumed that the longitudinal inertia and damping can be neglected. In our model, we considered only the loading situation of $X(t) = 0$ and $Y(t) = q(t)$. Substituting *Equation* (2.5) into *Equation* (2.6) and using *Equations* (2.1)-(2.4) and (2.8) we finally arrived at

the equation of motion for the nonlinear vibration of a rod. The result is,

$$\rho A w_{tt} + \xi w_t + P\left(w_{xx} - \frac{u_{xx}w_x}{1+u_x}\right) - (EA+P)\left(1 - \frac{1}{\sqrt{(1+u_x)^2 + w_x^2}}\right)\left(w_{xx} - \frac{u_{xx}w_x}{1+u_x}\right)$$
$$+ \frac{EI}{1+u_x}\frac{\partial^2}{\partial x^2}\left[\frac{w_{xx}(1+u_x) - w_x u_{xx}}{\left(\sqrt{(1+u_x)^2 + w_x^2}\right)^3}\right] - \frac{EI\left(u_{xx} + \frac{w_{xx}w_x}{(1+u_x)}\right)}{(1+u_x)^2 + w_x^2}\frac{\partial}{\partial x}\left[\frac{w_{xx}(1+u_x) - w_x u_{xx}}{\left(\sqrt{(1+u_x)^2 + w_x^2}\right)^3}\right] = q(t). \tag{2.9}$$

To solve *Equation* (2.9), boundary conditions corresponding to a hinged-hinged rod are used, namely,

$$\left.\begin{aligned} u = w = 0, \\ u_{xx} = w_{xx} = 0, \end{aligned}\right\} \quad \text{at } x = 0 \quad \text{and} \quad x = l. \tag{2.10}$$

Integrating *Equation* (2.5), we get

$$N\cos\theta - Q_s \sin\theta = e(t), \tag{2.11}$$

where $e(t)$ is an arbitrary function. Similar to Nayfeh (1973), we considered small transverse shear component in comparison with the normal force component, namely, $Q_s \sin\theta << N\cos\theta$ in *Equation* (2.11). In view of *Equations* (2.1) and (2.4), we have:

$$e(t) \approx \frac{-P + EA\left[\sqrt{(1+u_x)^2 + w_x^2} - 1\right]}{\sqrt{(1+u_x)^2 + w_x^2}}(1+u_x). \tag{2.12}$$

From *Equation* (2.12), we conclude that for small strains, $e(t) = O(P) << EA$. Also, the traditional assumptions in the beam theory, i.e., $|u| << |w|$ and $|u_x| << |w_x| < 1$, can be employed to further assist in the evaluation of *Equation* (2.12). Noting that, $u_x = O(w_x^2)$, *Equation* (2.12) reduces to,

$$u_x \approx \frac{P+e(t)}{EA} - \frac{1}{2}w_x^2 \tag{2.13}$$

Observe that $e(t)$ can now be easily solved from *Equation* (2.13). Invoking boundary conditions in *Equation* (2.10) and integrating, we get

$$\left.\begin{aligned} e(t) &= -P + \frac{EA}{2l}\int_0^l w_x^2 dx, \\ u_x &\approx \frac{1}{2l}\int_0^l w_x^2 dx - \frac{1}{2}w_x^2. \end{aligned}\right\} \tag{2.14}$$

Substituting *Equation* (2.14) into *Equation* (2.9) and applying the beam assumptions, we finally get the 1-D differential equation governing the motion of the nonlinear rod, that is,

$$\rho A w_{tt} + \xi w_t + \left[\frac{Pw_{xx}}{\sqrt{1+\frac{1}{l}\int_0^l w_x^2 dx}} - EAw_{xx}\left(1 - \frac{1}{\sqrt{1+\frac{1}{l}\int_0^l w_x^2 dx}}\right)\right]\frac{\left(1+\frac{1}{2l}\int_0^l w_x^2 dx + \frac{1}{2}w_x^2\right)}{\left(1+\frac{1}{2l}\int_0^l w_x^2 dx - \frac{1}{2}w_x^2\right)} \tag{2.15}$$

$$+ EI\left[\frac{w_{xxxx}\left(1+\frac{1}{2}w_x^2 + \frac{1}{2l}\int_0^l w_x^2 dx\right) + 3w_{xxx}w_{xx}w_x + w_{xx}^3}{\left(\sqrt{1+\frac{1}{l}\int_0^l w_x^2 dx}\right)^3\left(1+\frac{1}{2l}\int_0^l w_x^2 dx - \frac{1}{2}w_x^2\right)}\right] = q(t).$$

Except for certain limiting cases, it is difficult to solve *Equation* (2.15) exactly. We will further introduce appropriate approximations so as to make the problem mathematically tractable. The assumption of $w_x < 1$ enables us to approximate the irrational terms in *Equation* (2.15) by means of a Taylor series expansion. For simplicity, we will neglect all powers of 5 and above. Thus we have:

$$\rho A w_{tt} + \xi w_t + P w_{xx}\left(1 + w_x^2 - \frac{1}{2l}\int_0^l w_x^2 dx\right) - EA w_{xx}\frac{1}{2l}\int_0^l w_x^2 dx + EI\left[w_{xxxx}\left(1 + w_x^2 - \frac{3}{2l}\int_0^l w_x^2 dx\right) + 3w_{xxx}w_{xx}w_x + w_{xx}^3\right] = q(x,t). \tag{2.16}$$

Assuming $w(x,t) = F(t)\sin(m\pi x/l)$ for the simply supported boundary conditions, and applying the Galerkin method to *Equation* (2.16) we get:

$$a f_{tt} + (P_{mcr} - P)f + \frac{1}{4}[EA - 2P_{mcr}]f^3 = Q(t), \tag{2.17}$$

where $f = f(t) = m\pi F(t)/l$, $a = l\rho A/(m\pi)$ and $P_{mcr} = (m\pi)^2 EI/l^2$. There are only four cases to be considered in solving *Equation* (2.17), as all the other remaining cases produce diverging results. These four cases are:

$$\left.\begin{array}{ll} \text{Case I} & P_{mcr} > P,\ 2P_{mcr} < EA \\ \text{Case II} & P_{mcr} > P,\ 2P_{mcr} > EA \\ \text{Case III} & P_{mcr} = P,\ 2P_{mcr} < EA \\ \text{Case IV} & P_{mcr} < P,\ 2P_{mcr} < EA\text{: } (a)E_0 > 0,\ (b)E_0 < 0 \text{ and } (c)E_0 = 0 \end{array}\right\} \tag{2.18}$$

where E_0 is the initial energy (or non-time dependent Hamiltonian, unperturbed Hamiltonian) defined in *Chapter* 3. The external excitation assumed is $Q = aQ_0\cos\Omega t$, where the parameter a is inserted for convenience. Furthermore, introducing $\alpha_1 = (P_{mcr} - P)/a$, $\alpha_2 = (EA - 2P_{mcr})/4a$, $\delta = \xi l/(m\pi a)$ and $x = f$, *Equation* (2.17) becomes

$$\ddot{x} + \delta\dot{x} + \alpha_1 x + \alpha_2 x^3 = Q_o\cos\Omega t. \tag{2.19}$$

Observe that *Equation* (2.19) takes the form of the Duffing equation. *Equation* (2.18) should now be re-expressed in terms of the newly defined parameters $\alpha_1, \alpha_2, \delta, \Omega$ and Q_0, and the results are listed in *Table* 2.1.

Table 2.1 Four Types of Duffing oscillator

Case I	$\alpha_1 > 0$ and $\alpha_2 > 0$	$\ddot{x} + \delta\dot{x} + \alpha_1 x + \alpha_2 x^3 = Q_o \cos\Omega t$
Case II	$\alpha_1 > 0$ and $\alpha_2 < 0$	$\ddot{x} + \delta\dot{x} + \alpha_1 x - \lvert\alpha_2\rvert x^3 = Q_o \cos\Omega t$
Case III	$\alpha_1 = 0$ and $\alpha_2 > 0$	$\ddot{x} + \delta\dot{x} + \alpha_2 x^3 = Q_o \cos\Omega t$
Case IV	$\alpha_1 < 0$ and $\alpha_2 > 0$; (a) $E_0 > 0$, (b) $E_0 < 0$, (c) $E_0 = 0$	$\ddot{x} + \delta\dot{x} - \lvert\alpha_1\rvert x + \alpha_2 x^3 = Q_o \cos\Omega t$

2.2 Periodic Solutions, Stability and Bifurcation

In this section, the development of an analytical procedure for the determination of the stability and bifurcation of periodic solutions of *Equation* (2.19) is presented. We will begin our discussion by first deriving the periodic solutions, and then we will examine their stability and bifurcation.

2.2.1 Periodic Solutions

Assume a periodic solution of *Equation* (2.19) to be given as follows:

$$x = u(t)\sin\Omega t + v(t)\cos\Omega t. \tag{2.20}$$

Substituting *Equation* (2.20) into *Equation* (2.19) yields:

$$\left.\begin{aligned} \frac{du}{dt} &= -k_{12}u + k_{11}v - k_{13}u(u^2+v^2) - k_{14}v(u^2+v^2) + k_{15} \\ \frac{dv}{dt} &= -k_{11}u - k_{12}v + k_{14}u(u^2+v^2) - k_{13}v(u^2+v^2) + k_{16} \end{aligned}\right\}, \tag{2.21}$$

in which the coefficients are defined as follows,

$$\left.\begin{aligned} k_{11} &= \frac{\Omega(2\Omega^2+\delta^2-2\alpha_1)}{4\Omega^2+\delta^2},\ k_{12} = \frac{(\Omega^2+\alpha_1)\delta}{4\Omega^2+\delta^2},\ k_{13} = \frac{3\delta\alpha_2}{4\left(4\Omega^2+\delta^2\right)} \\ k_{14} &= \frac{3\Omega\alpha_2}{2\left(4\Omega^2+\delta^2\right)_1},\ k_{15} = \frac{2\Omega Q_0}{4\Omega^2+\delta^2},\ k_{16} = \frac{\delta Q_0}{4\Omega^2+\delta^2} \end{aligned}\right\}. \tag{2.22}$$

Since periodic solutions of *Equation* (2.19) are computed from the static equilibrium solutions of *Equation* (2.20), we set $du/dt = 0$ and $dv/dt = 0$. This leads to,

$$\left.\begin{aligned} \delta\Omega u_0 + \left[\left(\alpha_1-\Omega^2\right)+\frac{3}{4}\alpha_1\left(u_0^2+v_0^2\right)\right]v_0 &= Q_0 \\ -\delta\Omega v_0 + \left[\left(\alpha_1-\Omega^2\right)+\frac{3}{4}\alpha_1\left(u_0^2+v_0^2\right)\right]u_0 &= 0 \end{aligned}\right\}. \tag{2.23}$$

Note that the k-coefficients have been replaced by their actual expressions in *Equation* (2.23). Also, the symbols u_0, v_0 represent the steady-state solutions. It is not easy to directly solve for u_0, v_0 in *Equation* (2.23). An indirect approach is necessary and this involves introducing $A = \sqrt{u_0^2+v_0^2}$ to denote the system response amplitude. In view of this, *Equation* (2.23) can now be compactly written as,

$$\left[\left(\alpha_1-\Omega^2\right)+\frac{3}{4}\alpha_2 A^2\right]^2 A^2 + \delta^2\Omega^2 A^2 = Q_0^2. \tag{2.24}$$

Observe that *Equation* (2.24) depicts the relationship between the response amplitude A and the system parameters $\alpha_1, \alpha_2, \Omega$ and Q_0. From *Equation* (2.24), it is easy to solve for A. Having determined this quantity, we can proceed to solve for u_0, v_0 from *Equation* (2.23) by noting that $u_0^2 + v_0^2 = A^2$. The results are,

$$u_0 = \frac{\delta\Omega A^2}{Q_0} \text{ and } v_0 = \frac{\left[\left(\alpha_1-\Omega^2\right)+\frac{3}{4}\alpha_1 A^2\right]A^2}{Q_0}. \tag{2.25}$$

Finally, the periodic solution is obtained by substituting *Equation* (2.25) into *Equation*

(2.20) and we get,

$$x = \frac{1}{Q_0}\left\{\delta\Omega A^2 \sin\Omega t + \left[\left(\alpha_1 - \Omega^2\right) + \frac{3}{4}\alpha_1 A^2\right] A^2 \cos\Omega t\right\}. \tag{2.26}$$

2.2.2 Stability and Bifurcation

Having solved for the steady-state solutions, we next examine their stability and bifurcation. To accomplish this task, it is necessary to linearize *Equation* (2.21) in the neighborhood of the steady-state solution (u_0, v_0) via a Taylor series expansion. Introducing $\xi = u - u_0$ and $\eta = v - v_0$, *Equation* (2.21) is linearized to

$$\begin{pmatrix}\dot{\xi}\\ \dot{\eta}\end{pmatrix} = Df(u_0, v_0)\begin{pmatrix}\xi\\ \eta\end{pmatrix}, \tag{2.27}$$

in which

$$Df(u_0, v_0) = \begin{bmatrix} -k_{12} - k_{13}\left(3u_0^2 + v_0^2\right) - 2k_{14}u_0v_0 & k_{11} - 2k_{13}u_0v_0 - k_{14}\left(u_0^2 + 3v_0^2\right) \\ -k_{11} - 2k_{13}u_0v_0 + k_{14}\left(3u_0^2 + v_0^2\right) & -k_{12} - k_{13}\left(u_0^2 + 3v_0^2\right) + 2k_{14}u_0v_0 \end{bmatrix}. \tag{2.28}$$

The characteristic equation of *Equation* (2.27) is therefore given by

$$\lambda^2 + Tr(Df_0)\lambda + Det(Df_0) = 0, \tag{2.29}$$

where the trace and determinant of the linearized matrix are defined respectively as

$$\left.\begin{aligned} Tr(Df_0) &= -2k_{12} - 4k_{13}A^2 \\ Det(Df_0) &= k_{11}^2 + k_{12}^2 + 4\left(k_{12}k_{13} - k_{11}k_{14}\right)A^2 + 3\left(k_{13}^2 + k_{14}^2\right)A^4 \end{aligned}\right\}. \tag{2.30}$$

Having expressed *Equation* (2.28) in a matrix form, it is now easy to determine the stability of periodic solution through an eigenanalysis. Since the steps are mechanical, we will just summarize the analytical results here as follows.

Stability Conditions

(a) The conditions for stable periodic solutions corresponding to a stable focus are,

$$\left.\begin{aligned} &2\left(\Omega^2+\alpha_1\right)+3\alpha_2A^2>0 \\ &\Omega^2\left(2\Omega^2+\delta^2-2\alpha_1\right)^2+\delta^2\left(\Omega^2+\alpha_1\right)^2+3\alpha_2\left(\delta^2+4\Omega^2\right)\left[\left(\alpha_1-\Omega^2\right)+\frac{9}{16}\alpha_2A^2\right]A^2>0 \end{aligned}\right\}. \quad (2.31)$$

(b) The conditions for unstable periodic solutions corresponding to an unstable focus are,

$$\left.\begin{aligned} &2\left(\Omega^2+\alpha_1\right)+3\alpha_2A^2<0 \\ &\Omega^2\left(2\Omega^2+\delta^2-2\alpha_1\right)^2+\delta^2\left(\Omega^2+\alpha_1\right)^2+3\alpha_2\left(\delta^2+4\Omega^2\right)\left[\left(\alpha_1-\Omega^2\right)+\frac{9}{16}\alpha_2A^2\right]A^2>0 \end{aligned}\right\}. \quad (2.32)$$

(c) The conditions for unstable periodic solution corresponding to a saddle is,

$$\Omega^2\left(2\Omega^2+\delta^2-2\alpha_1\right)^2+\delta^2\left(\Omega^2+\alpha_1\right)^2+3\alpha_2\left(\delta^2+4\Omega^2\right)\left[\left(\alpha_1-\Omega^2\right)+\frac{9}{16}\alpha_2A^2\right]A^2<0\,. \quad (2.33)$$

It is also trivial to obtain the associated bifurcation conditions for the periodic solutions. As before, we will simply summarize the results as follows.

Bifurcation Conditions

(a) Hopf bifurcation occurs when

$$\left.\begin{aligned} &A^2=-\frac{2}{3}\frac{\Omega^2+\alpha_1}{\alpha_2}\geq 0 \\ &Q_0^2=-\frac{1}{6}\frac{\Omega^2+\alpha_1}{\alpha_2}\left[\left(3\Omega^2-\alpha_1^2\right)^2+4\delta^2\Omega^2\right] \\ &\Omega^2\left(2\Omega^2+\delta^2-2\alpha_1\right)^2+\delta^2\left(\Omega^2+\alpha_1\right)^2-\frac{1}{4}\left(\alpha_1+\Omega^2\right)\left(\delta^2+4\Omega^2\right)\left(5\alpha_1-11\Omega^2\right)>0 \end{aligned}\right\}. \quad (2.34)$$

(b) Saddle-node bifurcation occurs when

$$\left.\begin{aligned} A^2 &= \frac{4}{9\alpha_2}\left[2\left(\Omega^2-\alpha_1\right)\pm\sqrt{\left(\Omega^2-\alpha_1\right)^2-3\delta^2\Omega^2\left(\frac{\delta^2-4\alpha_1}{\delta^2+4\Omega^2}\right)^2}\right]\geq 0 \\ Q_0{}^2 &= \frac{4}{81\alpha_2}\left[\left(\left(\alpha_1-\Omega^2\right)\pm\sqrt{\left(\Omega^2-\alpha_1\right)^2-3\delta^2\Omega^2\left(\frac{\delta^2-4\alpha_1}{\delta^2+4\Omega^2}\right)^2}\right)^2+9\delta^2\Omega^2\right] \\ &\quad\times\left[2\left(\Omega^2-\alpha_1\right)\pm\sqrt{\left(\Omega^2-\alpha_1\right)^2-3\delta^2\Omega^2\left(\frac{\delta^2-4\alpha_1}{\delta^2+4\Omega^2}\right)^2}\right] \end{aligned}\right\}. \qquad (2.35)$$

For the occurrence of the saddle-node bifurcation in going from the stable node to the saddle, we must satisfy the following additional condition,

$$\left(\Omega^2+\alpha_1\right)+\frac{2}{3}\left[2\left(\Omega^2-\alpha_1\right)\pm\sqrt{\left(\Omega^2-\alpha_1\right)^2-3\delta^2\Omega^2\left(\frac{\delta^2-4\alpha_1}{\delta^2+4\Omega^2}\right)^2}\right]>0. \qquad (2.36)$$

Similarly, for the saddle-node bifurcation to occur in going from the unstable node to the saddle, the additional condition is,

$$\left(\Omega^2+\alpha_1\right)+\frac{2}{3}\left[\left(\Omega^2-\alpha_1\right)\pm\sqrt{\left(\Omega^2-\alpha_1\right)^2-3\delta^2\Omega^2\left(\frac{\delta^2-4\alpha_1}{\delta^2+4\Omega^2}\right)^2}\right]<0. \qquad (2.37)$$

Next, a qualitatively sketch of the nature of the stability of the periodic solutions (or more precisely, period-1 solutions) for the four case types is presented. As shown in *Figure* 2.2, stable solutions are represented by the bold solid lines and unstable solutions by the dash lines. *Figures* 2.2(a) to (d) correspond to Cases I to IV respectively. Observe that for Cases I and III, the unstable solution is bounded by the 'outer' and 'inner' stable solutions. For Case II the 'outer' and 'inner' stable solutions encapsulating the unstable solutions occur entirely inside the heteroclinic orbit. Outside the heteroclinic orbit, we have only the unstable solutions (not shown). The behavior of the periodic solutions for Case IV is even more complicated. Observe that the 'outer' and 'inner' stable solutions encapsulating the

unstable solutions occur outside the homoclinic orbit, and therefore are termed "large-orbit" solutions. However, upon a careful inspection, there exists a 'large' orbit solution at the *crossing* of the homoclinic orbit and is shown by the dash line, i.e., unstable. It should be mentioned that it is not possible to analyze this solution via the present procedure. *Inside* the homoclinic orbit (two potential wells), there are the so-called, "small-orbit" solutions. To study the nature of these solutions, an alternative approach has been proposed by Luo and Han (1995e) and Han and Luo (1995a), but not reported here.

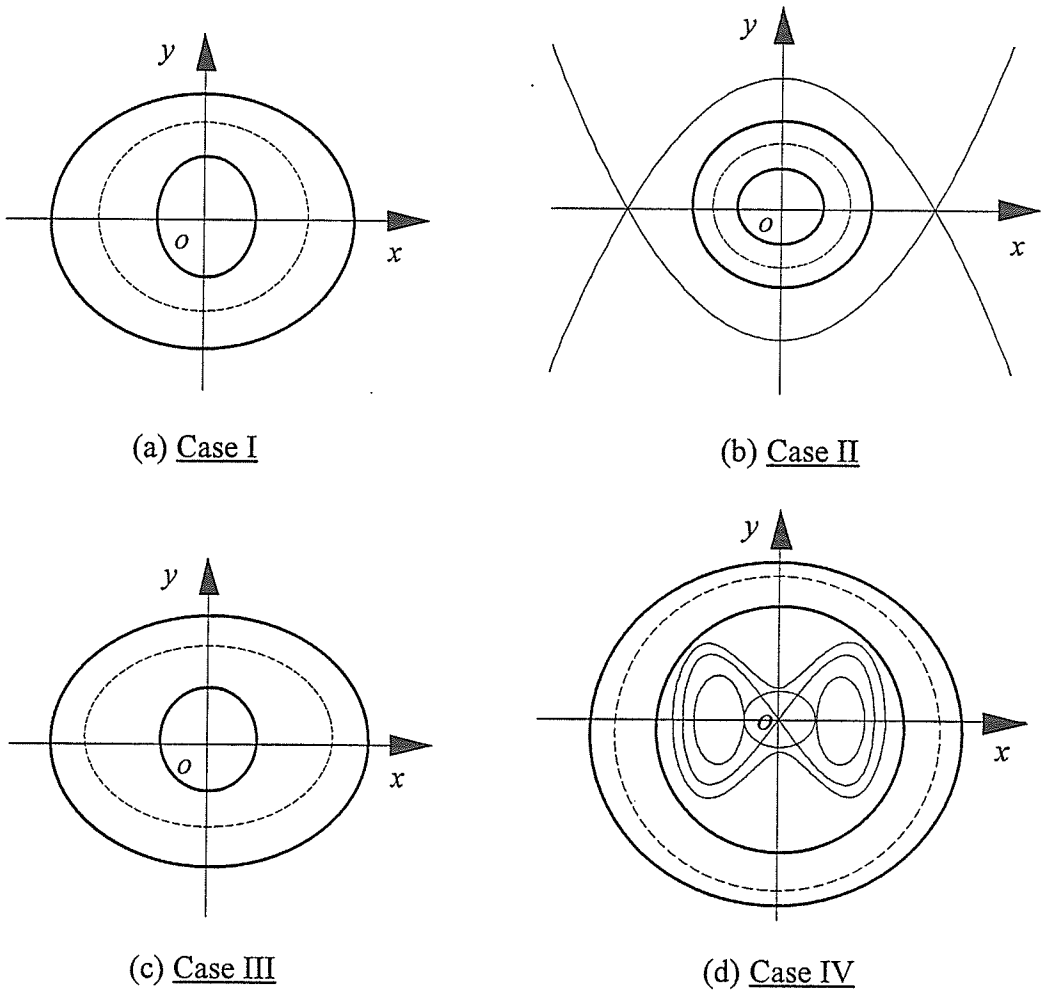

Figure 2.2 Phase trajectories of the damped driven Duffing oscillator (—— stable, — — unstable).

2.3 Comparison of Analytical Results with Numerical Solutions

A comparison of the analytical predictions with the numerical results is outlined here. The intention is not only to verify the proposed method, but also, to demonstrate the analytical procedure by carrying out a parametric study. We will restrict our model to the period-1 motion of the Duffing oscillator.

The term 'numerical solutions' is used here to imply results obtained via a numerical integration of the differential equations. The algorithm employed is based on the automatic time-stepping Runge-Kutta integrator (a standard IMSL routine). To minimize the computational effort, we adopted the initial conditions calculated by the analytical method. The results are plotted in *Figure* 2.3 where the lines denote the analytical response and the symbols the numerical solutions in the excitation frequency-response amplitude curves. Note also, the solid, dash and dot lines respectively represent, the stable, saddle and unstable focus (or node)-type periodic solutions. Obviously, only stable period-1 solutions are obtained in the numerical simulation. In addition, the hatched areas indicate numerically computed complex motions which could include higher-periodic and chaotic motions. Also, the subharmonic solutions are not considered in these regions of complex motions.

As shown in the graphs, the lines and the symbols match quite closely indicating good agreement between the analytical and numerical solutions. However, at the tip of the curves, the agreement is not that great and this is attributed to the fact that we did not consider the superharmonic terms in the assumed solutions. As presented in Han and Luo (1994), the exact undamped period-1 solutions take the form of the highly complicated Jacobi-elliptic functions. The overall good agreement indicates that our proposed analytical model is sufficiently accurate and can be a viable alternative to the tedious and extremely time-consuming numerical simulations.

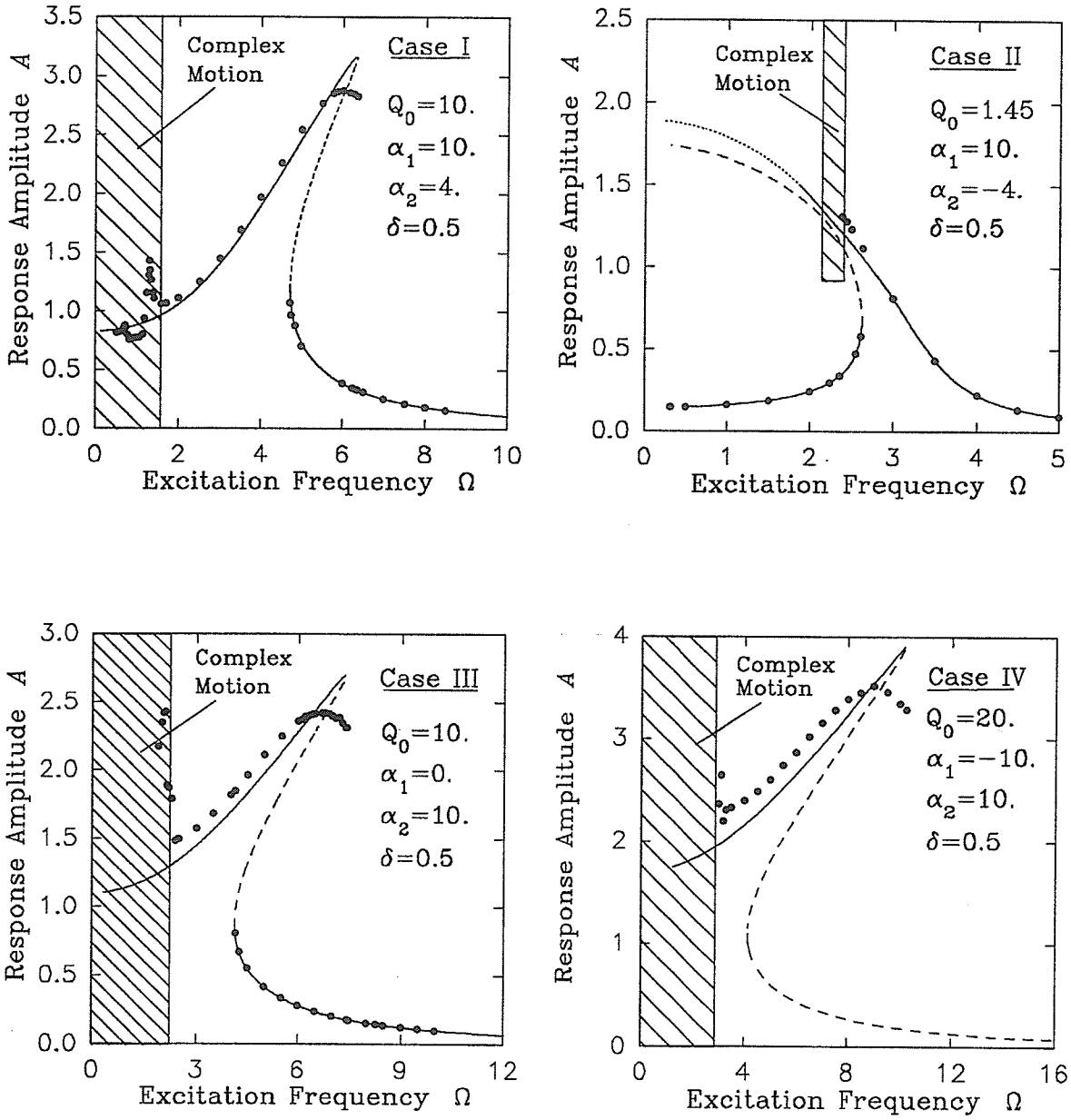

Figure 2.3 Comparison between analytical and numerical results for stable and unstable manifolds for Cases I-IV in $A-\Omega$ plane (—— stable, — — unstable, • • • numerical results).

Having verified the analytical model, it would be useful to carry out some parametric studies of the method. The parameter manifolds involving the excitation frequency Ω versus the excitation amplitude Q_0 is plotted in *Figure* 2.4, and the excitation frequency Ω versus the response amplitude A in *Figure* 2.5. For both plots, $\delta = 0.5$ is used. Once again, all four loading cases are considered. We first present a discussion of *Figure* 2.4, followed by a discussion of *Figure* 2.5.

Note that in *Figure* 2.4, the broken lines (i.e. dot and dash lines) represent the symmetric saddle and saddle-node bifurcation in going from the saddle to the unstable node (or vice-versa), respectively. Also, the bold and thin continuous lines mark the boundaries of the Hopf (HB) and saddle-node (SNB) bifurcations, respectively. Observe that the graphs for Cases I and III are very similar in that they only have SNB and thus, they will be discussed together. They have only two regions; in Regions I there is only one period-1 solution which is stable; and in Region II are three period-1 solutions, 2 stable and 1 unstable. As Ω increases, the Region II solution jumps to the Region I at the lower branch of the SNB and likewise, as Ω decreases, the jump occurs at the upper branch of the SNB.

Next, we discuss the Cases II and IV which have five regions of stability, Regions I-V. For Case II, there are one stable, one saddle and one unstable node or focus solutions in Regions I and II. In Region III, we have only one unstable focus or node solution; in Region IV, only one stable focus solution and finally, in Region V, there are three solutions, of which one is a saddle, and the other two are stable. In going from Regions IV to III and from Regions V to II, HB takes place; and in going from Regions IV into V, SNB is observed. For Case IV, the solutions in Regions I and II are similar to Case II. However, for Region III there exists only one stable solution; in Region IV, there is only one saddle among the three equilibrium solutions; and finally, in Region V, there exists one stable solution. Note also that the points (a, b, c) marked in the figure will be discussed later as these are used in the numerical simulation section.

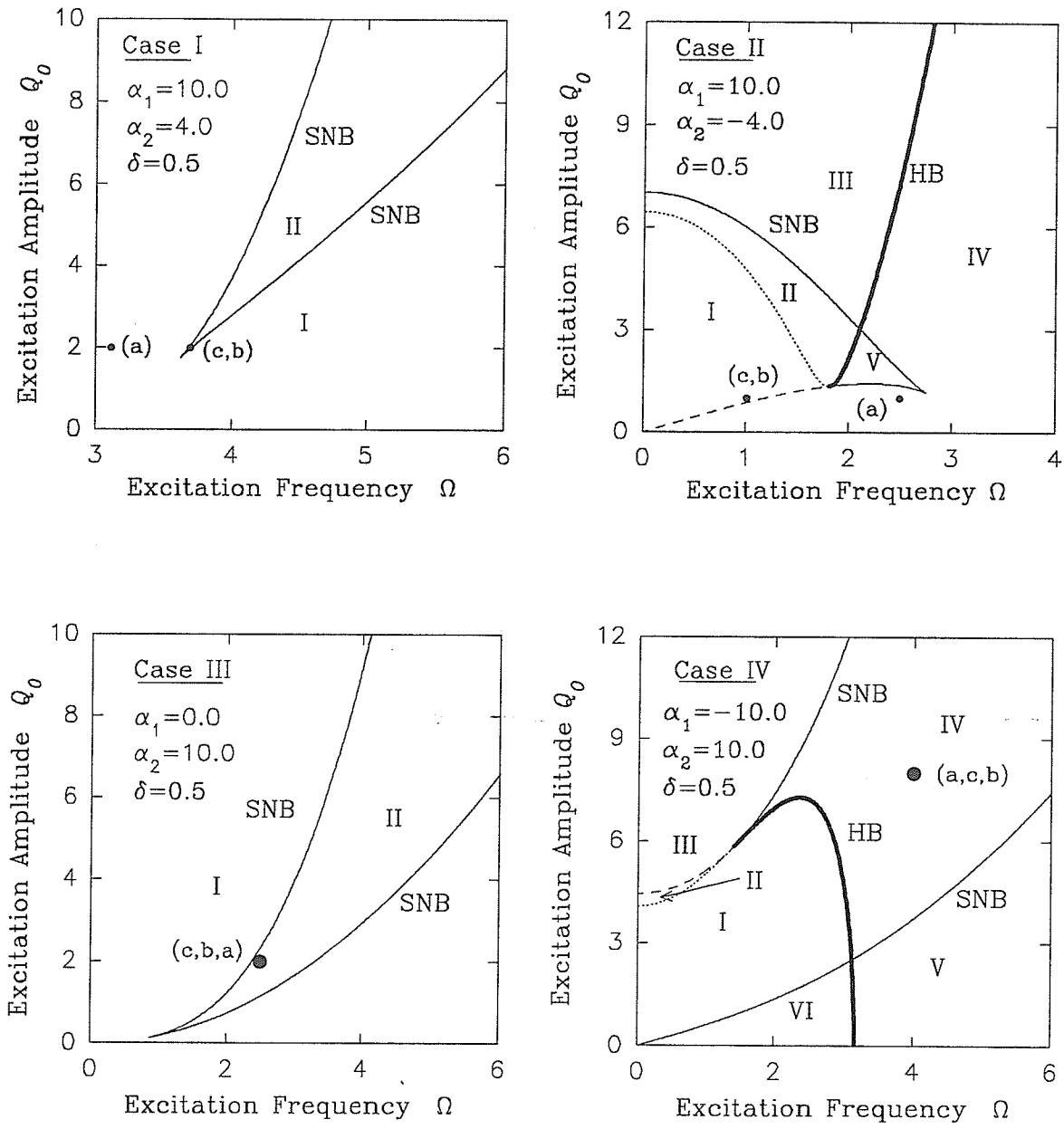

Figure 2.4 Analytical stability and bifurcation conditions for Cases I-IV in $Q_0 - \Omega$ plane (—— stable SNB, —— HB, — — unstable SNB, ---- symmetric saddle).

Figure 2.5 shows the stable and unstable manifolds in the Ω-A plot for Cases I-IV, for varying Q_0. Note that here we employed the following line notations: solid, dash and dot lines to denote respectively the stable, saddle and unstable focus solutions. As before, Cases I and III are very similar where the two stable branches connected by one unstable branch. However, this is not necessarily the situation with Cases II and IV where for some of the curves, the stable branch becomes unstable. As in *Figure* 2.4, the points (a)-(c) will be discussed later as these are used in the numerical simulation section.

2.4 Numerical Simulations

Numerical integration of *Equation* (2.19) for its period-1 solutions are presented here. To expedite the numerical experimentation, the analytically computed stability conditions are employed in the computer simulations. The motivation for this section is to produce a computerized plot of the phase portraits, similar to the hand-drawn plot in page 72 of Guckenheimer and Holmes (1983). It should be pointed out that our numerical simulation is based on the original equation of motion for the Duffing oscillator (*Equation* (2.19)) whereas in Guckenheimer and Holmes (1983), they used the approximate equations (similar to our *Equation* (2.21)). In our opinion, it is more appropriate to use the original equation rather than the approximate equation.

Input data comprising system parameters and initial conditions for the numerical simulation are tabulated in *Table* 2.2. For the selected stability conditions, the appropriate system parameters are computed from the analytical model. The initial conditions are calculated rather than prescribed, as done traditionally. The basis of the computation of these initial conditions is by solving *Equation* (2.26), re-expressed here as follows,

$$x_0 = \frac{\left[\left(\alpha_1 - \Omega^2\right) + \frac{3}{4}\alpha_1 A^2\right] A^2}{Q_0}, \quad \dot{x}_0 = \frac{\delta \Omega^2 A^2}{Q_0} \qquad \text{at } t = 0.0. \tag{2.38}$$

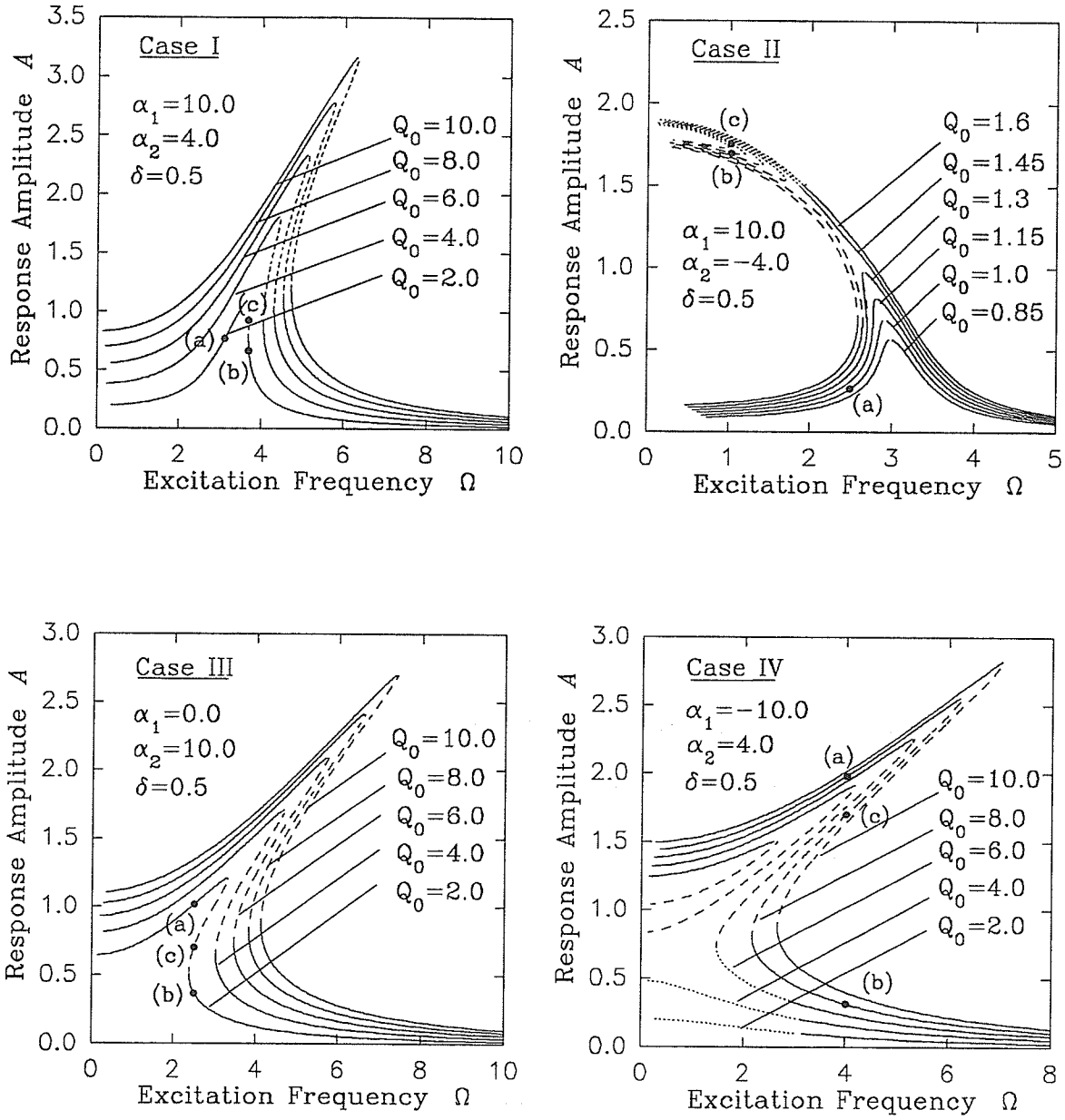

Figure 2.5 Analytically stable and unstable manifolds for Cases I-IV in $A-\Omega$ plane (—— stable,— — saddle, ---- unstable node).

Table 2.2 Computed input data for numerical simulations for periodic solutions

$\delta = 0.5$		α_1	α_2	Q_0	Ω	Initial Conditions x_0	$\dot{x}_0$	Stability Status
Case I	(a)	10.0	4.0	2.0	3.11446	0.616269	1.437760	Stable
	(b)				3.70101	-0.524218	1.514300	Stable
	(c)				3.69951	-0.478948	2.927610	Unstable
Case II	(a)	10.0	-4.0	1.0	2.49546	0.250093	0.218681	Stable
	(b)				1.01700	0.854611	1.494450	Unstable
	(c)				1.01125	-0.809155	1.574860	Unstable
Case III	(a)	0.0	10.0	2.0	2.50921	0.783871	1.637621	Stable
	(b)				2.50695	-0.359914	0.215098	Stable
	(c)				2.50463	-0.632589	0.779483	Unstable
Case IV	(a)	-10.0	10.0	8.0	4.00683	1.722370	3.953690	Stable
	(b)				4.00772	-0.314018	0.099608	Unstable*
	(c)				4.00572	-1.541860	2.915350	Unstable

*This result can be proved using an alternative analytical method (Han and Luo (1995a), and Luo and Han (1995e)).

Using these computed initial conditions, we are able to exactly predict the period-1 solutions. Note that (a)-(c) marked in *Table* 2.2 correspond to points (a)-(c) in *Figures* 2.4-2.5. The time interval employed in the numerical integration is 50 seconds, starting from 0. The results are presented in *Figure* 2.6. The starting points for the phase portraits are marked by the dots labeled with an "I.C.". Once again, all four cases are presented.

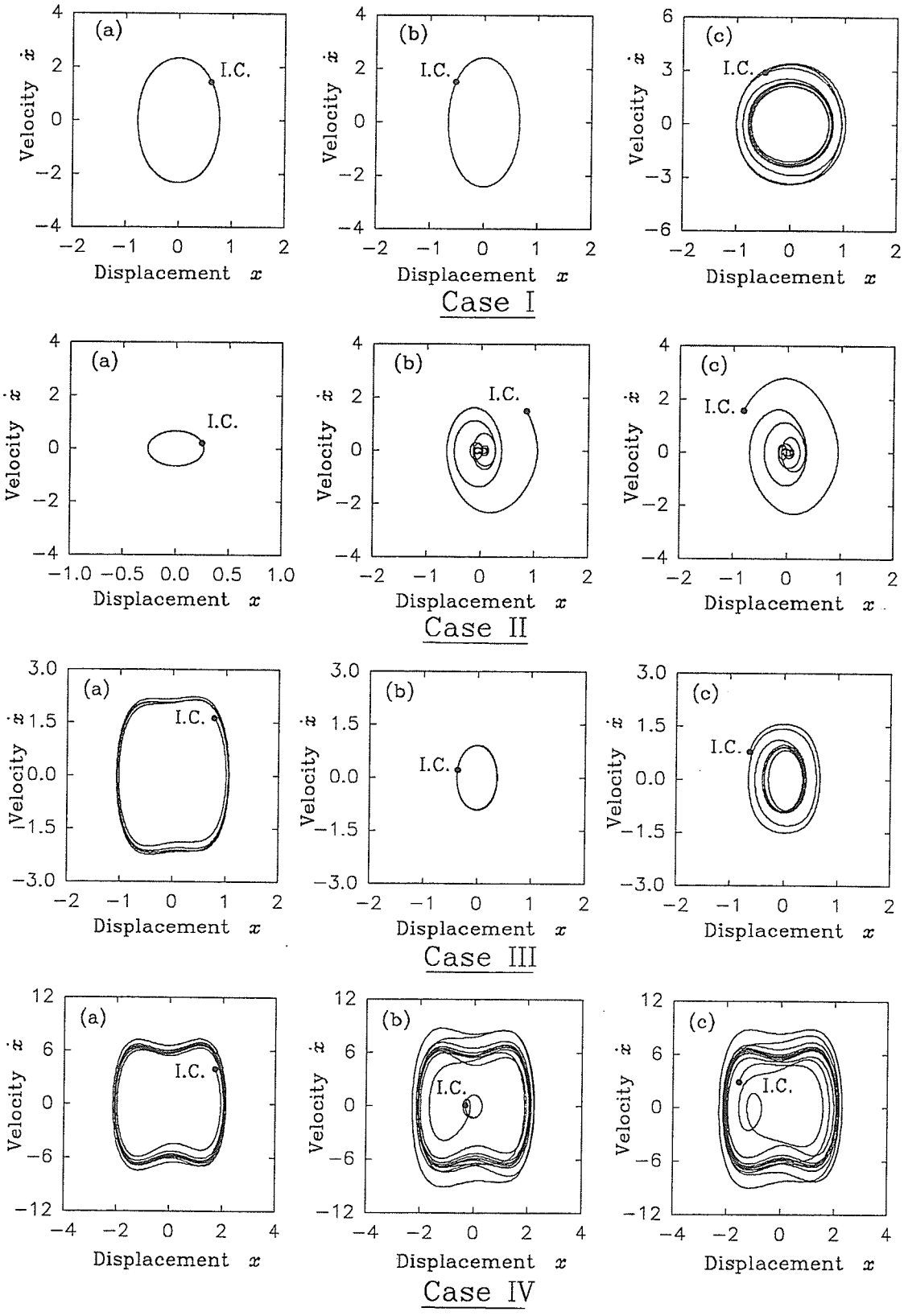

Figure 2.6 Phase portraits for Cases I-IV.

Graphs (a)-(c) of Case I show two stable and one unstable (saddle) solutions as predicted by the analytical model, and they correspond to points (a)-(c) of Case I in *Figures* 2.4-2.5. Observe that the stable periodic solution exhibits only one cycle. On the other hand, the unstable solution which cannot maintain this status quo in the numerical simulation, must eventually move to the stable solution as it passes through its transients.

In Case II, graphs (a)-(c) confirm that there are only one analytically predicted stable and two unstable (saddle and unstable node) solutions and they correspond exactly to points (a)-(c) of Case II in *Figures* 2.4-2.5. As before, the two numerically determined unstable solutions must move eventually to their stable solutions via their transients.

In Case III, graphs (a)-(c) exhibit two stable and one unstable (saddle) solutions, which agree completely with the analytical predictions. Note that these graphs correspond to points (a)-(c) of Case III in *Figures* 2.4-2.5. Observe that the periodic solution of graph (a) is not exactly an expected single orbit, but rather a series of very close orbits and this is due to the not so precise agreement with the analytical model as shown in Case III of *Figure* 2.3. Also, as before, the unstable solution in graph (c) eventually gravitates to a stable solution via several transient states.

In Case IV, graphs (a)-(c) show one stable and two unstable solutions as predicted analytically, and they correspond to points (a)-(c) in *Figures* 2.4-2.5. As in Case III (a), graph (a) of Case IV exhibits similar behavior and once again, the absence of an expected single orbit is due to the imprecision of the analytical model which is evident in Case IV of *Figure* 2.3. The unstable solution in graph (b) is of the saddle-type as defined by Guckenheimer and Holmes (1983) (see page 87). The two unstable solutions in graphs (b)-(c) must eventually move to the stable solutions by going through several transients. We should also point out that the predictions here are only for large orbits. For small orbits, this technique does not work and an alternative method as reported in Luo and Han (1995e), and Han and Luo (1995a) must be employed.

2.5 Conclusions

An improved harmonic balance technique for predicting stability and bifurcation of periodic solutions in a nonlinear dynamic system is presented via an investigation of the Duffing oscillator. Comparison of the analytical model with numerical simulation are shown and good agreement is observed. Using these analytical conditions, stable and unstable manifolds are plotted in the amplitude-frequency curves. All input data for the numerical simulations are calculated and not prescribed as done traditionally. This significantly reduces the amount of numerical experimentations required to simulate the nonlinear dynamics phenomena. The number of numerically determined stable and unstable solutions agree exactly with the analytical predictions.

CHAPTER 3

ANALYTICAL CONDITIONS FOR CHAOS

It is very useful to be able to predict the onset of chaos and strange attractors in a nonlinear dynamical system. There are only a handful of analytical methods available for the determination of critical conditions for the onset of chaos. Methods such as the Chirikov resonance overlap criterion (Chirikov (1979)), and the renormalization group technique (Escande and Doveil (1981), Escande (1985)) yield critical conditions for the undamped Duffing oscillator near subharmonic resonant orbits. For a weakly damped oscillator, the Melnikov method is available for the computation of the critical conditions for chaos and subharmonic bifurcations (Moon and Holmes (1979), Moon (1980a) and Holmes and Moon (1983)). The stability and bifurcation of the Duffing oscillator were studied in the previous chapter. In this chapter, four cases of *Equation* (2.19) corresponding to an undamped oscillator are considered. The equivalent forms of their first order differential equations are:

Case I:
$$\left.\begin{aligned}\dot{x} &= y \\ \dot{y} &= -\alpha_1 x - \alpha_2 x^3 + Q_0 \cos(\Omega t)\end{aligned}\right\}, \tag{3.1}$$

Case II:
$$\left.\begin{aligned}\dot{x} &= y \\ \dot{y} &= -\alpha_1 x + \alpha_2 x^3 + Q_0 \cos(\Omega t)\end{aligned}\right\}, \tag{3.2}$$

Case III:
$$\left.\begin{aligned}\dot{x} &= y \\ \dot{y} &= -\alpha_2 x^3 + Q_0 \cos(\Omega t)\end{aligned}\right\}, \tag{3.3}$$

Case IV:
$$\left.\begin{aligned}\dot{x} &= y \\ \dot{y} &= \alpha_1 x - \alpha_2 x^3 + Q_0 \cos(\Omega t)\end{aligned}\right\}; \text{ (a) } E_0 > 0, \text{ (b) } E_0 < 0, \text{ (c) } E_0 = 0, \tag{3.4}$$

in which all parameters α_1, α_2, Q_0, Ω and E_0 are positive and represent respectively, the system parameters, the excitation amplitude and frequency, and initial energy.

3.1 Energy Analysis for Case I

We first present the procedure of the determination of critical conditions for Case I as governed by *Equation* (3.1). Then, we will simply state the results for Cases II-IV(b) in *Appendix* B.1. The remaining Case IV(c) requires special handling and will be treated in a separate section. From *Equation* (3.1), the Hamiltonian for Case I is given by,

$$H = \frac{1}{2}y^2 + \frac{1}{2}\alpha_1 x^2 + \frac{1}{4}\alpha_2 x^4 - xQ_0 \cos\Omega t. \tag{3.5}$$

This Hamiltonian can be separated into the non-time dependent part (unperturbed) H_0 and the time-dependent part (perturbed) H_1. That is

$$H = H_0 + H_1, \tag{3.6}$$

where

$$H_0 = \frac{1}{2}y^2 + \frac{1}{2}\alpha_1 x^2 + \frac{1}{4}\alpha_2 x^4, \tag{3.7}$$

$$H_1 = -xQ_0 \cos\Omega t. \tag{3.8}$$

The phase plane energy contour for three given values of H_0 is sketched in *Figure* 3.1, using $\alpha_1 = \alpha_2 = 1.0$. The three values of the initial energy are $H_0 = E_0 < E_1 < E_2$. Solving the energy equation of *Equation* (3.7) for the situation of $H_0 = E_0$, the results are (Han and Luo (1994)),

$$x = h\,\mathrm{cn}\left[\frac{2K(k)\theta}{\pi}, k\right], \tag{3.9}$$

$$y = \pm\sqrt{\frac{\alpha_2}{2}}\frac{h^2}{k}\mathrm{sn}\left[\frac{2K(k)\theta}{\pi}, k\right]\mathrm{dn}\left[\frac{2K(\theta)}{\pi}, k\right], \tag{3.10}$$

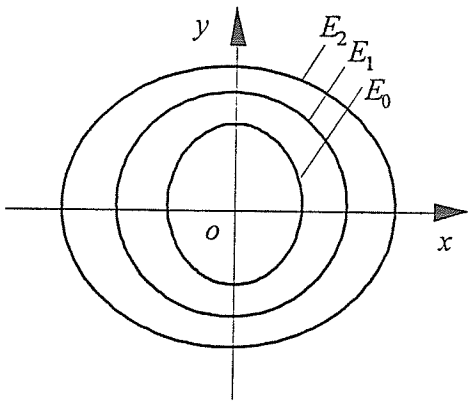

Figure 3.1 Phase plane energy trajectories for the undamped Case I.

in which cn, sn and dn are the Jacobi-elliptic functions, $K(k)$ the complete elliptic integral of the first kind, and k the modulus of the Jacobi-elliptic function. The other parameters h and θ in these expressions are defined by

$$h^2 = \frac{2k^2\alpha_1}{(1-2k^2)\alpha_2}, \qquad \theta = \omega t, \tag{3.11}$$

where ω is the nonlinear natural frequency of the undamped Duffing oscillator for Case I and is computed from,

$$\omega = \frac{1}{2}\sqrt{\frac{\alpha_2}{2}}\frac{h\pi}{kK(k)}. \tag{3.12}$$

The particular value E_0 can then be calculated using

$$E_0 = \frac{k^2(1-k^2)\alpha_1^2}{\left(1-2k^2\right)^2\alpha_2}, \tag{3.13}$$

and the action variable J for an orbit is given by

$$J = \frac{\sqrt{2\alpha_2}h^3}{3\pi k^3}\left[\left(1-k^2\right)K(k)+\left(2k^2-1\right)E(k)\right], \tag{3.14}$$

where the symbol $E(k)$ in *Equation* (3.14) denotes the complete elliptic integral of the second kind. The period T is given by

$$T = \frac{2\pi}{\omega}. \tag{3.15}$$

Substituting *Equations* (3.9)-(3.10) into *Equation* (3.5) and expanding the time-dependent term, the complete Hamiltonian function now becomes

$$H = H_0(J) - Q_0 \sum_{n=1}^{\infty} 2Q_{2n-1} \cos[(2n-1)\omega t]\cos(\Omega t), \tag{3.16}$$

or

$$H = H_0(J) - Q_0 \sum_{n=1}^{\infty} Q_{2n-1} \{\cos[(2n-1)\omega - \Omega]t + \cos[(2n-1)\omega + \Omega]t\} \tag{3.17}$$

in which

$$Q_{2n-1} = \frac{\pi h}{2kK \cosh\left[\pi\left(n-\frac{1}{2}\right)\frac{K'}{K}\right]}, \tag{3.18}$$

where $K' = K(k')$ and $k' = 1-k^2$. Except for the term of the $(2n-1)th$ primary resonance, all other terms in H will average to zero over time t. Hence, we have, in combination with *Equation* (3.11) and *Equation* (3.12), the following expression

$$\omega = \frac{\Omega}{2n-1} = \frac{\pi}{2K(k)}\sqrt{\frac{\alpha_1}{1-2k^2}} \tag{3.19}$$

from which we can determine k at the $(2n-1)th$ primary resonance for some given n. Let this value be symbolized by k_{2n-1}^{c}. Now, we are interested in the region near the $(2n-1)th$ primary resonance influenced by the $(2n+1)$th primary resonance. Assuming the effects of the other resonances to be negligible, the Hamiltonian can be expanded by Taylor series

about the $(2n-1)th$ primary resonance. That is

$$H = H_0\left(J_{2n-1}^c\right) + \left(\frac{dH_0}{dJ}\right)_{J_{2n-1}^c}\left(J - J_{2n-1}^c\right) + \frac{1}{2}\left(\frac{d^2H_0}{dJ^2}\right)_{J_{2n-1}^c}\left(J - J_{2n-1}^c\right)^2 + \cdots$$
$$-Q_0\left\{Q_{2n-1}\left(J_{2n-1}^c\right)\cos\left[(2n-1)\omega - \Omega\right]t + Q_{2n+1}\left(J_{2n+1}^c\right)\cos\left[(2n+1)\omega - \Omega\right]t\right\} \quad (3.20)$$

Noting that $H_0 = E_0$, the following parameter can be introduced:

$$G_0 = \left(\frac{d^2E_0}{dJ^2}\right)_{J_{2n-1}^c} = \frac{\pi^2}{4h^2K\left(k_{2n-1}^c\right)^3}\left[K\left(k_{2n-1}^c\right) - \frac{1-2\left(k_{2n-1}^c\right)^2}{1-\left(k_{2n-1}^c\right)^2}E\left(k_{2n-1}^c\right)\right]. \quad (3.21)$$

A new canonical coordinate system $(\bar{p}, \bar{\phi})$ can be introduced, where $\bar{p} = 0$ when $J = J_{2n-1}^c$. The generating function is

$$G(J, \bar{\phi}) = -(J - J_{2n-1}^c)(\frac{\bar{\phi} + \Omega t}{2n-1}). \quad (3.22)$$

Then we have

$$\bar{p} = -\frac{\partial G}{\partial \bar{\phi}} = \frac{J - J_{2n-1}^c}{2n-1}, \quad (3.23)$$

and $\bar{\phi}$ can be evaluated from

$$= \omega t = -\frac{\partial G}{\partial J} = \frac{\bar{\phi} + \Omega t}{2n-1}. \quad (3.24)$$

The new Hamiltonian is now given by

$$\bar{H} = H + \frac{\partial G}{\partial t} \approx H_0(J_{2n-1}^c) - \frac{1}{2}B_0(2n-1)^2\bar{p}^2$$
$$-Q_0\left\{Q_{2n-1}\left(J_{2n-1}^c\right)\cos\bar{\phi} + Q_{2n+1}\left(J_{2n-1}^c\right)\cos\left[\frac{2n+1}{2n-1}\bar{\phi} + \Omega_1 t\right]\right\}, \quad (3.25)$$

in which $\Omega_1 = 2\Omega/(2n-1)$. Note in *Equation* (3.25), $\partial G/\partial t = -\left(dE_0/dJ\right)_{J^c_{2n-1}}\left(J - J^c_{2n-1}\right)$ has already been involved. It is convenient to re-scale *Equation* (3.25) by introducing

$$\left.\begin{aligned} \phi &= \overline{\phi} \\ p &= \frac{(2n-1)^2(2n+1)G_0}{\Omega}\overline{p} \\ H &= \frac{(2n-1)^2(2n+1)G_0}{\Omega^2}\left[\overline{H} - E_0\left(J^c_{2n-1}\right)\right] \end{aligned}\right\}; \tag{3.26}$$

and thus, the re-scaled Hamiltonian is

$$H = \frac{1}{2}p^2 - U_0\cos\phi - V_0\cos\left(\frac{2n-1}{2n+1}\phi + \Omega_1 t\right), \tag{3.27}$$

where

$$U_0 = \frac{(2n-1)^2(2n+1)^2 G_0}{\Omega^2}Q_0 Q_{2n-1}, \tag{3.28}$$

$$V_0 = \frac{(2n-1)^2(2n+1)^2 G_0}{\Omega^2}Q_0 Q_{2n+1}; \tag{3.29}$$

and

$$Q_{2n-1} = \frac{\sqrt{2}\Omega}{\sqrt{\alpha_2}(2n-1)\cosh\left[\pi\left(n-\frac{1}{2}\right)\frac{K^{c'}_{2n-1}}{K^c_{2n-1}}\right]}, \tag{3.30}$$

$$Q_{2n-1} = \frac{\sqrt{2}\Omega}{\sqrt{\alpha_2}(2n+1)\cosh\left[\pi\left(n+\frac{1}{2}\right)\frac{K^{c'}_{2n+1}}{K^c_{2n+1}}\right]}. \tag{3.31}$$

3.2 Chaotic Conditions for the Undamped Duffing oscillator

To predict onset of chaos (from local to global stochasticity) in *Equation* (3.27), Chirikov (1979) provided the following condition (for more information, the reader is directed to Lichtenberg and Lieberman(1992) and Reichl (1992)):

$$2\sqrt{U_0}+2\sqrt{V_0}=1, \tag{3.32}$$

we obtained the chaotic condition governing the onset of global stochasticity near the $(2n-1)th$ primary resonance as influenced by the $(2n+1)th$ primary resonance, that is,

$$Q_0=\frac{\Omega^2}{4(2n-1)^2(2n+1)^2G_0}\left(\frac{1}{\sqrt{Q_{2n-1}}+\sqrt{Q_{2n-1}}}\right)^2. \tag{3.33}$$

Using the renormalization group technique, Escande and Doveil (1981) and Escande (1985) developed a mathematically more consistent method for the prediction of chaos, and obtained the following expression which agrees quite closely with *Equation* (3.32):

$$2\sqrt{U_0}+2\sqrt{V_0}=0.7. \tag{3.34}$$

From Escande (1985) result, the chaotic condition in *Equation* (3.33) gets modified to,

$$Q_0=\frac{0.49\Omega^2}{4(2n-1)^2(2n+1)^2G_0}\left(\frac{1}{\sqrt{Q_{2n-1}}+\sqrt{Q_{2n-1}}}\right)^2. \tag{3.35}$$

Having determined the two parameters E_0, Q_0 analytically, we can use them to predict the onset of chaos. Note that in determining these parameters it is necessary to evaluate a number of intermediate parameters, such as G_0, Q_{2n-1}, Q_{2n+1} etc. It will be useful to show the relationship between Ω andE_0, Q_0. For the undamped Case I, these relationships are depicted in *Figure* 3.2 for $\alpha_1=\alpha_2=1.0$. Observe that both the resonant and chaotic conditions as described by *Equations* (3.19) and (3.33) respectively, are displayed.

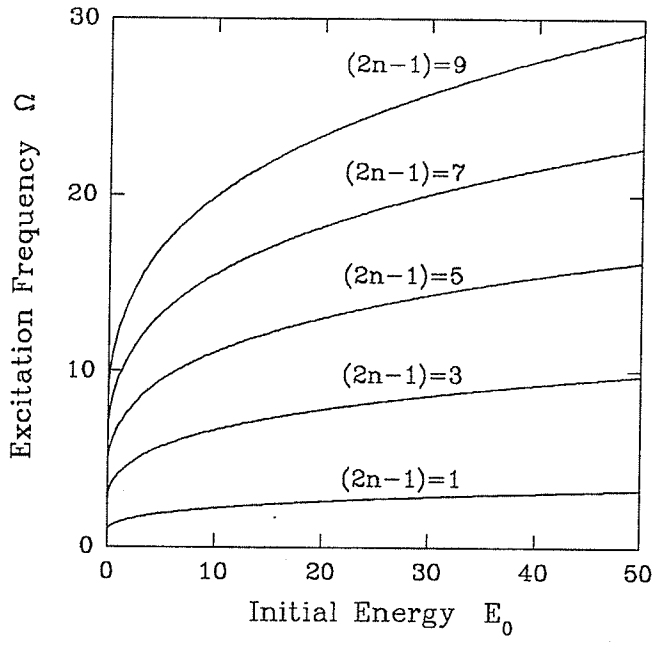

(a) Resonant condition

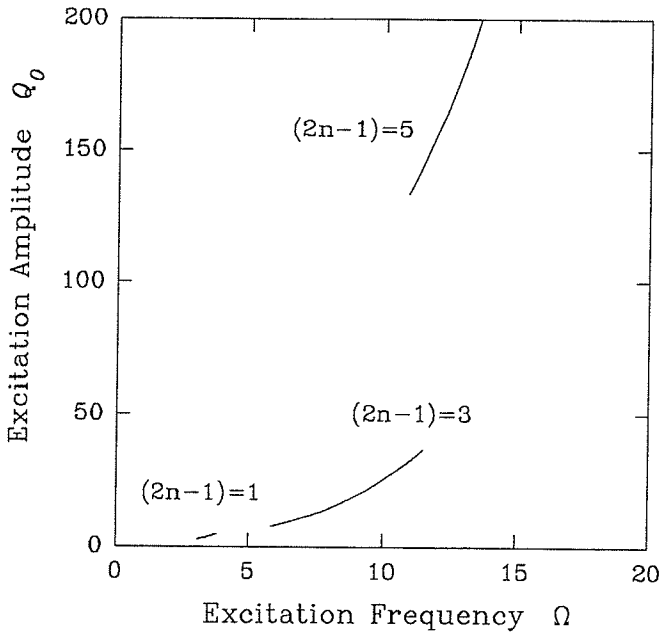

(b) Chaotic condition

Figure 3.2 Resonant and chaotic conditions for the undamped Case I.

We can derive in a similar fashion the corresponding results for all other cases. The only exception to this is Case IV(c) which requires special handling. This is reported in *Section* 3.3. For Cases II to IV(b), their formulas are summarized in *Appendix* B.1. The phase plane energy contours for Cases II-IV are sketched in *Figure* 3.3.

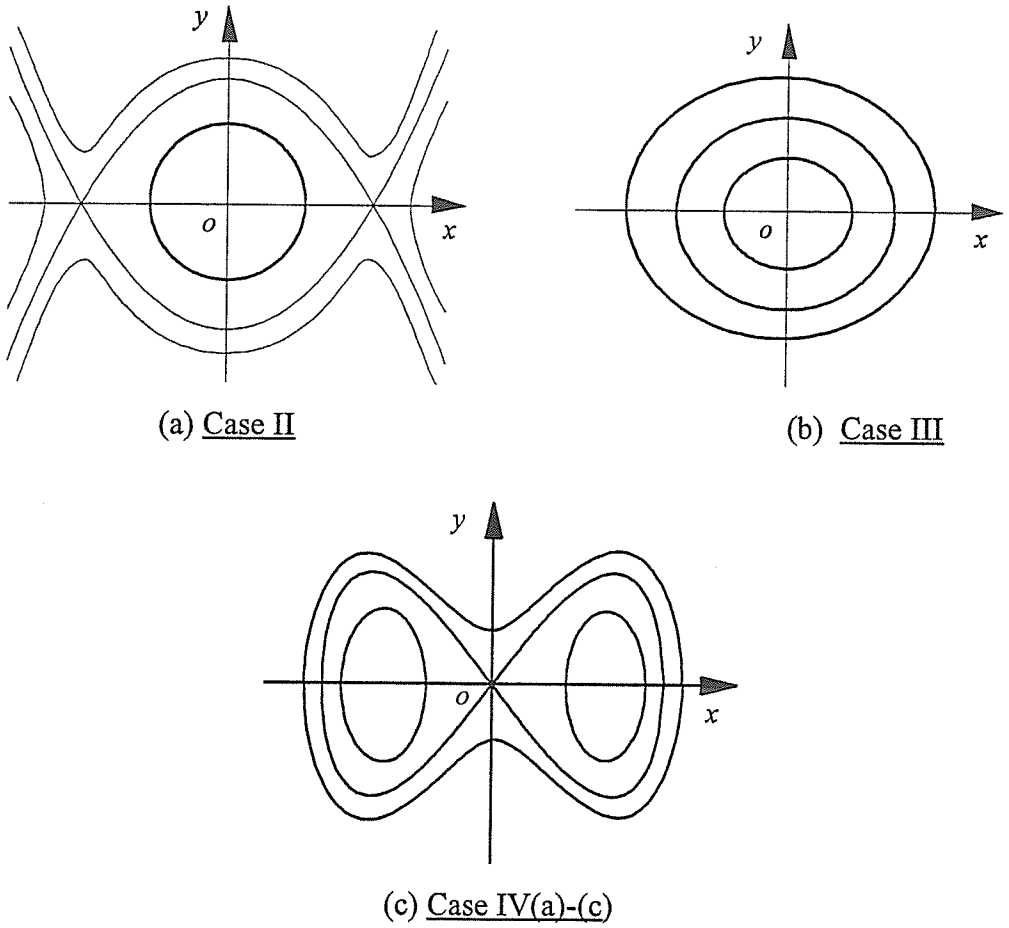

Figure 3.3 Phase plane energy trajectories for undamped Cases II-IV.

The values of G_0, Q_{2n-1} and Q_{2n+1} for each of the Cases II to IV(b) are different and thus the relationships between Ω and E_0, Q_0 are not the same. Using $\alpha_1 = \alpha_2 = 1.0$, these relationships are plotted in *Figures* 3.4-3.7 for Cases II-IV(b) respectively. Once again, both the resonant and chaotic conditions as described by their respective equations in *Appendix* B.1 are depicted.

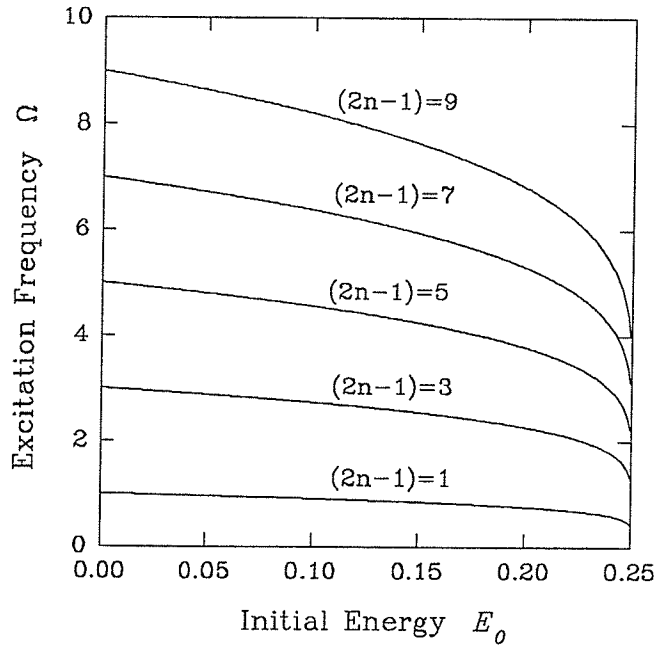

(a) Resonant condition

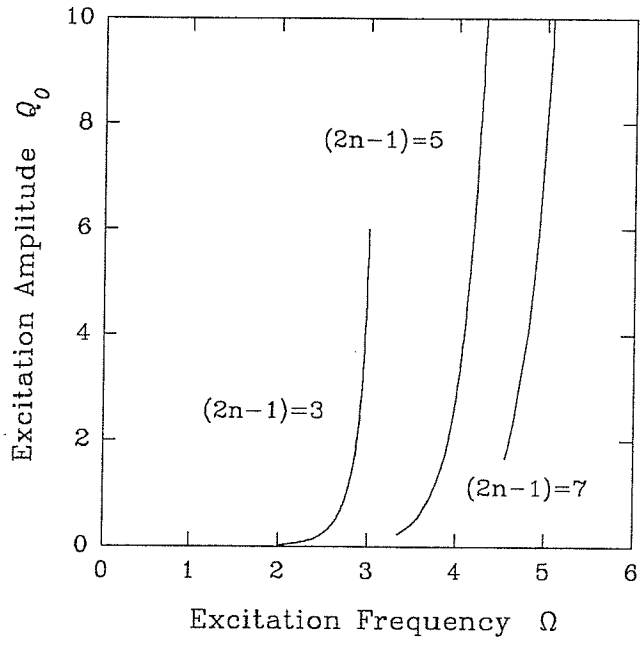

(b) Chaotic condition

Figure 3.4 Resonant and chaotic conditions for the undamped Case II.

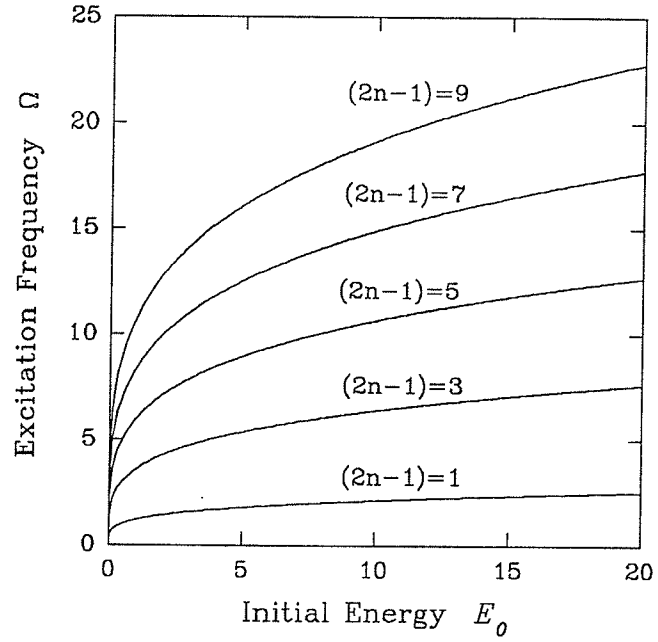

(a) Resonant condition

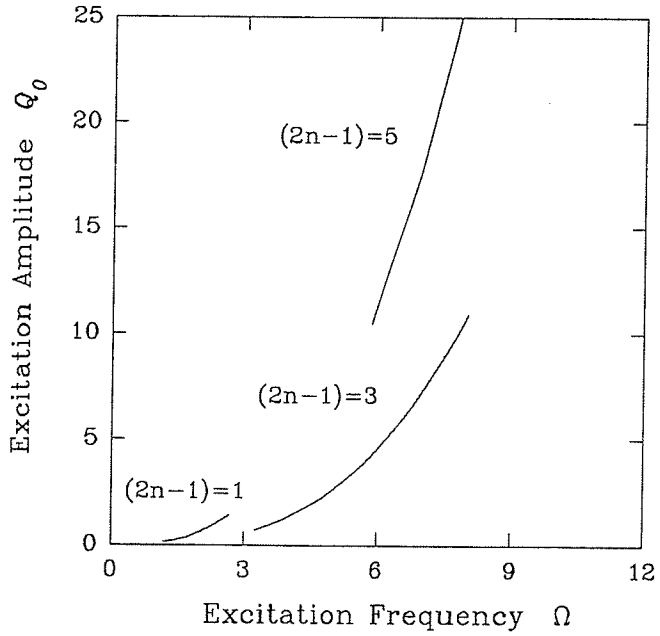

(b) Chaotic condition

Figure 3.5 Resonant and chaotic conditions for the undamped Case III.

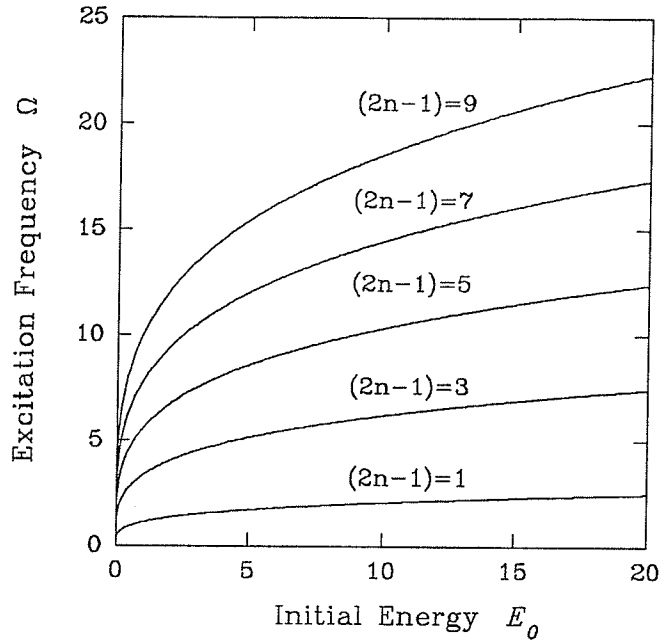

(a) Resonant condition

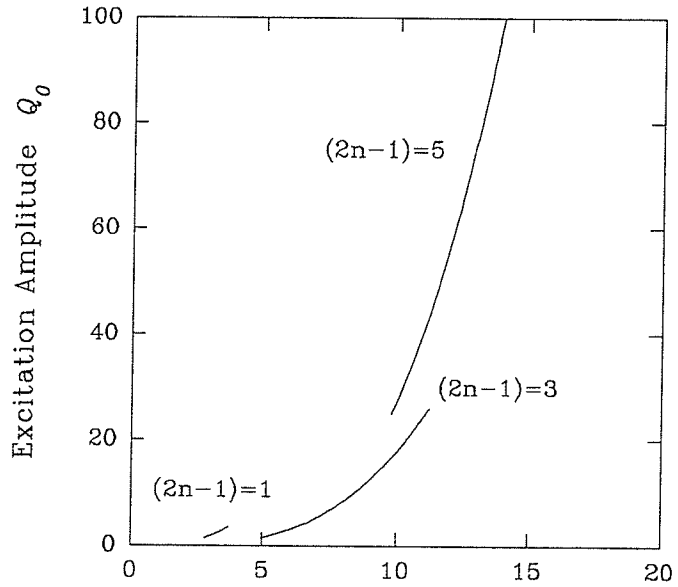

(b) Chaotic condition

Figure 3.6 Resonant and chaotic conditions for the undamped Case IV(a).

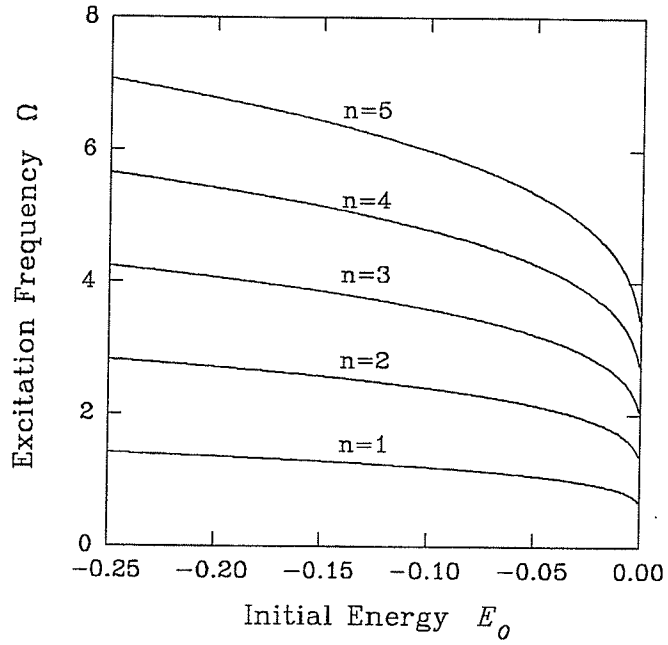

(a) Resonant condition

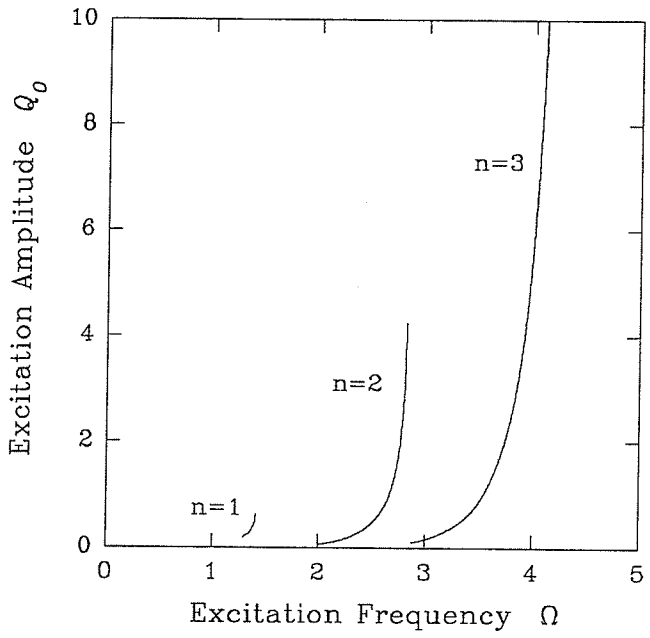

(b) Chaotic condition

Figure 3.7 Resonant and chaotic conditions for the undamped Case IV(b).

3.3 Chaotic Conditions for the Undamped Case IV(c)

This case requires special handling because $E_0 = 0$. As before, the Hamiltonian can be separated in the non-time dependent part and the time-dependent part. That is,

$$H_0 = \frac{1}{2}y^2 - \frac{1}{2}\alpha_1 x^2 + \frac{1}{4}\alpha_2 x^4 = 0, \tag{3.36}$$

$$H_1 = -xQ_0 \cos\Omega t. \tag{3.37}$$

Using *Equation* (3.36), the solutions for this case are given by

$$x = \pm\sqrt{\frac{2\alpha_1}{\alpha_2}}\operatorname{sech}\left(\sqrt{\alpha_2}t\right), \tag{3.38}$$

$$y = \pm\sqrt{\frac{2}{\alpha_2}}\alpha_1 \operatorname{sech}\left(\sqrt{\alpha_2}t\right)\tanh\left(\sqrt{\alpha_2}t\right). \tag{3.39}$$

As $k \to 1$, $E_0 \to 0$, that is, near the separatrix manifold of Case IV(a). Using the results of Case IV(a) in *Appendix* B.1 we have:

$$h^2 = \frac{2\alpha_1}{\alpha_2}, \quad E_0 \approx \frac{\alpha_1^2}{\alpha_2}\left(1-k^2\right), \tag{3.40}$$

and the nonlinear period T is

$$T = \frac{4\sqrt{2}k}{\sqrt{\alpha_2}h}K(k). \tag{3.41}$$

From Cayley (1895), we have

$$K(k) \approx \frac{1}{2}\ln\left(\frac{16}{1-k^2}\right). \tag{3.42}$$

In view of *Equation* (3.40) and (3.42) and as $k \to 1$, *Equation* (3.39) simplifies to

$$T \approx \frac{2}{\sqrt{\alpha_1}} \ln\left(\frac{16\alpha_1^2}{\alpha_2 E_0}\right). \tag{2.43}$$

The energy increment for one period is

$$\Delta H = \int_0^T \left(\frac{\partial H_0}{\partial y}\frac{\partial H_1}{\partial x} - \frac{\partial H_0}{\partial x}\frac{\partial H_1}{\partial y}\right) dt = -2Q_0 \pi\Omega \sqrt{\frac{2}{\alpha_2}} \operatorname{sech}\left(\frac{\pi\Omega}{2\sqrt{\alpha_1}}\right) \sin(\Omega t_0). \tag{3.44}$$

The phase angle increment of the trajectory for one period is

$$\Delta\phi = \Omega T = \frac{2\Omega}{\sqrt{\alpha_1}} \ln\left(\frac{16\alpha_1^2}{\alpha_2 E_0}\right). \tag{3.45}$$

where t_0 is the initial time. For the convenience of notation for numerical simulation, we let $w = H_0$ (and $\Delta w = \Delta H_0$) and $\phi = \Omega t_0$. Hence, near the separatrix, the energy and the phase angle of the $(i+1)$th period and the ith period are:

$$w_{i+1} = w_i + \Delta w = w_i - 2Q_0 \pi\Omega \sqrt{\frac{2}{\alpha_2}} \operatorname{sech}\left(\frac{\pi\Omega}{2\sqrt{\alpha_1}}\right) \sin(\phi_i), \tag{3.46}$$

$$\phi_{i+1} = \phi_i + \frac{2\Omega}{\sqrt{\alpha_1}} \ln\left(\frac{16\alpha_1^2}{\alpha_2 w_{i+1}}\right). \tag{3.47}$$

Equations (3.46)-(3.47) represent the separatrix mapping with period-1 fixed points at

$$\frac{2\Omega}{\sqrt{\alpha_1}} \ln\left(\frac{16\alpha_1^2}{\alpha_2 w_1}\right) = 2\pi(2n-1), \tag{3.48}$$

where $(2n-1)$ is an integer and w_1 is the energy of the $(2n-1)$th fixed point. To convert the separatrix mapping to the standard mapping form, we put $w_i = w_1 + \Delta w_i$, and

linearizing in w yields

$$I_{i+1} = I_i + K\sin(\phi_i), \tag{3.49}$$

$$\phi_{i+1} = \phi_i + I_{i+1} \tag{3.50}$$

in which

$$I_i = -\frac{2\Omega}{\sqrt{\alpha_1}}\frac{\Delta w_i}{w_1} \tag{3.51}$$

is the new action and K is the strength of the stochasticity parameter defined by

$$K = \frac{4Q_0\pi\Omega^2}{w_1\sqrt{\alpha_1}}\sqrt{\frac{2}{\alpha_2}}\operatorname{sech}\left(\frac{\pi\Omega}{2\sqrt{\alpha_1}}\right). \tag{3.52}$$

For standard mapping, the transition to chaos occurs at $K^* = 0.9716\cdots$. The KAM torus will disappear and thus, we can determine the chaotic condition related to the resonant orbits outside the homoclinic orbit:

$$Q_0 = \frac{4K^*}{\pi}\left(\frac{\alpha_1}{\Omega}\right)^2\sqrt{\frac{\alpha_1}{2\alpha_2}}e^{-\left[(2n-1)\pi\sqrt{\alpha_1}/\Omega\right]}\cosh\left(\frac{\pi\Omega}{2\sqrt{\alpha_1}}\right). \tag{3.53}$$

Similarly, the chaotic condition related to resonant orbits inside the homoclinic orbit is:

$$Q_0 = \frac{16K^*}{\pi}\left(\frac{\alpha_1}{\Omega}\right)^2\sqrt{\frac{\alpha_1}{2\alpha_2}}e^{-\left[n\pi\sqrt{\alpha_1}/(2\Omega)\right]}\cosh\left(\frac{\pi\Omega}{2\sqrt{\alpha_1}}\right). \tag{3.54}$$

Figure 3.8 displays the relationships between Ω and E_0, Q_0 in the neighborhood of Case IV(c) for $\alpha_1 = \alpha_2 = 1.0$. Note that the chaotic conditions are plotted in *Figure* 3.8(b).

3.4 Critical Conditions for a Weakly Damped Duffing Oscillator

The system considered here is a forced integral system with a dissipative perturbation.

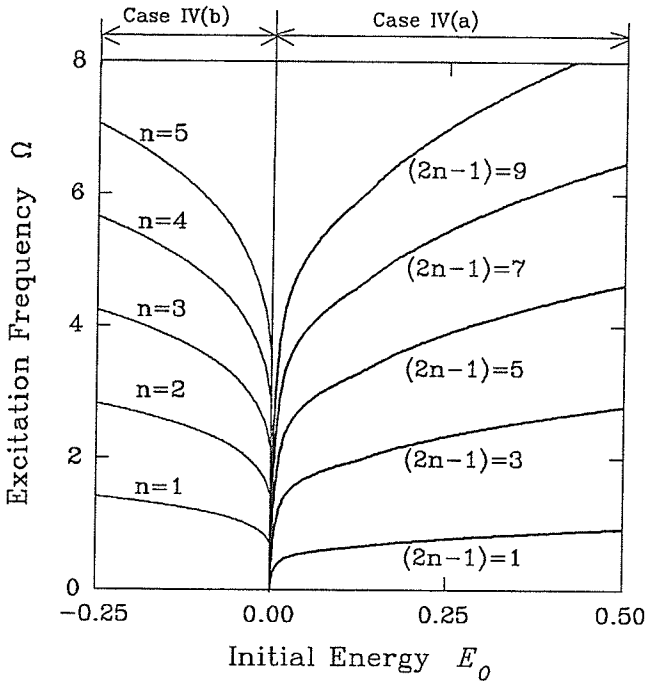

(a) Resonant conditions

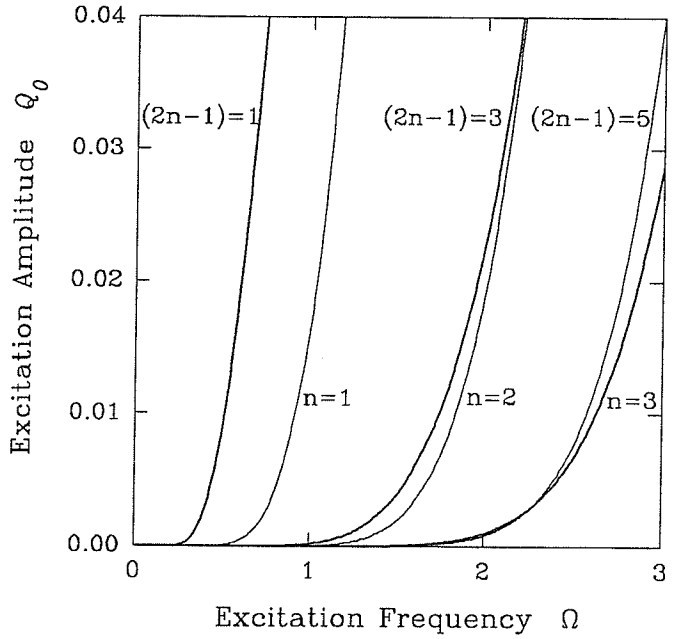

(b) Chaotic condition

Figure 3.8 Resonant and chaotic conditions for the undamped Case IV(c) (—— Case IV(a), —— Case IV(b)).

To study the chaotic motion, Melnikov method is employed. The necessary conditions for the subharmonic bifurcation and the occurrence of the chaotic layer around the separatrix are derived. Then to recover the original system, we let the perturbation parameter $\varepsilon = 1$. As done previously, we will once again consider the four cases. We will derive the results for Cases I and IV(c), and deduce and list the results for Cases II-IV(b) in *Appendix* B.2.

Case I

We consider a damped system with a dissipative perturbation ε. From *Equation* (2.19), we have,

$$\left.\begin{aligned} \dot{x} &= y \\ \dot{y} &= -\alpha_1 x - \alpha_2 x^3 + \varepsilon\left(Q_0 \cos\Omega t - \delta\dot{x}\right) \end{aligned}\right\}. \tag{3.55}$$

The Melnikov function for this system can be defined as

$$M^{\frac{(2n-1)}{j=1}}(t_0, Q_0, \delta, \Omega) = \int_0^T y\left[Q_0 \cos\left(\Omega(t+t_0) - \delta y\right)\right]dt, \tag{3.56}$$

where T is the period of the *un*damped Duffing oscillator. Recall from the previous section, the various parameters pertaining to the *un*damped system have already been derived. Hence, the integration can be carried out and the Melnikov function can be computed. For compactness, let it be expressed as

$$M^{\frac{(2n-1)}{1}}(t_0, Q_0, \delta, \Omega) = -\delta I_1 + Q_0 I_2, \tag{3.57}$$

where
$$I_1(2n-1, j=1) = \frac{8\alpha_1\sqrt{\alpha_1}}{3\sqrt{\left(1-k^2\right)^3}\,\alpha_2}\left[\left(1-k^2\right)K(k) + \left(2k^2-1\right)E(k)\right], \tag{3.58}$$

$$I_2(2n-1, j=1, \Omega) = \frac{2\pi\sqrt{2}\Omega}{\sqrt{\alpha_2}}\operatorname{sech}\left[\left(n-\frac{1}{2}\right)\pi\frac{K'}{K}\right]\sin(\Omega t_0). \tag{3.59}$$

Defining
$$R^{2n-1}(\Omega)=\frac{I_1(2n-1,1)}{I_2(2n-1,1,\Omega)}, \tag{3.60}$$

we find that if $Q_0/\delta > R^{2n-1}(\Omega)$, there exists a pair of subharmonics of the order $(2n-1)$, and period $2(2n-1)\pi/\Omega$, which appears on a bifurcation manifold. The subharmonic bifurcation condition is thus given by

$$Q_0 = R^{2n-1}(\Omega)\delta. \tag{3.61}$$

Note that in *Equation* (3.61), if Q_0 is known, then the amount of damping δ can be computed. On the other hand, if the damping is prescribed, Q_0 can then be computed. Also, no ultra-subharmonics (Guckenheimer and Holmes (1983)) can occur here. As before, the conditions for subharmonic bifurcation for Cases II to IV (b) are given in *Appendix* B.2. We will now consider the special case of $E_0 = 0$ for Case IV(c).

Case IV(c)

For this case, the Melnikov function is defined as

$$M_{\overline{1}}^{\overline{(2n-1)}}(t_0,Q_0,\delta,\Omega)=\int_{-\infty}^{+\infty} y[Q_0\cos\{\Omega(t+t_0)-\delta y]dt=-\delta I_1+Q_0 I_2 \tag{3.62}$$

in which
$$I_1=\frac{4\alpha_1\sqrt{\alpha_1}}{3\alpha_2}, \tag{3.63}$$

$$I_2=\frac{2\pi\sqrt{2}\Omega}{\sqrt{\alpha_2}}\operatorname{sech}\left(\frac{\pi\Omega}{2\sqrt{\alpha_1}}\right)\sin(\Omega t_0). \tag{3.64}$$

Introducing
$$R^0(\Omega)=\frac{I_1}{I_2}, \tag{3.65}$$

and if $Q_0/\delta > R^0(\Omega)$, then the stable manifold intersects the unstable manifold, and we

have a minimum chaotic condition as

$$Q_0 = R^0(\Omega)\delta. \tag{3.66}$$

This is of the same form as in *Equation* (3.61). In fact, all the cases have this form, with the appropriate I_1, I_2 substituted into the expression. Graphical plots of the subharmonic bifurcation condition near the homoclinic orbits for $\alpha_1 = \alpha_2 = 1.0$, and $\delta = 0.5$ for all cases are depicted in *Figure* 3.9.

3.5 Numerical Simulations

To verify the formulation for the analytical prediction of the subharmonic bifurcation and chaos, numerical simulations based on Runge-Kutta integration of the appropriate differential equations for the four cases are performed. The ability to analytically predict the onset of chaos is a useful one as it implies that unnecessary prolonged and tedious numerical experimentations are eliminated. Verification is achieved when the number of numerically predicted subharmonic resonance agrees with that obtained theoretically.

Chaotic solutions are obtained in the numerical simulation by inputting parameters that satisfy the derived chaotic condition for the four cases. However, the computation of these input parameters is not trivial and a systematic approach is adopted. The technique starts off by specifying appropriate initial conditions of displacement x_0 and either the initial energy E_0 or the initial velocity y_0, since it is straight forward to calculate one from the other via *Equation* (3.2). In this work, we have prescribed as initial conditions the quantities x_0, E_0 and, y_0 as the calculated quantity. From the curves depicted by *Figures* 3.2 and 3.4-3.9, the excitation frequency Ω and excitation amplitude Q_0 corresponding to the chosen case are determined. Since Q_0 satisfies the critical conditions computed via Chirikov overlap criterion and renormalization group techniques, numerical integration of

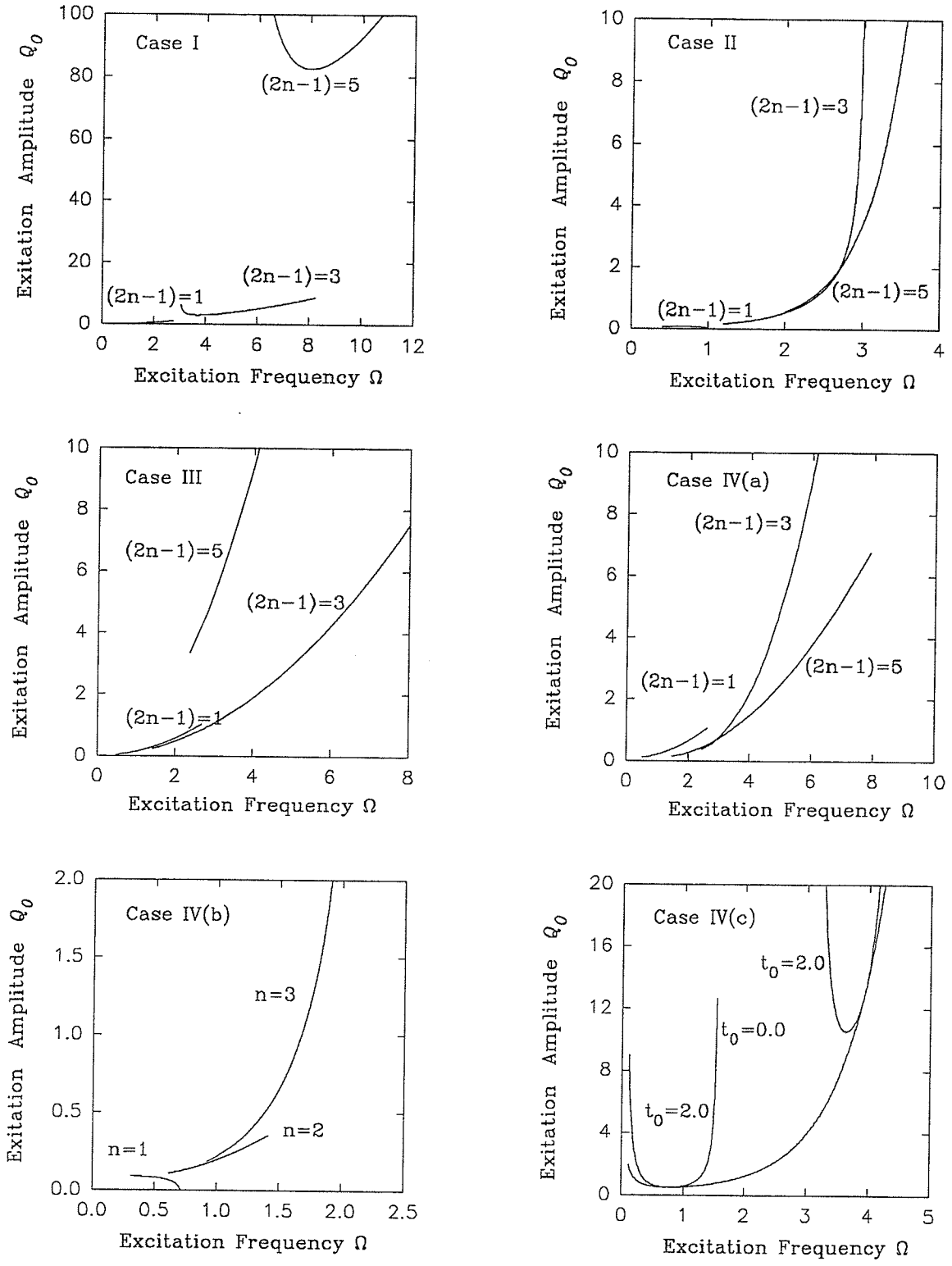

Figure 3.9 Critical conditions for bifurcation and chaos of damped Cases I-IV.

the differential equations now produces chaotic solutions. For a damped Duffing oscillator, it is necessary to use *Figure* 3.9 which is generated for a system with damping. The various input parameters of the numerical simulation are summarized in *Table* 3.1. Note that the two structural parameters α_1, α_2 have values of 1.0 in all the numerical simulation runs.

Table 3.1 System input parameters for numerical simulations

$\alpha_1 = \alpha_2 = 1$	Case Types	d	x_0	y_0	W	Q_0	
	Case I	0.0	0.0	6.0415	7.6452	13.0916[a]	6.4149[b]
	Case II	0.0	0.0	0.5592	2.5172	0.2598[a]	0.1273[b]
Undamped	Case III	0.0	0.0	1.1619	3.2582	0.7260[a]	0.3357[b]
Systems	Case IV(a)	0.0	0.0	3.2171	5.1955	1.6664[a]	0.8165[b]
	Case IV(b)	0.0	0.8	0.3667	2.5771	0.1638[a]	0.0802[b]
	Case IV(c)	0.0	0.0	0.0	3.1400	0.0425[c]	0.0213[d]
	Case I(a)	0.0005	0.0	6.0415	7.6452	13.0916[e]	
	Case I(b)	0.0020	0.0	6.0415	7.6452	13.0916[e]	
	Case I(c)	0.0100	0.0	6.0415	7.6452	13.0916[e]	
Damped	Case II	0.0001	0.0	0.5592	2.5172	0.2598[e]	
Systems	Case III	0.0001	0.0	1.1619	3.2582	0.7260[e]	
	Case IV(a)	0.0001	0.0	3.2171	5.1955	1.6664[e]	
	Case IV(b)	0.0001	0.8	0.3667	2.5771	0.1638[e]	
	Case IV(c)	0.0001	0.0	0.0	3.1400	0.0851[e]	

[a]Chirikov overlap (Han and Luo (1994)).
[b] renormalization group technique (Luo (1993c,1994), Luo, Han and Xiang (1995)).
[c]standard mapping method based on the outside orbit (Han and Luo (1994)).
[d]standard mapping method based on the inside orbit.
[e]Melnikov method for a damped Duffing oscillator (Han and Luo (1994)).

The Poincare mappings of the undamped Duffing oscillator are sketched as follows:

- *Figure* 3.10 for Cases I-II,
- *Figure* 3.11 for Cases III-IV(a), and
- *Figure* 3.12 for Cases IV(b)-(c).

For Case I, the chaotic motion based on the primary resonance of order $(2n-1)=3$ is simulated via numerical integration using the two critical conditions, and the result is shown in *Figure* 3.10(a) using Chirikov overlap criterion, and in *Figure* 3.10(b) based on the renormalization group technique. The computed input parameters for this simulation are also tabulated in *Table* 3.1. Since the chaotic motion with a primary resonance of order 3 is desired, the subharmonic resonance of order 3 will appear first. However, due to the influence of the energy of the fifth-order primary resonance arising from the $(2n+1)=3$ term, the KAM torus for the resonance of order 3 is destroyed. Note that the influence from the other higher primary resonances are very small and thus, can be neglected. The chaotic motion which is simulated based on the third primary resonance for Case II is plotted in *Figure* 3.10(c) using Chirikov overlap criterion, and in *Figure* 3.10(d) based on the renormalization group technique. Note that the maximum energy of this system cannot be larger than the energy of the separatrix, otherwise the solution will diverge.

Figure 3.11 depicts the Poincare mappings for Case III: (i) is based on the Chirikov overlap criterion, and (ii) on the renormalization group technique. For this situation, the structure is in a critical buckling state since it is loaded by its buckling load (see *Equation* (2.14)). As before, the chaotic motion based on the third primary resonance is shown. When the loading exceeds the buckling load, which is the situation for Case IV, there exists three distinct parts separated in the phase plane by its separatrix. As a result, the chaotic motion can take very different forms, depending on the three values of E_0. As given in *Figure* 3.11(c)-(d), the motion of Case IV(a) is similar to that of Case I. As before, *Figure* 3.11(c)-(d) is generated based on the Chirikov overlap criterion, and the renormalization group technique respectively.

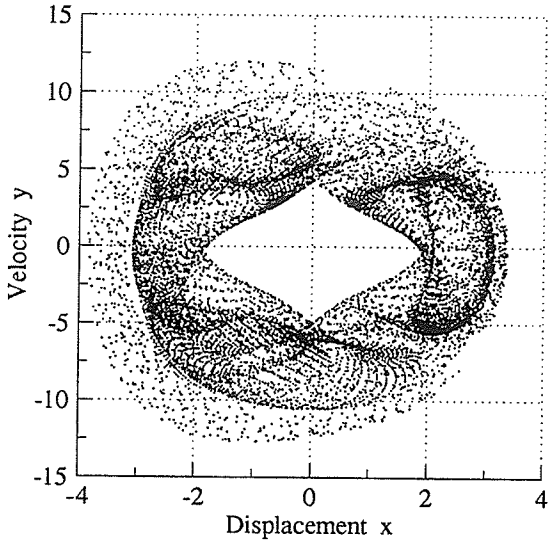

(a) Case I

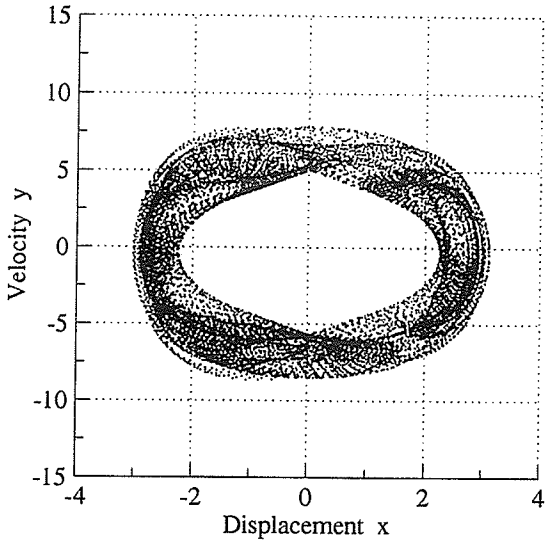

(b) Case I

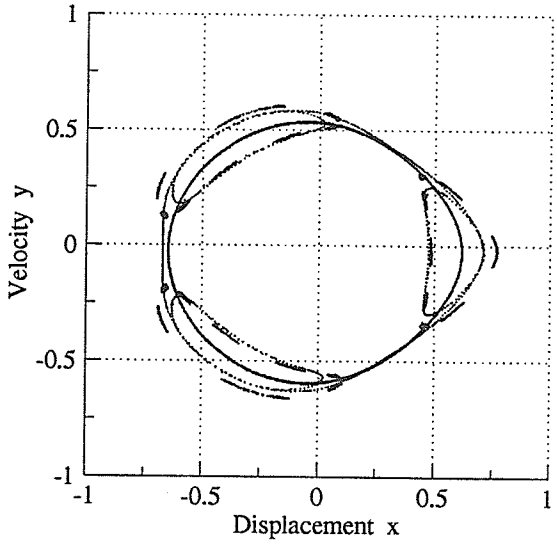

(c) Case II

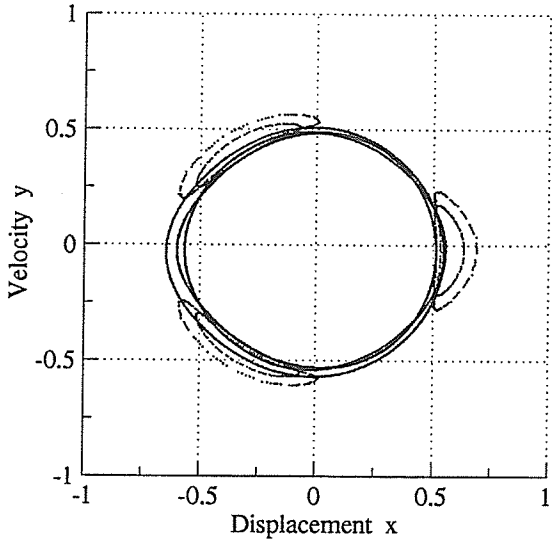

(c) Case II

Figure 3.10 Poincare mapping sections for undamped Cases I-II.

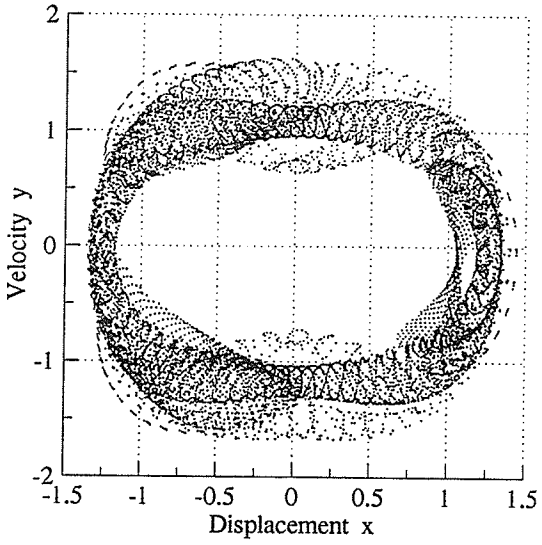

(a) Case III

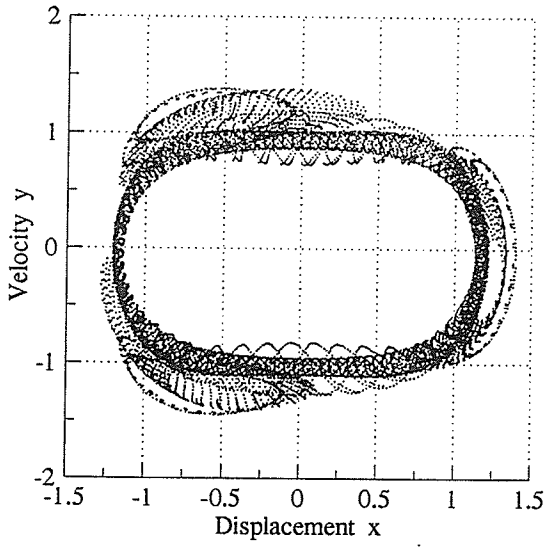

(b) Case III

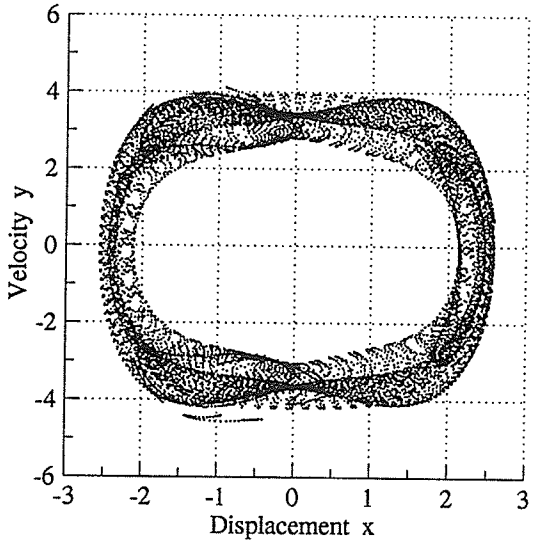

(c) Case IV(a)

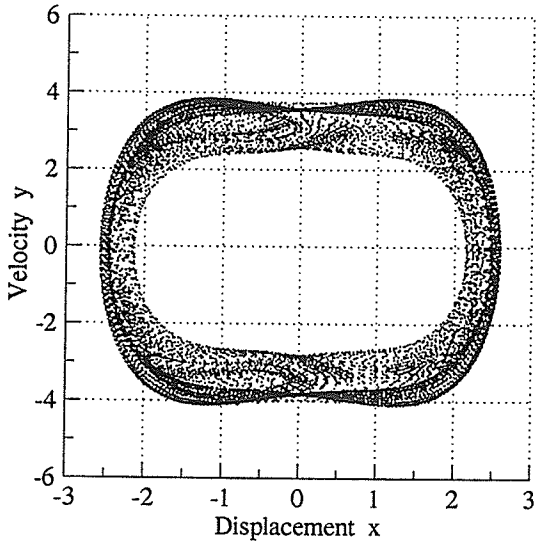

(d) Case IV(a)

Figure 3.11 Poincare mapping sections for undamped Cases III-IV(a).

Figure 3.12 plots the Poincare mapping sections of the Cases IV(b)-(c). The results for Case IV(b) are sketched in *Figure* 3.12(a) and (b) generated using the Chirikov overlap criterion, and the renormalization group technique respectively. Likewise, the results for Case IV(c) are sketched in *Figure* 3.12(c) and (d) but now, the graphs are generated based on the standard mapping for the outside and inside orbits respectively. For Case IV(b), the chaotic motion is based on the primary resonance of order 2 in the right potential well, and for Case IV(c) the chaotic motion is based on the separatrix or homoclinic orbit.

The Poincare mappings of the damped Duffing oscillator are sketched as follows:

- *Figure* 3.13 for Cases I-II,
- *Figure* 3.14 for Cases III-IV

In *Figure* 3.13, since it is desired to obtain chaos and strange attractors in the plots, the damping coefficient chosen for the numerical simulation is less than the critical damping $\delta_{cr} \approx 0.8468$. For Case I, three different damping coefficients are employed (see *Table* 3.1) and their corresponding Poincare mapping sections are identified as Case I(a), I(b), I(c). In Case I(a), the chaotic motion based on the third primary resonance is depicted. Observe the presence of the strange attractors. In comparing with the undamped Case I of *Figure* 3.10, it is clear that the difference in the chaotic motion is due to the introduction of the small dissipation in the system. Increasing the damping, the chaotic motion for Case I(b) is obtained. Note that the strange attractor is based on the third subharmonic resonance. Increasing the damping still further as shown in Case I(c), the third primary resonance disappears and goes into the first primary subharmonic resonance. For Case II the strange attractor is almost cyclically symmetric.

The Poincare mapping sections for Cases III-IV are given in *Figure* 3.14. For Case IV, once again we have the same three situations corresponding to the three values of E_0. Qualitatively, the same description as given for the undamped system applies.

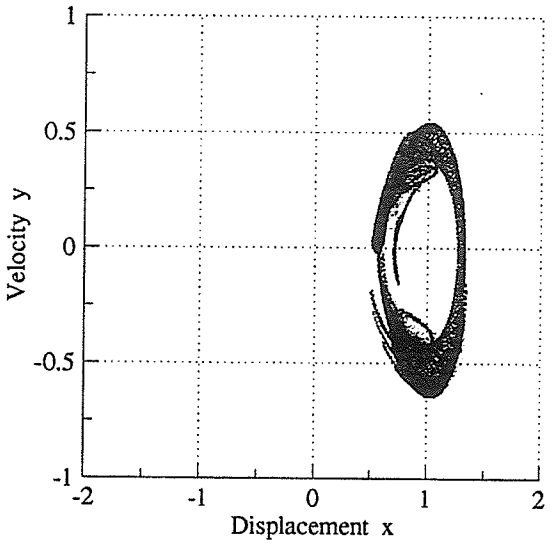

(a) Case IV(b)

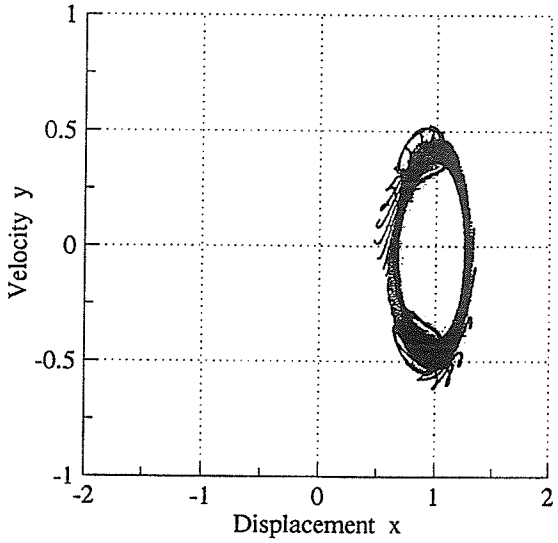

(b) Case IV(b)

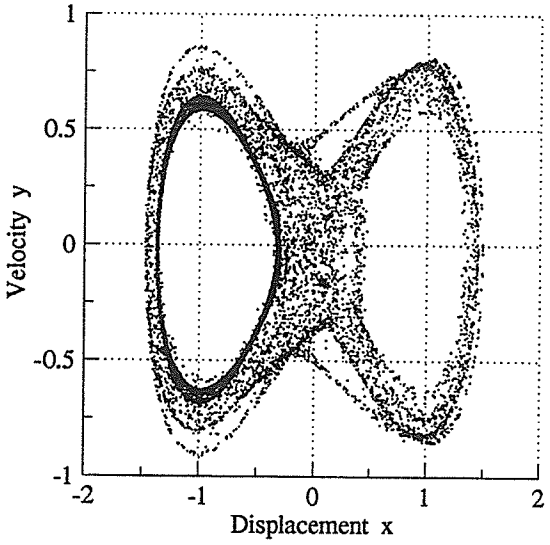

(c) Case IV(c)

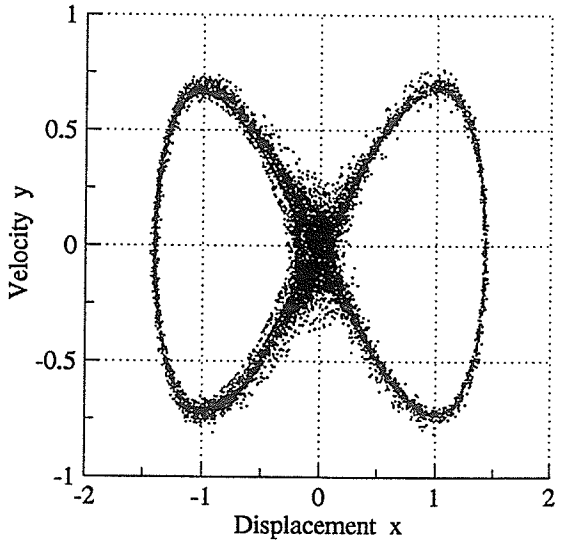

(d) Case IV(c)

Figure 3.12 Poincare mapping sections for undamped Cases IV(b)-IV(c).

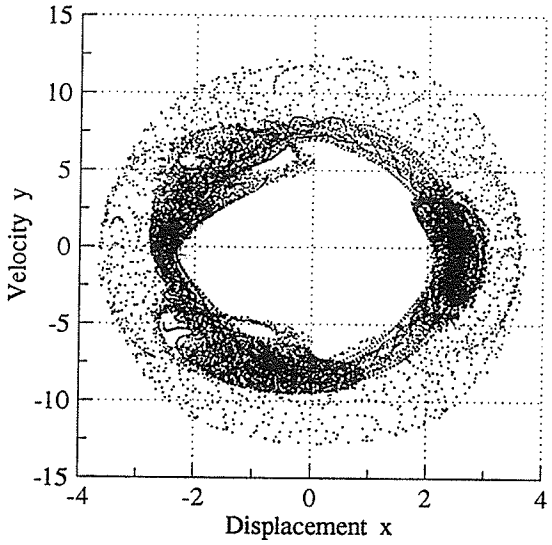

(a) Case I

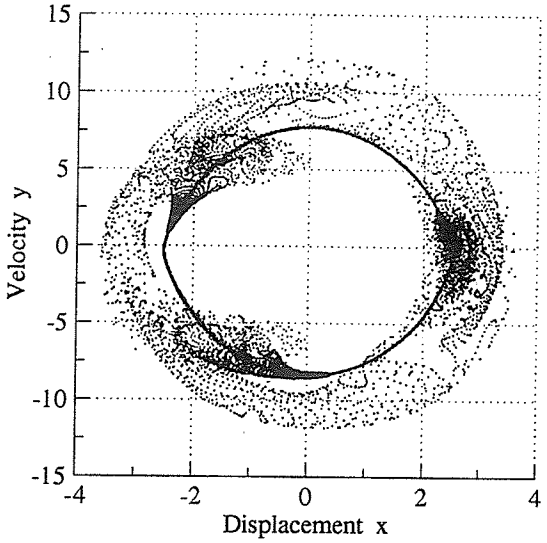

(b) Case I

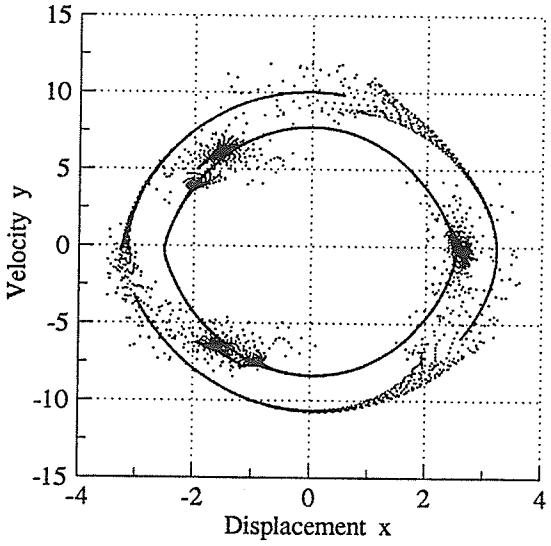

(c) Case I

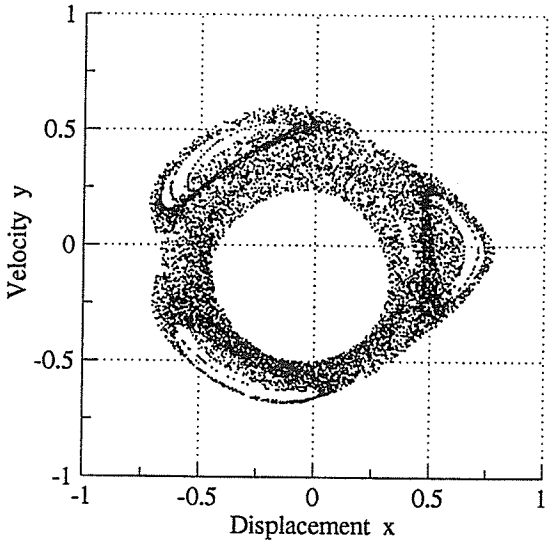

(d) Case II

Figure 3.13 Poincare mapping sections for damped Cases I-II.

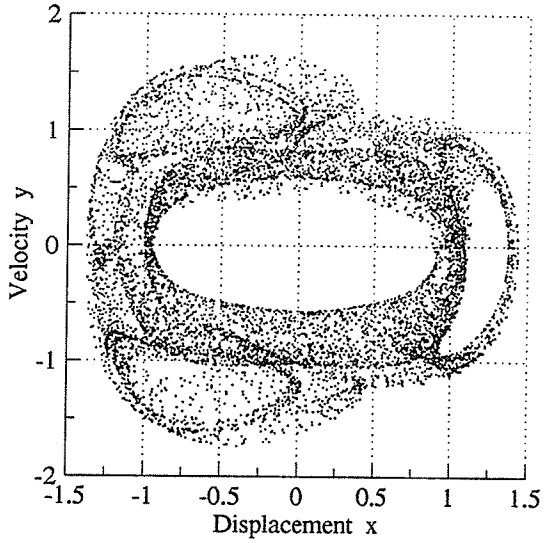

(a) Case III

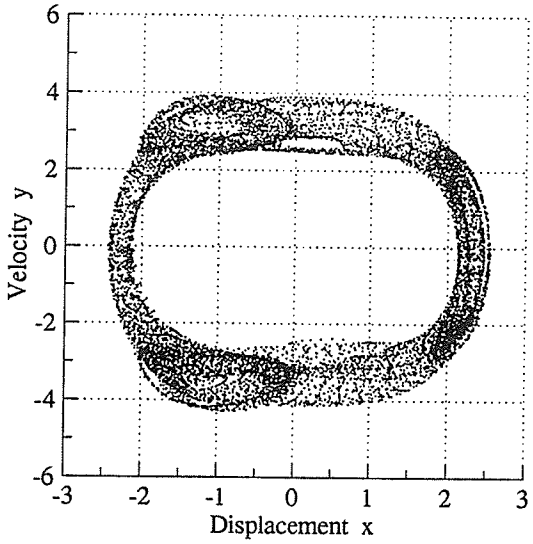

(b) Case IV(a)

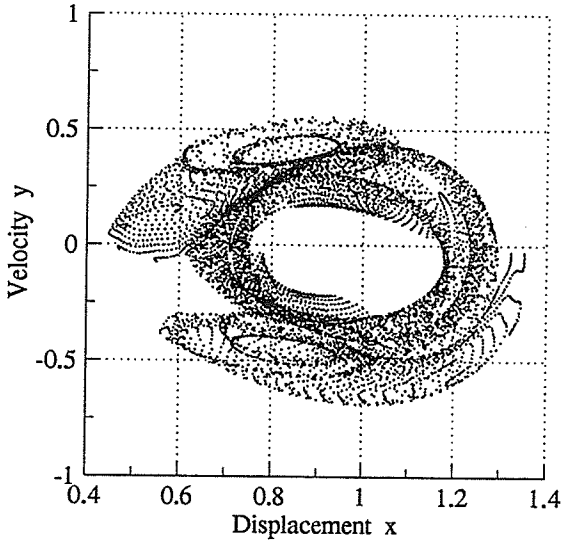

(c) Case IV(b)

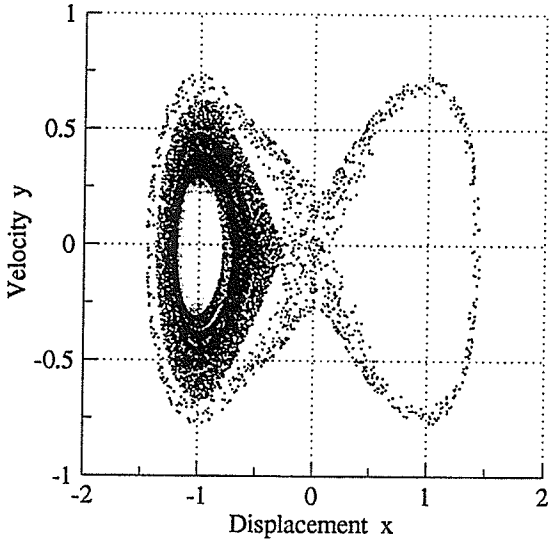

(d) Case IV(c)

Figure 3.14 Poincare mapping sections for damped Cases III-IV(c).

3.6 Conclusions

In this chapter, the Chirikov overlap criterion and renormalization group technique are used for the first time to derive the chaotic conditions near a subharmonic resonant orbit for the undamped Duffing oscillator. The analytically predicted chaos by these two methods is confirmed numerically and perfect agreement in their number of subharmonic resonances is observed. The chaotic motion of a forced integrable system with a dissipative perturbation is studied via the Melnikov method. Plots of the Poincare mapping section indicate the presence of strange attractors in the damped system.

CHAPTER 4

STOCHASTIC LAYERS IN NONLINEAR DYNAMICS

In the vicinity of the homoclinic and the heteroclinic orbits of a nonlinear dynamic system, there exist domains where the motion is stochastic. These domains are termed "stochastic layers", also sometimes referred to as *homoclinic tangles* (Guckenheimer and Holmes (1983)). They are actually very complicated sets of invariant curves. The determination of the strength (or *width*, chaotic condition), of the stochastic layer is very useful for the understanding of the stochasticity of the motion. Using the Chirikov overlap criterion, Reichl and Zheng (1984a, b) and Reichl (1992) estimated the strength of the stochastic layers for the undamped Duffing oscillator, and they showed qualitatively that these results are in agreement with the estimates obtained using the standard map for this system. In a later publication, Lin and Reichl (1986) employed the renormalization group method to compute the strength of the stochastic layer for a particle in an infinite square well potential and they compared their results with those from numerical experimentations.

In this chapter, a new approach is presented to predict the presence of stochastic layers near the separatrix and the computation of their strengths. The method is based on an incremental energy approach and involves determining the relationship between energy increments along the entire homoclinic (or heteroclinic) orbit and the resonant orbit. To demonstrate the procedure, two common undamped nonlinear oscillators are analyzed: the Duffing oscillator and forced planar-pendulum oscillator. To verify the results, numerical experimentation is performed to observe the presence of the stochastic layers in these oscillators and the computation of their strength.

4.1 Methodology

In this section, a new method is developed for the study of a stochastic layer near the separatrix (of either a homoclinic or a heteroclinic orbit). We consider a time-periodic system defined by

$$\dot{x} = f(x) + g(x,t); \qquad x = \begin{pmatrix} x \\ y \end{pmatrix} \in R^2, \tag{4.1}$$

where $f(x)$ is a Hamiltonian vector field defined on R^2 and $g(x,t)$, is a T-periodic (fixed period) Hamiltonian in time t. Specifically, they are of the form

$$f(x) = \begin{pmatrix} f_1(x) \\ f_2(x) \end{pmatrix}, \text{ and } g(x,t) = \begin{pmatrix} g_1(x,t) \\ g_2(x,t) \end{pmatrix}, \tag{4.2}$$

and are assumed to be sufficiently smooth $(C^r, r \geq 2)$ and bounded on bounded sets $D \subset R^2$ in the phase space. We introduce the following assumptions (see *Figure* 4.1).

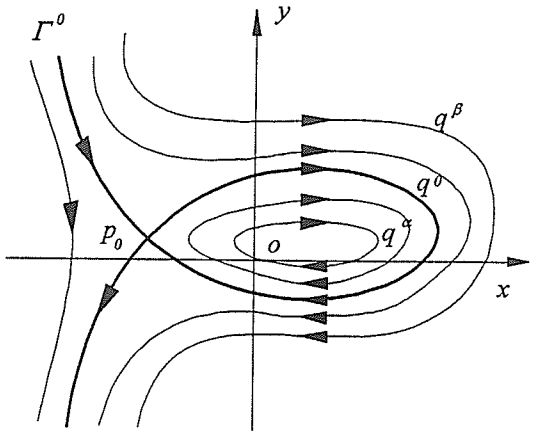

Figure 4.1 Phase portrait of a conservative system

(i) The conservative system possesses a separatrix $q^0(t)$ with at least one hyperbolic saddle point p_0.

(ii) Defining a set $\Gamma^0 = \{q^0(t) | t \in R\} \cup \{p_0\}$, the interior and exterior of Γ^0 are filled with two continuous families of periodic orbits $q^\alpha(t)$ for $\alpha \in [-1, 0)$ and $q^\beta(t)$ for $\beta \in (0, 1]$, respectively.

(iii) Introducing Hamiltonian functions $E_\alpha = H_0(q^\alpha(t))$ and $E_\beta = H_0(q^\beta(t))$ for two selected orbits; and T_α and T_β are periods of $q^\alpha(t)$ and $q^\beta(t)$, respectively; we set $dT_\alpha/dE_\alpha > 0$ inside Γ^0 and $dT_\beta/dE_\beta > 0$ outside Γ^0.

Note that H_0 is the unperturbed Hamiltonian or energy function of the conservative system, and assumptions (ii)-(iii) imply that $T_\alpha \to \infty$ ($T_\beta \to \infty$) monotonically as $\alpha \to 0$ ($\beta \to 0$). For simplicity, we consider the system to have a Hamiltonian described by,

$$H(x, y, t) = H_0(x, y) + H_1(x, y, t). \tag{4.3}$$

where $H_1(x, y, t)$ is the perturbed Hamiltonian or energy function of the external periodic excitation with

$$\left.\begin{aligned} f_1 &= \frac{\partial H_0}{\partial y}, \quad g_1 = \frac{\partial H_1}{\partial y} \\ f_2 &= -\frac{\partial H_0}{\partial x}, \quad g_2 = -\frac{\partial H_1}{\partial x} \end{aligned}\right\}. \tag{4.4}$$

To obtain the critical conditions for the prediction of the stochastic layer, we compute the energy increment along the separatrix of *Equation* (4.1). The result for a conservative system subjected to the external excitation along the separatrix $T_\alpha \to \infty$ (or $T_\beta \to \infty$) is,

$$\Delta H \approx \int_{t_0}^{T_\alpha + t_0} \frac{dH(x, y, t)}{dt} dt = \int_{t_0}^{T_\alpha + t_0} \{H_0, H_1\}_{Poisson} dt = \int_{t_0}^{T_\alpha + t_0} (f_1 g_2 - f_2 g_1) dt \tag{4.5}$$

where $\{\ \}_{Poisson}$ denotes the Poisson bracket. As an example, we consider the stochastic layer sketched in *Figure* 4.2(a). For any given external excitation frequency Ω, there exists a resonant α-orbit satisfying $\omega = m/n\Omega$ in the neighborhood of the separatrix;

where m, n are positive integers, and ω is a nonlinear natural frequency for the α-orbit. Similarly, the β-orbit is characterized in the same manner. Let $E_a = E_1^i$ and $E_\beta = E_2^j$ denote respectively, the energies of any one of the subharmonic resonant α-orbits and β-orbits, as shown in *Figure* 4.2(b). Note that the superscripts i and j represent positive integers pertaining to the strength of the stochastic layer. As shown in *Chapter* 3, these energies can be computed by the resonant conditions depicted in *Figure* 4.2(b). Note that in the stochastic layer, the energy of its elliptic orbits is bounded in the neighborhood of the energy of the separatrix E_0 (see *Appendix* B.3). Next we consider 3 theorems governing the stochastic layer. The proofs are summarized in *Appendix* B.3.

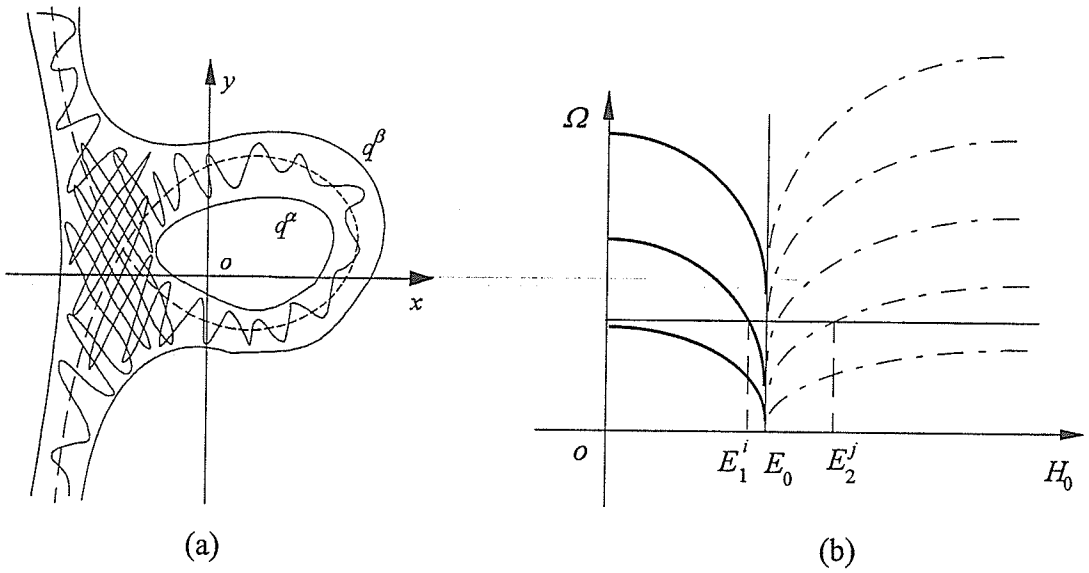

Figure 4.2 Stochastic layer: (a) phase portrait and (b) resonant conditions.

Theorem 4.1: *Consider a system described by Equation* (4.1) *and invoke assumptions* (i)-(iii). *For any sufficiently small* $\varepsilon > 0$, *the elliptic orbits of the Hamiltonian vector field* $f(x)$ *in Equation* (4.1) *near the separatrix must satisfy the following condition:*

$$\frac{1-k^2}{4}\left(1-\frac{2}{\ln\left(16/1-k^2\right)}\right) \equiv o(\varepsilon), \tag{4.6}$$

then there exists a stochastic layer near that separatrix.

Note that k is the modulus of the Jacobi-elliptic function associated with the energy H_0. The strength of the stochastic layer can be determined via the second theorem as follows.

Theorem 4.2: *Consider a system described by Equation* (4.1) *and invoke assumptions* (i)-(iii). *For some* $\delta > 0$, *there exists a neighborhood* $N(E_0)$ *of* $E_0(x_0, y_0)$, *in which all the elliptic orbits satisfy Equation* (4.6). *If* $E_1^i (\text{or } E_2^j) \in N(E_0)$ *is computed based on* $\omega = m/n\Omega$, *then the strength of the stochastic layer in* $N(E_0)$ *for selected values of i and j* can be *determined from the incremental energy* ΔH *using*

$$|\Delta H| = \left\{ \left| E_1^i - E_0 \right| \text{ or } \left| E_2^j - E_0 \right| \right\} \le \delta, \tag{4.7}$$

in which the symbol $|\cdot|$ *represents the absolute value. For the disappearance of a stochastic layer, we must have*

$$|\Delta H| = \min \max_{i,j} \left\{ \left| E_1^i - E_0 \right|, \left| E_2^j - E_0 \right| \right\} \le \delta. \tag{4.8}$$

As the excitation increases, more and more primary resonances get absorbed by the stochastic layer which then becomes thicker and thicker. Eventually, it may coalesce with the resonant layer (see next chapter). The merging of the primary resonances leads to the onset of *global stochasticity* in the motion, and we have named this enlarged stochastic layer the "*global*" stochastic layer. The ability to model the global stochastic layer is very useful and in the next theorem, an approximate analytical method is suggested.

Theorem 4.3: *Consider a system described by Equation* (4.1) and invoke assumptions (i)-(iii). *For any* E_1 *or* E_2 *of the prescribed resonant orbits, the incremental energy can be approximated by*

$$|\Delta H| = \left\{ \left| E_1 - E_0 \right| \text{ or } \left| E_2 - E_0 \right| \right\} > \delta. \tag{4.9}$$

4.2 Computation of the Strength of Stochastic Layers

In this section, the computation of the strength of stochastic layers is demonstrated by applying the procedure to two very popular nonlinear oscillators: the Duffing oscillator and the forced planar-pendulum oscillator. The former represents the computation of the stochastic layer for the homoclinic orbit and the latter, for the heteroclinic orbit.

4.2.1 An undamped Case IV(c) Duffing oscillator

An undamped Duffing oscillator of Case IV(c) as described in Chapter 3 is considered here. We will demonstrate the appearance of the stochastic layer and compute its strength for a given level of the Hamiltonian energy. The Hamiltonian of *Equation* (3.4 (c)) is $H = H_0 + H_1$, where

$$H_0 = \frac{1}{2}y^2 - \frac{1}{2}\alpha_1 x^2 + \frac{1}{4}\alpha_2 x^4, \tag{4.10}$$

$$H_1 = -xQ_0\cos(\Omega t). \tag{4.11}$$

The saddle point (0,0) of the conservative system can be easily calculated. A homoclinic orbit passing through this saddle point can then be determined. The resulting stochastic layer is qualitatively sketched in *Figure* 4.3. Note that the darker region constitutes the *inner* layer and the lighter region, the *outer* layer. It is important to make this distinction between the inner and outer stochastic layers since the motion characteristics in these layers are not the same. From *Equation* (4.5) the energy increment along the homoclinic orbit can be computed by setting $T_\beta \to \infty$ (or $T_\alpha \to \infty$). That is,

$$\Delta H = \int_{t_0}^{T_\beta + t_0} (f_1 g_2 - f_2 g_1)dt = 2\sqrt{\frac{2}{\alpha_2}}Q_0\pi\Omega\,\mathrm{sech}\left(\frac{\pi\Omega}{2\sqrt{\alpha_1}}\right)\sin(\Omega t_0), \tag{4.12}$$

where

$$\left.\begin{aligned} f_1 &= y,\ f_2 = \alpha_1 x - \alpha_2 x^3 \\ g_1 &= 0,\ g_2 = Q_0\cos(\Omega t) \end{aligned}\right\}. \tag{4.13}$$

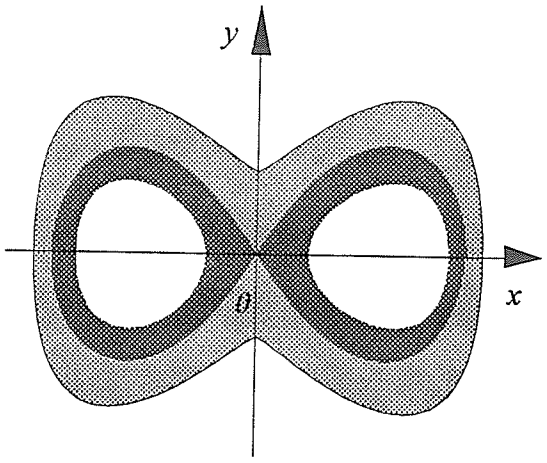

Figure 4.3 Stochastic layer for the undamped Case IV(c) Duffing oscillator.

For the inner layer, we have from *Figure* 4.2(b) $H_0 < E_0$. Since H_0 is the energy of the primary subharmonic resonant orbit, i.e., $H_0 = E_1$, resonance will occur. Thus, the resonant condition (see Han and Luo 1994) can be written as

$$n\omega = \Omega, \quad \text{for } H_0 < E_0. \tag{4.14}$$

Similarly for the outer layer, we have from *Figure* 4.2(b) $H_0 > E_0$ and $H_0 = E_2$, and the resonant condition is

$$(2n-1)\omega = \Omega, \quad \text{for } H_0 > E_0. \tag{4.15}$$

The situations described by *Equations* (4.14) and (4.15) correspond to Cases IV(b) and (a) respectively (see *Chapter* 3). The equations governing these situations are presented in *Appendix* B.1 (*Equations* (B.18)-(B.19) and (B.26)-(B.27)). Using these equations, the resonant energy E_1 and E_2 for the primary subharmonic resonant orbit can be computed. From *Equations* (4.6) and (4.7), the strength for the stochastic layer of the homoclinic orbit for Case IV Duffing oscillator as described by *Equation* (3.4) can be determined as follows,

$$|\Delta H| = \{2|E_1| \text{ or } |E_2|\}. \tag{4.16}$$

From *Equation* (4.12) we have

$$2Q_0\pi\Omega\sqrt{\frac{2}{\alpha_2}}\operatorname{sech}\left(\frac{\pi\Omega}{2\sqrt{\alpha_1}}\right)=\{2|E_1| \text{ or } |E_2|\} \tag{4.17}$$

Choosing $\alpha_1=\alpha_2=1.0$, a graphical plot of the resonant condition and strength of the stochastic layer for the Duffing oscillator are plotted in *Figures* 4.4(a)-(b) respectively. We denote the stochastic layer by solid lines: bold for inner and light for outer. Adopting $\varepsilon=10^{-2}$, *Equation* (4.6) can be solved for the maximum k. Then from *Equation* (B.26) for the inner layer (or (B.18) for the outer layer) of *Appendix* B.1, the energy E_1 for the inner layer (or E_2 for the outer layer) can be computed. With this information, Ω can be determined from *Figure* 4.4(a) and the strength of the stochastic layer Q_0 can then be obtained from *Figure* 4.4(b). The results are plotted in *Figure* 4.5 as solid line, together with strength results from 4 other independent methods: i) dotted line for the standard mapping method based on the homoclinic orbit (see *Equation* (3.53) for the outer layer and *Equation* (3.54) for the inner layer); ii) dash line for the standard mapping method based on the resonant orbit (see *Equation* (B.20)) for the outer layer and *Equation* (B.28) for the inner layer); iii) hollow circle for the Chirikov overlap criterion approach (see *Appendix* B.1 Case IV(a) for the outer layer and Case IV(b) for the inner layer); and iv) solid circle for the renormalization group technique (see *Appendix* B.1 Case IV(a) for the outer layer and Case IV(b) for the inner layer). *Figure* 4.5(a) depicts the strength of the outer stochastic layer and *Figure* 4.5(b) the strength of the inner stochastic layer.

Observe that very good agreement is obtained for the lower-order resonances but becomes progressively poorer as the order of the resonance increases. This can be attributed to the fact that the 4 independent methods constitute approximate solutions. For example, the standard mapping approach is based on linearized energy and phase angle. In the case of the Chirikov overlap criterion and the renormalization group methods, they contain only 2 resonant terms instead of infinite number. On the other hand, our method which is based on an incremental energy approach is solved without introducing any approximations. On this basis, we feel that our method is more accurate than the 4 independent methods.

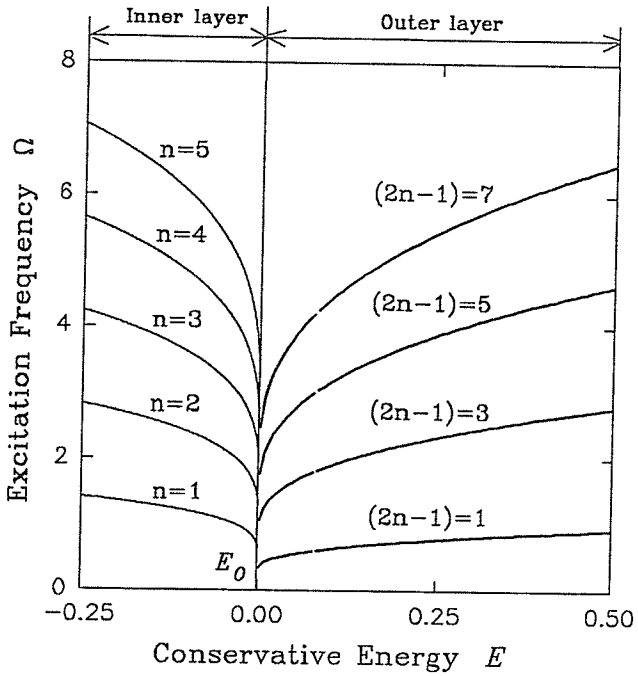

(a) Resonant conditions

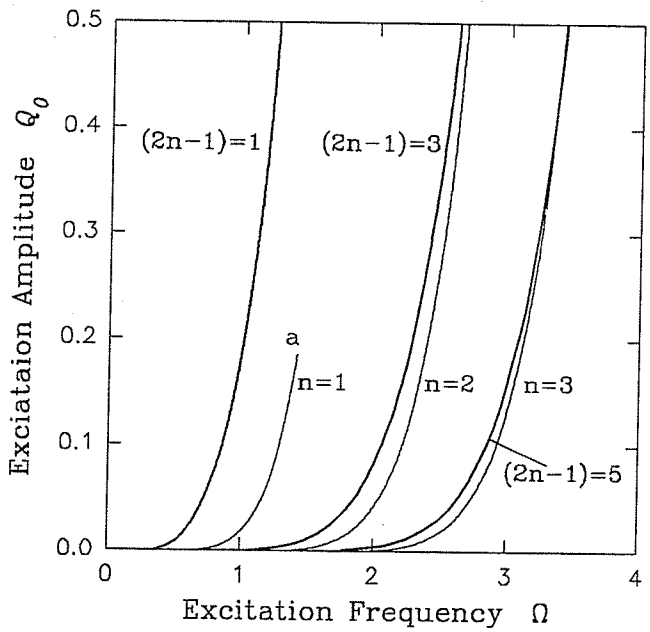

(b) Strength of stochastic layer

Figure 4.4 Resonant condition and strength plots for the Case IV(c) Duffing oscillator (—— inner layer, —— outer layer).

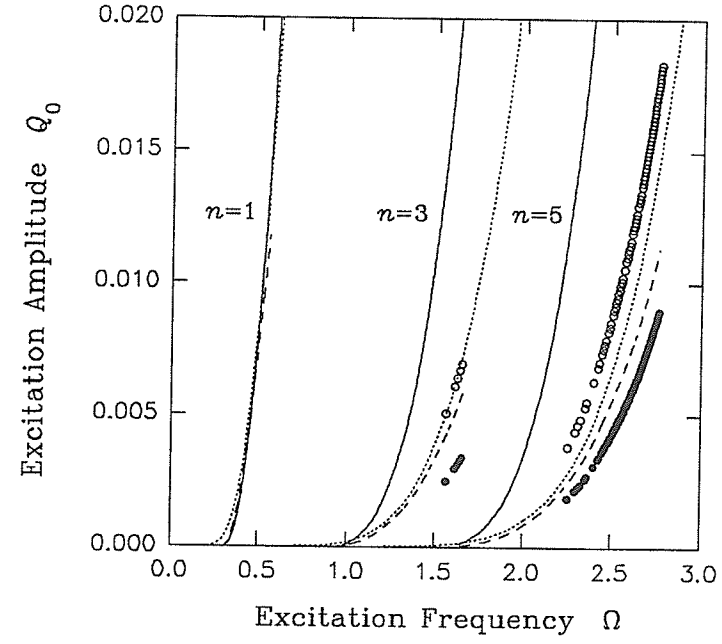

(a) Outer stochastic layer

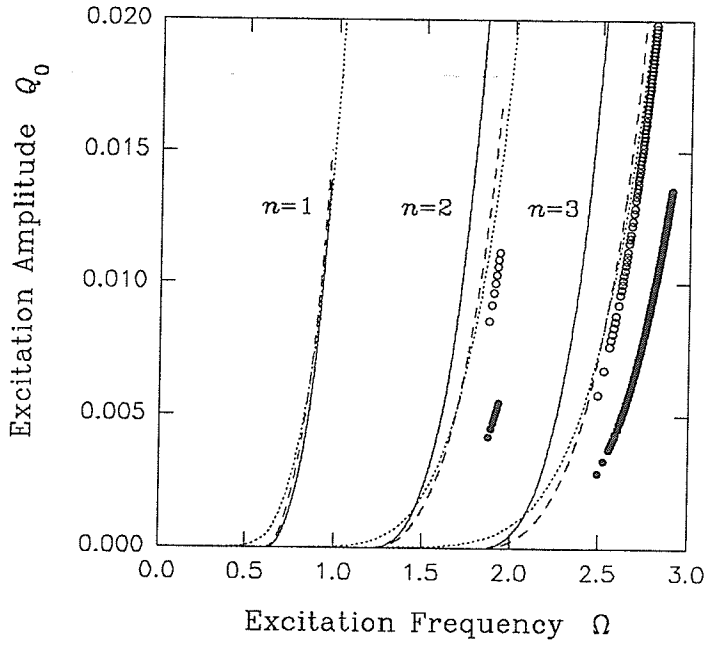

(b) Inner stochastic layer

Figure 4.5 Comparison of strength computations for the Case IV(c) Duffing oscillator (—— present study, ∘ ∘ ∘ Chirikov overlap, ● ● ● renormalization, — — standard mapping (resonant), ---- standard mapping (homoclinic)).

4.2.2 An undamped forced planar-pendulum oscillator

As a second example, a forced planar-pendulum oscillator is investigated. This oscillator has a stochastic layer located near the heteroclinic orbit as depicted in *Figure* 4.6. Consider the differential equation of the planar-pendulum oscillator:

$$\left.\begin{aligned}\dot{x} &= y \\ \dot{y} &= -\lambda \sin x + Q_0 \cos \Omega t\end{aligned}\right\}. \tag{4.18}$$

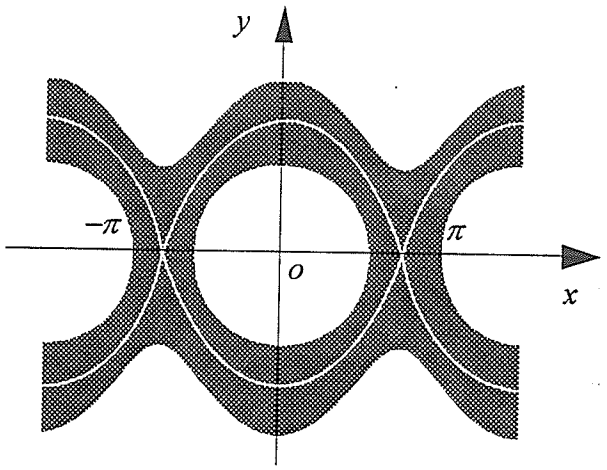

Figure 4.6 Stochastic layer for an undamped forced planar pendulum.

As before, its Hamiltonian consists of the unperturbed and perturbed parts, namely,

$$H_0 = \frac{1}{2}y^2 - \lambda \cos x, \qquad H_1 = -Q_0 x \cos \Omega t. \tag{4.19}$$

The center and saddle points of the unperturbed component of *Equation* (4.18) are $(\pm 2j\pi,\ 0)$ and $(\pm(2j+1)\pi,\ 0)$ at $j = 0,1,2,\cdots$, respectively. Substituting the saddle point into H_0, the energy of the heteroclinic orbit is obtained. Let this quantity be denoted by $H_0 = E_0 = \lambda$. Also, denoting the energy of either the libration or the rotation orbits by $H_0 = E$, it is easy to show that their nonlinear frequencies are given respectively by,

$$\omega = \frac{\pi\sqrt{\lambda}}{2K(k)}, \qquad k < 1 \quad \text{for the libration orbit,} \tag{4.20}$$

and

$$\omega = \frac{\pi\sqrt{\lambda}}{2K(k^{-1})}, \qquad k > 1 \quad \text{for the rotation orbit,} \tag{4.21}$$

where $k = \sqrt{1 + E/\lambda}/\sqrt{2}$. For a conservative system, the solution at the heteroclinic orbit is given by,

$$x(t) = \pm 2\arcsin(\tanh(t)), \quad y(t) = \pm 2\sqrt{\lambda}\,\mathrm{sech}(t). \tag{4.22}$$

Therefore, the energy increment along this heteroclinic orbit, i. e., $T_\alpha \to \infty \left(\text{or } T_\beta \to \infty\right)$, is

$$\Delta H = \int_{t_0}^{T_\alpha + t_0} (f_1 g_2 - f_2 g_1)dt = 2Q_0\pi\sqrt{\lambda}\,\mathrm{sech}\left(\frac{\pi\Omega}{2}\right)\sin(\Omega t_0), \tag{4.23}$$

where

$$\left.\begin{array}{ll} f_1 = y, & f_2 = -\lambda\sin(x) \\ g_1 = 0.0, & g_2 = Q_0\cos(\Omega t) \end{array}\right\}. \tag{4.24}$$

Following the approach employed in the energy analysis described in *Chapter* 3, the subharmonic resonant condition for the libration orbit is,

$$n\omega = \Omega \qquad \text{for } H_0 < \lambda. \tag{4.25}$$

Likewise, the resonant condition for the rotation orbit is

$$(2n-1)\omega = \Omega \quad \text{for } H_0 > \lambda. \tag{4.26}$$

Substituting *Equation* (4.23) into *Equations* (4.7) and (4.9) yields the strength of the stochastic layer for the forced pendulum,

$$2Q_0\pi\sqrt{\alpha}\,\mathrm{sech}\left(\frac{\pi\Omega}{2}\right) = \left\{\left|E_1 - \lambda\right| \text{ or } \left|E_2 - \lambda\right|\right\}. \tag{4.27}$$

The strength computation equation from the standard mapping model is based on the heteroclinic orbit and is given by (see *Section* 3.3),

$$Q_0 = \frac{8\lambda K^*}{\pi\Omega} e^{-(m\pi\sqrt{\lambda}/\Omega)} \cosh\left(\frac{\Omega\pi}{2}\right). \tag{4.28}$$

Choosing $\lambda = 1.0$, a graphical plot of the resonant condition and strength of the stochastic layer for the pendulum are plotted in *Figures* 4.7(a)-(b) respectively. As before, the stochastic layer is represented by solid lines: bold for inner and light for outer. Using $\varepsilon = 10^{-2}$, *Equation* (4.6) can be solved for the maximum k. Then from *Equation* (4.20) for the inner layer (or (4.21) for the outer layer), the energy E_1 for the inner layer (or E_2 for the outer layer) can be computed. With this information, Ω can be determined from *Figure* 4.7(a) and the strength of the stochastic layer Q_0 can then be obtained from *Figure* 4.7(b). The results are plotted in *Figure* 4.8 as solid line, together with strength results from the standard mapping method based on the heteroclinic orbit shown as dotted line. *Figure* 4.8(a) depicts the strength of the *outer* stochastic layer and *Figure* 4.8(b) the strength of the *inner* stochastic layer. Observe that very good agreement is obtained for the lower-order resonances but becomes progressively poorer as the order of the resonance increases. The reason for this behavior is precisely the same as discussed in the previous section for the Duffing oscillator.

4.3 Numerical Experimentations

In this section, we report the results of numerical simulations using an automatic time-stepping Runge-Kutta integrator. The intent here is to provide an additional check on the proposed model by ensuring that the analytically computed number of resonances agrees with that observed in the numerical simulations. Poincare mapping sections are plotted in the numerical runs and the number of resonances generated via numerical integration is noted. The initial conditions for the numerical experimentations are chosen on the homoclinic orbit for the Duffing oscillator and on the heteroclinic orbit for the pendulum.

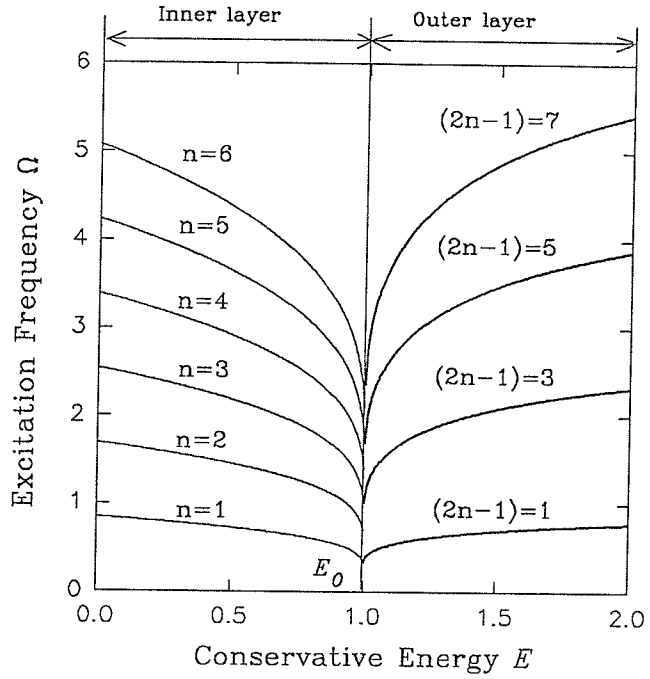

(a) Resonant conditions

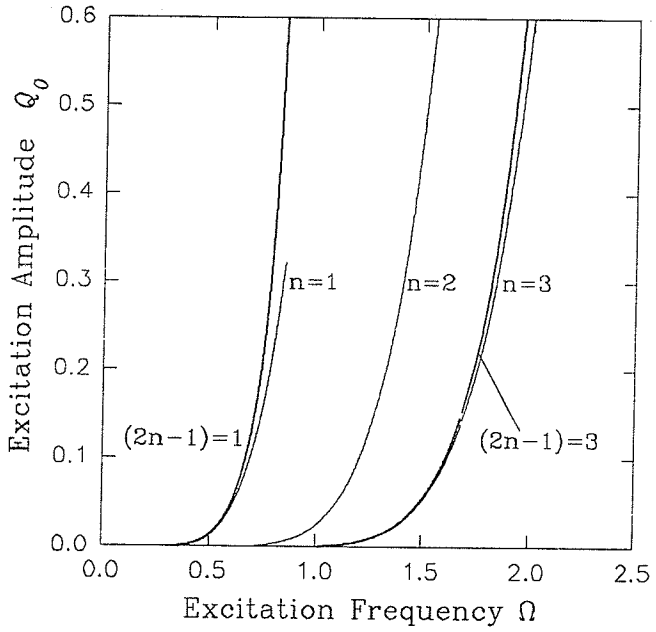

(b) Strength of stochastic layer

Figure 4.7 Resonant condition and strength plots for the forced planar-pendulum oscillator (—— inner layer, —— outer layer).

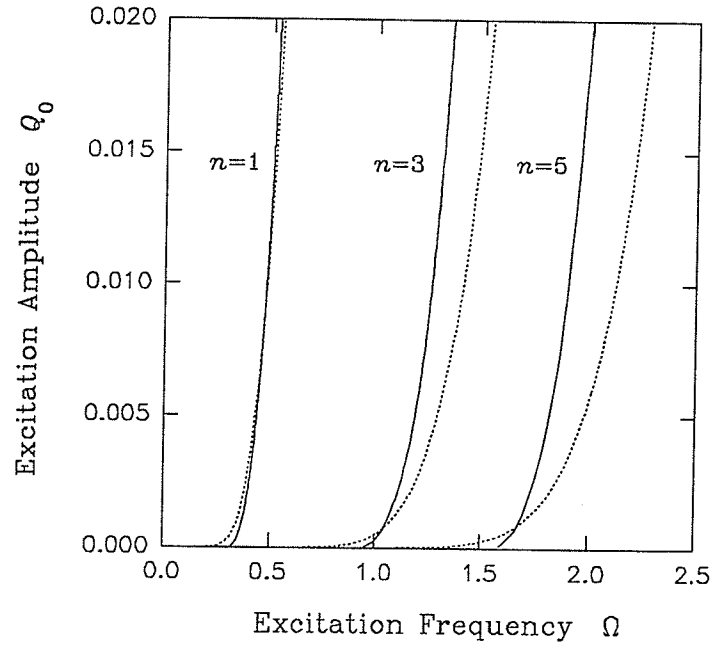

(a) Outer stochastic layer

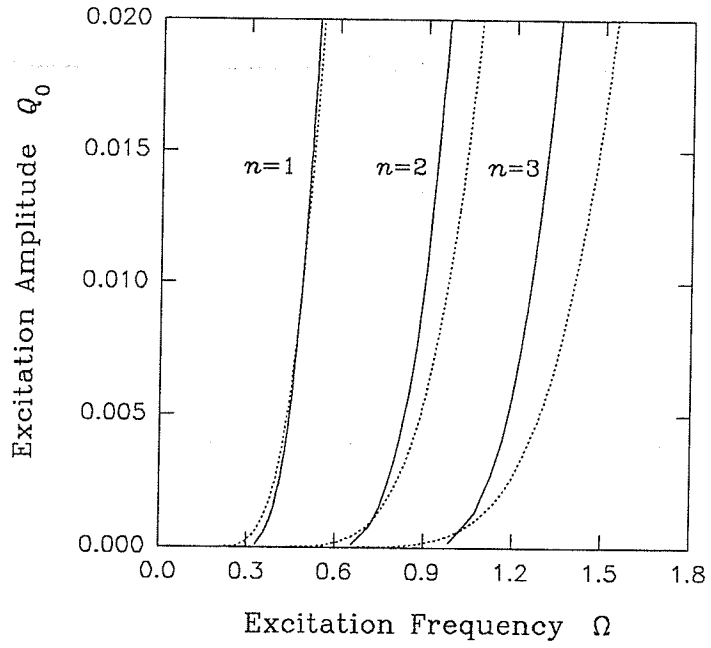

(b) Inner stochastic layer

Figure 4.8 Comparison of strength computations for the forced planar-pendulum oscillator (—— present study, ---- standard mapping (homoclinic)).

The selection of the strength Q_0 and the subsequent numerical simulation runs are plotted in *Figures* 4.9-4.12 for the Duffing oscillator and *Figures* 4.13-4.14 for the pendulum. The details are explained as follows.

4.3.1 Case IV(c) Duffing oscillator

Figure 4.9 depicts the $Q_0 - \Omega$ graph for varying values of n: the outer stochastic layer is shown in *Figure* 4.9(a) and the inner layer in *Figure* 4.9(b). The points A, B, C, D, E, F marked as shown are the locations for carrying out the numerical experimentations. To perform the numerical simulations so that the results make sense, it is crucial that Ω and Q_0 be selected appropriately. Take for example, choosing $\Omega = 0.50$ and $Q_0 = 0.01$ we arrived at point A. Observe that for point A in the outer layer graph, the influence of the n=1 curve is very strong. This implies that we expect to see in the numerical simulations, just one n=1 resonance in the outer layer. On the other hand, from the inner layer graph, the influence of the n=1 curve is extremely weak and we will not be able to see any resonance in the inner layer. This is obvious in the numerical simulation plot of *Figure* 4.10(a). Observe that there is only one resonance in the outer layer as indicated by the "arrow" symbol and also, the inner layer is very weak which is what we expected even though we had plotted approximately 10,000 Poincare mapping points.

At point $B(\Omega = 1.0, Q_0 = 0.01)$ in *Figure* 4.9, we expect to see in the outer layer an extremely weak n=3 resonance but in the inner layer, a very strong n=1 resonance. This is very clear from the numerical simulation plot of *Figure* 4.10(b).

At point $C(\Omega = 1.5, Q_0 = 0.01)$ in *Figure* 4.9, we expect to see in the outer layer a strong n=3 resonance but in the inner layer, a very weak n=2 resonance. Once again, this is obvious from the numerical simulation plot of *Figure* 4.11(a).

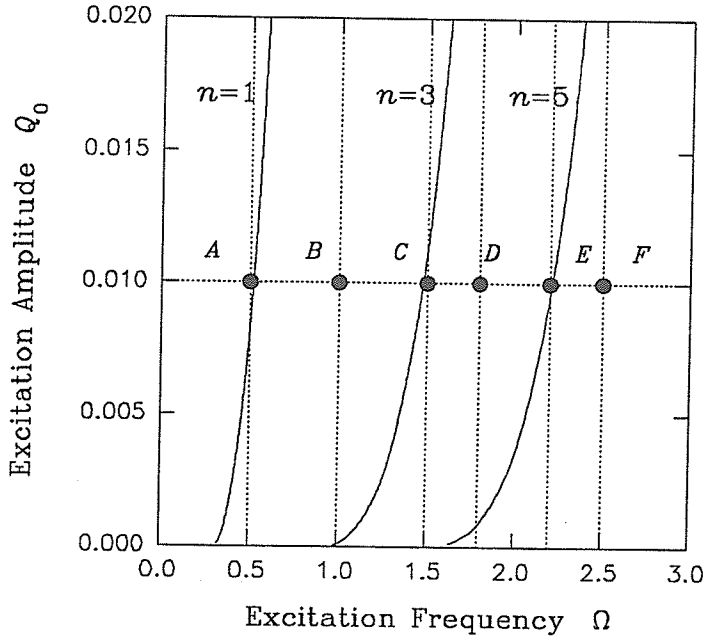

(a) Outer stochastic layer

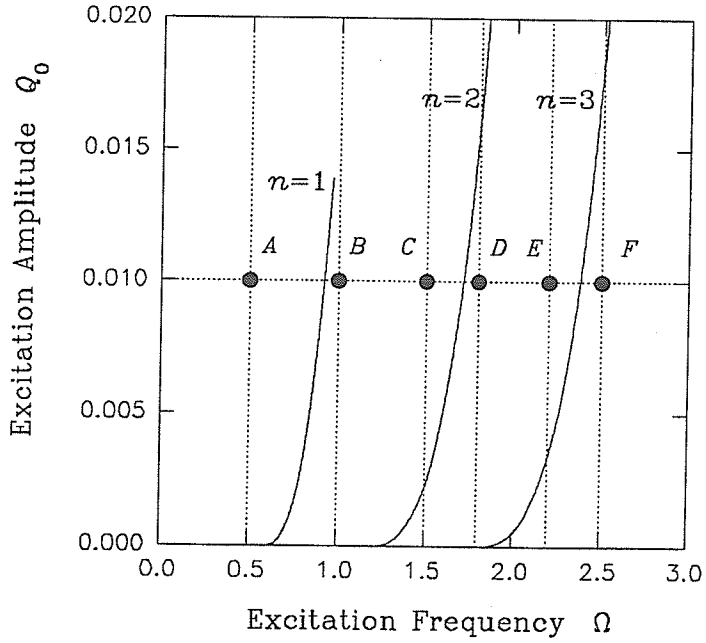

(b) Inner stochastic layer

Figure 4.9 Selection of input parameters for numerical simulations for the Case IV(c) Duffing oscillator.

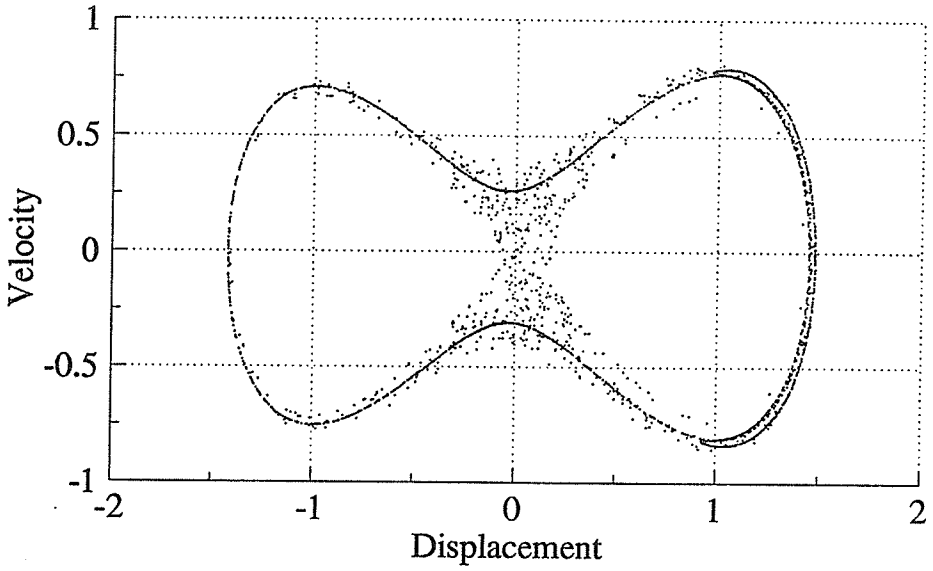

(a) Point *A*

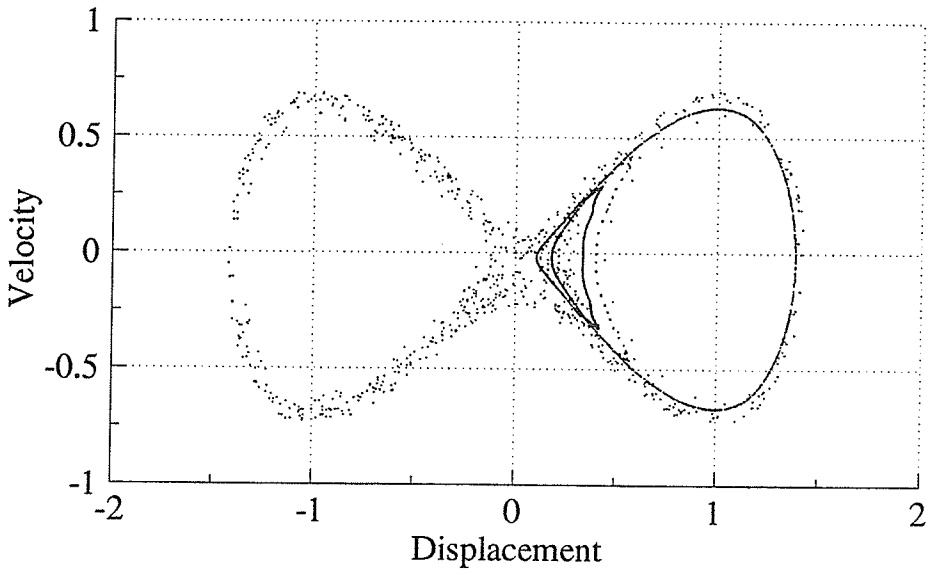

(b) Point *B*

Figure 4.10 Poincare mappings at points *A*, *B* for the Case IV(c) Duffing oscillator.

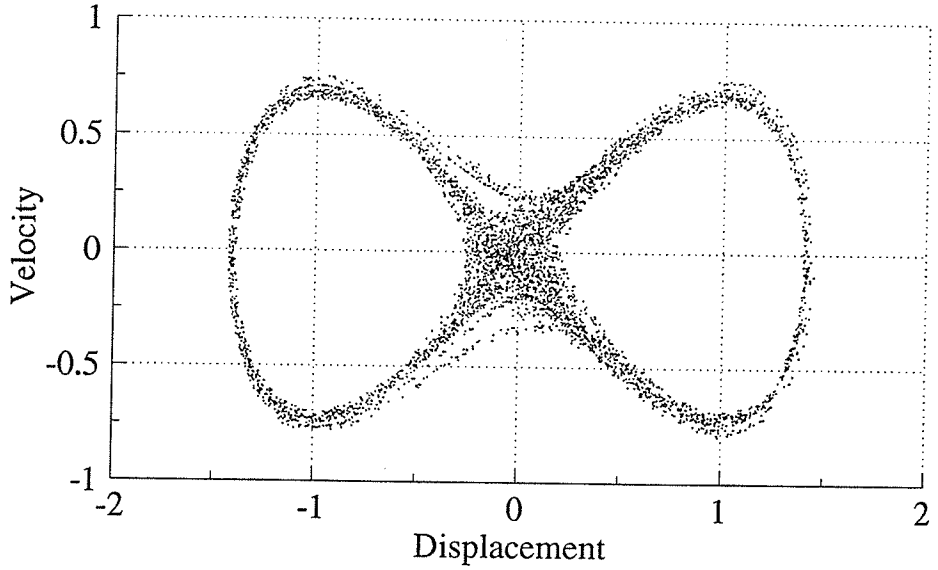

(a) Point C

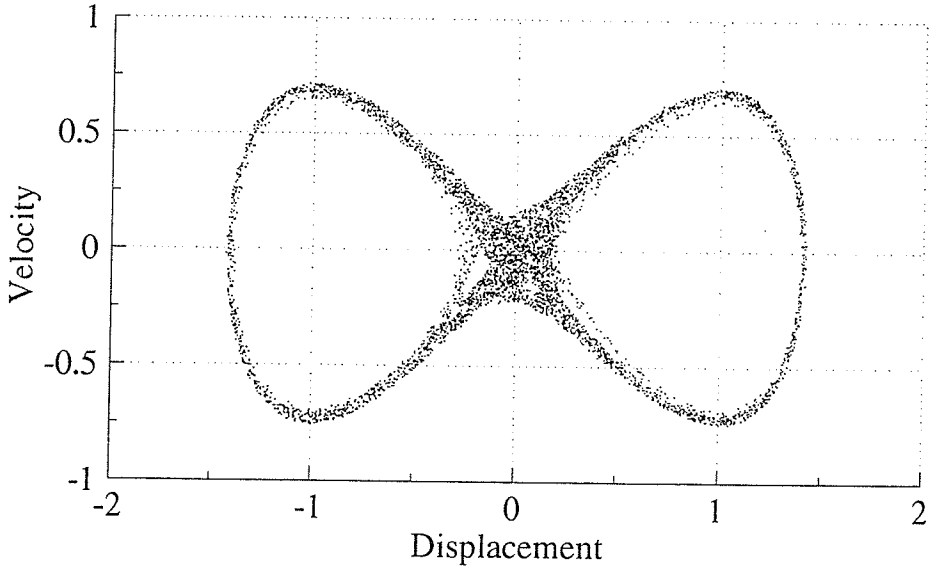

(b) Point D

Figure 4.11 Poincare mappings at points C, D for the Case IV(c) Duffing oscillator.

At point $D(\Omega = 1.8, Q_0 = 0.01)$ in *Figure* 4.9, we expect to see in the outer layer a weak n=5 resonance but in the inner layer, a very strong n=2 resonance. This is very clear from the numerical simulation plot of *Figure* 4.11(b).

At point $E(\Omega = 2.2, Q_0 = 0.01)$ in *Figure* 4.9, we expect to see in the outer layer a strong n=5 resonance and in the inner layer, a weak n=3 resonance. This is clearly shown in the numerical simulation plot of *Figure* 4.12(a).

Finally, at point $F(\Omega = 2.5, Q_0 = 0.01)$ in *Figure* 4.9, we expect to see in the outer layer a reasonably strong n=7 resonance and in the inner layer, a weak n=4 resonance. This is obvious in the numerical simulation plot of *Figure* 4.12(b).

4.3.2 Forced planar-pendulum oscillator

We repeat the same process here for the pendulum. *Figure* 4.13 depicts the $Q_0 - \Omega$ graph for varying values of n: the outer stochastic layer is shown in *Figure* 4.13(a) and the inner layer in *Figure* 4.13(b). For brevity, we will present discussion for only two points; A, B, marked as shown for carrying out the numerical experimentations. To plot the Poincare mapping for the pendulum, we note that due to its multiple saddle points, we will define the Poincare mapping section as,

$$\Sigma = \left\{ (x(t), y(t)) \middle| \, |x(t)| \bmod 2\pi, \; t = 2n\pi / \Omega, n = 1,2,3\cdots \right\}. \tag{4.29}$$

At point $A(\Omega = 0.4, Q_0 = 0.01)$ in *Figure* 4.13, we expect to see in the outer layer a strong n=1 resonance and in the inner layer, a strong n=1 resonance. This is very clear from the numerical simulation plot of *Figure* 4.14(a).

At point $B(\Omega = 0.8, Q_0 = 0.01)$ in *Figure* 4.13, we expect to see in the outer layer a weak n=3 resonance but in the inner layer, a strong n=2 resonance. This is clearly shown in the numerical simulation plot of *Figure* 4.14(b).

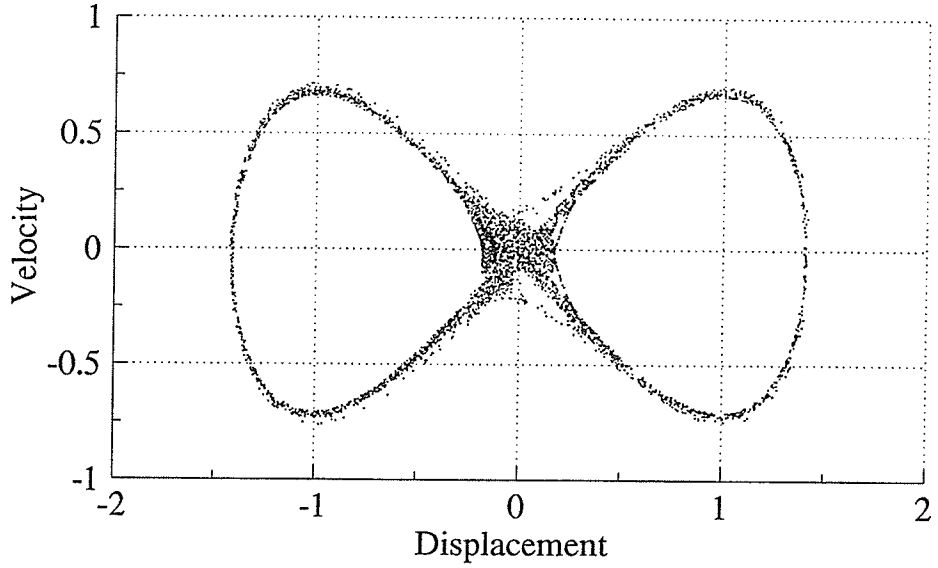

(a) Point E

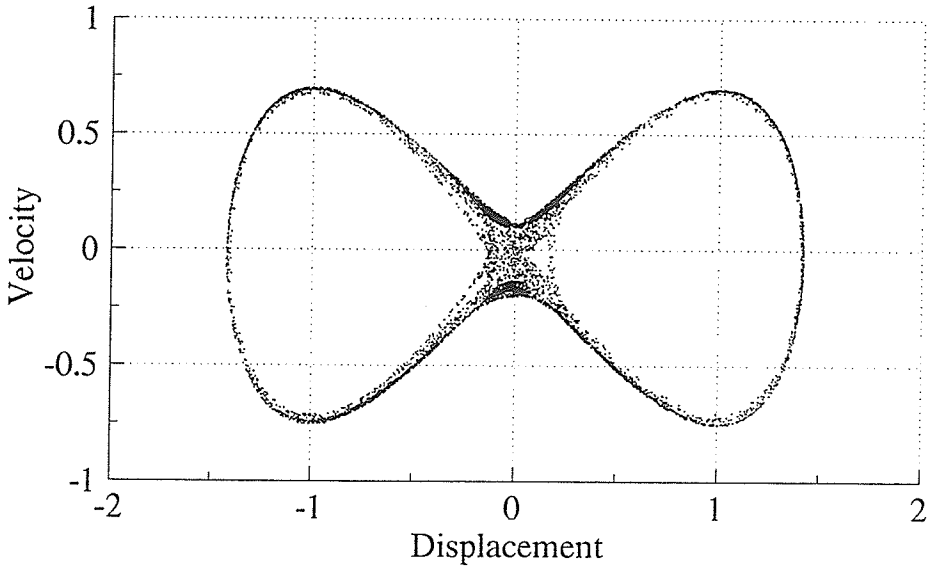

(b) Point F

Figure 4.12 Poincare mappings at points E, F for the Case IV(c) Duffing oscillator.

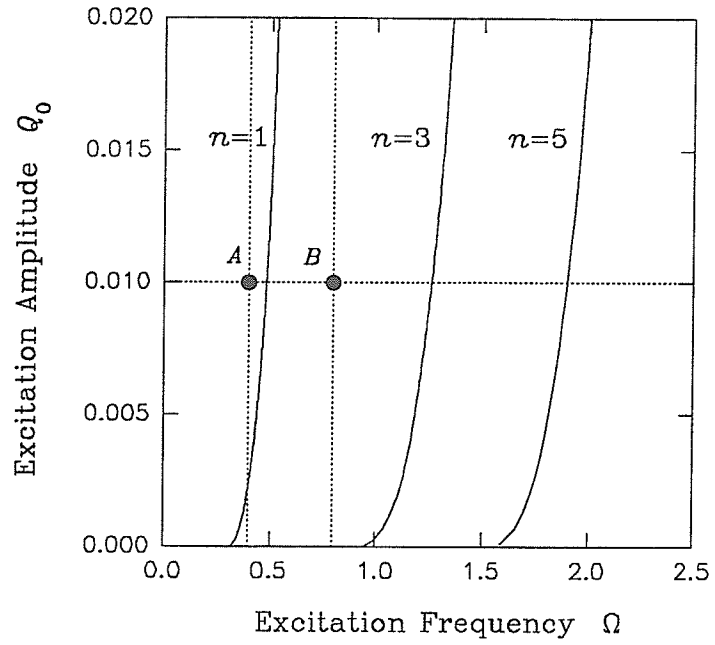

(a) Outer stochastic layer

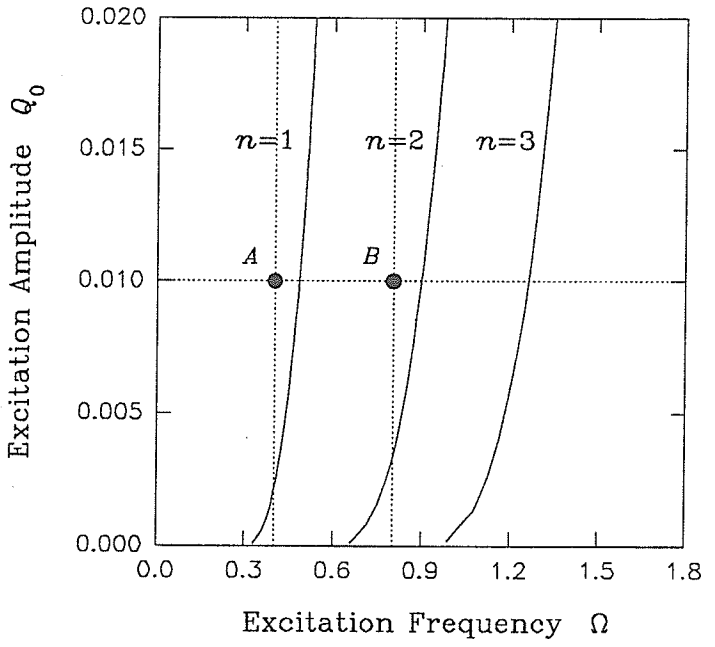

(b) Inner stochastic layer

Figure 4.13 Selection of input parameters for numerical simulations for the forced planar-pendulum oscillator.

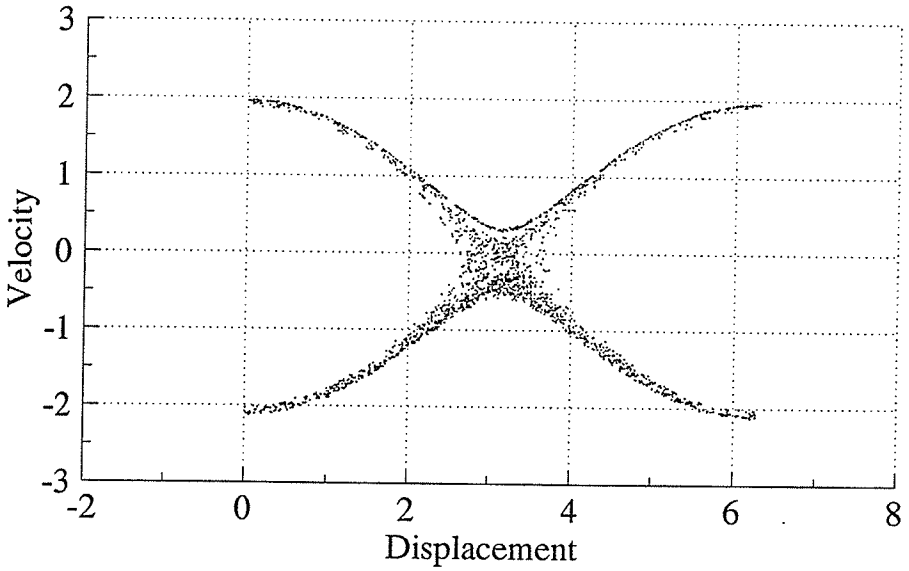

(a) Point *A*

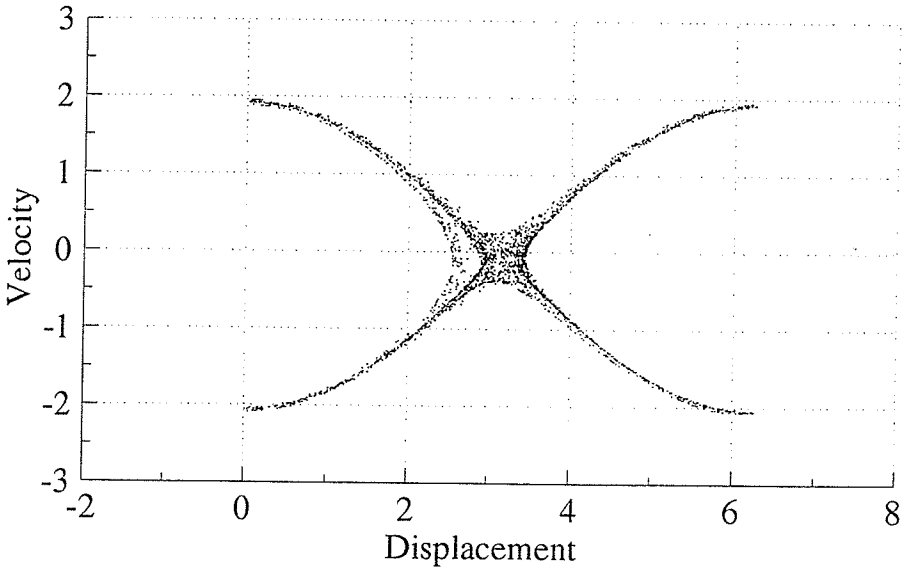

(b) Point *B*

Figure 4.14 Poincare mappings at points *A*, *B* for the forced planar-pendulum oscillator.

4.4 Conclusions

A new method is developed to predict the presence of stochastic layers near the separatrix of a nonlinear system. Two undamped systems are analyzed: the Case IV(c) Duffing oscillator and a forced planar-pendulum oscillator. The outer and inner strengths of the stochastic layer for these two oscillators are computed and verified by comparing with results obtained based on other methods. For the Case IV(c) Duffing oscillator, we employed two standard mapping methods, the Chirikov overlap criterion and the renormalization group technique; and for the forced planar-pendulum oscillator, we utilized the standard mapping method based on the heteroclinic orbit. Good agreement is observed, particularly for the lower-order resonances. From the results of the numerical simulations, the analytically computed number of the resonance agrees perfectly with that generated numerically for both oscillators.

CHAPTER 5

RESONANT LAYERS IN NONLINEAR DYNAMICS

In *Chapter* 4, the stochastic layer near the homoclinic and the heteroclinic orbits was discussed. In this chapter, we look at another type of stochastic layer, one that is located in the vicinity of the resonant orbit. To avoid confusion with the stochastic layer located in the vicinity of the separatrix, we propose to name the region of stochasticity near the resonant orbit the *"resonant"* layer. The condition of resonance with the unperturbed oscillation at frequency ω is

$$m\omega = n\Omega \tag{5.1}$$

in which Ω denotes the excitation frequency, and m, n are positive integers. Thus, the resonant orbit leads to a separation between the actions of neighboring resonances. The resonant layers are isolated from each other and motion from one layer to another is generally forbidden except when the external excitation is very strong. When this happens, the last invariant curve separating the layers surrounding the adjacent elliptic orbits is destroyed and the layers merge together. We can now talk of *global* resonant layers, in analogy to *global* stochastic layers as introduced in *Chapter* 4.

An approximate analytical model of the resonant layer is developed for the first time in this thesis. It is based on the incremental energy approach described in *Chapter* 4. The theory is then applied to compute the strength of the resonant layer for the four types of Duffing oscillator identified as Cases I to IV in the previous chapters. To verify the model, comparisons of results with those computed by applying the Chirikov overlap criterion, the renormalization group technique and from numerical experimentations are made.

5.1 Stochasticity near a Resonant Orbit

We consider a nonlinear conservative dynamical system subjected to an external excitation with a frequency Ω. Repeating *Equation* (4.3) here, the total energy of the system is,

$$H(x,y,t) = H_0(x,y) + H_1(x,y,t), \tag{5.2}$$

where $H_0(x,y)$ and $H_1(x,y,t)$ are the energy functions of the conservative system and external excitation (unperturbed and perturbed Hamiltonians) respectively. For a given energy level, i.e. $H_0 = E_0 = \text{constant}$, the nonlinearly natural frequency and the unperturbed solution can be similarly obtained as described in *Chapter* 3. Applying Taylor series expansion to the perturbed Hamiltonian H_1, the resonant condition given by *Equation* (5.1) becomes,

$$\Omega_{\frac{m}{n}} = \frac{m}{n}\Omega. \tag{5.3}$$

Note that $\Omega_{\frac{m}{n}}$ denotes the (m:n) resonant frequency. Consider in the neighborhood of a natural frequency ω close to $\Omega_{\frac{m}{n}}$, that is,

$$\left|\omega - \Omega_{\frac{m}{n}}\right| \le \varepsilon \quad \text{and} \quad T(E_0) = \frac{2\pi}{\Omega_{\frac{m}{n}}},\ T(E_1) = \frac{2\pi}{\omega}; \tag{5.4}$$

where $\varepsilon << 1$ and T is the nonlinear period. Choosing the odd-order subharmonic resonance as an example, *Equation* (5.4) can be illustrated as shown in *Figure* 5.1. From *Chapter* 4 and *Equation* (5.4), the energy increment along the resonant orbit of the forced conservative system is,

$$\Delta H_0 \approx \int_{t_0}^{T(E_0)+t_0} \frac{dH(x,y,t)}{dt} dt = \int_{t_0}^{T(E_0)+t_0} \{H_0, H_1\}_{\text{Possion}}\, dt = \int_{t_0}^{T(E_0)+t_0} (f_1 g_2 - f_2 g_1) dt, \tag{5.5}$$

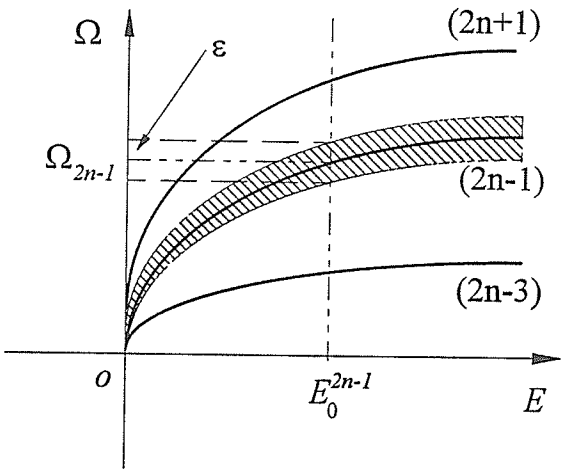

Figure 5.1 Neighborhood of the $(2n-1)$th resonant frequency.

where t_0 is the initial time. Note that *Equation* (5.5) has the form,

$$\Delta H_0 = U_0 F(\phi_0), \tag{5.6}$$

in which U_0 is a system parameter function excluding the initial phase angle $\phi_0 = \Omega t_0$, and $F(\phi_0)$ is a bounded and periodic function. For the elliptic orbits in the neighborhood of the prescribed resonant orbit, the change of phase angle over one period is

$$\Delta\phi = \phi_{i+1} - \phi_i = \Omega T(E_1) = V_0(E_1), \tag{5.7}$$

where V_0 is a function associated with energy E_1. To calculate this new energy iteratively, we introduce the following notation: $E_1 = w_{i+1}$ at the $(i+1)$th period and the corresponding phase angle is ϕ_{i+1}. *Equations* (5.6)-(5.7) can now be written as,

$$\left.\begin{aligned} w_{i+1} &= w_i + U_0 F(\phi_i) \\ \phi_{i+1} &= \phi_i + V_0(w_{i+1}) \end{aligned}\right\}. \tag{5.8}$$

Observe that *Equation* (5.8) is now expressed in a form that permits the resonant layer to

be investigated iteratively. It is a map of the energy change and phase change of a trajectory for each period of its motion. It resembles a perturbed twist map and when applied to the Duffing oscillator, it becomes the whisker map. In the neighborhood of the resonant layer, *Equation* (5.8) can be linearized about a fixed point and we obtain a map similar to the standard map. Considering the period-1 motion, its fixed point can be easily determined: $w_{i+1} = w_i = w_0$ and $\phi_{i+1} = \phi_i + 2m\pi/n = \phi_0 + 2m\pi/n$. This implies,

$$\left.\begin{aligned} F(\phi_0) &= 0 \\ V_0(w_0) &= 2\pi\frac{m}{n} \end{aligned}\right\}. \tag{5.9}$$

Defining a new dimensionless energy

$$I_i = \left.\frac{\partial V_0(w_j)}{\partial w_j}\right|_{w_j = w_0} (w_i - w_0), \tag{5.10}$$

and linearizing *Equation* (5.8) about the fixed point yields

$$\left.\begin{aligned} I_{i+1} &= I_i + KF(\phi_i) \\ \phi_{i+1} &= \phi_i + I_{i+1} \end{aligned}\right\}, \tag{5.11}$$

where $K = U_0\, \partial V_0 / \partial w_0$. Observe that *Equation* (5.11) resembles the standard map and as shown in the next section, when applied to the Duffing oscillator, it becomes the standard map. From *Equation* (5.11) the mechanism involved in the transition to global stochasticity in a conservative system is very clear. The coefficient K is the only control parameter for the characterization of the KAM tori. For instance, for the standard map, a critical value of K is attained when $K = K^* = 0.9716354\cdots$, since at this value, the last remaining KAM torus is broken. When this happens we have,

$$U_0 \frac{\partial V_0}{\partial w_0} = K^*, \tag{5.12}$$

Increasing the excitation results in the merging of the primary resonant layers until they

come into contact the closest resonant orbit. When this happens, the resonant layers will be destroyed, and a new stochastic motion near that resonant orbit will appear. This is qualitatively sketched in *Figure* 5.2 where *Figures* 5.2(a) and (b) show appearance and disappearance of the resonant layer respectively, near the inner most resonant orbit. Depending on the physical system modeled, it is also possible for the resonant layer to come into contact with an outer resonant orbit, instead of the inner orbit as depicted.

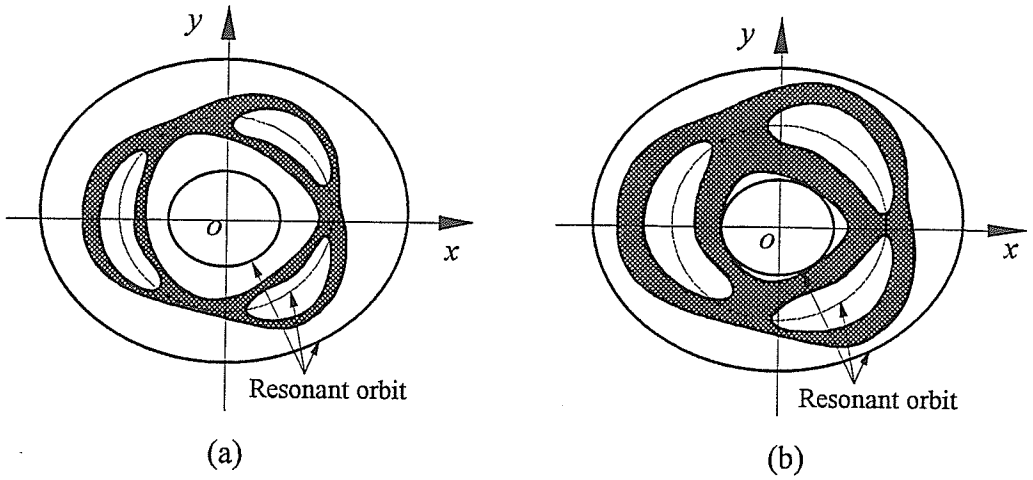

Figure 5.2 Resonant layer: (a) appearance and (b) disappearance

We postulate that when the resonant layer is destroyed, the energy increment in *Equation* (5.5) is given by the energy difference between the two closest resonant orbits, one of which is associated with the destroyed resonant layer. That is,

$$\min\left(\left|E_0^{2n-3}-E_0^{2n-1}\right|,\ \left|E_0^{2n+1}-E_0^{2n-1}\right|\right)=\left|\Delta H_0{}^{(2n-1)}\right|=U_0\left|f(\phi_0)\right|. \tag{5.13}$$

Equation (5.13) constitutes the critical condition for the disappearance of the resonant layer. From this equation, the *disappearance* strength of the resonant layer can be computed. To compute the *appearance* strength, we can resort to *Equation* (5.12). For greater accuracy, we should consider the effects of the secondary resonances in the neighborhood of the intermediate resonant layer shown by the dash line in *Figure* 5.2.

5.2 Resonant Layers for the Undamped Duffing Oscillator

The resonant layers for the four undamped Duffing oscillators are discussed in this section. As presented in *Chapter* 3, the four oscillators are described by *Equations* (3.1)-(3.4) representing Cases I to IV, respectively.

Case I

Resonant layers for the Case I Duffing oscillator are qualitatively sketched in *Figure* 5.3. Note that the *outer* dark patch is bounded by the 1st and 3rd resonant orbits and the *inner* dark patch by the 3rd and 5th resonant orbits. Thus, these outer and inner dark patches are respectively, the resonant layers of the first and third order. There are other resonant layers which are near the neighborhood of the origin, but these are not shown.

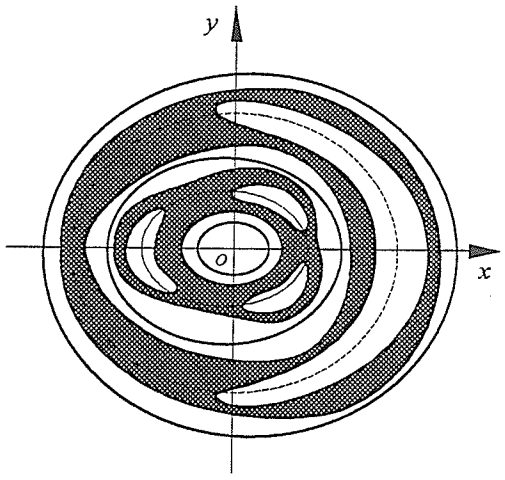

Figure 5.3 Resonant layers near the first and third resonant orbits for Case I.

The unperturbed Hamiltonian for this oscillator is given by *Equation* (3.7) and for a given energy $H_0 = E_0$, its solutions are listed in *Equations* (3.9)-(3.10). The resonant condition as described by *Equation* (3.19) is obtained by analyzing the perturbed Hamiltonian given by *Equation* (3.8). The result is,

$$\Omega_{2n-1} = \frac{\Omega}{2n-1}. \tag{5.14}$$

The period of the resonant orbit is computed using Ω_{2n-1}. However, for all other orbits in the resonant layer, the period is calculated based on ω, that is,

$$T(E_1) = \frac{2\pi}{\omega}. \tag{5.15}$$

The change of phase angle over one period $T(E_1)$ is

$$\Delta\phi = \Omega T(E_1) = V_0 \tag{5.16}$$

in which

$$V_0 = 4\Omega K(k)\sqrt{\frac{2}{\alpha_2}}\frac{k}{h}. \tag{5.17}$$

Therefore, from *Equation* (5.5), the energy increment over one period $T(E_1)$ can be approximated by

$$\Delta H_0 \approx \int_{t_0}^{T(E_0)+t_0} yQ_0 \cos(\Omega t)dt = U_0 \sin(\Omega t_0), \tag{5.18}$$

where

$$U_0 = \frac{2\sqrt{2}\pi\Omega Q_0}{\sqrt{\alpha_2}}\operatorname{sech}\left[\left(n-\frac{1}{2}\right)\pi\frac{K'_{2n-1}}{K_{2n-1}}\right]. \tag{5.19}$$

Note that $K'(k) = K(k')$. Observe that the function U_0 identified in *Section* 5.1 is given by *Equation* (5.19) and comprises only of system parameters. Following the procedure outlined in that section, *Equations* (5.16) and (5.18) are written as

$$\left.\begin{aligned} w_{i+1} &= w_i + U_0 \sin(\phi_i) \\ \phi_{i+1} &= \phi_i + V_0(w_{i+1}) \end{aligned}\right\}. \tag{5.20}$$

Note that *Equation* (5.20) is the whisker map. To obtain the standard map, we linearize *Equation* (5.20) in the neighborhood of the resonant orbits about the period-1 fixed point $w_{i+1} = w_i = w_0$ and $\phi_{i+1} - \phi_i = 2(2n-1)\pi$. The resonant energy is given by

$$2(2n-1)\pi = V_0(w_0). \tag{5.21}$$

From *Equation* (5.10) a new dimensionless energy $I_i = G_1 \Delta w_i$ can be defined, where the function $G_1 = \partial V_0 / \partial w_{i+1}$ at $w_{i+1} = w_i = w_0$, is given by

$$G_1 = -\frac{2\Omega\alpha_2}{(k_{2n-1})^2}\left(\frac{1-2(k_{2n-1})^2}{\alpha_1}\right)^{\frac{5}{2}}\left[K(k_{2n-1}) - \frac{1-2(k_{2n-1})^2}{1-(k_{2n-1})^2}E(k_{2n-1})\right]. \tag{5.22}$$

Linearizing *Equation* (5.20) about the fixed point, we get

$$\left.\begin{aligned} I_{i+1} &= I_i \pm K\sin(\phi_i) \\ \phi_{i+1} &= \phi_i + I_{i+1} \end{aligned}\right\}, \tag{5.23}$$

where $K = U_0|G_1|$. Observe that *Equation* (5.23) is now the standard map. Employing the universal constant of the standard map, i.e. $K = K^* = 0.9716354\cdots$, we can compute the *appearance* strength of the resonant layer and the result is,

$$2Q_0\pi\Omega\sqrt{\frac{2}{\alpha_2}}\operatorname{sech}\left[\left(n-\frac{1}{2}\right)\pi\frac{K'(k_{2n-1})}{K(k_{2n-1})}\right]|G_1| = K^* \approx 0.9716354. \tag{5.24}$$

As a check of *Equation* (5.24), we can use anyone of the 3 methods: Chirikov overlap criterion, renormalization group technique and numerical simulation; to compute the appearance strength. The results based on the Chirikov overlap criterion and the renormalization group technique have already been derived in *Chapter* 3 as *Equations* (3.33) and (3.35). We will simply re-quote them here. Based on Chirikov overlap criterion, the appearance strength is

$$Q_0 = \frac{\Omega^2}{4(2n-1)^2(2n+1)^2 G_0}\left(\frac{1}{\sqrt{Q_{2n-1}}+\sqrt{Q_{2n-1}}}\right)^2. \tag{5.25}$$

Using the renormalization group technique, the appearance strength is,

$$Q_0 = \frac{0.49\Omega^2}{4(2n-1)^2(2n+1)^2 G_0}\left(\frac{1}{\sqrt{Q_{2n-1}}+\sqrt{Q_{2n-1}}}\right)^2. \tag{5.26}$$

The comparison of the predictions of the Chirikov overlap criterion, renormalization group technique and numerical simulation with our results based on the incremental energy approach is listed in the next section.

To compute the *disappearance* strength we assume that our energy postulate which is described mathematically by *Equation* (5.13) holds. This yields the critical condition for the disappearance of the resonant layer, from which the disappearance strength of the resonant layer can estimated. The result is,

$$2Q_0\pi\Omega\sqrt{\frac{2}{\alpha_2}}\operatorname{sech}\left[\left(n-\frac{1}{2}\right)\pi\frac{K'(k_{2n-1})}{K(k_{2n-1})}\right] = \min\left\{\left|E_0^{2n+1}-E_0^{2n-1}\right| \text{ and } \left|E_0^{2n-1}-E_0^{2n-3}\right|\right\}. \tag{5.27}$$

If the incremental energy along a resonant obit is set equal to $\left|E_0^{2n-1}-E_0^c\right|$, where $E_0^c = 0$ is the energy at the origin, *Equation* (5.27) describes the *accumulated* disappearance strength of all the possible resonances higher than order $(2n-1)$ of the system. Therefore, we get the *maximum* critical condition for the accumulated disappearance strength:

$$2Q_0\pi\Omega\sqrt{\frac{2}{\alpha_2}}\operatorname{sech}\left[\left(n-\frac{1}{2}\right)\pi\frac{K'(k_{2n-1})}{K(k_{2n-1})}\right] = E_0^{2n-1}. \tag{5.28}$$

A more accurate model is to sum the effects of each individual resonant layer instead of simply setting the incremental energy to $\left|E_0^{2n-1}-E_0^c\right|$.

Case II

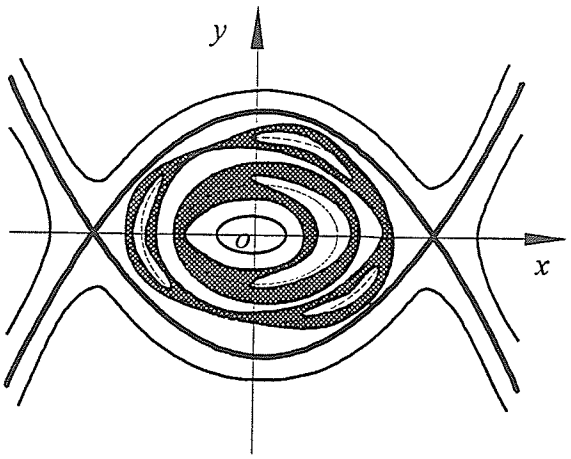

Figure 5.4 Resonant layers near the first and third resonant orbits for Case II.

Resonant layers for the Case II Duffing oscillator are qualitatively sketched in *Figure* 5.4. The structure of the resonant layer differs from that of the Case I oscillator because as shown in *Figure* 5.4, we now have a heteroclinic orbit. For this situation, the resonant layer exist only inside the heteroclinic orbit, otherwise, this layer will lose its stability when it comes into contact with the heteroclinic orbit. The maximum critical condition for instability of the resonant layer is,

$$2Q_0\pi\Omega\sqrt{\frac{2}{\alpha_2}}\operatorname{csch}\left[\left(n-\frac{1}{2}\right)\pi\frac{K'(k_{2n-1})}{K(k_{2n-1})}\right]=\left|E_0^{sx}-E_0^{2n-1}\right|, \tag{5.29}$$

in which E_0^{sx} is the energy of the separatrix, i.e., $E_0^{sx}=\alpha_1^2/(4\alpha_2)$. For brevity, all the results pertaining to the appearance and disappearance strengths are listed in *Appendix* B.

Case III

Resonant layers for the Case III Duffing oscillator are qualitatively sketched in *Figure* 5.5. This oscillator is a special situation of Case I and therefore, all its results, with the exception of the maximum critical condition for the accumulated disappearance strength,

are summarized in *Appendix* B. The maximum critical condition is,

$$2Q_0\pi\Omega\sqrt{\frac{2}{\alpha_2}}\operatorname{sech}\left[\left(n-\frac{1}{2}\right)\pi\frac{K'(k_{2n-1})}{K(k_{2n-1})}\right]=\left|E_0^{2n+1}-E_0^{2n-1}\right|, \tag{5.30}$$

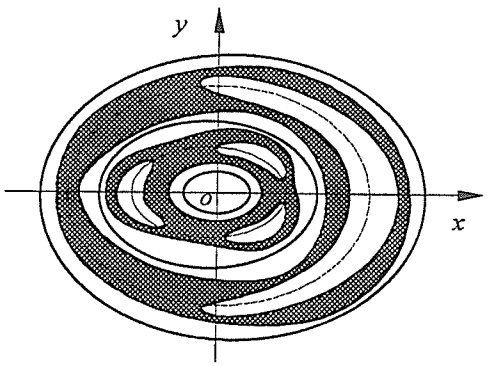

Figure 5.5 Resonant layers near the first and third resonant orbits for Case III.

Case IV

For the Case IV Duffing oscillator, there are two kinds of resonant layers as qualitatively sketched in *Figure* 5.6, representing $E_0<0$ and $E_0>0$. Recall that Case IV(c) which is described by $E_0=0$, possesses only stochastic layers as discussed in *Chapter* 4. Once again, for these two situations, all their results listed in *Appendix* B, with exception of the maximum critical condition for the accumulated disappearance strength. The result for Case IV(a) is obtained by noting that $E_0^c=0$. That is,

$$2Q_0\pi\Omega\sqrt{\frac{2}{\alpha_2}}\operatorname{sech}\left[\left(n-\frac{1}{2}\right)\pi\frac{K'(k_{2n-1})}{K(k_{2n-1})}\right]=E_0^{2n-1}, \tag{5.31}$$

and for the Case IV(b) we have,

$$Q_0\pi\Omega\sqrt{\frac{2}{\alpha_2}}\operatorname{sech}\left[n\pi\frac{K'(k_n)}{K(k_n)}\right]=\left|E_0^n\right|. \tag{5.32}$$

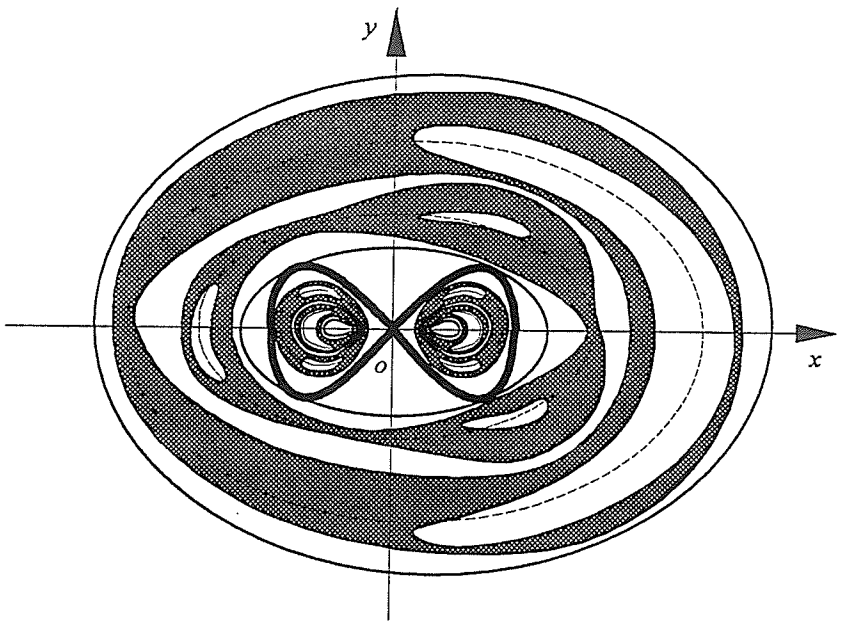

(a) Case IV

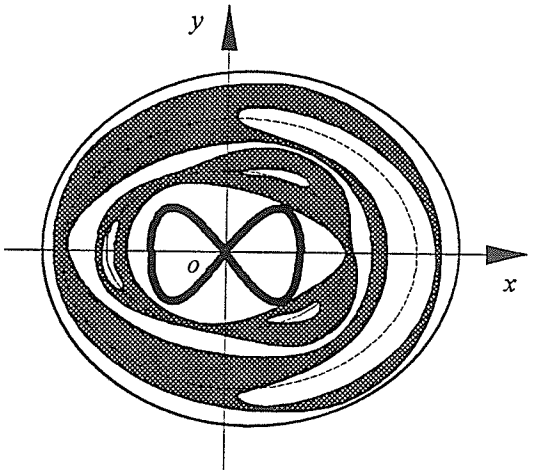

(b) Case IV(a)

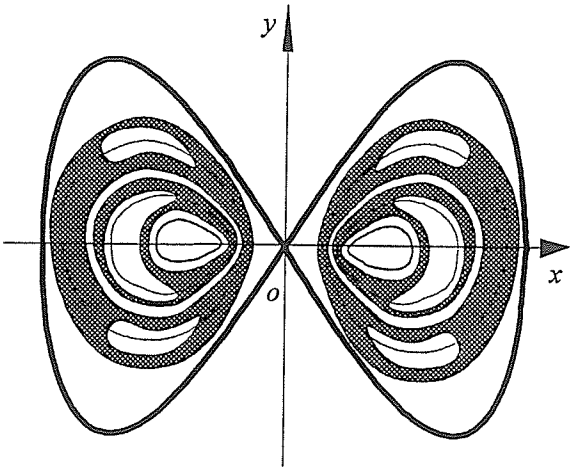

(c) Case IV(b)

Figure 5.6 Resonant layers for Case IV, Case IV(a) and Case IV(b).

5.3 Comparison of Appearance Strength of Resonant Layers

Having obtained the appearance strength of resonant layers based on our proposed incremental energy approach (**IE**), we will now present verification of its predictions. To accomplish this comparative study, three independent methods are employed: Chirikov overlap criterion (**CC**), renormalization group technique (**RG**) and numerical simulations (**NS**). We set $\alpha_1 = \alpha_2 = 1.0$ in *Equations* (3.1)-(3.4) and based on the prescribed initial conditions and the resonant conditions depicted in *Figures* 3.2(a), and 3.4(a) to 3.7(a), we can compute the appearance strengths using *Equation* (5.24) for **IE**, *Equation* (5.25) for **CC**, and *Equation* (5.26) for **RG**. As for the numerical simulation, we used the automatic time-stepping Runge-Kutta integrator with a prescribed tolerance of 10^{-6}. To determine the appearance strength during the numerical experimentation, we check for the appearance of the resonance. For example, if we use input parameters pertaining to say, the third-order resonance and during the numerical experimentation, the third-order resonance visually appears, we record the value of appearance strength.

The results are tabulated in *Table* 5.1 for all four types of Duffing oscillator. We have also listed both the computed input parameters and the computed excitation frequency (to guarantee resonance of the appropriate order). Observe that the agreement among **IE**, **CC** and **RG** are generally better at lower-order resonances and this is attributed to the fact **CC** and **RG** are based on a 2-term approximation which becomes increasingly less accurate as the order of resonance increases. On the other hand, the agreement between **IE** and **NS** is quite good.

Note that we did not give any comparison between the disappearance strength and the accumulated disappearance strength. This is because there are currently no known procedures to compute these quantities other than our proposed incremental energy method.

Table 5.1 Comparison of strength computations

	Order of Resonance	Input Parameters	Excitation Frequency	Appearance Strength Q_0			
		(x, y)	Ω	IE[a]	CC[b]	RG[c]	NS[a]
Case I	1st	(0,10.271)	3.28265	3.04401	3.22748	1.58146	3.04995
	3rd	(0,6.042)	7. 64517	4.25025	13.09158	6.414878	3.60555
	5th	(0,4.701)	11.3406	33.1472	142.4808	69.21561	33.2000
Case II	1st	(0,0.447)	0.91066	0.08633	--	--	0.02873
	3rd	(0,0.559)	2.51717	0.28158	0.25983	0.12732	0.25875
	5th	(0,0.629)	3.80862	1.02497	1.32309	0.64831	1.02500
Case IV(a)	1st	(0,9.877)	3.11735	2.53486	1.99073	0.97513	2.54550
	3rd	(0,3.217)	5.19558	0.77066	1.66639	0.81653	0.75750
	5th	(0,3.471)	9.01867	5.602845	17.47684	8.56365	5.90000
Case IV(b)	1st	(0.8,0.259)	1.33651	0.04687	0.06420	0.03145	0.03547
	2nd	(0.8,0.367)	2.57710	0.08425	016379	0.08026	0.10500
	3rd	(0.8,0.432)	3.73673	0.21239	0.49209	0.24109	0.19985

[a]Luo and Han (1995f).
[b]Han and Luo (1994b).
[c]Luo, Han and Xiang (1995).

5.4 Comparison of the Resonant Layers

In this section, we present a comparison of the resonant layers predicted by IE and NS via their Poincare mapping sections. Once again the results for all four Duffing oscillators are compared, but because the Case III oscillator is very similar to the Case I oscillator, the results of the former are not shown. The input parameters for the numerical experimentations are summarized in *Table* 5.2. The use of these computed input

parameters ensures that we obtained resonant layers during the numerical simulations. We considered only the third-order resonance. Once again, $\alpha_1 = \alpha_2 = 1.0$ is employed.

Table 5.2 Computed input data for numerical simulations for resonant layers

Figure No.	Oscillator Type	(x, y)	Ω	Q_0 (IE)	Q_0 (NS)
Figure 5.7(a)-(b)	Case I	(0.0,5.042)	7.645169	4.25025	3.60555
Figure 5.7(c)-(d)	Case II	(0.0,0.559)	2.517172	0.28158	0.25875
Figure 5.8(a)-(b)	Case IV(a)	(0.0,3.217)	5.195584	0.77066	0.75750
Figure 5.8(c)-(d)	Case IV(b)	(0.8,0.432)	3.736736	0.21239	0.19985

Figures 5.7(a)-(d) show the result for the Cases I and II Duffing oscillators, and *Figures* 5.8(a)-(d) show the result for the Cases IV(a) and IV(b) Duffing oscillators. We have plotted only the right-hand side of the resonant layer for the Case IV(b) Duffing oscillator. Observe the close qualitative agreement between the **IE** and **NS** predictions for all the 4 oscillators. Also, the number of resonances obtained is 3 which is expected for the 3rd-order resonant layer.

5.5 Conclusions

A new method based on an incremental energy approach is proposed for the study of resonant layers in Duffing oscillators. This procedure can be quite easily extended to other nonlinear dynamical systems. The appearance, disappearance and accumulated disappearance strengths of the resonant layers are derived. Both quantitative and qualitative verifications of the appearance strength are provided. In former, 3 independent methods are employed: **CC**, **RG**, and **NS** to check the results computed by our **IE** technique, and in the latter, comparison between **NS** and **IE** are made. Good quantitative and qualitative agreements are observed for all four Duffing oscillators.

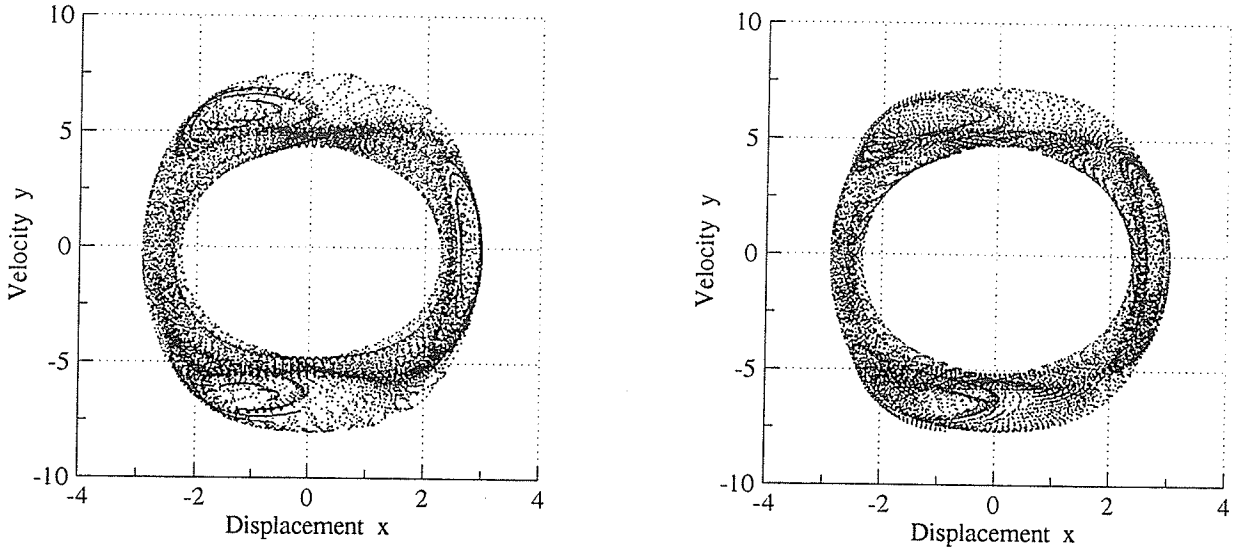

Case I

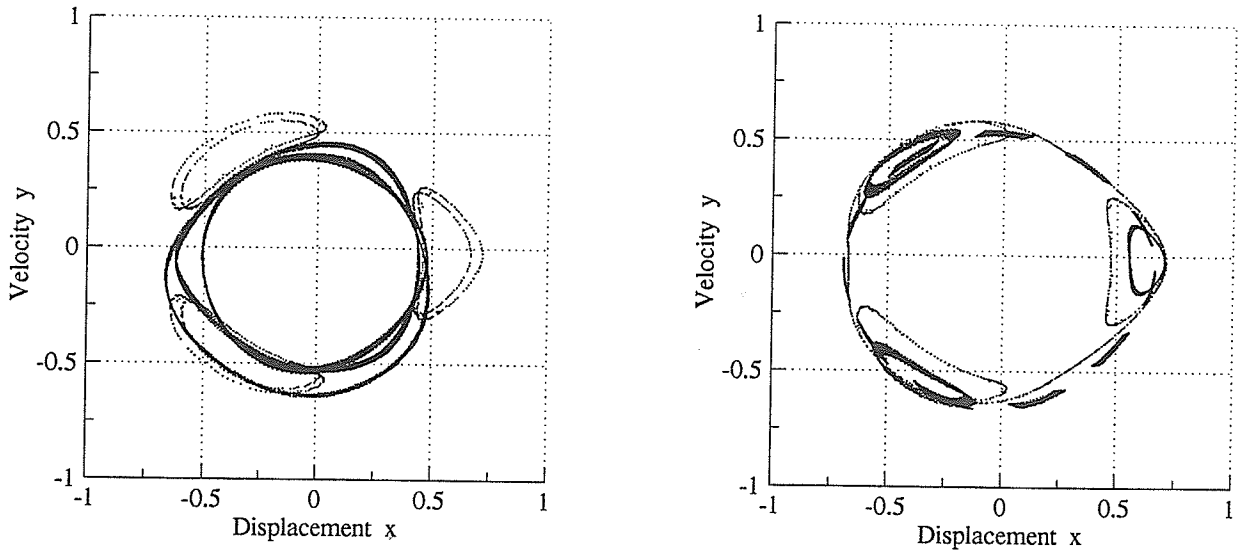

Case II

Figure 5.7 Resonant layers for undamped Cases I and II oscillators.

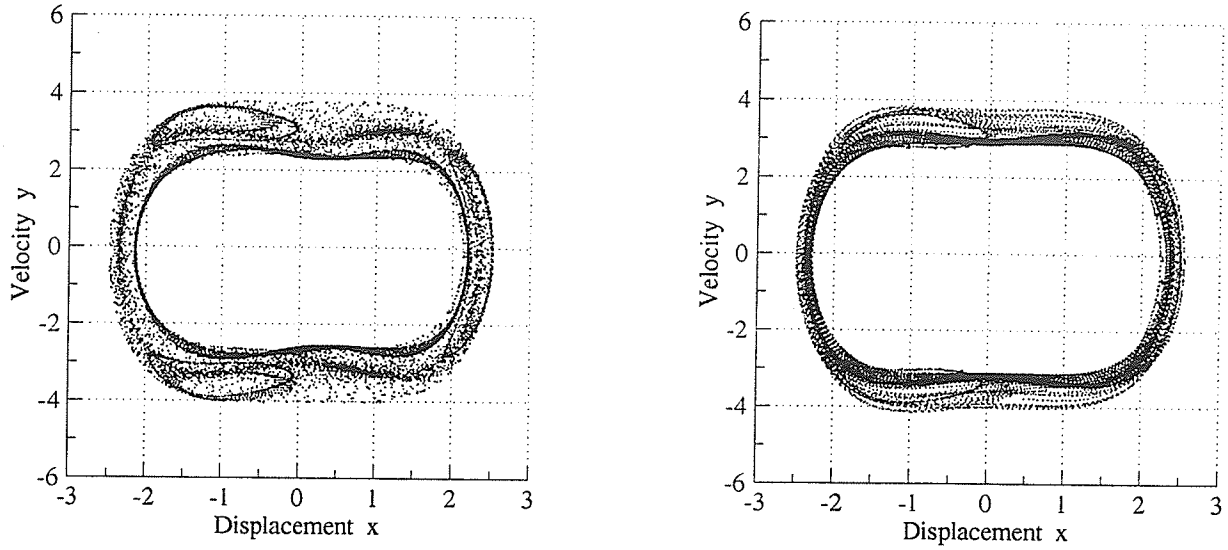

Case IV(a)

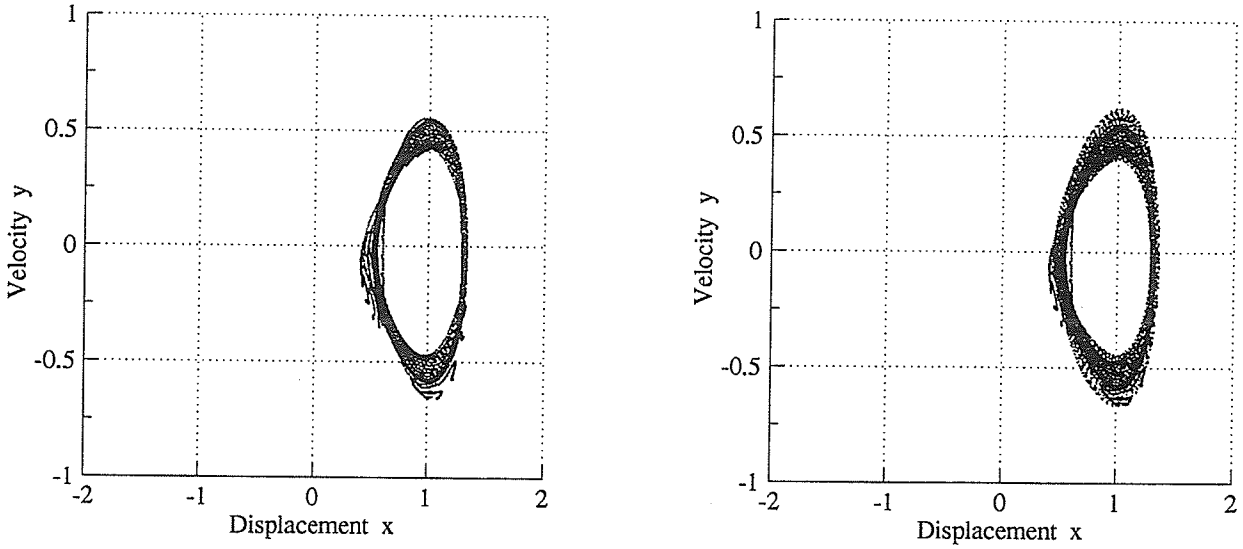

Case IV(b)

Figure 5.8 Resonant layers for undamped Cases IV(a) and IV(b) oscillators.

CHAPTER 6

UNIVERSALITY IN A DAMPED DUFFING OSCILLATOR

In *Chapter* 2, the local bifurcation and stability of the periodic solutions of the damped Duffing oscillator are discussed. In *Chapters* 3-5, we focused on the analytical conditions for the predictions of the stochastic and resonant layers for the undamped Duffing oscillator. In this chapter, we are interested in deriving analytical conditions for the prediction of chaos for the damped Duffing oscillator by examining its universal character.

Universality in a dynamical system was shown by Feigenbaum (1979) for the period-doubling bifurcation sequence to chaos. Collet and Eckmann (1982) later developed an exact renormalization theory for a systematic investigation via mapping. This technique, however, is hard to use and Helleman (1980a, 1980b, 1983) provided an approximate renormalization theory based on period doubling sequence for all one-humped mappings. Holmes (1979) suggested a two-dimensional cubic map which has some features similar to our Case IV Duffing oscillator. However, to the best of our knowledge, we are unable to find in the literature any work done directly on the Poincare map of the Duffing attractor (see also, Moon (1987)). In our model as reported in Luo and Han (1995a, 1995c), the discrete Duffing equation is derived by applying the Naive discretization to its continuous system. Based on this Duffing map, we suggested a cubic renormalization scheme for the computation of its universal property. We demonstrated that self-similarity between the re-scaled and the original maps exist which implies that the fixed points of the re-scaled map exhibit a cascade of period-doubling bifurcations. Verifications via numerical simulations are also provided.

6.1 Discrete Duffing Oscillator

Applying the Naive discretization of *Equation* (2.19) with respect to time yields a discrete map for studying qualitatively the bifurcation and universal behavior of the Duffing oscillator. This leads to the discrete Duffing equation at $x_n = x(t = 2n\pi/\Omega)$ and time step $\Delta t = 2\pi/\Omega$, namely,

$$x_{n+1} - 2x_n + x_{n-1} + (1-b)(x_n - x_{n-1}) + cx_n + dx_n^3 = (1-b)\varpi, \tag{6.1}$$

where the various parameters are defined by

$$\left.\begin{aligned} b &= 1 - \frac{2\pi}{\Omega}\delta, & c &= \left(\frac{2\pi}{\Omega}\right)^2 \alpha_1, \\ d &= \left(\frac{2\pi}{\Omega}\right)^2 \alpha_2, & \varpi &= \frac{Q_0}{\alpha_1}\frac{2\pi}{\Omega}. \end{aligned}\right\} \tag{6.2}$$

From *Equation* (6.1), the discrete map is,

$$P: \left.\begin{aligned} x_{n+1} &= x_n + \varpi + y_{n+1} \\ y_{n+1} &= by_n - cx_n - dx_n^3 \end{aligned}\right\}. \tag{6.3}$$

6.2 Cubic Renormalization for the Discrete Duffing Equation

In this section we present the derivation of the condition governing the onset of chaos for the discrete Duffing equation. This is then followed by a quantitatively analysis of the Feigenbaum cascade as illustrated in *Figure* 6.1. In the sketch, we have shown the route to chaos via period-doubling bifurcations on the positive branch of X_n and further bifurcations result in either the onset of chaos and/or the route "jumping" to the negative branch of X_n until fully developed chaos occurs. Note that this jump phenomenon is unique to the Duffing map and may or may not be present in other dissipative maps.

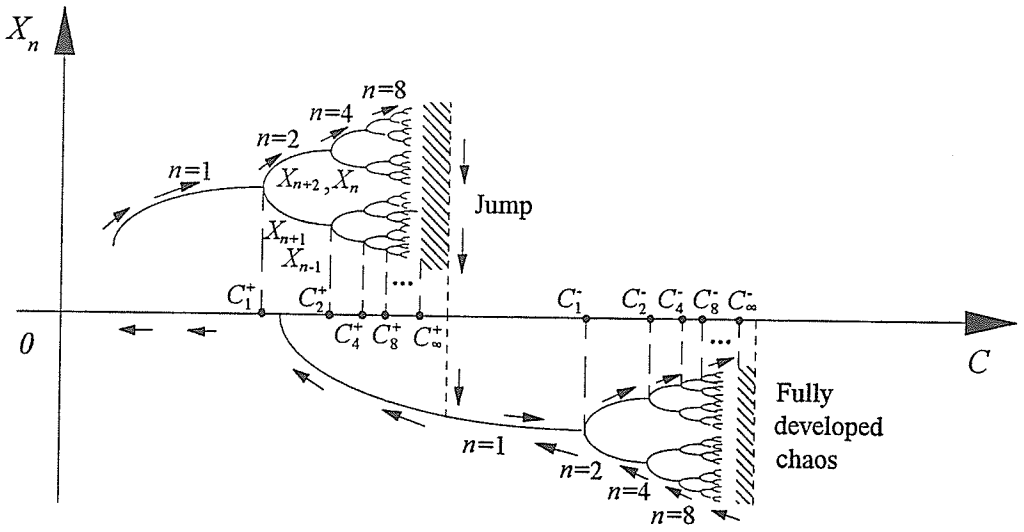

Figure 6.1 Cascade of bifurcations for the discrete Duffing map.

The points of bifurcations are indicated by $C_1^+, C_2^+, C_4^+, C_8^+, \cdots$ for the positive branch and $C_1^-, C_2^-, C_4^-, C_8^-, \cdots$ for the negative branch. Observe that there are two "special" points denoted by C_∞^+ and C_∞^- representing respectively, the onset of chaos for the positive and negative branches. They are the universal parameters of the dissipative Duffing map. In our work here, we have proposed a model for computing them analytically and to verify the results, we have also generated them via numerical simulations. In our model, a cubic renormalization scheme for *Equation* (6.3) is set up. Introducing the following transformation,

$$\left.\begin{aligned} x_n &= X_n + \bar{\delta} \\ y_n &= Y_n - \varpi \end{aligned}\right\}, \tag{6.4}$$

and substituting into *Equation* (6.3) yields,

$$\left.\begin{aligned} X_{n+1} &= X_n + Y_{n+1} \\ Y_{n+1} &= BY_n + CX_n + DX_n^2 - EX_n^3 \end{aligned}\right\}; \tag{6.5}$$

where

$$-d\bar{\delta}^3 + c\bar{\delta} + (-1+b)\varpi = 0 \tag{6.6}$$

and

$$\left.\begin{aligned} B &= b,\ \ C = -\left(c + 3d\bar{\delta}^2\right) \\ D &= -3d\bar{\delta},\ \ E = d \end{aligned}\right\}. \tag{6.7}$$

Note that the parameter $\bar{\delta}$ can be evaluated using *Equation* (6.6). From *Equation* (6.5), the period-1 solution can be computed, i.e.

$$\left.\begin{aligned} Y_n &= 0 \\ X_{n_1} &= 0 \end{aligned}\right\} \quad \text{and} \quad \left.\begin{aligned} Y_n &= 0 \\ X_{n_{2,3}} &= \frac{D \pm \sqrt{D^2 + 4CE}}{2E} \end{aligned}\right\}. \tag{6.8}$$

Eliminating Y_n in *Equation* (6.5) leads to,

$$X_{n+1} + BX_{n-1} = (1 + B + C)X_n + DX_n^2 - EX_n^3. \tag{6.9}$$

Taking the second iteration of *Equation* (6.9), we get

$$X_{n+2} + BX_n = (1 + B + C)X_{n+1} + DX_{n+1}^2 - EX_{n+1}^3. \tag{6.10}$$

To compute the period-2 solution (see *Figure* 6.1), we set $X_{n+2} = X_n$ and $X_{n+1} = X_{n-1}$ in *Equations* (6.9)-(6.10) and after a considerable algebraic effort in solving for the coefficients, we arrive at

$$a_6 X_n^6 + a_5 X_n^5 + a_4 X_n^4 + a_3 X_n^3 + a_2 X_n^2 + a_1 X_n + a_0 = 0, \tag{6.11}$$

in which

$$\left.\begin{aligned} a_0 &= (1+B)^2\left[C + 2(1+B)\right], & a_3 &= 2DE\left[C - (1+B)\right], \\ a_1 &= D(1+B)\left[C + 2(1+B)\right], & a_4 &= E^2\left[3(1+B) + 2C\right] - D^2E, \\ a_2 &= D^2(1+B) + EC^2 - 3E(1+B)\left[C + (1+B)\right], & a_5 &= 2DE^2, \qquad a_6 = -E^3. \end{aligned}\right\} \tag{6.12}$$

Solving *Equation* (6.11) numerically, we get $X_n = X_n^*$ as solutions. Then from *Equation* (6.9) (or (6.10)) and invoking solution periodicity, namely, $X_{n+2} = X_n$ and $X_{n+1} = X_{n-1}$, we get the second set of (unstable) solutions $X_{n+1} = X_{n+1}^*$. Next, a perturbation in the

neighborhood of these two solutions X_n^* and X_{n+1}^* is introduced:

$$\left.\begin{aligned} X_n &= X_n^* + \Delta X_n \\ X_{n+1} &= X_{n+1}^* + \Delta X_{n+1} \end{aligned}\right\}. \tag{6.13}$$

Likewise, we have

$$\left.\begin{aligned} X_{n+2} &= X_n^* + \Delta X_{n+2} \\ X_{n-1} &= X_{n+1}^* + \Delta X_{n-1} \end{aligned}\right\}. \tag{6.14}$$

Substituting *Equations* (6.13)-(6.14) into *Equations* (6.9)-(6.10) and noting that X_n^* satisfy *Equation* (6.11), we get a new group of iterative equations:

$$\Delta X_n + B\Delta X_{n-2} = e_1\Delta X_{n-1} + e_2\Delta X_{n-1}^2 - E\Delta X_{n-1}^3, \tag{6.15}$$

$$\Delta X_{n+1} + B\Delta X_{n-1} = e_3\Delta X_n + e_4\Delta X_n^2 - E\Delta X_n^3, \tag{6.16}$$

$$\Delta X_{n+2} + B\Delta X_n = e_1\Delta X_{n+1} + e_2\Delta X_{n+1}^2 - E\Delta X_{n+1}^3; \tag{6.17}$$

where e_1, e_2, e_3, e_4 are given by

$$\left.\begin{aligned} e_1 &= 1+B+C+2DX_n^* - 3E\left(X_n^*\right)^2, & e_2 &= D-3EX_n^*, \\ e_3 &= 1+B+C+2DX_{n+1}^* - 3E\left(X_{n+1}^*\right)^2, & e_4 &= D-3EX_{n+1}^*. \end{aligned}\right\} \tag{6.18}$$

Multiplying *Equation* (6.15) by B and *Equation* (6.16) by e_1, we have after substituting into *Equation* (6.17):

$$\begin{aligned} \Delta X_{n+2} + B^2\Delta X_{n-2} = {} & \left(e_1e_3 - 2B\right)\Delta X_n + e_1e_4\Delta X_n^2 - e_1E\Delta X_n^3 \\ & + e_2\left(\Delta X_{n+1}^2 + B\Delta X_{n-1}^2\right) - E\left(\Delta X_{n+1}^3 + B\Delta X_{n-1}^3\right). \end{aligned} \tag{6.19}$$

In the neighborhood of the period-2 solution, ΔX_{n+1} and ΔX_{n-1} are very close. A scale ratio r can be defined as follows,

$$r = \frac{\Delta X_{n+1}}{\Delta X_{n-1}}. \tag{6.20}$$

Neglecting the nonlinear terms in *Equation* (6.16), an approximate expression of ΔX_{n-1} is obtained as a function of ΔX_n:

$$\Delta X_{n-1} \approx \frac{e_3}{r+B}\Delta X_n. \tag{6.21}$$

Substituting *Equations* (6.20)-(6.21) into *Equation* (6.19) produces

$$\begin{aligned}\Delta X_{n+2} + B^2\Delta X_{n-2} = (e_1e_3 - 2B)\Delta X_n + \left[e_1e_4 + \frac{e_2e_3^2(r^2+B^2)}{(r+B)^2}\right]\Delta X_n^2 \\ - E\left[e_1 + \frac{e_3^3(r^3+B^3)}{(r+B)^3}\right]\Delta X_n^3\end{aligned} \tag{6.22}$$

To make *Equation*(6.22) algebraically similar to *Equation* (6.9) we perform the following re-scaling,

$$\left.\begin{aligned} X_n' &= \varepsilon\Delta X_n \\ X_{n+1}' &= \varepsilon\Delta X_{n\pm2}\end{aligned}\right\}, \tag{6.23}$$

where ε is a scaling constant. Substituting *Equation* (6.23) into *Equation* (6.22) yields

$$X_{n+1}' + B'X_{n-1}' = \overline{C'}X_n' + D'X_n'^2 - E'X_{n+1}'^3, \tag{6.24}$$

in which

$$\left.\begin{aligned} B' &= B^2, \quad \overline{C'} = e_1e_3 - 2B, \quad \overline{C} = 1+B+C \\ D' &= \varepsilon\left[e_1e_4 + \frac{e_2e_3^2(r^2+B^2)}{(r+B)^2}\right], \quad E' = \varepsilon^2E\left[e_1 + \frac{e_3^3(r^3+B^3)}{(r+B)^3}\right]\end{aligned}\right\}. \tag{6.25}$$

By setting the scaling ratio $r = 1$, self-similarity exist between the re-scaled map given by *Equation* (6.24) and the original map described by *Equation* (6.9). That is, *Equations*

(6.9) and (6.24) have identical form, implying that the fixed points of the re-scaled map exhibit a cascade of bifurcations with B', C' replacing B, C. Chaos via period-doubling bifurcations will ensue at $B' = B = B_\infty$, $\overline{C'} = \overline{C} = \overline{C}_\infty$, $D' = D = D_\infty$ and $E' = E = E_\infty$. Thus, for a dissipative map from *Equation* (6.25), we have:

$$B = 0 \text{ or } 1, \tag{6.26}$$

$$\overline{C} + 2B = \left[\overline{C} + 2DX_n - 3EX_n^2\right]\left[\overline{C} + 2DX_{n+1} - 3EX_{n+1}^2\right], \tag{6.27}$$

$$D = \varepsilon\left[e_1 e_4 + \frac{e_2 e_3^2\left(1+B^2\right)}{(1+B)^2}\right], \tag{6.28}$$

$$\varepsilon^2\left[e_1 + \frac{e_3^3\left(1+B^3\right)}{(1+B)^3}\right] = 1. \tag{6.29}$$

Observe that there are five unknown parameters B, $\overline{C}$, D, E and ε in four *Equations* (6.26)-(6.29). Fortunately, from *Equations* (6.6)-(6.7), D is related to B, C, and E. These results clearly portray the universal character of the dissipative map near the transition to chaos. In general, there are several fixed points and each must undergo the period-doubling bifurcation in the transition to global chaos.

6.3 Verification through Universality Computation

Employing *Equations* (6.11) and (6.26)-(6.29), the universal character of a damped Duffing oscillator is studied by computing the universal parameter $\overline{C}_\infty$. To verify the computed solutions, the discrete Duffing *Equation* (6.5) is then solved numerically via iteration. The results are tabulated in *Table* 6.1. Note that our computed universal results are denoted by **CR** (cubic renormalization) and the numerically obtained solutions by **NS** (numerical simulation). Also, the superscript "+" and "-"signs represent the positive and

negative values of X_n, respectively (see *Figure* 6.1). We will present comparison studies for Cases II and IV Duffing oscillators since they are the only ones that have saddles.

Table 6.1 Comparison of **CR** and **NS** values for universal parameter $\overline{C}_\infty$.

Equivalent Damping B	Case II Oscillator ($D = E = -1.0$)			Case IV Oscillator ($D = E = 1.0$)					
	CR	**NS**	Error %	**CR**$^+$	**NS**$^+$	Error %	**CR**$^-$	**NS**$^-$	Error %
0.0	-1.562	-1.560	0.13	1.434	1.590	9.81	2.812	2.790	0.79
0.1	-1.640	-1.640	0.00	1.638	1.760	6.93	3.032	2.980	1.75
0.2	-1.724	-1.720	0.24	1.834	1.970	6.90	3.262	3.250	0.37
0.3	-1.824	-1.820	0.22	2.014	2.110	4.55	3.486	3.370	3.44
0.4	-1.916	-1.910	0.31	2.200	2.270	3.08	3.704	3.590	3.18
0.5	-2.024	-1.990	1.71	2.384	2.450	2.69	3.916	3.800	3.05
0.6	-2.110	-2.100	0.48	2.566	2.630	2.43	4.132	4.010	3.04
0.7	-2.228	-2.200	1.30	2.746	2.810	2.28	4.342	4.220	2.89
0.8	-2.344	-2.315	1.27	2.926	2.990	2.14	4.548	4.440	2.43
0.9	-2.444	-2.425	0.78	3.102	3.000	3.40	4.774	4.670	2.23
1.0	-2.570	-2.240	14.73*	3.286	2.180	50.73*	4.958	4.660	6.40*

*Hamiltonian System

The Feigenbaum cascade in phase plane for Case II Duffing oscillator is sketched in *Figure* 6.2. Since bifurcation points at the positive and negative branches of X_n are the same, it is not necessary to treat them separately, i.e., $C_1^+ = C_1^- = C_1$, $C_2^+ = C_2^- = C_2$, $\cdots$. Observe the excellent agreement obtained between the **CR** and **NS** results. The only exception is at B=1.0 where the system is Hamiltonian and the model is no longer valid.

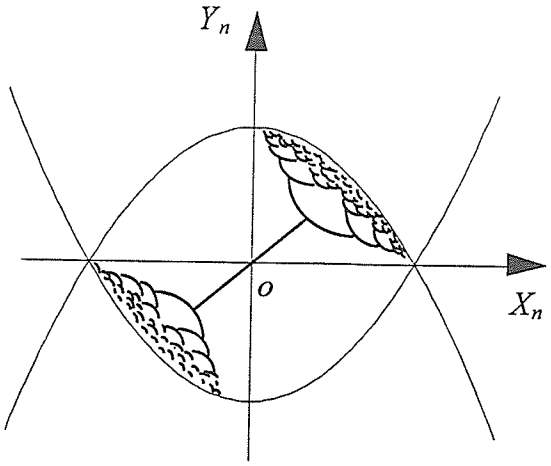

Figure 6.2 Feigenbaum cascade for the Case II Duffing oscillator.

The Feigenbaum cascade in phase plane for Case IV Duffing oscillator is sketched in *Figure* 6.3. For this system, it is necessary to consider both the positive and negative branches of X_n . Observe that very good agreement is obtained between the **CR** and **NS** results. As before, the model breaks down at B=1.0.

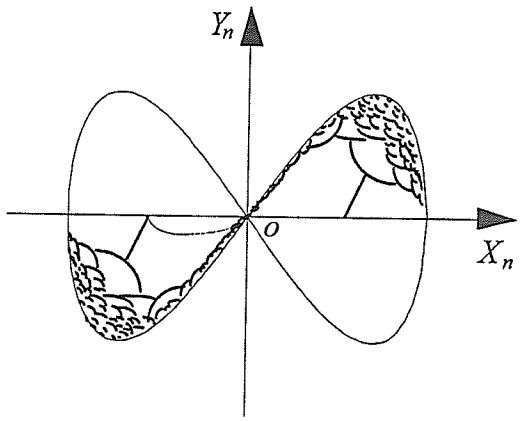

Figure 6.3 Feigenbaum cascade for the Case IV Duffing oscillator.

The results of the Cases II and IV Duffing oscillators obtained via numerical simulations are depicted in *Figures* 6.4-6.5 respectively. The prescribed parameters for Case II oscillator are $B = 0.0$, $D = E = -1.0$ and for Case IV, we have $B = 0.0$, $D = E = 1.0$. Note

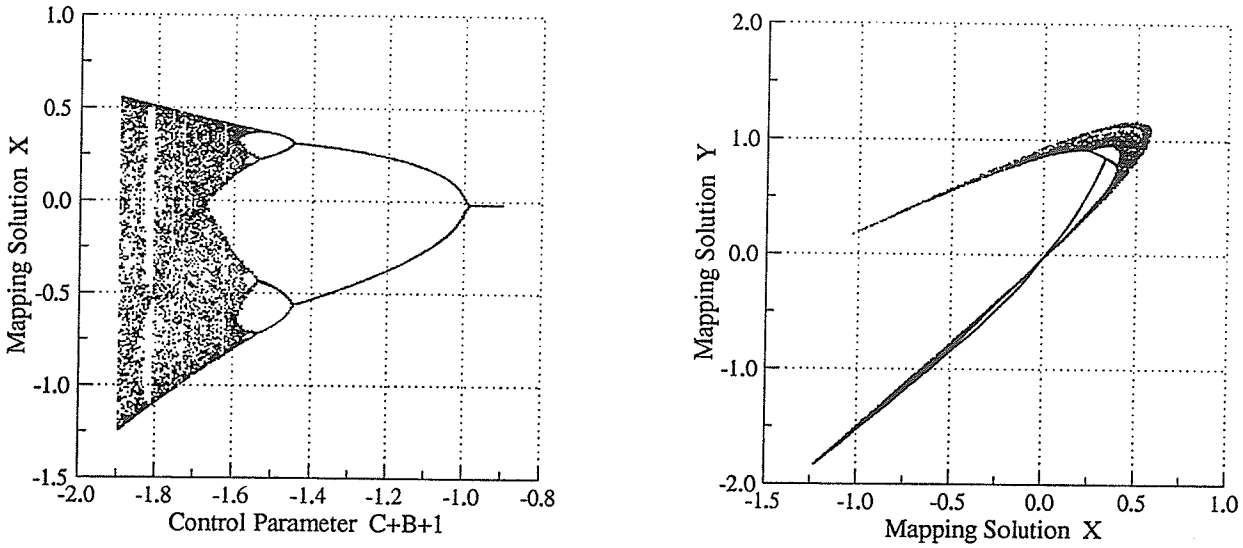

(a) Increasing $\overline{C}$

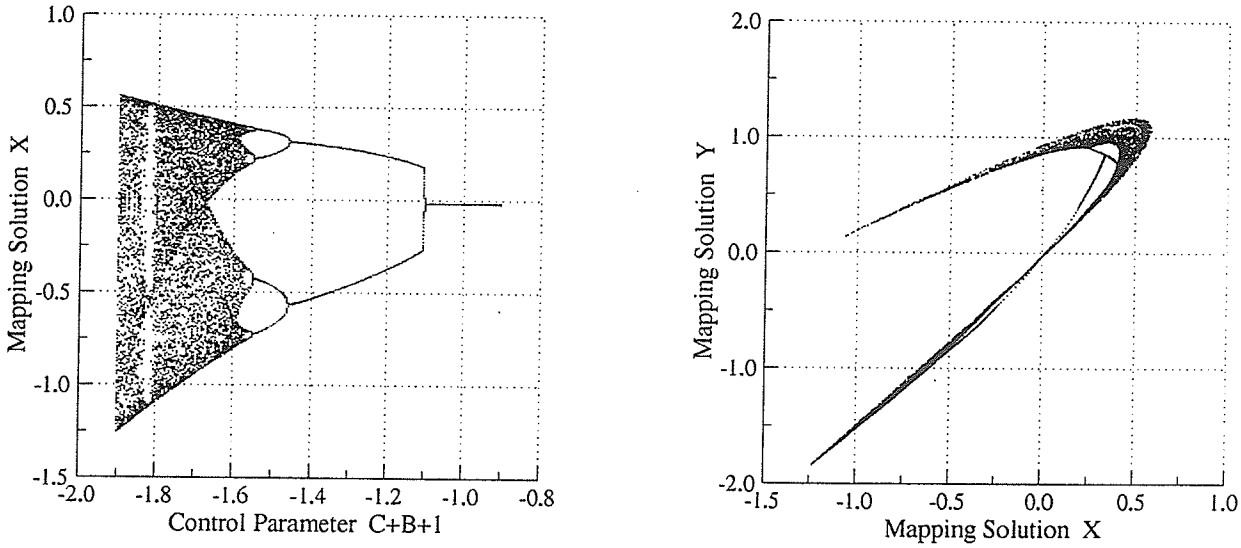

(b) Decreasing $\overline{C}$

Figure 6.4 Numerically simulated cascades of bifurcation for the Case II Duffing oscillator.

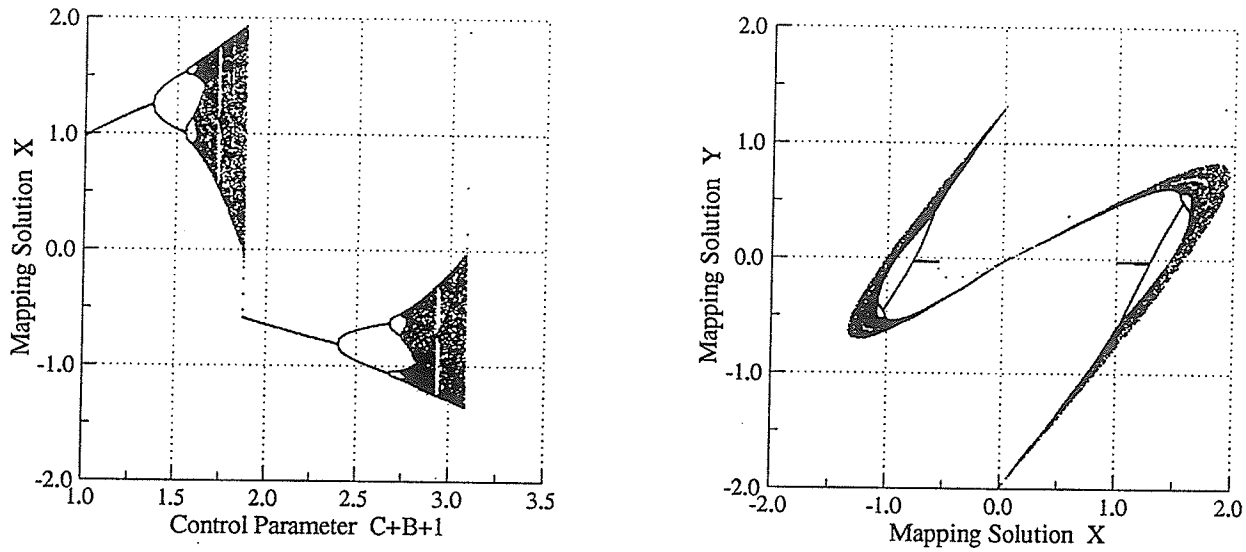

(a) Increasing $\overline{C}$

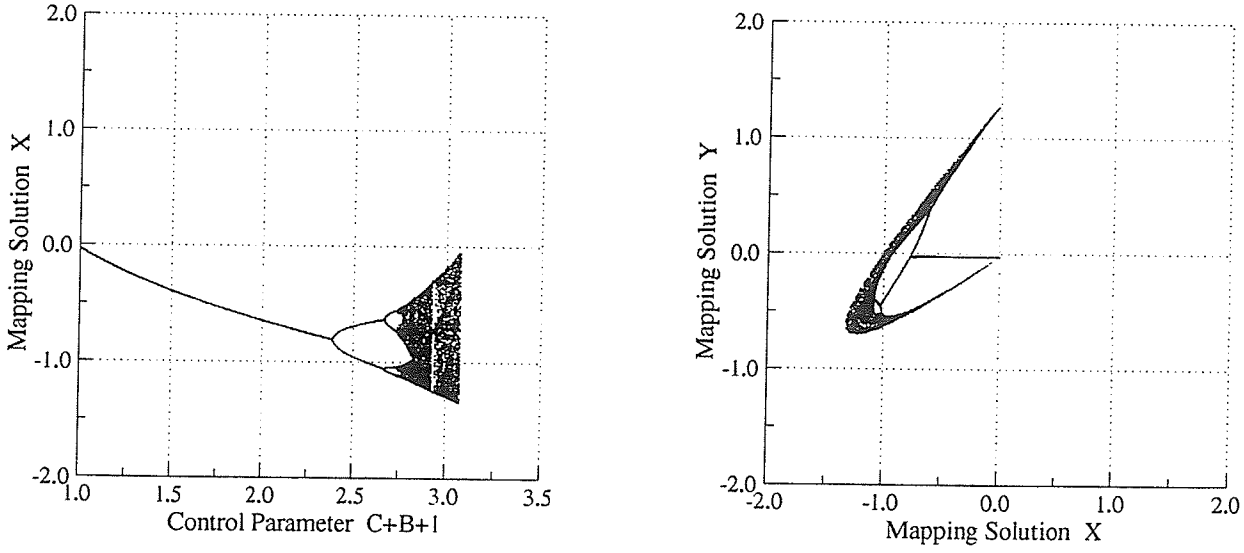

(b) Decreasing $\overline{C}$

Figure 6.5 Numerically simulated cascades of bifurcation for the Case IV Duffing oscillator.

that for each figure, we have plotted both the increasing and decreasing $\overline{C}$. For Case II oscillator, observe that the $C_1^+ = C_1^- = C_1$, $C_2^+ = C_2^- = C_2$, $\cdots$ and it exhibits a catastrophe bifurcation when $\overline{C}$ is increasing. For Case IV oscillator, the jump phenomenon is clearly visible. These numerical results qualitatively confirm our analytical model.

6.4 Numerical Experimentations

In this section, we are interested in employing the analytically computed universal parameters to numerically simulate the continuous Duffing equation as described by *Equation* (2.19). To carry out the numerical experiments, it is necessary to compute the original system parameters $\delta, \alpha_1, \alpha_2, Q_0$ of the continuous Duffing equation. They are given by *Equations* (6.2), and (6.6)-(6.7); and the expressions are:

$$\delta = \frac{\Omega}{2\pi}(1-B), \tag{6.30}$$

$$\alpha_1 = -\left(\frac{\Omega}{2\pi}\right)^2\left[\overline{C}_\infty - 1 - B + \frac{D^2}{3E}\right], \tag{6.31}$$

$$\alpha_2 = \left(\frac{\Omega}{2\pi}\right)^2 E, \tag{6.32}$$

$$Q_0 = \frac{1}{3}\left[\frac{4D^2}{9E} + \left(\overline{C}_\infty - 1 - B\right)\right]\left(\frac{\Omega}{2\pi}\right)^2. \tag{6.33}$$

The results are plotted in *Figure* 6.6 for varying values of B. From this plot and *Equation* (2.19), we numerically simulated the bifurcation cascade and strange attractor for the damped Case IV Duffing oscillator in *Figure* 6.7. Once again, the jump phenomenon is clearly visible.

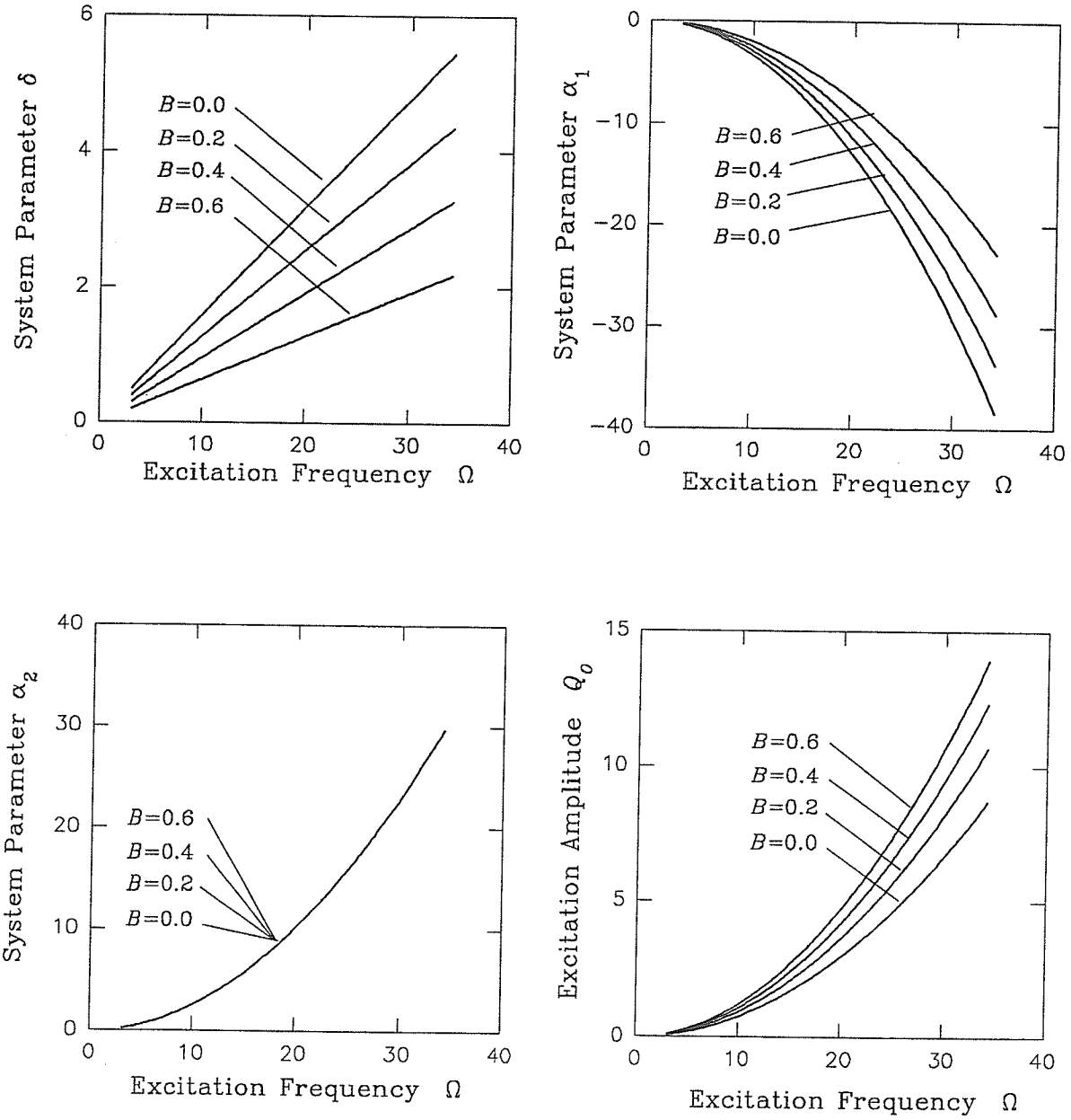

Figure 6.6 System parameters versus excitation frequency based on the universal parameters for the continuous Case IV Duffing oscillator.

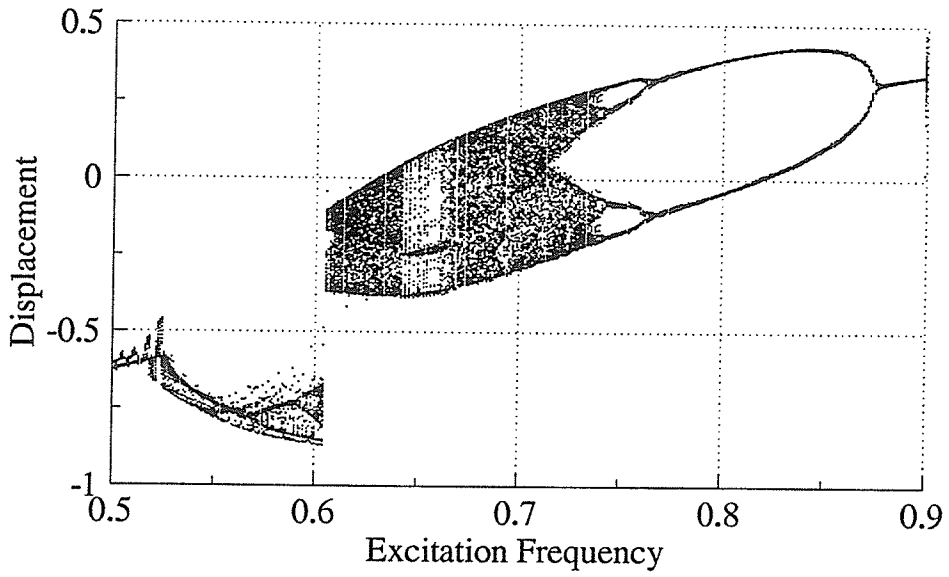

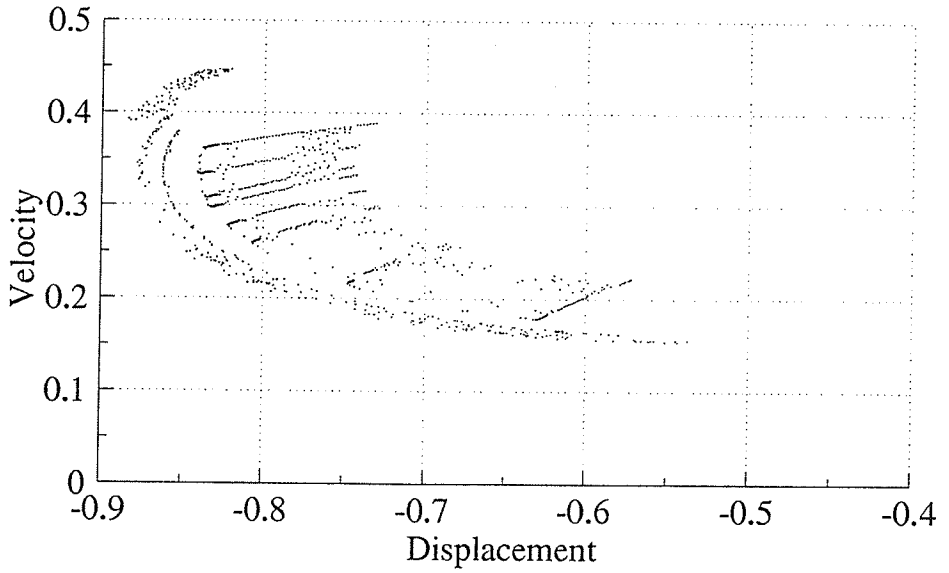

Figure 6.7 Numerically simulated cascades of bifurcation and strange attractor for the continuous Case IV Duffing oscillator.

6.5 Conclusions

This chapter investigates for the first time, the universal character of the Duffing oscillator via its discrete mapping. The approach used is based on the Naive discretization of the differential equation of motion and the subsequent application of the cubic renormalization on its discrete equation. The analytically computed universal parameters are compared with the numerically simulated solutions of the mapping. Very good agreement is observed. Based on the analytically obtained universal parameters, results of numerical simulations for the discrete and continuous Duffing systems are performed. From the graphs of the bifurcation cascades, the jump phenomenon and the strange attractor for a damped Duffing oscillator are clearly seen.

PART II

DISCONTINUOUS SYSTEMS: IMPACT OSCILLATORS

CHAPTER 7

DYNAMICS OF A BOUNCING BALL

Holmes (1982) can be credited as the first person to systematically study the nonlinear dynamics of a ball bouncing vertically on a sinusoidally vibrating table. The ball was considered small compared to the massive table and thus, the motion of the table was not affected by the repeated impacts of the ball. He also assumed that the distance traveled by the free-falling ball between impacts is large compared to the overall displacement of the table and proceeded to give an approximate equation for the time interval between impacts. On the basis of this model, he arrived at a simple difference equation which he used to demonstrate the various periodic and non-periodic motions and other chaotic phenomena. In our opinion this simplified model based on a discrete mapping approach is unnecessary and in some respects, inadequate. We will present a model that is based on the differential equation of motion of the ball (Luo and Han (1994)).

Impact motion exists in a wide spectrum of engineering applications, ranging from moored ships undergoing repeated contacts with fenders to moving parts in machinery and fluid induced vibration in tubes. An engineer is not only concerned with the wear and fatigue generated by the impacting system, but also the undesirable noise level that accompanies such motion. A simple model of this discontinual system is to employ a single degree-of-freedom impact oscillator. This deceptively simple model can exhibit an amazingly rich variety of nonlinear behaviors, (see for example, Masri and Caughey (1966), Shaw and Holmes (1983), Everson (1986), Reithmeier (1989), Bishop (1994)). Wood and Byrne (1981) presented an interesting analysis of a randomly repeated impacting process and hinted that such random non-periodic motion apparently exist even when the system is

forced by sinusoidal excitations. This motivated Holmes (1982) to launch an investigation into the problem. Everson (1986) investigated the chaotic response of a bouncing ball using a model similar to Holmes's. Other studies related to the dynamics of a bouncing ball are the motion of impact dampers, see for example, Bapat and Bapat (1988), Heiman, Sherman and Bajaj (1987), Shaw and Shaw (1989), Whiston (1992), Peterka and Vacik (1992), Bayly and Virgin (1993), Han, Luo and Deng (1995).

In this work, the dynamics of a bouncing ball impacting on a harmonically excited massive table is not only revisited, but also, generalized for higher-order motions. Unlike Holmes (1982) our model is based on the differential equation of motion of the ball and from this, an appropriate mapping (or switch plane) is constructed. We did not have to assume that the distance traversed by the free-falling ball is large compared to the motion of the table and this enables us to model large amplitude excitations. Accordingly, our computed time interval between impacts is exact, whereas it was approximate in Holmes. The stability and bifurcation conditions of the system are derived and presented here. To verify the results, numerical simulations are carried out.

7.1 Equation of Motion, Discontinual Subsets and Poincare Mapping

*Figure 7.*1 depicts the mechanical model of a bouncing ball m moving freely in the vertical direction with a vibrating table of mass M. It is assumed that the table is massive compared to the ball; therefore, the motion of the table is not affected by the repeated impacts of the bouncing ball, i.e. $m << M$. As in the work of Holmes (1982), the external excitation, namely, the motion of the table, is taken to be that of simple harmonic motion. That is,

$$E = A\sin(\omega t + \varphi), \tag{7.1}$$

where A, ω and φ are the forcing amplitude, the forcing frequency and the initial phase angle. Denoting the absolute and relative (to the table) displacements of the ball by x, y

respectively, and if $\dot{(\ )}$ represents time derivatives, we have:

$$\left.\begin{aligned} x &= y + E(t,A) \\ \dot{x} &= \dot{y} + \dot{E}(t,A) \\ \ddot{x} &= \ddot{y} + \ddot{E}(t,A) \end{aligned}\right\} \tag{7.2}$$

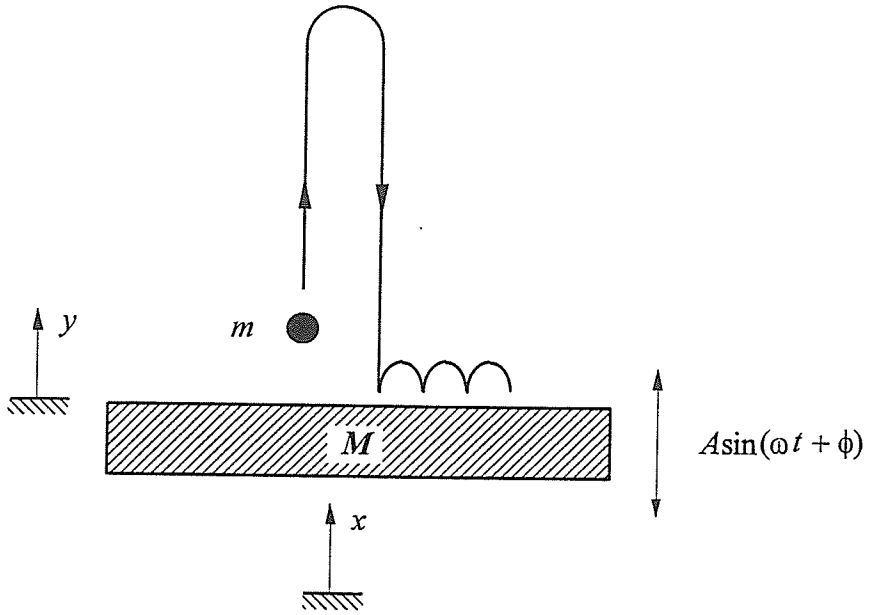

Figure 7.1 Mechanical model of the bouncing ball with a vibrating table.

Substituting *Equation* (7.1) into *Equation* (7.2) and considering gravity but neglecting friction, yields the equation of motion in the relative coordinate system:

$$\ddot{y} = A\omega^2 \sin(\omega t + \varphi) - g \tag{7.3}$$

where g is the gravitational acceleration. Integrating *Equation* (7.3) and invoking initial conditions $(y_0, \dot{y}_0)$, the velocity and displacement of the ball are,

$$\dot{y} = -A\omega\cos(\omega t + \varphi) - gt + \left[\dot{y}_0 + gt_0 + A\omega\cos(\omega t_0 + \varphi)\right] \tag{7.4}$$

$$y = -A\sin(\omega t+\varphi) - \frac{1}{2}gt^2 + \left[\dot{y}_0 + gt_0 + A\omega\cos(\omega t_0+\varphi)\right](t-t_0) + A\sin(\omega t_0+\varphi) + \frac{1}{2}gt_0^2 + y_0. \tag{7.5}$$

For a system with discontinuities such as the impact problem here, all results concerning the existence, stability and bifurcation of periodic solutions of a nonlinear system are, with some modifications, directly applicable (Reithmeier (1989)). The discontinuities caused by the impacts between the ball and the table imply that the state-space of the bouncing ball can be divided into many continuous subsets X_i. For the subset between the ith and $(i+1)$th impacts, the values of the ith impact just after the impact can be chosen as initial conditions for X_i. This subset can be determined from *Equations* (7.4)-(7.5) as,

$$\dot{y} = -A\omega\cos(\omega t+\varphi) - gt + \left[\dot{y}_i^+ + gt_i + A\omega\cos(\omega t_i+\varphi)\right], \tag{7.6}$$

$$y = -A\sin(\omega t+\varphi) - \frac{1}{2}gt^2 + \left[\dot{y}_i^+ + gt_i + A\omega\cos(\omega t_i+\varphi)\right](t-t_i) + A\sin(\omega t_i+\varphi) + \frac{1}{2}gt_i^2 + y_i^+, \tag{7.7}$$

in which $t \in [t_i,\ t_{i+1}]$, $y_i^+ = y^+(t_i)$ and $\dot{y}_i^+ = \dot{y}^+(t_i)$. Note that the superscript "+" denotes immediately *after* an impact and likewise, the superscript "-" for immediately *before* an impact. The boundary of X_i, ∂X_i constitutes the switch plane of codimension 1 and to study the impact process, we would be interested to obtain the discontinual subset ∂X_{i+1} immediately prior to the $(i+1)$th impact. Therefore, taking values of state variables at $t = t_{i+1}$ in *Equation* (7.8), we have:

$$y_{i+1}^- - y_i^+ = -A\sin(\omega t_{i+1}+\varphi) - \frac{1}{2}gt_{i+1}^2 + A\sin(\omega t_i+\varphi) + \frac{1}{2}gt_i^2 + \left[\dot{y}_i^+ + gt_i + A\omega\cos(\omega t_i+\varphi)\right](t_{i+1}-t_i). \tag{7.8}$$

Neglecting the duration of the impact and considering only the simplest impact law, namely, the modeling of impacts via a constant coefficient of restitution $e \le 1$, the impact

process can be described by,

$$\left.\begin{aligned} y_i^- &= y_i^+ = 0 \\ \dot{y}_i^+ &= -e\dot{y}_i^- \end{aligned}\right\}. \tag{7.9}$$

An impact is deemed to occur when *Equation* (7.9a) is satisfied and the resulting loss of energy is captured by *Equation* (7.9b). Substituting *Equation* (7.9) into *Equations* (7.6) and (7.8), and replacing $y_i^-, \dot{y}_i^-$ by $y_i, \dot{y}_i$ respectively, to simplify notation usage, we get:

$$\dot{y}_{i+1} = -A\omega\cos(\omega t_{i+1} + \varphi) - gt_{i+1} + \left[-e\dot{y}_i + gt_i + A\omega\cos(\omega t_i + \varphi)\right], \tag{7.10}$$

$$\begin{aligned} 0 = &-A\sin(\omega t_{i+1} + \varphi) - \frac{1}{2}gt_{i+1}^2 + A\sin(\omega t_i + \varphi) + \frac{1}{2}gt_i^2 \\ &+\left[-e\dot{y}_i + gt_i + A\omega\cos(\omega t_i + \varphi)\right](t_{i+1} - t_i). \end{aligned} \tag{7.11}$$

For an impact problem, the discontinual boundary (or switch plane) is the Poincare mapping section Σ which therefore, can be defined by

$$\Sigma = \bigcup_{i=0}^{N} \Sigma_i, \tag{7.12}$$

where

$$\Sigma_i = \left\{ (t_i, \dot{y}_i) \,\middle|\, y_i = 0,\ t_i \bmod \frac{2\pi}{\omega} \right\}. \tag{7.13}$$

When the absolute reference frame is considered, the Poincare mapping section is defined by

$$\Sigma_{i(a)} = \left\{ (t_i, \dot{x}_i) \,\middle|\, y_i = 0,\ t_i \bmod \frac{2\pi}{\omega} \right\}. \tag{7.14}$$

Note that all quantities measured in the absolute reference frame carry the subscript "a" as shown in *Equation* (7.14). The Poincare mapping P can now be defined as

$$P:\ \Sigma_i \to \Sigma_{i+1}. \tag{7.15}$$

7.2 Periodic Motion

The periodic solutions of the bouncing ball are derived in this section. First, the period-1 motion is formulated, followed by the period-2 motion and finally, generalizing the results for the period-k motion.

7.2.1 Period-1 motion

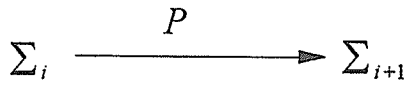

Figure 7.2 Mapping diagram for the period-1 motion.

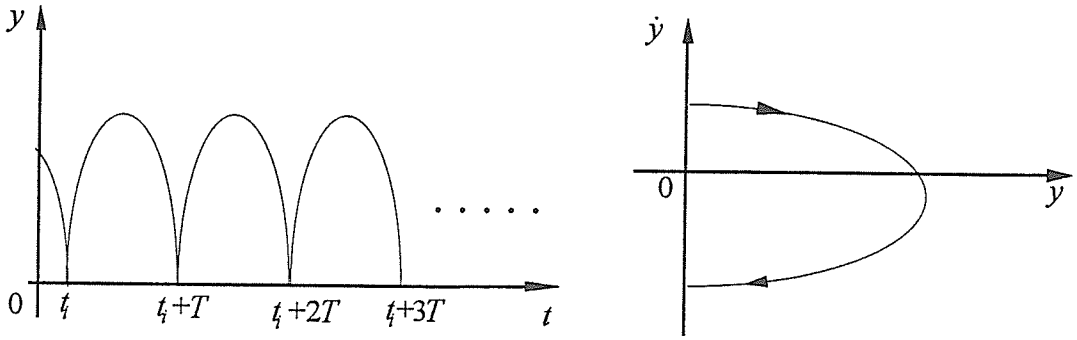

(a) time-displacement (b) phase-plane

Figure 7.3 Qualitative sketch of the period-1 motion in the relative reference frame.

The mapping diagram for the period-1 motion and its corresponding physical motion are sketched respectively in *Figures* 7.2 and 7.3. For any $\boldsymbol{x} = (t_i, \dot{y}_i)^{tp} \in \Sigma$ we have $P\boldsymbol{x} = \boldsymbol{x}$, and this leads to the following two equations:

$$t_{i+1} = t_i + \frac{2n\pi}{\omega} = t_i + nT, \qquad n = 1,2,3,\cdots \tag{7.16}$$

$$\dot{y}_{i+1} = \dot{y}_i \tag{7.17}$$

where the superscript *tp* implies transpose (of a matrix) and T is the period of the excitation. Substituting *Equations* (7.16)-(7.17) into *Equations* (7.10)-(7.11) and simplifying yields

$$\dot{y}_i = -\frac{g}{1+e}\frac{2n\pi}{\omega}, \tag{7.18}$$

$$\frac{A\omega^2}{g}\cos(\omega t_i + \varphi) = n\pi\left(\frac{1-e}{1+e}\right). \tag{7.19}$$

Equations (7.18)-(7.19) represent the initial impact conditions for the period-1 motion to occur in the repeated impacts of a ball with a massive vibrating table. These are just the necessary conditions and in a later section, we will provide the sufficient conditions as well. Noting that $\left|\cos(\omega t_i + \varphi)\right| \le 1$ in *Equation* (7.19) the following more general conditions can be derived:

$$2l\pi - \frac{\pi}{2} \le \omega t_i + \varphi \le 2l\pi + \frac{\pi}{2} \tag{7.20}$$

$$\frac{A\omega^2}{g} \ge n\pi\left(\frac{1-e}{1+e}\right) \tag{7.21}$$

where l is a positive integer. Note that the impact conditions $(t_i, \dot{y}_i)$ derived here actually represent the fixed points of the discrete mapping, from which the stability of the motion can be ascertained. This is outlined in *Section* 7.3.

7.2.2 Period-2 motion

The mapping diagram for the period-2 motion and its corresponding physical motion are depicted in *Figures* 7.4 and 7.5, respectively. As before, its mapping $P^{(2)}\boldsymbol{x} = \boldsymbol{x}$ indicates

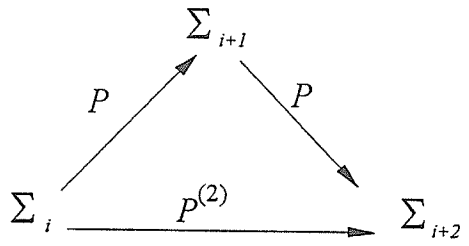

Figure 7.4 Mapping diagram for the period-2 motion.

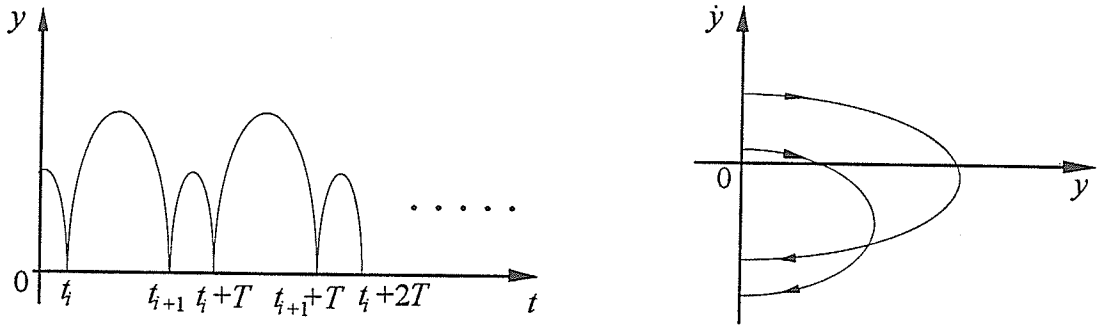

(a) time-displacement (b) phase-plane

Figure 7.5 Qualitative sketch of the period-2 motion in the relative reference frame.

that $t_{i+2} = t_i + 2n\pi/\omega = t_i + nT$ and $\dot{y}_i = \dot{y}_{i+2}$. Substituting into *Equations* (7.10)-(7.11) and simplifying, we get:

$$\dot{y}_{i+1} = -A\omega\cos(\omega t_{i+1} + \varphi) - gt_{i+1} + \left[-e\dot{y}_i + gt_i + A\omega\cos(\omega t_i + \varphi)\right], \tag{7.22}$$

$$\begin{aligned} 0 = &-A\left[\sin(\omega t_{i+1} + \varphi) - \sin(\omega t_i + \varphi)\right] - \frac{1}{2}g\left(t_{i+1}^2 - t_i^2\right) \\ &+\left[-e\dot{y}_i + gt_i + A\omega\cos(\omega t_i + \varphi)\right](t_{i+1} - t_i), \end{aligned} \tag{7.23}$$

$$\dot{y}_{i+2} = \dot{y}_i = -A\omega\cos(\omega t_i + \varphi) - g\left(t_i + \frac{2n\pi}{\omega}\right) + \left[-e\dot{y}_{i+1} + gt_{i+1} + A\omega\cos(\omega t_{i+1} + \varphi)\right], \tag{7.24}$$

$$\begin{aligned} 0 = &-A\sin(\omega t_i + \varphi) - \frac{1}{2}g\left(t_i + \frac{2n\pi}{\omega}\right)^2 + A\sin(\omega t_{i+1} + \varphi) + \frac{1}{2}gt_{i+1}^2 \\ &+\left[-e\dot{y}_{i+1} + gt_{i+1} + A\omega\cos(\omega t_{i+1} + \varphi)\right]\left(t_i + \frac{2n\pi}{\omega} - t_{i+1}\right). \end{aligned} \tag{7.25}$$

To obtain the parameter manifold and its corresponding initial conditions for the period-2 motion, two methods of algebraic manipulation are developed: Method 1 is more direct and obvious, and Method 2 is more general and can be easily extended to handle the formulation for the period-k motion.

Method 1

Adding *Equations* (7.22) and (7.24) yields

$$\dot{y}_{i+1} + \dot{y}_i = -\frac{g}{1+e}\frac{2n\pi}{\omega}, \tag{7.26}$$

Similarly, adding *Equations* (7.23) and (7.25) leads to

$$t_{i+1} = t_i + \frac{\omega\dot{y}_i + A\omega^2\cos(\omega t_i + \varphi) + n\pi g}{2n\pi g + (1+e)\omega\dot{y}_i}\frac{2n\pi}{\omega}. \tag{7.27}$$

For simplicity, we introduce a new parameter such that $0 \le q \le 1$. Then, the time interval between two consecutive impacts is computed from

$$t_{i+1} - t_i = q\frac{2n\pi}{\omega}. \tag{7.28}$$

Note that by setting $q = 1$ we can recover from *Equation* (7.28), period-1 motion from period-2 motion (it is also possible to come to the same conclusion by setting $q = 0$ in *Equation* (7.28), but it would be necessary to replace q by $(1-q)$ in the expression). Substituting *Equation* (7.28) into *Equation* (7.27) we get:

$$\dot{y}_i = -\frac{A\omega\cos(\omega t_i + \varphi) + \left(\frac{1}{2} - q\right)\frac{2n\pi}{\omega}g}{1 - q(1+e)}. \tag{7.29}$$

Observe that $q \neq 1/(1+e)$ in *Equation* (7.29). In the limit $q \to 1/(1+e)$ then we get

$$\left.\begin{aligned} \dot{y}_i &= -\frac{1}{1+e}\frac{2n\pi g}{\omega}, \\ \cos(\omega t_i + \varphi) &= -\left(\frac{1}{2} - \frac{1}{1+e}\right)\frac{2n\pi g}{A\omega^2}. \end{aligned}\right\} \tag{7.30}$$

Eliminating $\dot{y}_{i+1}$ from *Equations* (7.22) and (7.26), and also using *Equation* (7.28) to simplify, we get:

$$-\left(q - \frac{1}{1+e}\right)\frac{2n\pi g}{\omega} - (1-e)\dot{y}_i = A\omega\left[\cos(\omega t_{i+1} + \varphi) - \cos(\omega t_i + \varphi)\right]. \tag{7.31}$$

Substituting *Equations* (7.27)-(7.28) into *Equation* (7.23) produces

$$-\frac{(q-q^2)}{A}\left[\frac{1}{2}\left(\frac{2n\pi}{\omega}\right)^2 g + \frac{2(1+e)n\pi\dot{y}_i}{\omega}\right] = \sin(\omega t_{i+1} + \varphi) - \sin(\omega t_i + \varphi). \tag{7.32}$$

From *Equations* (7.31)-(7.32), eliminating the sine and cosine terms we have:

$$A = \frac{1}{2\left|\sin(nq\pi)\right|}\sqrt{\left[\left(q - \frac{1}{1+e}\right)\frac{2n\pi g}{\omega^2} - \frac{(1-e)\dot{y}_i}{\omega}\right]^2 + (q-q^2)^2\left(\frac{2n\pi}{\omega}\right)^2\left[\frac{n\pi g}{\omega} + (1+e)\dot{y}_i\right]^2}. \tag{7.33}$$

Equation (7.33) for calculating the excitation amplitude A, depicts the parameter manifold for the period-2 motion for prescribed values of q. Note that from its denominator, it is obvious that A will not exist for $q = l/n$ where $l \le n$ is integer. Physically, it implies the motion is unattainable. For example, if $q = 1/4$, then $n \neq 4,8,12,\cdots$; if $q = 1/2$, then n cannot take even values; if $q = 1$, then n cannot any integer values; and so on.

In the limit $q \to 1/(1+e)$, we get a much simpler expression of *Equation* (7.33):

$$A = \frac{1}{2\left|\sin(nq\pi)\right|}\sqrt{\left[\frac{(1-e)\dot{y}_i}{\omega}\right]^2 + \left[\frac{e}{(1+e)^2}\frac{2n\pi}{\omega}\right]^2\left[\frac{n\pi g}{\omega} + (1+e)\dot{y}_i\right]^2}. \tag{7.34}$$

Method 2

As mentioned, this approach is an alternative to Method 1 and because it is more general, it can be easily generalized to handle the analysis of the period-k motion. Once again, substituting *Equation* (7.28) into *Equations* (7.22)-(7.23) and performing the algebraic manipulations for the sine and cosine terms, we have:

$$\left.\begin{aligned}\cos(\omega t_i+\varphi)&=\frac{K_1^q+eK_2^q\dot{y}_i+K_3^q\dot{y}_{i+1}}{A\omega K^q},\\ \sin(\omega t_i+\varphi)&=\frac{K_4^q+eK_5^q\dot{y}_i+K_6^q\dot{y}_{i+1}}{A\omega K^q}.\end{aligned}\right\} \tag{7.35}$$

in which the various coefficients $K^q, K_1^q, \cdots, K_6^q$ are defined in *Appendix* C.1. Substituting *Equation* (7.35) into *Equation* (7.22) leads to

$$\dot{y}_{i+1}=\frac{L_1^q+L_2^q\dot{y}_i}{L^q}. \tag{7.36}$$

where the coefficients L^q, L_1^q, L_2^q are also listed in *Appendix* C.1. Once again, following the same procedure as in deriving *Equation* (7.35), but now, from *Equations* (7.24)-(8.25) we get,

$$\dot{y}_{i+2}=\dot{y}_i=\frac{L_1^{1-q}+L_2^{1-q}\dot{y}_{i+1}}{L^{1-q}} \tag{7.37}$$

In view of *Equation* (7.36), we get after eliminating $\dot{y}_{i+1}$ from *Equation* (7.37):

$$\dot{y}_i=\frac{L_1^{1-q}L^q+L_1^qL_2^{1-q}}{L^qL^{1-q}-L_2^qL_2^{1-q}}. \tag{7.38}$$

We can obtain *Equation* (7.26) from *Equations* (7.36)-(7.38). Eliminating the sine and cosine terms in *Equation* (7.35) leads to,

$$A=\frac{1}{\omega K^q}\sqrt{\left[K_1^q-\frac{2n\pi g}{(1+e)\omega}K_3^q+\left(eK_2^q-K_3^q\right)\dot{y}_i\right]^2+\left[K_4^q-\frac{2n\pi g}{(1+e)\omega}K_6^q+\left(eK_5^q-K_6^q\right)\dot{y}_i\right]^2}. \tag{7.39}$$

Observe that *Equations* (7.35) and (7.36) are expressed in terms of coefficients L^q, L_1^q, L_2^q $K^q, K_1^q, \cdots, K_6^q$ which are defined in *Appendix* C.1. Expressing them in this form makes the task of extending the formulation to handle the analysis of the period-k motion more intuitive and thus, easier. It can be shown that *Equations* (7.38) and (8.39) are identical respectively, to *Equations* (7.29) and (7.33) derived in Method 1.

Discussion

It would be interesting to examine the situation of even values of n for $q = 1/2$. That is replacing n by $2m$. For this situation, we have from *Appendix* C.1, the following results for the impact velocity and phase angle:

$$\left.\begin{aligned} \dot{y}_i = \dot{y}_{i+1} &= -\frac{g}{(1+e)}\frac{n\pi}{\omega} = -\frac{g}{(1+e)}\frac{2m\pi}{\omega} \\ A\omega\cos(\omega t_i + \varphi) &= g\left(\frac{1}{2} - \frac{e}{1+e}\right)\frac{2m\pi}{\omega} \end{aligned}\right\}. \tag{7.40}$$

Observe that *Equation* (7.40) is identical to *Equations* (7.18)-(7.19) which have been derived for the period-1 motion. What this implies is that we actually get period-1 motion from period-2 motion if the table motion is vibrating with a period $2mT$.

7.2.3 Period-k motion

We will formulate the necessary condition for the period-k motion, i.e. $P^{(k)}\boldsymbol{x} = \boldsymbol{x}$ over nT period. The mapping diagram and its corresponding physical motion are qualitatively sketched in *Figures* 7.6-7.7. We will extend Method 2 described previously to handle this period-k motion. Introducing a series of impact time-interval parameter $0 \le q_j \le 1$ and $\sum_{j=1}^{k} q_j = 1$, the jth impact time-interval is given by,

$$t_{i+j} - t_{i+j-1} = q_j nT. \tag{7.41}$$

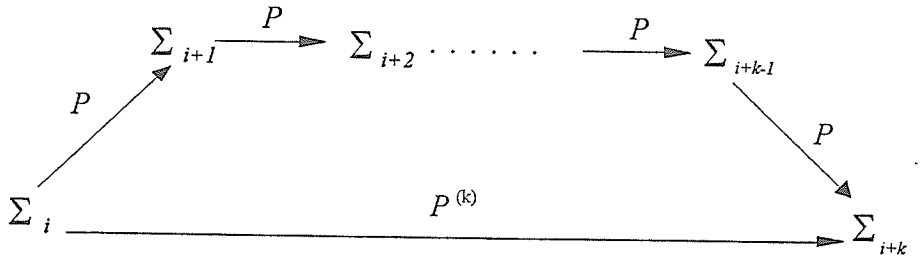

Figure 7.6 Mapping diagram for the period-k motion.

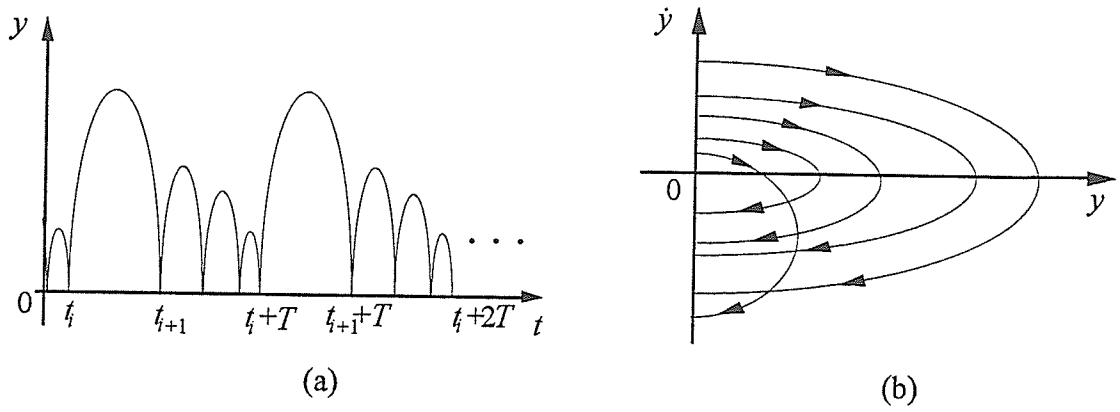

Figure 7.7 Qualitative sketch of the period-k motion in the relative reference frame.

Note that it is necessary to introduce a series of q_j, instead of a single q in the previous section, since we are now dealing with the period-k motion. The mapping equations of motion pertaining to the q_j impact time-intervals can be obtained by suitably modifying *Equations* (7.10)-(7.11). That is,

$$\dot{y}_{i+j} = -A\omega\cos\left(\omega t_{i+j}+\varphi\right) - g t_{i+j} + \left[-e\dot{y}_{i+j-1} + g t_{i+j-1} + A\omega\cos\left(\omega t_{i+j-1}+\varphi\right)\right], \quad (7.42)$$

$$\begin{aligned} 0 = &-A\sin\left(\omega t_{i+j}+\varphi\right) - \frac{1}{2}g t_{i+j}^2 + A\sin\left(\omega t_{i+j-1}+\varphi\right) + \frac{1}{2}g t_{i+j-1}^2 \\ &+\left[-e\dot{y}_{i+j-1} + g t_{i+j-1} + A\omega\cos\left(\omega t_{i+j-1}+\varphi\right)\right]\left(t_{i+j} - t_{i+j-1}\right). \end{aligned} \quad (7.43)$$

Substituting *Equation* (7.41) into *Equations* (7.42)-(7.43), and carrying out the algebraic manipulation as before, we get:

$$\left.\begin{aligned}\cos\left(\omega t_{i+j-1}+\varphi\right)&=\frac{K_1^{q_j}+eK_2^{q_j}\dot{y}_{i+j-1}+K_3^{q_j}\dot{y}_{i+j}}{A\omega K^{q_j}},\\ \sin\left(\omega t_{i+j-1}+\varphi\right)&=\frac{K_4^{q_j}+eK_5^{q_j}\dot{y}_{i+j-1}+K_6^{q_j}\dot{y}_{i+j}}{A\omega K^{q_j}}.\end{aligned}\right\} \tag{7.44}$$

where the various coefficients $K^{q_j},K_1^{q_j},\cdots,K_6^{q_j}$ are given in *Appendix* C.1. Substituting *Equations* (7.41) and (7.44) into *Equation* (7.42) produces,

$$\dot{y}_{i+j}=\frac{L_1^{q_j}+L_2^{q_j}\dot{y}_{i+j-1}}{L^{q_j}}. \tag{7.45}$$

in which the coefficients $L^{q_j},L_1^{q_j},L_6^{q_j}$ are also listed in *Appendix* C.1. Repeating this process for all the k-time intervals and back substituting to recover the $(i+k)$th impact velocity results in

$$\dot{y}_i=\frac{H_k}{1-H}, \tag{7.46}$$

where

$$\left.\begin{aligned}H_k&=\frac{L_1^{q_k}}{L^{q_k}}+\frac{L_2^{q_k}}{L^{q_k}}H_{k-1},\\ H&=\prod_{j=1}^{k}\frac{L_2^{q_j}}{L^{q_j}}.\end{aligned}\right\} \tag{7.47}$$

The excitation amplitude A for the period-k motion is given by eliminating the trigonometric terms and setting $j=1$. The result is,

$$A=\frac{1}{\omega K^{q_1}}\sqrt{\left(K_1^{q_1}+eK_2^{q_1}\dot{y}_i+K_3^{q_1}\dot{y}_{i+1}\right)^2+\left(K_4^{q_1}+eK_5^{q_1}\dot{y}_i+K_6^{q_1}\dot{y}_{i+1}\right)^2}. \tag{7.48}$$

As before, *Equation* (7.48) constitutes only the necessary condition for the existence of the period-k motion.

7.3 Stability and Bifurcation Conditions

To determine the sufficient condition for the periodic motion of the bouncing ball, it is necessary to carry out a stability analysis. Both stability and bifurcation are discussed in this section. For the period-1 motion, the results of Holme (1982) are available for comparison. For the period-2 motion, its stability conditions are presented both analytically and numerically. For the period-k motion, we indicate only the procedures as the problem very rapidly becomes numerically very intensive.

7.3.1 Period-1 motion

The stability and bifurcation conditions for the period-1 motion are obtained by studying the characteristics of the fixed points of the linearized discrete mapping of *Equations* (7.10)-(7.11):

$$\begin{pmatrix} t_{i+1} \\ \dot{y}_{i+1} \end{pmatrix} = DP \cdot \begin{pmatrix} t_i \\ \dot{y}_i \end{pmatrix} = \left[\frac{\partial P(t_{i+1}, \dot{y}_{i+1})}{\partial (t_i, \dot{y}_i)} \right] \begin{pmatrix} t_i \\ \dot{y}_i \end{pmatrix} = \begin{pmatrix} \frac{\partial t_{i+1}}{\partial t_i} & \frac{\partial t_{i+1}}{\partial \dot{y}_i} \\ \frac{\partial \dot{y}_{i+1}}{\partial t_i} & \frac{\partial \dot{y}_{i+1}}{\partial \dot{y}_i} \end{pmatrix} \begin{pmatrix} t_i \\ \dot{y}_i \end{pmatrix}, \tag{7.49}$$

where DP is the Jacobian matrix and its elements, $\partial t_{i+1}/\partial t_i$, $\partial t_{i+1}/\partial \dot{y}_i$, $\partial \dot{y}_{i+1}/\partial t_i$, $\partial \dot{y}_{i+1}/\partial \dot{y}_i$, are defined in the *Appendix* C.1. Evaluating DP at the fixed points $(t_i, \dot{y}_i)$ by substituting *Equations* (7.18)-(7.19) into *Equations* (C.28)-(C.31) yields,

$$\frac{\partial t_{i+1}}{\partial t_i} = 1 - \frac{1+e}{g} A\omega^2 \sin(\omega t_i + \varphi), \tag{7.50}$$

$$\frac{\partial t_{i+1}}{\partial \dot{y}_i} = -\frac{e(1+e)}{g}; \tag{7.51}$$

$$\frac{\partial \dot{y}_{i+1}}{\partial t_i} = -\frac{1+e}{g} \left[A\omega^2 \sin(\omega t_i + \varphi) \right]^2 + (1+e) A\omega^2 \sin(\omega t_i + \varphi), \tag{7.52}$$

$$\frac{\partial \dot{y}_{i+1}}{\partial \dot{y}_i} = e^2 - A\omega^2 \sin(\omega t_i + \varphi)\frac{e(1+e)}{g}. \tag{7.53}$$

The trace and determinant of the Jacobian DP of mapping are

$$Tr(DP) = 1 + e^2 - \frac{(1+e)^2}{g} A\omega^2 \sin(\omega t_i + \varphi), \tag{7.54}$$

$$Det(DP) = e^2. \tag{7.55}$$

The eigenvalues λ_1, λ_2 can be computed from

$$\lambda_{1,2} = \frac{Tr(DP) \pm \sqrt{Tr(DP)^2 - 4Det(DP)}}{2}. \tag{7.56}$$

Stability conditions can be stated as follows: if $|\lambda_1|, |\lambda_2| < 1$, then we have a sink (stable node or focus); if $|\lambda_1| < 1 < |\lambda_2|$, then we have a saddle; and if $|\lambda_1|, |\lambda_2| > 1$, then we have a source. Since $\lambda_1 \cdot \lambda_2 = Det(DP) = e^2$, only sinks and saddles are found for $e < 1$. For the specific situation of $e = 1$, centers and saddles are obtained. If $|\lambda_j| = 1$ for both eigenvalues, then the norm is preserved in the directions associated with these eigenvalues. Using the stability conditions of the discrete mapping, the stability and bifurcation for period-1 motion can be qualitatively determined as shown in *Figure* 7.8. A summary is given as follows:

Stability conditions

From *Figure* 7.8(a) $\sin(\omega t_i + \varphi) > 0$ (or $2l\pi < \omega t_i + \varphi < 2l\pi + \pi/2$), the parameter range of the stable period-1 motion is

$$B_{n1} < \frac{A\omega^2}{g} < B_{n4} \tag{7.57}$$

in which the constants $B_{n1}, \cdots, B_{n4}$ in *Figure* 7.8 are defined as,

$$B_{n1} = n\pi\left(\frac{1-e}{1+e}\right), \tag{7.58}$$

$$B_{n2} = \frac{1-e}{1+e}\sqrt{\left(\frac{1-e}{1+e}\right)^2 + (n\pi)^2}, \tag{7.59}$$

$$B_{n3} = \sqrt{1+\left(\frac{n\pi(1-e)}{1+e}\right)^2}, \tag{7.60}$$

and

$$B_{n4} = \sqrt{\frac{4\left(1+e^2\right)^2}{(1+e)^4} + \left(\frac{n\pi(1-e)}{1+e}\right)^2}. \tag{7.61}$$

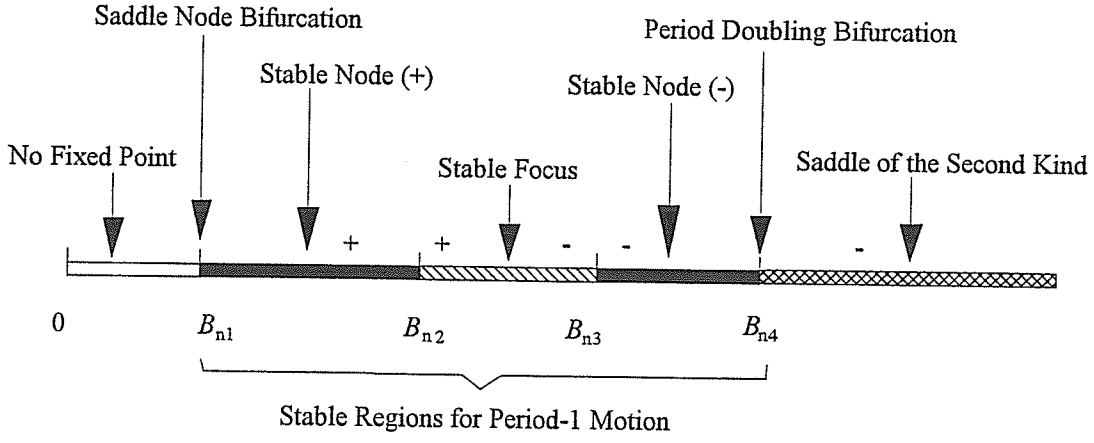

(a) for $\sin(\omega t_i + \varphi) > 0$

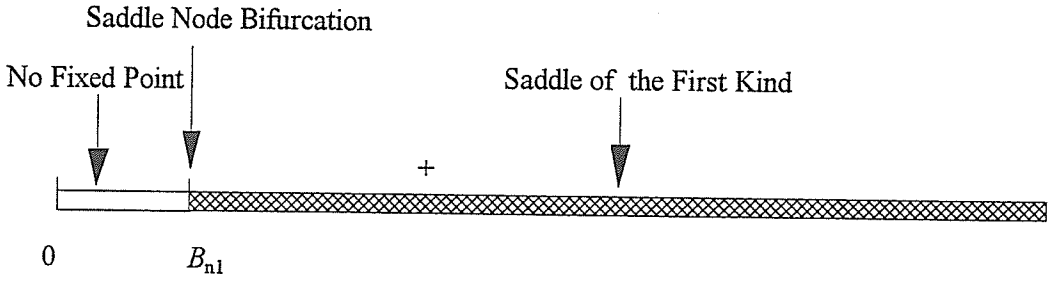

(b) for $\sin(\omega t_i + \varphi) < 0$

Figure 7.8 Qualitative analysis of stability and bifurcation for the period-1 motion.

Discussion

(a) *Stable motion*:

(i) For $B_{n1} < A\omega^2/g \le B_{n2}$, the eigenvalues of DP are real and for the range $0 < \lambda_{1,2} < 1$ the fixed point of the mapping is a stable node (+).

(ii) For $B_{n2} < A\omega^2/g \le B_{n3}$, the eigenvalues of DP are complex conjugate in the range $|\lambda_{1,2}| < 1$. The real part $\mathrm{Re}(\lambda_{1,2})$ changes from positive to negative, and therefore the fixed point of the mapping is a stable focus.

(iii) for $B_{n3} < A\omega^2/g \le B_{n4}$, eigenvalues of DP are real and for $-1 < \lambda_{1,2} < 0$, therefore fixed point of the mapping is a stable node (-).

(b) *Comparison with Holmes's result* (1982):

(i) Holmes (1982) presented the following result for the stable motion of the bouncing ball,

$$B_{n1} < \frac{A\omega^2}{g} < B_{n3}. \tag{7.62}$$

Comparing our results in *Equation* (7.57) with Holmes's expression in *Equation* (7.62), it is clear that the upper limit of the stability condition is different except at $e = 1$. The upper limit of Holmes's result in *Equation* (7.62) is just the extreme point of the stable focus (-) as depicted in *Figure* 7.8. On the other hand, the upper limit of our result in *Equation* (7.57) goes a little further, to the point B_{n4} which corresponds to the period-doubling bifurcation condition. We will show through numerical experimentation, that our result is more accurate.

(c) *Unstable motion*:

(i) The parameter range for the unstable motion of the bouncing ball is given by

$$\frac{A\omega^2}{g} > B_{n4}. \tag{7.63}$$

For this situation, the eigenvalues $\lambda_{1,2} < 0$ are such that $\lambda_1 < -1 < \lambda_2$, and therefore, all saddles of this unstable motion are of the second kind.

(ii) From *Figure* 7.8(b) $\sin(\omega t_i + \varphi) < 0$ (or $2l\pi + 3\pi/2 < \omega t_i + \varphi < 2(l+1)\pi$), stable motion cannot exist and thus, we have only the unstable motion governed by,

$$\frac{A\omega^2}{g} > B_{n1}. \tag{7.64}$$

The eigenvalues $\lambda_{1,2} > 0$ for this unstable motion are such that $\lambda_1 < 1 < \lambda_2$, and thus, this unstable motion is different from the unstable motion in (i). The fixed points of this unstable motion is the saddle of the first kind.

Bifurcation conditions

The bifurcation conditions of period-1 motion of the bouncing ball are:

(i) $A\omega^2/g = B_{n1}$ for saddle-node bifurcation, and

(ii) $A\omega^2/g = B_{n4}$ for period doubling bifurcation.

The stability and bifurcation conditions are summarized qualitatively in *Figure* 7.8. However, it would be much more informative to sketch them quantitatively. We can for example, get a feel for the relative sizes of the stable and unstable regions. The quantitative plots are presented in *Figure* 7.9. To generate the plots, the following values are used: $g = 9.8$, $e = 0.5$, $n = 1$ and $t_i = 2l\pi/\omega + 2 \mod 2\pi/\omega$. As shown, the dash-line denotes saddle of the first kind; the darkened solid-line, stable node point; the dotted-line, stable focus point; and the dash-dotted-line, saddle of the second kind. To clearly indicate the start/end points of the stable regions, $B_{n1}, \cdots, B_{n4}$ are marked on these graphs. As in *Figure* 7.8, B_{n1} in these graphs corresponds to the saddle-node bifurcation (SNB) and likewise, B_{n4} to the period doubling bifurcation (PDB). Note that the *unmarked gaps*

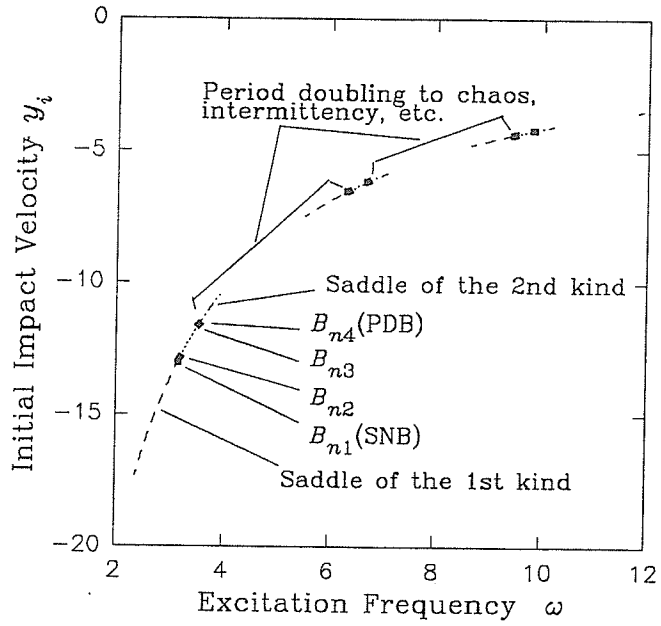

(a) Initial Impact Conditions

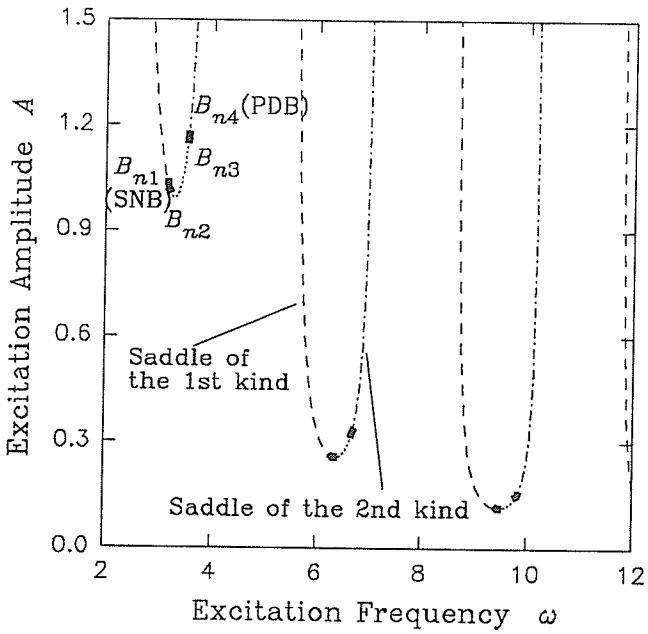

(b) Parameter Manifold

Figure 7.9 Quantitative analysis of stability and bifurcation for the period-1 motion (—— stable node, ---- stable focus, — — 1st saddle, — · 2nd saddle).

between two saddles (including the saddles themselves) represent the period doubling route to chaos, intermittency, etc. Further research is required to quantitatively chart these unmarked gaps.

To provide a comparison with *Figure* 1 of Holmes (1982), *Figure* 7.10 is plotted using $g = 9.8$, $e = 0.5$ and $\omega = \pi$. It should be emphasized that the comparison here is qualitative rather than quantitative in nature since it is difficult to obtain the exact values of the parameters used in generating Holmes's solution. For our figures, it is more appropriate to plot them without shifting the graphs by $\pm\pi$ as done by Holmes. Qualitatively, our result compares well with Holmes in the sense that both of them are very similar. However, there is one notable difference. While the starting points of the stable regions are the same, the ending points are not: Holmes's stable region ends at B_{n3} whereas ours, at B_{n4}. Also, note that our curves contain additional information pertaining to the nature of the stability which is absent in Holmes's plot.

7.3.2 Period -2 motion

As before, the eigenvalues of the linearized $\boldsymbol{x}_{i+2} = P^{(2)}\boldsymbol{x}_i$ are computed via the Jacobian listed in *Appendix* C.1.2. For the period-2 motion, its Jacobian is given by,

$$DP^{(2)} = DP \cdot DP = \left[\frac{\partial P(t_{i+2}, \dot{y}_{i+2})}{\partial(t_{i+1}, \dot{y}_{i+1})}\right]\left[\frac{\partial P(t_{i+1}, \dot{y}_{i+1})}{\partial(t_i, \dot{y}_i)}\right]_{\binom{t_{i+2}}{\dot{y}_{i+2}}=\binom{t_i+2N\pi/\omega}{\dot{y}_i}} \tag{7.65}$$

in which

$$\frac{\partial t_{i+1}}{\partial t_i} = \frac{1}{\dot{y}_{i+1}}\left\{-e\dot{y}_i + \left[A\omega^2 \sin(\omega t_{i+1} + \varphi) - g\right](t_{i+1} - t_i)\right\}, \tag{7.66}$$

$$\frac{\partial t_{i+1}}{\partial \dot{y}_i} = \frac{e}{\dot{y}_{i+1}}(t_{i+1} - t_i), \tag{7.67}$$

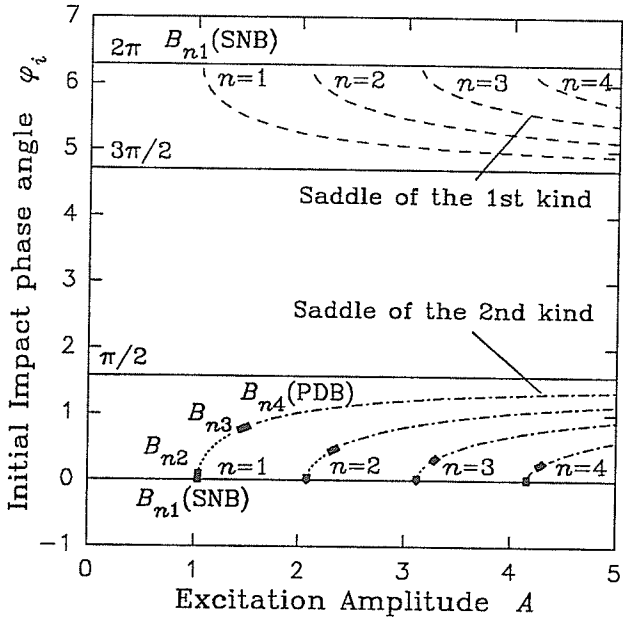

(a) Varying n

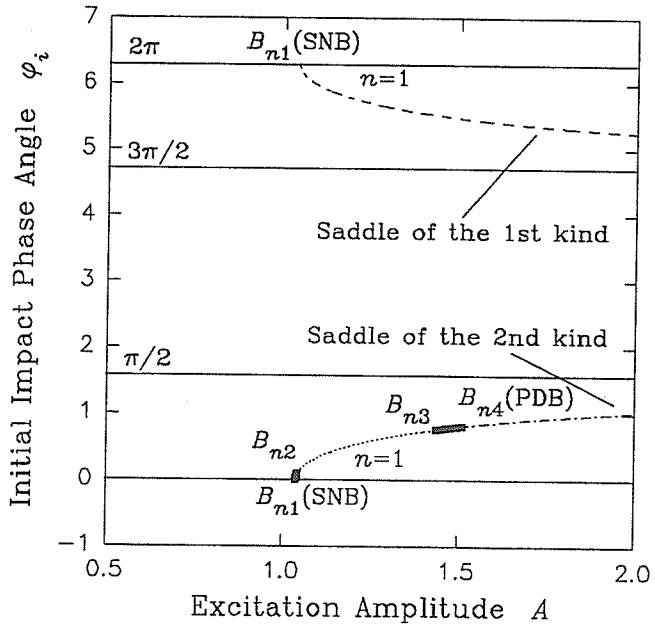

(b) Zoomed View at n=1

Figure 7.10 Variation of the initial impact phase angle with excitation amplitude. (—— stable node, ---- stable focus, — — 1st saddle, — · 2nd saddle)

$$\frac{\partial \dot{y}_{i+1}}{\partial t_i} = \left[A\omega^2 \sin(\omega t_{i+1} + \varphi) - g\right]\frac{\partial t_{i+1}}{\partial t_i} - \left[A\omega^2 \sin(\omega t_i + \varphi) - g\right], \tag{7.67}$$

$$\frac{\partial \dot{y}_{i+1}}{\partial \dot{y}_i} = \left[A\omega^2 \sin(\omega t_{i+1} + \varphi) - g\right]\frac{\partial t_{i+1}}{\partial \dot{y}_i} - e, \tag{7.68}$$

$$\frac{\partial t_{i+2}}{\partial t_{i+1}} = \frac{1}{\dot{y}_i}\left\{-e\dot{y}_{i+1} + \left[A\omega^2 \sin(\omega t_i + \varphi) - g\right]\left(t_i + \frac{2n\pi}{\omega} - t_{i+1}\right)\right\}, \tag{7.69}$$

$$\frac{\partial t_{i+2}}{\partial \dot{y}_{i+1}} = \frac{e}{\dot{y}_i}\left(t_i + \frac{2n\pi}{\omega} - t_{i+1}\right), \tag{7.70}$$

$$\frac{\partial \dot{y}_{i+2}}{\partial t_{i+1}} = \left[A\omega^2 \sin(\omega t_i + \varphi) - g\right]\frac{\partial t_{i+2}}{\partial t_{i+1}} - \left[A\omega^2 \sin(\omega t_{i+1} + \varphi) - g\right], \tag{7.71}$$

and

$$\frac{\partial \dot{y}_{i+2}}{\partial \dot{y}_{i+1}} = \left[A\omega^2 \sin(\omega t_i + \varphi) - g\right]\frac{\partial t_{i+2}}{\partial \dot{y}_{i+1}} - e. \tag{7.72}$$

Substituting the solutions of the period-2 motion into *Equations* (7.66)-(7.72), we obtain the period-2 Jacobian defined by *Equation* (7.65). This then allows the trace $Tr\left(DP^{(2)}\right)$ and the determinant $Det\left(DP^{(2)}\right)$ to be calculated, yielding the eigenvalues of the period-2 motion:

$$\lambda_{1,2} = \frac{Tr\left(DP^{(2)}\right) \pm \sqrt{Tr\left(DP^{(2)}\right)^2 - 4Det\left(DP^{(2)}\right)}}{2}. \tag{7.73}$$

The stability and bifurcations of period-2 motion are computed from *Equation* (7.73). The input parameters are $g = 9.8$, $\omega = \pi$ and $e = 0.5$. The stability and bifurcation results for $\sin(\omega t_i + \varphi) \geq 0$ and $\sin(\omega t_i + \varphi) \leq 0$ are plotted respectively, in *Figures* 7.11(a)-(c) and 7.11(d)-(f). Note that the line types used have the same interpretations as those employed in *Figures* 7.9-7.10. Due to the small size of the individual graphs, the start/end points of the stable regions, $B_{n1}, \cdots, B_{n4}$ are not marked in *Figure* 7.11. Observe that unlike the period-1 motion, it is possible to have stable motion for $\sin(\omega t_i + \varphi) \leq 0$.

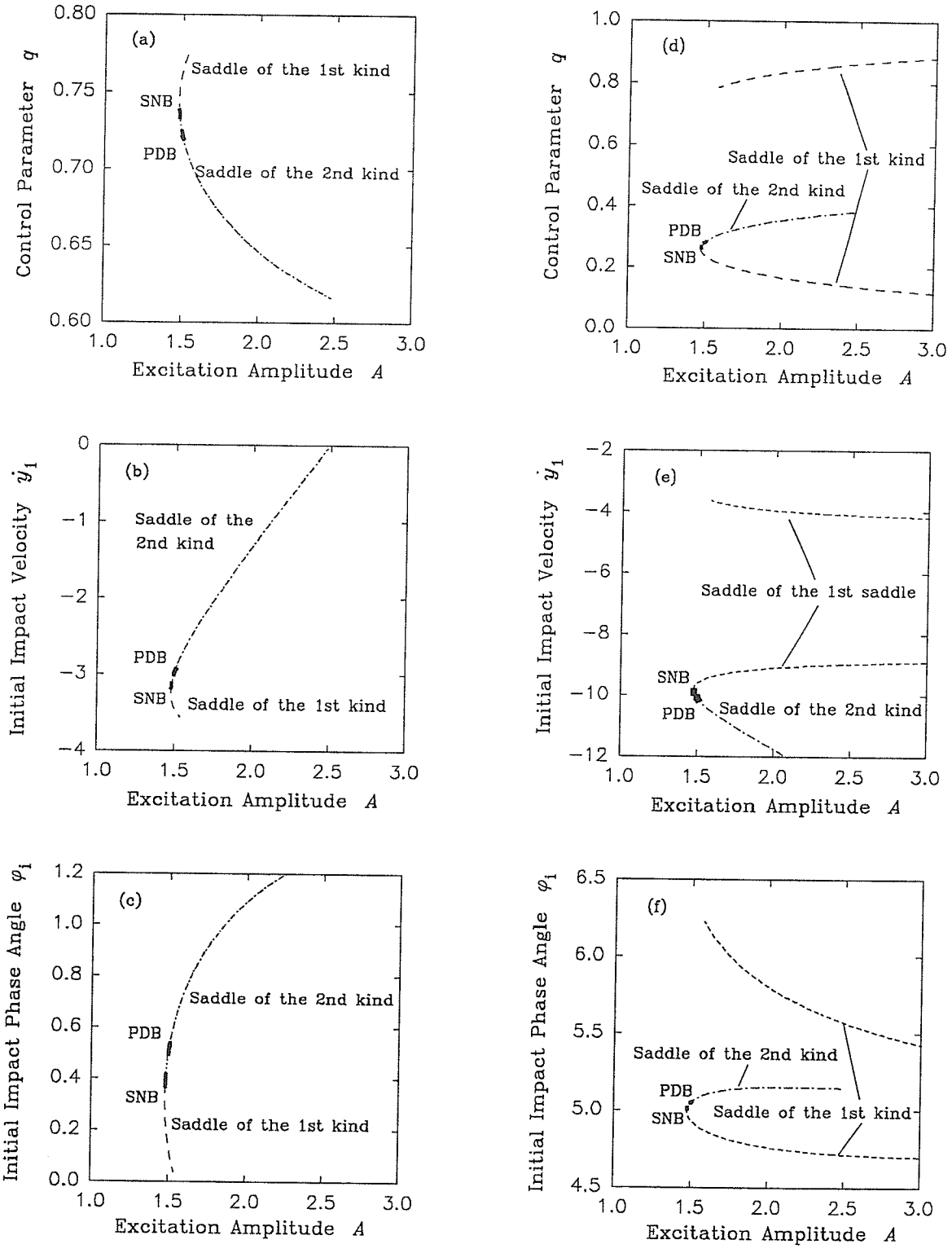

Figure 7.11 Stability and bifurcation for the period-2 motion (—— stable node, ---- stable focus, — — 1st saddle, — · 2nd saddle).

7.3.3 Period-k motion

The procedures for determining the stability and bifurcation of the period-k motion are discussed here. Following the steps outlined previously, the eigenvalues of the linearized matrix of $\boldsymbol{x}_{i+k} = P^{(k)}\boldsymbol{x}_i$ are computed using the period-k Jacobian which is defined by

$$DP^{(k)} = \underbrace{DP\cdots DP}_{k} = \left[\frac{\partial P(t_{i+k},\dot{y}_{i+k})}{\partial(t_{i+k-1},\dot{y}_{i+k-1})}\right]\cdots\left[\frac{\partial P(t_{i+1},\dot{y}_{i+1})}{\partial(t_i,\dot{y}_i)}\right]_{\binom{t_{i+k}}{\dot{y}_{i+k}}=\binom{t_i+2N\pi/\omega}{\dot{y}_i}}. \tag{7.74}$$

Substituting the solutions for the period-k motion into *Equation* (7.74), the trace $Tr\left(DP^{(k)}\right)$ and determinant $Det\left(DP^{(k)}\right)$ can be computed. This then permits the eigenvalues of the linearized matrix to be evaluated,

$$\lambda_{1,2} = \frac{Tr\left(DP^{(k)}\right) \pm \sqrt{Tr\left(DP^{(k)}\right)^2 - 4Det\left(DP^{(k)}\right)}}{2}. \tag{7.75}$$

As shown in the period-2 motion, the stability and bifurcation for the period-k motion can be determined from *Equation* (7.75).

7.4 Numerical Simulations

As a verification of the stability and bifurcation conditions for the period-1 and period-2 motions, numerical simulations are performed. To guarantee stable motion, input parameters are chosen such that they lie within the theoretically determined stable range, and similarly, to simulate unstable motion, input parameters within the theoretically obtained unstable range are used.

7.4.1 Period-1 motion

The computed input parameters for numerical simulations of n=1, period-1 motion are

tabulated in *Table* 7.1. For stable motion, we have plotted time-displacement and phase-plane curves based on the equations of motion described by *Equations* (7.6)-(7.7) and (7.9); for unstable motion, we presented Poincare mapping sections generated via *Equations* (7.6)-(7.7), (7.9) and (7.13)-(7.14).

Table 7.1 Computed input data for period-1 motion ($g = 9.8$, $e = 0.5$, $\omega = \pi$ and $t_i = 0.0$).

Figure No.	A	$\dot{y}_i$	φ_i	Types of Stability
		Period-1 Motion		
Figures 7.12 (a) & 7.14 (a)	1.0400639	-13.0666666	0.0219918	Stable Node (+)
Figures 7.12 (b) & 7.14 (b)	1.2518871	-13.0666666	0.5966194	Stable Focus
Figures 7.12 (c) & 7.14 (c)	1.5039512	-13.0666666	0.8073893	Stable Node (-)
		Chaotic Motion		
Figures 7.13 (a) & 7.14 (d)	2.0003417	-13.0666666	1.0241592	2nd Saddle
Figures 7.13 (b) & 7.14 (e)	2.0003417	-13.0666666	5.2590265	1st Saddle

Figure 7.12 depicts the steady period-1 motion of the bouncing ball, in the form of time-displacement and phase-plane curves, corresponding to the three kinds of stability conditions: (a) stable node (+), (b) stable focus and (c) stable node (-). Observe that these three phase-plane curves change their shapes in accordance to the three types of stability, and approach a "D"-shaped curve in (c).

Figure 7.13 shows the Poincare mapping sections for the two saddles associated with the period-1 unstable motion. We have plotted the saddle of the second kind ($\sin(\omega t_i + \varphi) \geq 0$) in *Figure* 7.13 (a) and saddle of the first kind ($\sin(\omega t_i + \varphi) \leq 0$) in *Figure* 7.13 (b). The graphs on the left pertain to the *relative* frame of reference, and on right, to the *absolute* frame of reference. The latter is provided to enable comparisons with physical experiments

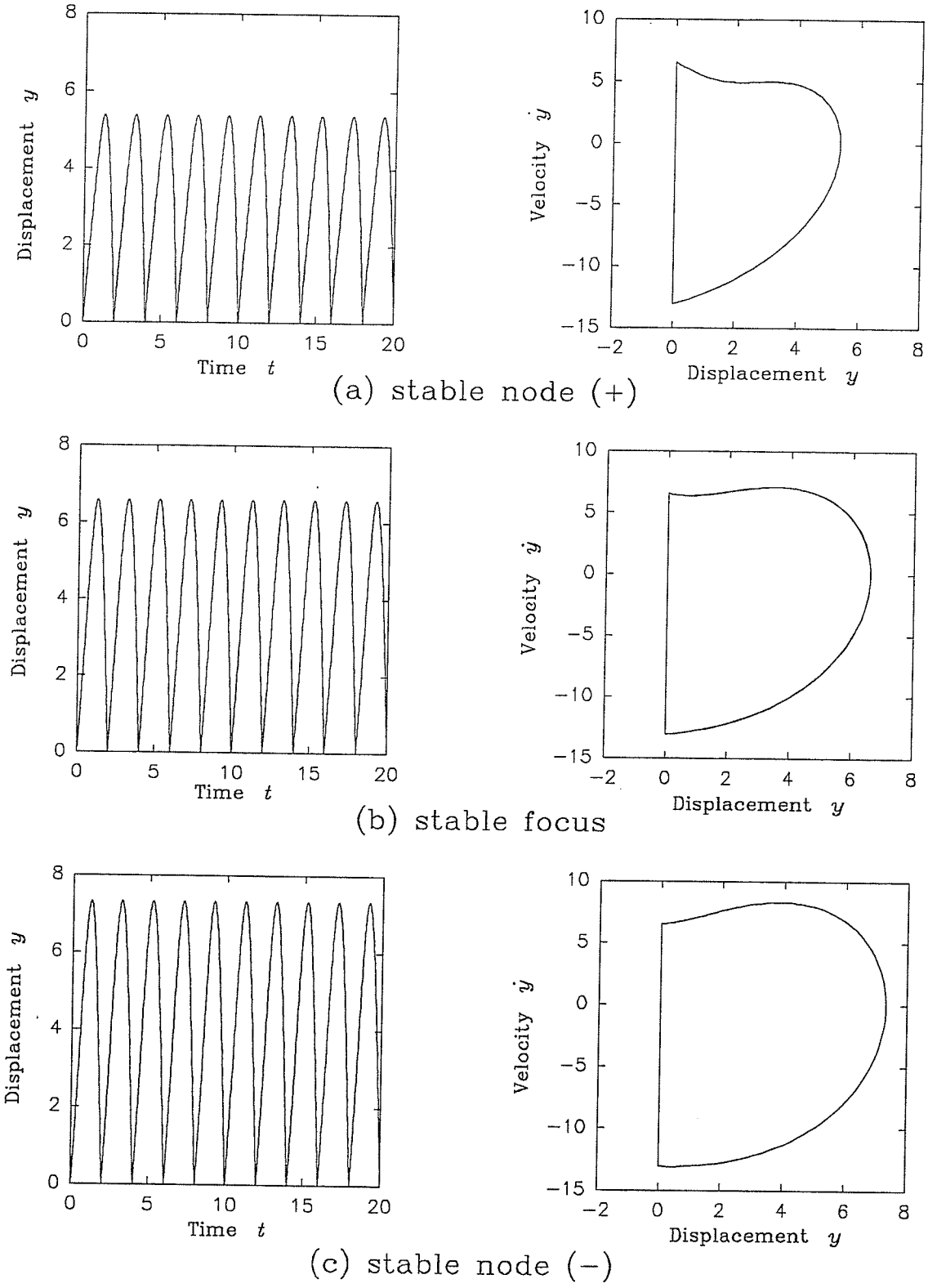

Figure 7.12 The three types of stable period-1 motion.

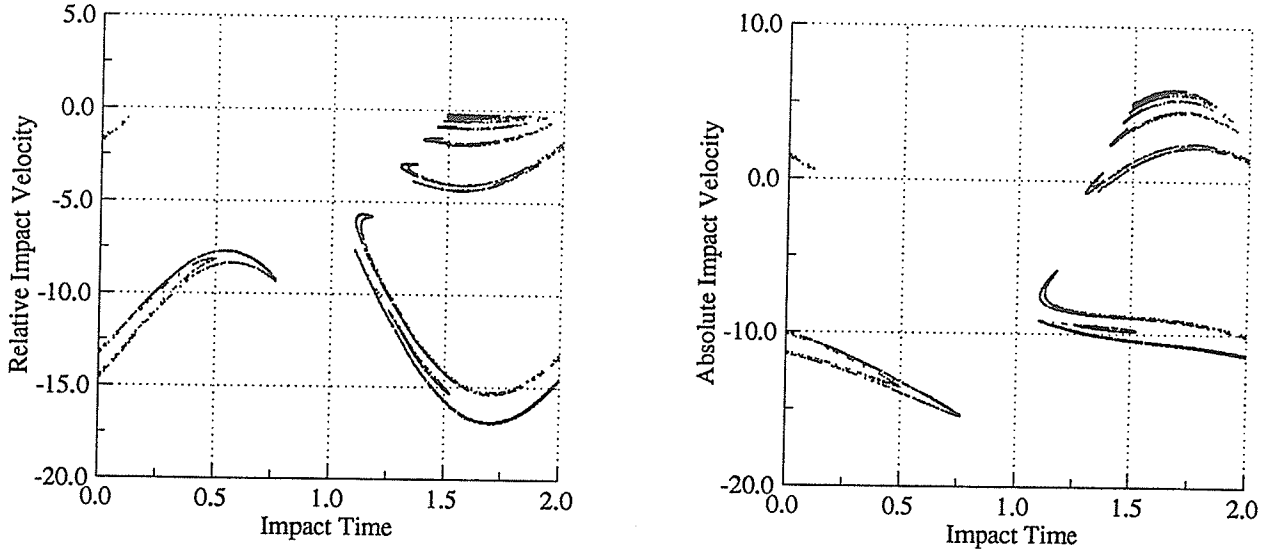

(a) Saddle of the second kind

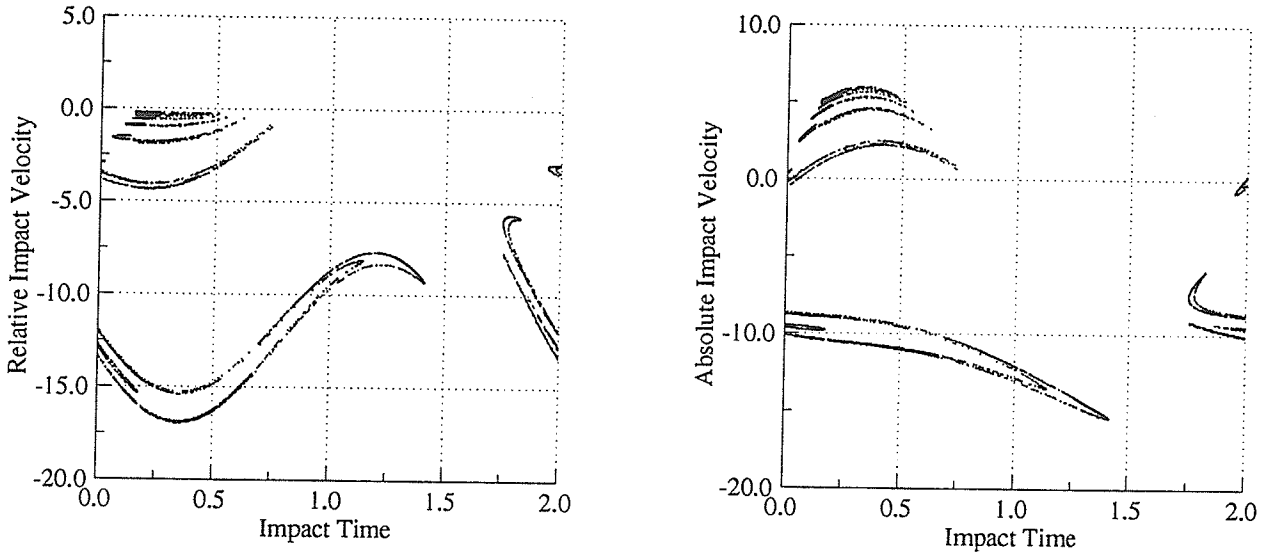

(b) Saddle of the first kind

Figure 7.13 Chaotic attractors associated with the unstable period-1 motion.

to be made should these be available. In plotting the two unstable motions, we varied only their phase angles. Observe that when the phase angles are shifted exactly by 2π, we still end up with completely identical Poincare mapping sections. What this implies is that the two saddles have *identical* Smale horseshoe structures. Furthermore, a careful scrutiny of *Figure* 7.13 reveals that there exists self-similarity, indicating the presence of fractals. Thus, a chaotic attractor is clearly evident in the plot for the parameters chosen.

It would be very interesting to view the physical motion of the bouncing ball. This illustrated in *Figure* 7.14, superimposed together with the physical motion of the vibrating table for up to $t = 50$s. Both stable and unstable motion are drawn. Since Holmes's model is based on a discrete mapping, he can only furnish a qualitative sketch and only for the stable motion. In contrast, based on our differential equation model, we can produce a quantitative description of the physical motion of the bouncing ball, for stable and as well as unstable motion. Note that for both *Figure* 7.14, the following graphs are plotted: (a) stable node (+), (b) stable focus, (c) stable node (-), (d) saddle of the second kind and (e) saddle of the first kind. Motion (a)-(c) are stable whereas (d)-(e) are chaotic.

In addition to the analytical checks presented in the previous section, we can also demonstrate physically that the motion in *Figures* 7.14(d)-(e) are indeed chaotic, by simulating the physical motion over a prolonged period of time and checking if they would repeat themselves. The results are shown in *Figure* 7.15 where the unstable motion is re-plotted for up to $t = 200$s. Observe that the motions do not repeat themselves for this duration of time.

7.4.2 Period-2 motion

Numerical simulations for time-displacement curves, phase planes and Poincare mappings for period-2 motion are presented here. The computed input parameters for n=1, period-2 motion are tabulated in *Tables* 7.3-7.4. Note *Table* 7.3 pertains to

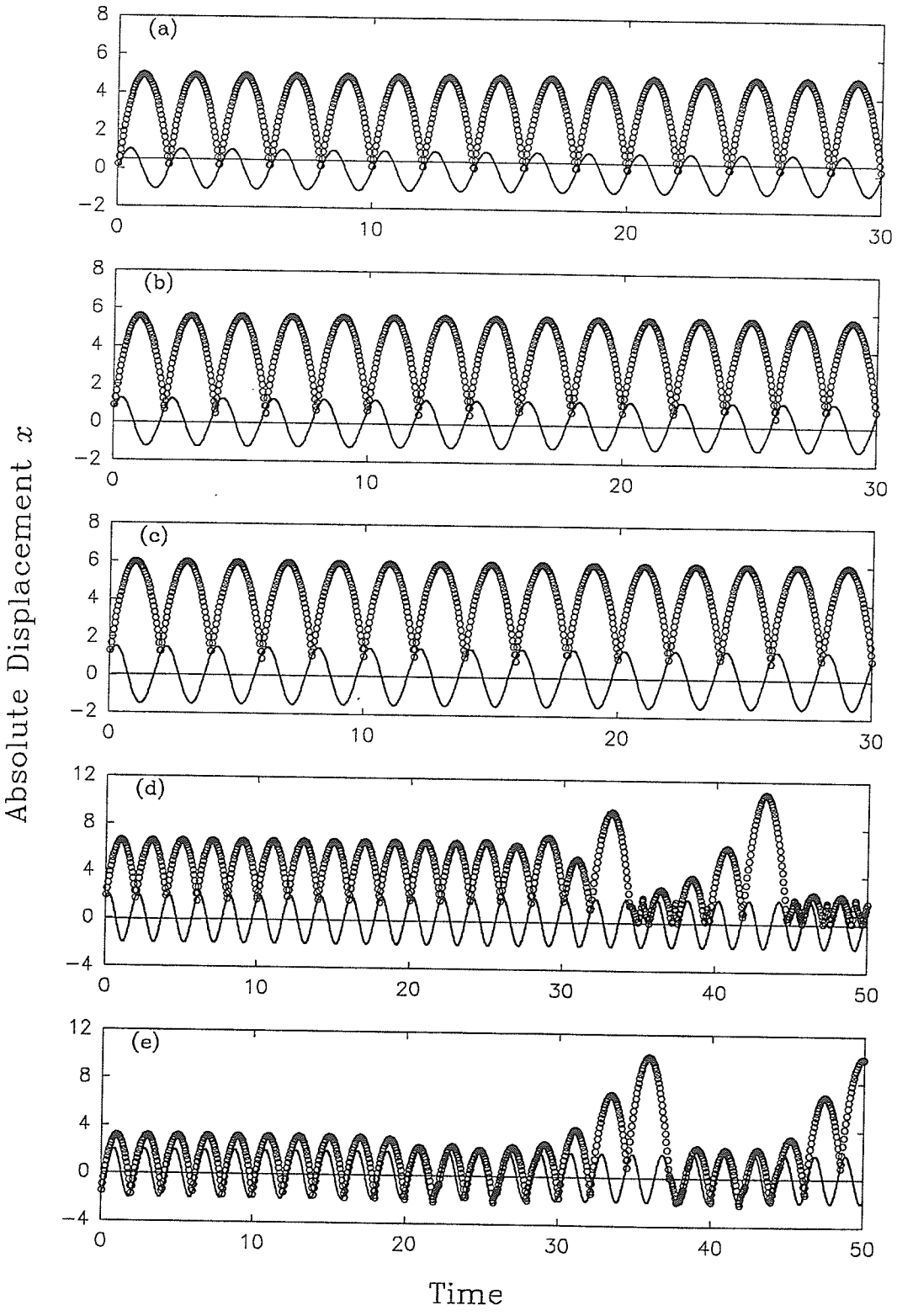

Figure 7.14 Period-1 physical motion: (a) stable node (+), (b) stable focus, (c) stable node (-), (d) 2nd saddle and (e) 1st saddle (∘ ∘ ∘ ball, —— table).

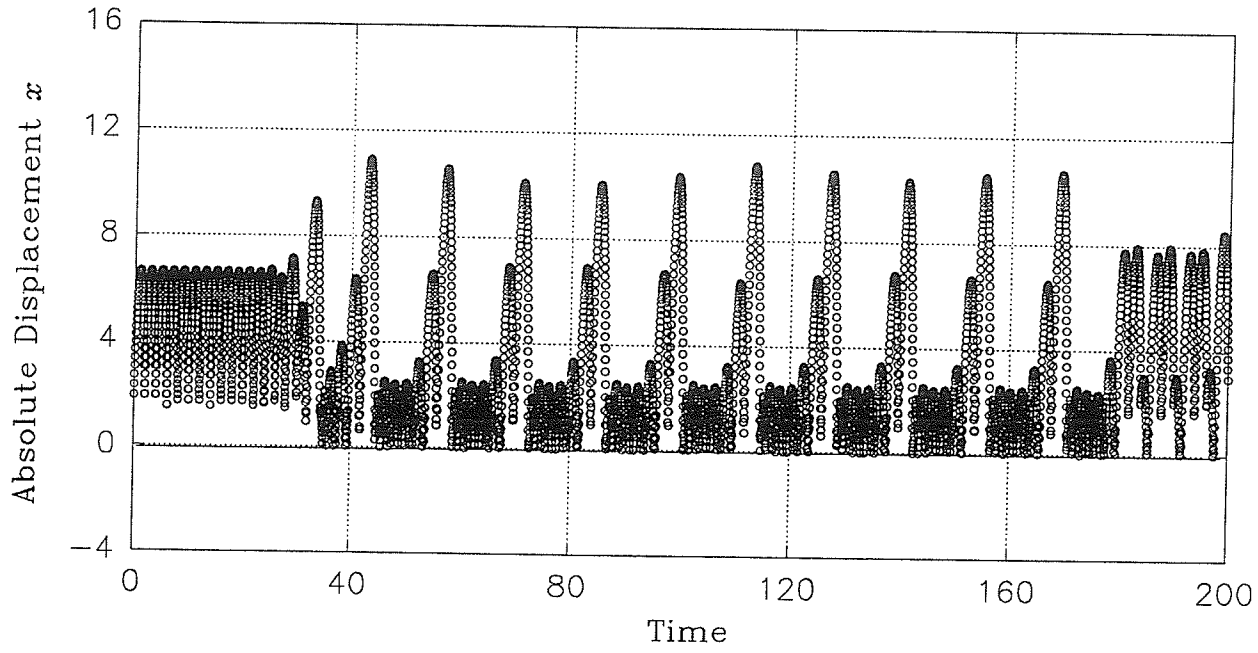

(a) Saddle of the Second Kind (n=1)

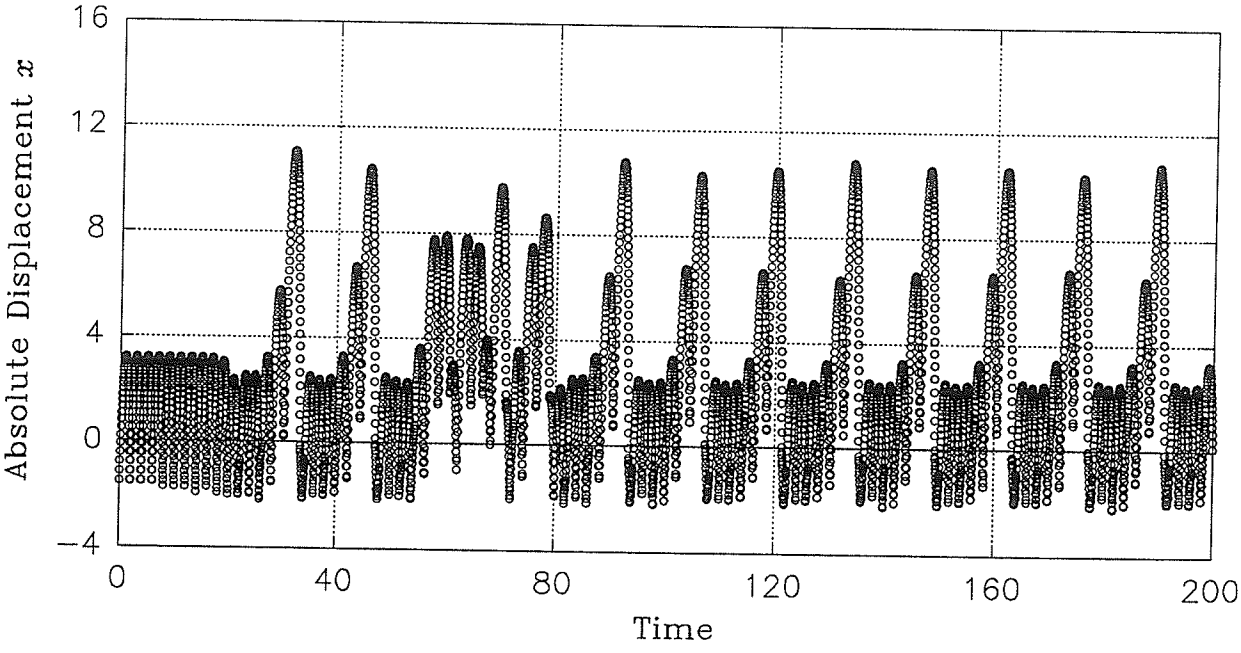

(b) Saddle of the First Kind (n=1)

Figure 7.15 Extended period-1 physical motion motion (∘ ∘ ∘ ball, —— table).

$\sin(\omega t_i + \varphi) \geq 0$ and for *Table* 7.4 to $\sin(\omega t_i + \varphi) \leq 0$. The time-displacement and phase-plane curves are plotted by using *Equations* (7.6)-(7.7) and (7.9) for unstable motion, and we presented Poincare mapping sections generated via *Equations* (7.6)-(7.7), (7.9) and (7.13)-(7.14). The stability results are plotted in *Figures* 7.16-7.17 for $\sin(\omega t_i + \varphi) \geq 0$ and *Figures* 7.18-7.19 for $\sin(\omega t_i + \varphi) \leq 0$.

Table 7.2 Input data for period-2 motion for $\sin(\omega t_i + \varphi) \geq 0$ ($e = 0.5$, $g = 9.8$, $A = 2.0$ and $t_i = 0.0$).

Figure No.	ω	$\dot{y}_i$	φ_i	q	Types of Stability
			Period-2 Motion		
Figures 7.16(a) & 7.20(a)	2.72000	-3.516950	0.518909	0.721	Stable Node (+)
Figures 7.16(b) & 7.20(b)	2.71000	-3.617650	0.474160	0.726	Stable Focus
Figures 7.16(c) & 7.20(c)	2.69750	-3.722500	0.358759	0.739	Stable Node (-)
			Chaotic Motion		
Figures 7.17(a) & 7.20(d)	3.49750	-0.018551	1.274840	0.616	2nd Saddle
Figures 7.17(b) & 7.20(e)	2.75625	-2.077890	0.016765	0.777	1st Saddle

Table 7.3 Input data for period-2 motion for $\sin(\omega t_i + \varphi) \leq 0$ ($e = 0.5$, $g = 9.8$, $A = 2.0$ and $t_i = 0.0$).

Figure No.	ω	$\dot{y}_i$	φ_i	q	Types of Stability
			Period-2 Motion		
Figures 7.18(a) & 7.21(a)	2.69750	-11.47990	4.998830	0.260	Stable Node (+)
Figures 7.18(b) & 7.21(b)	2.70000	-11.55360	5.014590	0.266	Stable Focus
Figures 7.18(c) & 7.21(c)	2.71500	-11.65660	5.041640	0.277	Stable Node (-)
			Chaotic Motion		
Figures 7.19(a) & 7.21(d)	3.00000	-9.62446	4.789790	0.181	2nd Saddle
Figures 7.19(b) & 7.21(e)	3.34000	-11.7321	5.148490	0.373	1st Saddle

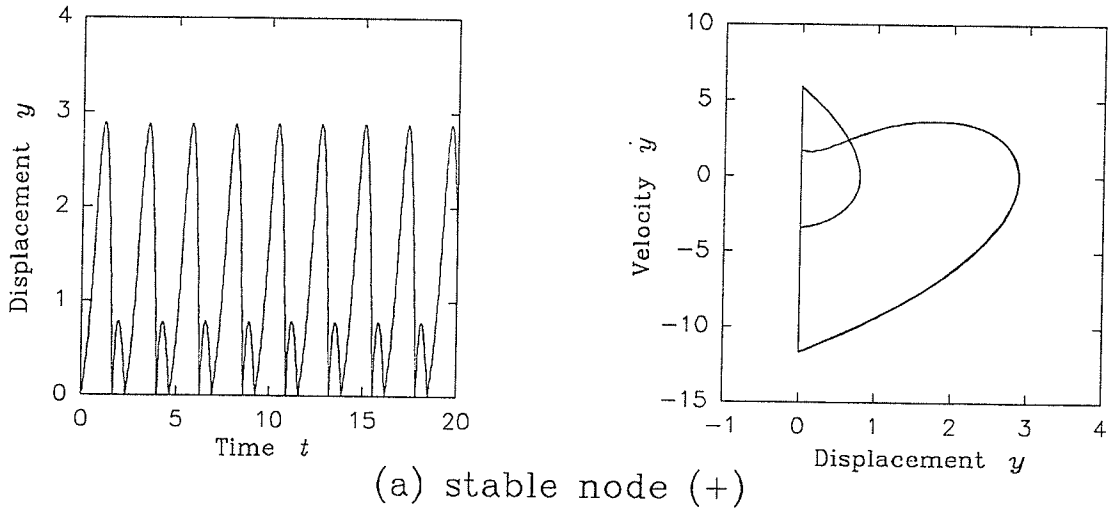

(a) stable node (+)

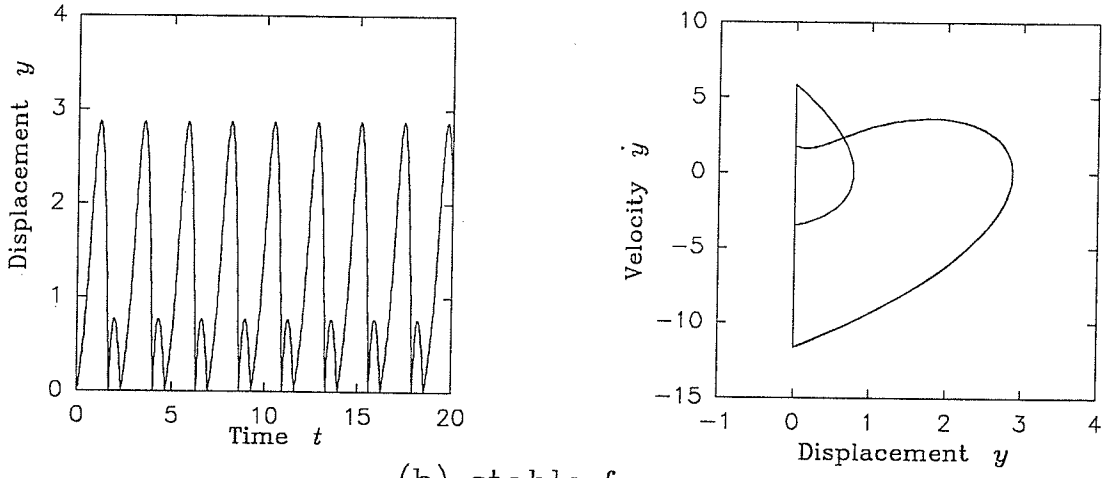

(b) stable fucus

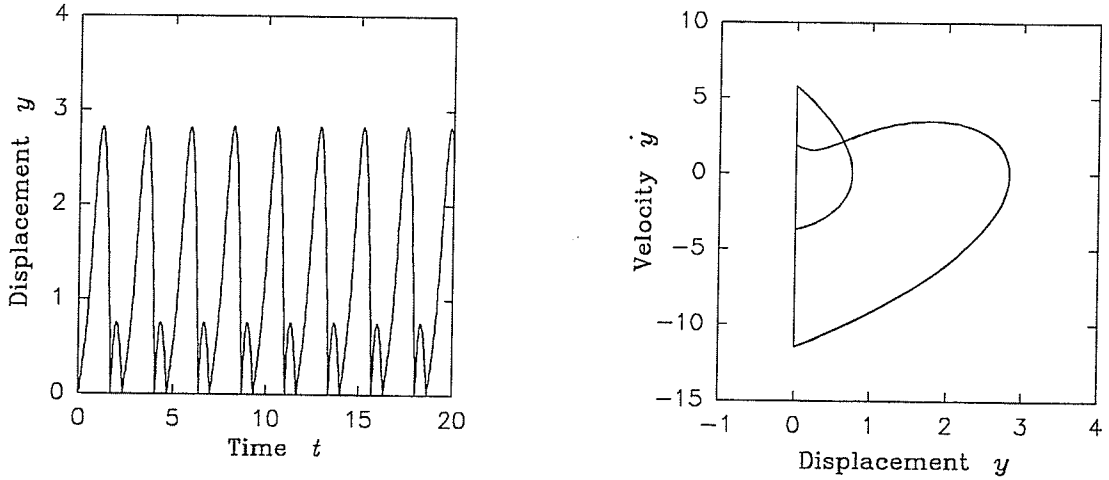

(c) stable node (−)

Figure 7.16 Three types of stable period-2 motion for $\sin(\omega t_i + \varphi) \geq 0$.

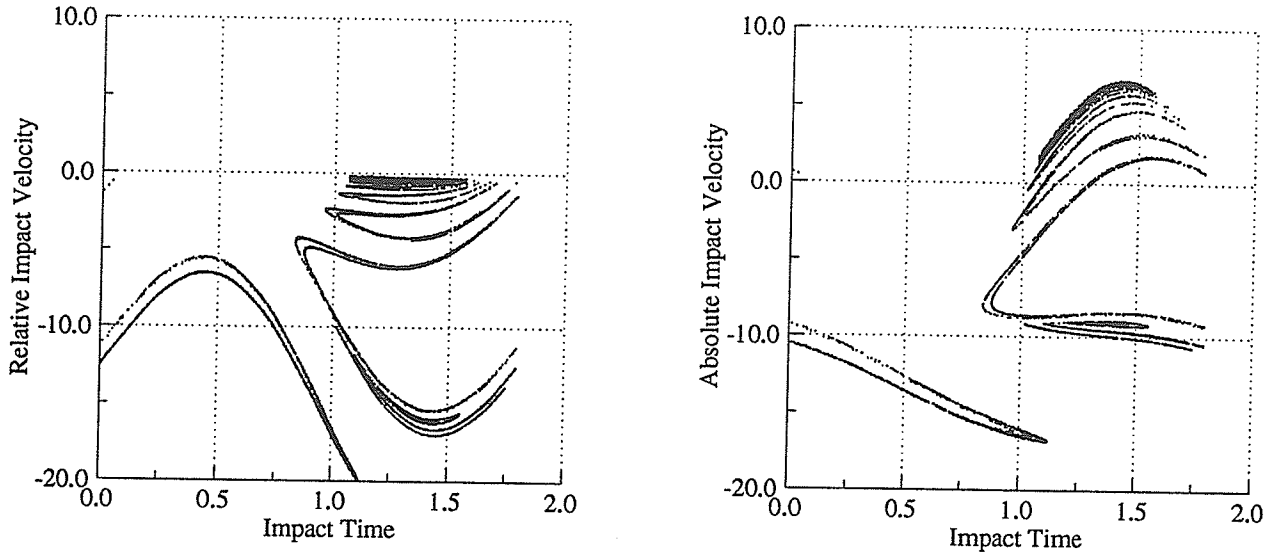

(a) 2nd saddle (-)

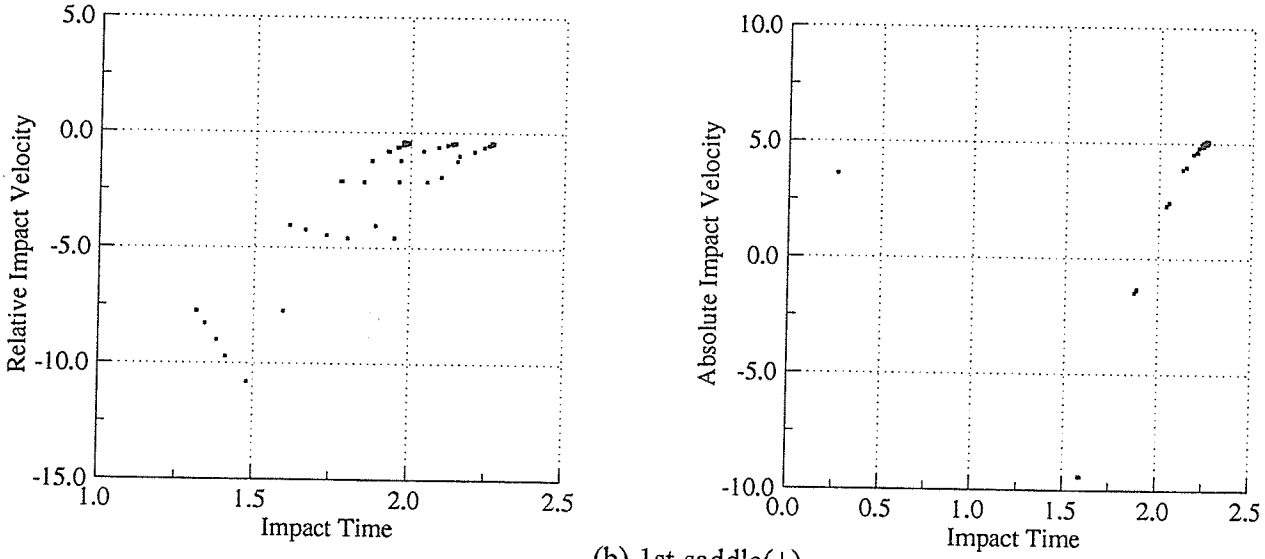

(b) 1st saddle(+)

Figure 7.17 Chaotic attractors associated with the unstable period-2 motion for $\sin(\omega t_i + \varphi) \geq 0$.

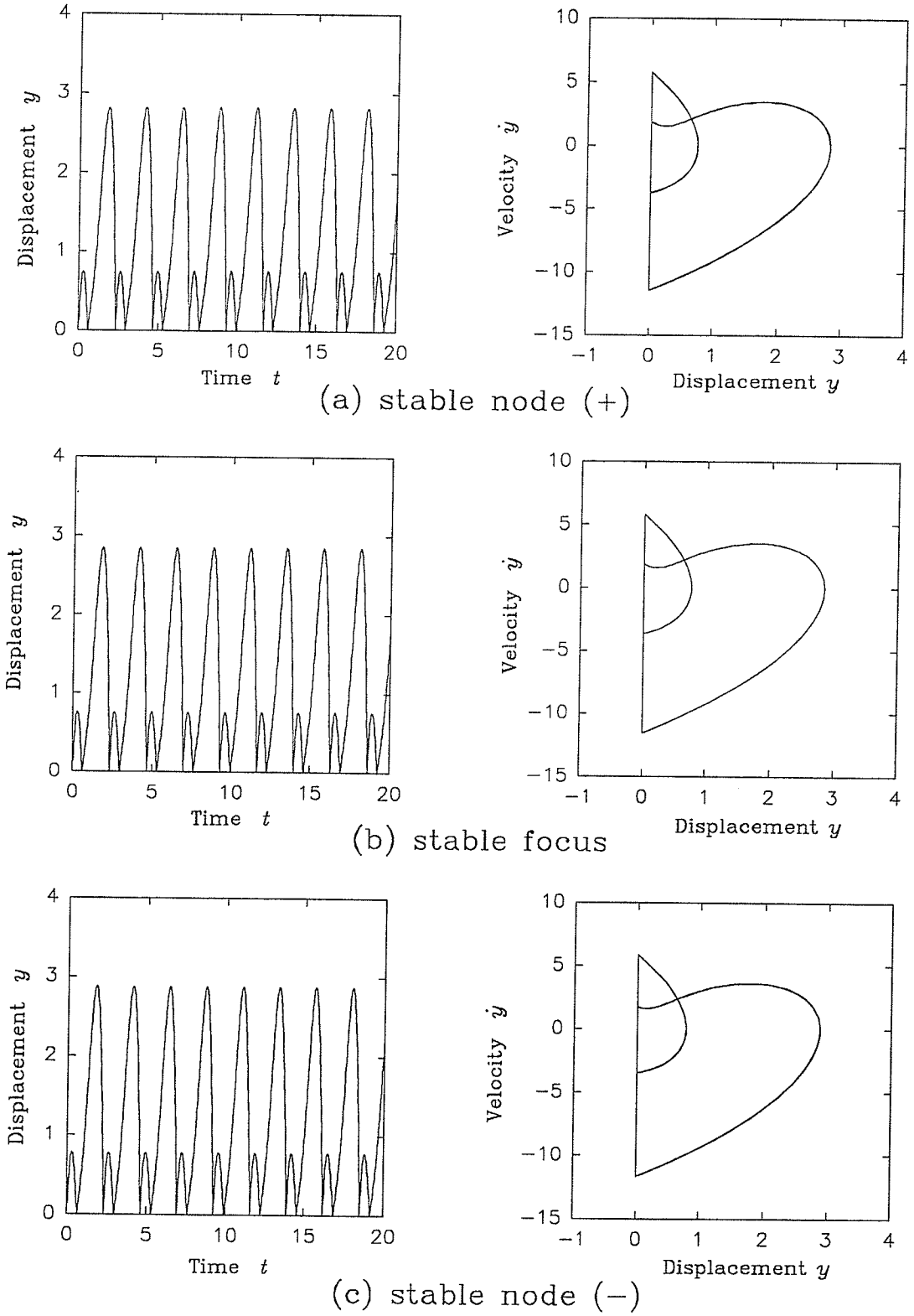

Figure 7.18 Three types of stable period-2 motion for $\sin(\omega t_i + \varphi) \le 0$.

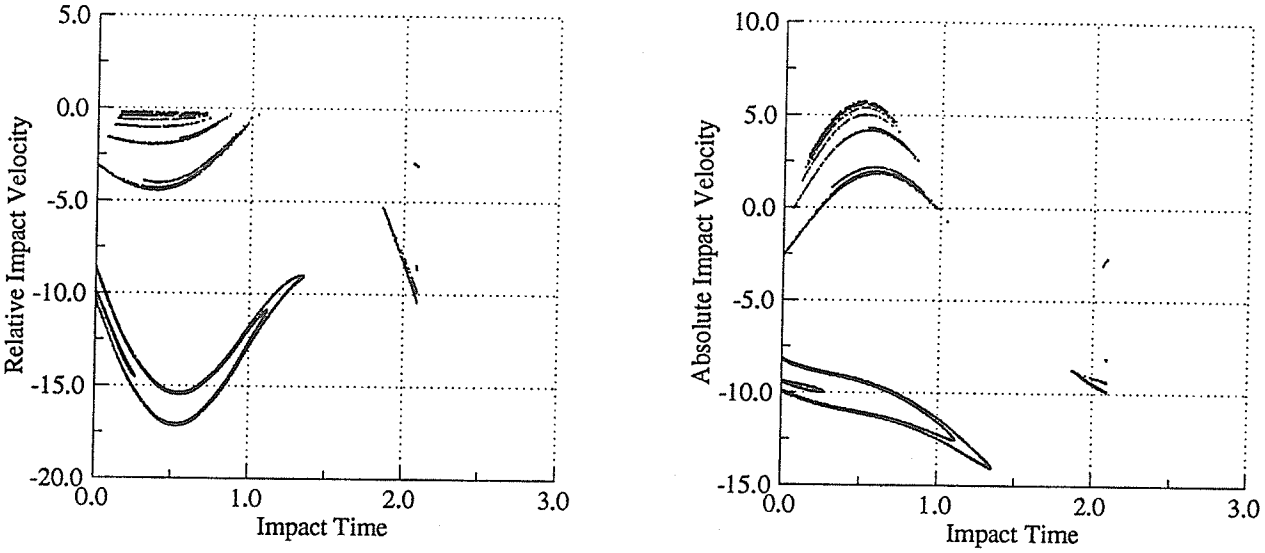

(a) 2nd saddle (-)

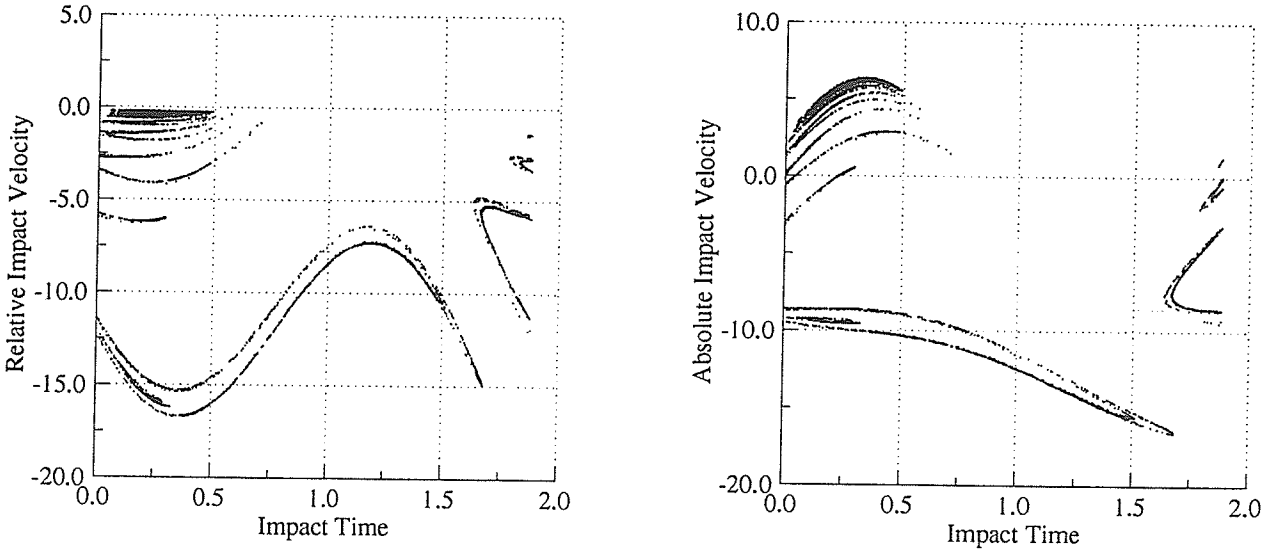

(b) 1st saddle(+)

Figure 7.19 Chaotic attractors associated with the unstable period-2 motion for $\sin(\omega t_i + \varphi) \le 0$.

Observe that for the period-2 motion there are only two possible types of impacts: a 'large' impact followed by a 'small' impact as depicted in *Figure* 7.16 (for $\sin(\omega t_i + \varphi) \geq 0$) and a 'small' impact followed by a 'large' impact as depicted in *Figure* 7.18 (for $\sin(\omega t_i + \varphi) \leq 0$). The Poincare mappings for $\sin(\omega t_i + \varphi) \geq 0$ are plotted in *Figure* 7.17 and for $\sin(\omega t_i + \varphi) \leq 0$ in *Figure* 7.19. Observe the presence of the Smale horseshoe structures which are not identical. However, their presence indicates the presence of fractals and thus, chaotic attractors in these figures.

The physical motion plots are shown in *Figure* 7.20 for $\sin(\omega t_i + \varphi) \geq 0$ and *Figure* 7.21 for $\sin(\omega t_i + \varphi) \leq 0$ and like those plotted for the period-1 motion, the unstable motions do not repeat themselves.

7.5 Conclusions

Based on the differential equation of motion, the stability and bifurcation conditions for a bouncing ball with a massive harmonically vibrating table are derived for the first time. The mappings for period-1, period-2 and finally, generalizing to period-k motion of the bouncing ball are derived. It is found that three types of stable motion exist: stable node (+), stable focus and stable node (-); and two-types of unstable motion exist: saddle of the first kind and saddle of the second kind. From the Poincare mappings of the unstable period-1 motion, the two saddles are found to possess identical Smale horseshoe structures. This is however, not true for period-2 motion (and period-k motion) where their horseshoe structures are not identical. As shown, the unstable motion exhibits chaotic attractors. Plots of the physical motion of the bouncing ball superimposed on the vibration of the table are also given.

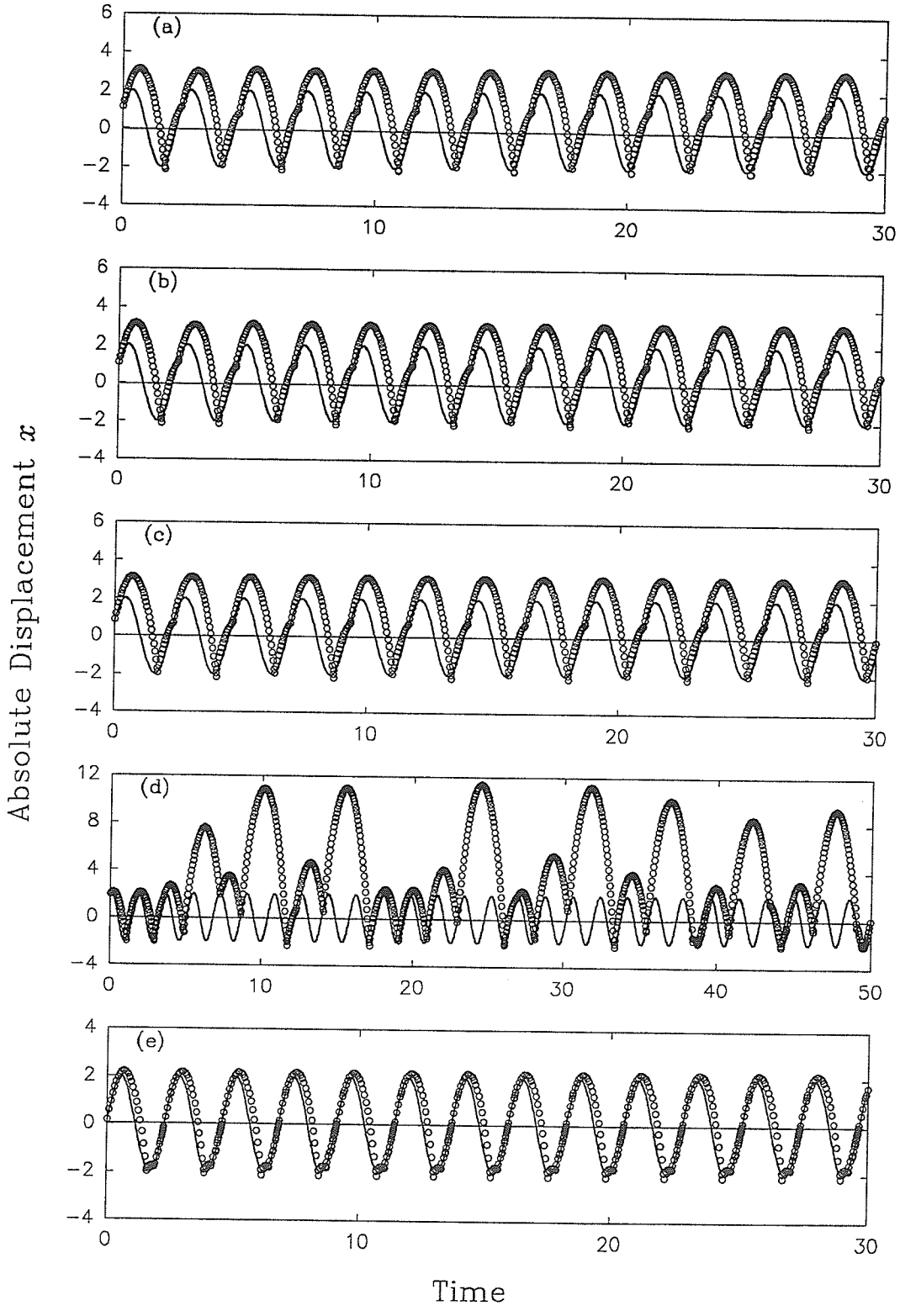

Figure 7.20 Period-2 physical motion for $\sin(\omega t_i + \varphi) \geq 0$: (a) stable node (+), (b) stable focus, (c) stable node (-), (d) 2nd saddle (-) and (e) 1st saddle (+) (∘ ∘ ∘ ball, —— table).

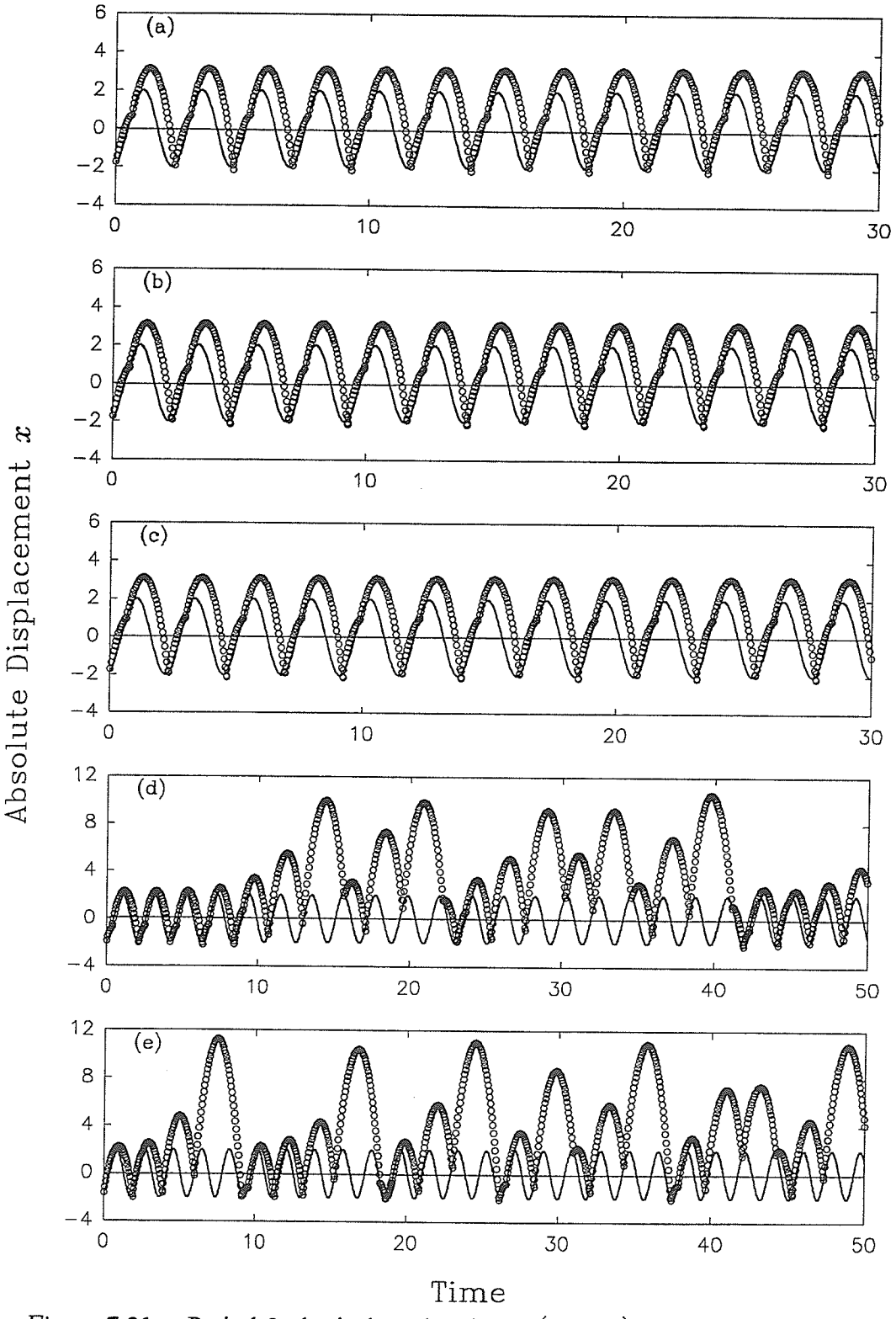

Figure 7.21 Period-2 physical motion for $\sin(\omega t_i + \varphi) \le 0$: (a) stable node (+), (b) stable focus, (c) stable node (-), (d) 2nd saddle (-) and (e) 1st saddle (+) (∘ ∘ ∘ ball, —— table).

CHAPTER 8

MOTION OF A HORIZONTAL IMPACT PAIR

Unlike *Chapter* 7 where the motion of the ball is *vertical* (and thus, gravity has to be considered), in this chapter, we are interested in the motion of a *horizontal* impact pair. Another major difference between *Chapter* 7 and this chapter is that, in the former, the impacts are free-falling onto one plane whereas, in here, we have rapid impacts on two closely-separated planes. This difference is significant in that the energy of the horizontal impact pair is much higher and therefore, leads more readily to chaotic motion. In this sense, the study of the motion of a horizontal impact pair is more general than the motion of a bouncing ball. Collisions or impacts caused by discontinual motion is complex and highly nonlinear, and the most basic model is that of an impact pair (Masri and Caughey (1966), Bapat and Bapat (1988), and Heiman, Bajaj and Sherman (1988)). Other impact models include the acceleration or impact dampers (Lieber and Jensen (1945), Grubin (1956), Warbuton (1957), Kobrinskii (1969), Bapat and Sankar (1985)) and the impact oscillators (Senator (1970), Shaw (1985a, b), Bishop (1994)).

This chapter is concerned with the dynamical modeling of a horizontal impact pair, subjected to a periodic base excitation. As in *Chapter* 7, applying the theory of discontinual motion, mappings for four switch-planes are defined, and from these, five possible impact motion models are developed: Model I, Model II, Model III, Model IV and Model V. Note that the most studied impact model pertains to that of the equispaced and non-equispaced, periodic two-impacts in exactly n-cycles of base motion, and is captured by the Model I motion. Numerical simulations are also presented.

8.1 System Description

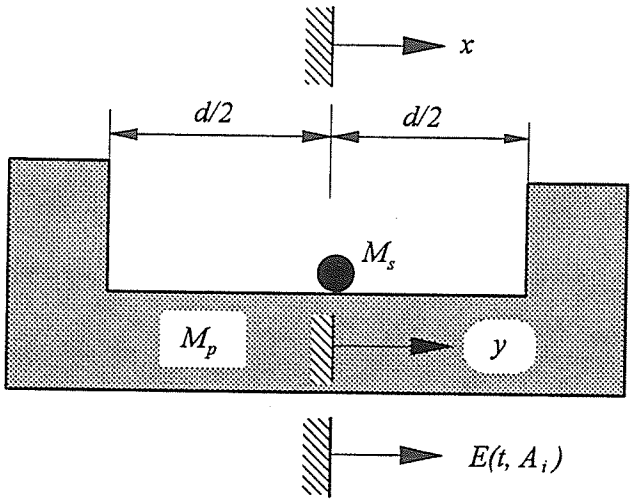

Figure 8.1 Mechanical model of an impact pair.

Figure 8.1 shows an impact pair consisting of a secondary mass (rigid ball) M_s moving freely within a gap d in a primary mass M_p, where $M_p >> m$. Assuming the excitation of the primary mass is harmonic, that is,

$$E(t, A_j, \omega_j, \varphi_j) = \sum_{j=1}^{n} A_j \sin(\omega_j t + \varphi_j), \tag{8.1}$$

where A_j, ω_j, φ_j are the jth-amplitude, jth-frequency and jth-phase angle, respectively. Let (x,t) denotes the absolute displacement of the secondary mass and (y,t) its displacement relative to M_p. For simplicity, a one-term expression is assumed and the external excitation becomes (Han, Luo and Deng (1995)):

$$E = A\sin(\omega t + \varphi). \tag{8.2}$$

Substituting *Equation* (8.2) into *Equation* (7.2)(c) and neglecting friction yields the equation of motion in relative coordinate system. That is,

$$\ddot{y} = A\omega^2 \sin(\omega t + \varphi). \tag{8.3}$$

Integrating *Equation* (8.3) leads to

$$\dot{y} = -A\omega\cos(\omega t + \varphi) + \dot{y}_0 + A\omega\cos(\omega t_0 + \varphi), \tag{8.4}$$

$$y = -A\sin(\omega t + \varphi) + [\dot{y}_0 + A\omega\cos(\omega t_0 + \varphi)](t - t_0) + A\sin(\omega t_0 + \varphi) + y_0. \tag{8.5}$$

Thus, the equation of motion for state subset X_{i+1} is

$$\dot{y} = -A\omega\cos(\omega t + \varphi) + \dot{y}_i^+ + A\omega\cos(\omega t_i + \varphi), \tag{8.6}$$

$$y = -A\sin(\omega t + \varphi) + \left[\dot{y}_i^+ + A\omega\cos(\omega t_i + \varphi)\right](t - t_i) + A\sin(\omega t_i + \varphi) + y_i^+. \tag{8.7}$$

in which $t \in [t_i, t_{i+1}]$, $y(t_{i+1}) = y_{i+1}^-$, $\dot{y}(t_{i+1}) = \dot{y}_{i+1}^-$. Note that $(\ )^-$ and $(\ )^+$ denote before and immediately after an impact, respectively. The switch-plane or the discontinued subset ∂X_{i+1} is

$$y_{i+1}^- - y_i^+ = -A\sin(\omega t_{i+1} + \varphi) + \left[\dot{y}_i^+ + A\omega\cos(\omega t_i + \varphi)\right](t_{i+1} - t_i) + A\sin(\omega t_i + \varphi). \tag{8.8}$$

An impact is deemed to occur whenever

$$\left|y_i^+\right| = \left|y_i^-\right| = \frac{d}{2}. \tag{8.9}$$

Assuming the simplest impact law, namely, one that considers the impact process is instantaneous and employs the concept of a constant coefficient of restitution e to model the energy loss during impact. The relative velocities before and after an impact are related by

$$\dot{y}_i^+ = -e\dot{y}_i^-. \tag{8.10}$$

In view of *Equations* (8.9)-(8.10), we have the switch-plane

$$\dot{y}_{i+1} = -A\omega\cos(\omega t_{i+1} + \varphi) + \left[-e\dot{y}_i^- + A\omega\cos(\omega t_i + \varphi)\right], \tag{8.11}$$

$$y_{i+1}^{-} - y_i^{-} = -A\sin(\omega t_{i+1} + \varphi) + \left[-e\dot{y}_i^{-} + A\omega\cos(\omega t_i + \varphi)\right](t_{i+1} - t_i) + A\sin(\omega t_i + \varphi). \quad (8.12)$$

For convenience, the minus superscript used for the relative coordinates will be dropped in the ensuing derivation. That is, y^{-}, $\dot{y}^{-}$ will be simply denoted by y, $\dot{y}$, respectively. The switch-plane is now defined as

$$\Sigma = \left\{(t_i, \dot{y}_i) \,\middle|\, |y_i| = \frac{d}{2},\ t \bmod \frac{2\pi}{\omega}\right\}. \quad (8.13)$$

Using *Equation* (8.5), for every discontinuity we have

$$\Sigma = \Sigma^{+} \bigcup \Sigma^{-}. \quad (8.14)$$

where

$$\Sigma^{+} = \left\{(t_i, \dot{y}_i) \,\middle|\, y_i = \frac{d}{2},\ t \bmod \frac{2\pi}{\omega}\right\}, \quad (8.15)$$

$$\Sigma^{-} = \left\{(t_i, \dot{y}_i) \,\middle|\, y_i = -\frac{d}{2},\ t \bmod \frac{2\pi}{\omega}\right\}. \quad (8.16)$$

In terms of the absolute coordinate reference frame, the corresponding expression for *Equation* (8.13) is

$$\Sigma = \left\{(x, \dot{x}) \,\middle|\, |y_i| = \frac{d}{2}\right\} = \Sigma^{-} \bigcup \Sigma^{+}, \quad (8.17)$$

or

$$\Sigma = \left\{(t, \dot{x}) \,\middle|\, |y_i| = \frac{d}{2},\ t \bmod \frac{2\pi}{\omega}\right\} = \Sigma^{-} \bigcup \Sigma^{+}. \quad (8.18)$$

where Σ^{+} and Σ^{-} can be similarly defined.

8.2 Possible Impact Motion Models

Based on the proposed formulation, four new mappings can be defined. These are

$$P_1: \Sigma^{+} \to \Sigma^{-}; \quad P_2: \Sigma^{-} \to \Sigma^{+}; \quad P_3: \Sigma^{+} \to \Sigma^{+}; \quad P_4: \Sigma^{-} \to \Sigma^{-}. \quad (8.19)$$

The switch-plane $\Sigma^{-}(\text{or}\,\Sigma^{+})$ can be interpreted as the Poincare section. Hence, the Poincare mapping P can be defined for several impact motion models.

8.2.1 Model I motion

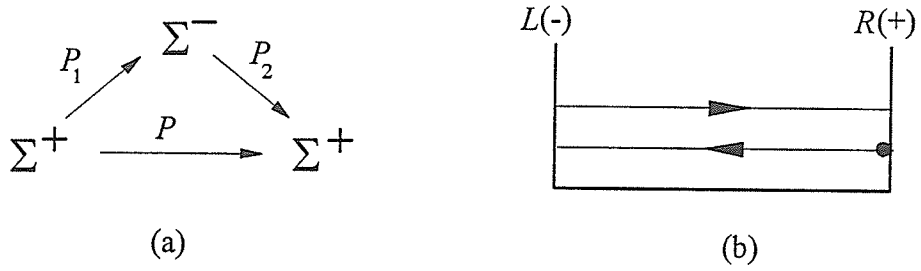

Figure 8.2 Model I motion - *RL* impact sequence: (a) commutative diagram and (b) physical model.

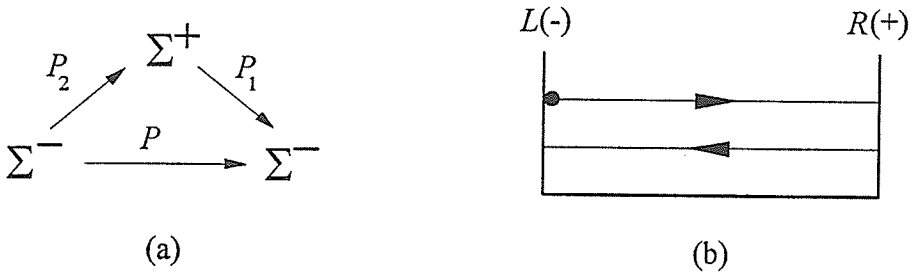

Figure 8.3 Model I motion - *LR* impact sequence: (a) commutative diagram and (b) physical model.

The commutative diagram for Model I motion is depicted in *Figure* 8.2(a) with the physical interpretation given in *Figure* 8.2(b). As shown, this model corresponds physically to the situation of just one impact per side or more commonly known as two alternating impacts. It could be either an impact on the left side followed by an impact on the right (*LR*), or an impact on the right side followed by an impact on the left (*RL*). The latter is depicted in *Figure* 8.3. Hence, there are two possible cases and since these two cases are the identical, we will consider only the *LR* impact sequence for further discussion. As discussed in the next section, this motion involves the *grazing* bifurcation at the parameter values of the saddle of the second kind. For this situation, we have

$\Sigma^+ \xrightarrow{P} \Sigma^+$ so that the mapping becomes,

$$P = P_2 \circ P_1. \tag{8.20}$$

This classical two alternating impacts per cycle of base motion is perhaps the most studied steady-state impact motion. A more general investigation involving two-impacts in exactly n-cycles of base motion will be presented later. For any $\mathbf{x} \in \Sigma^+$ we have,

$$P\mathbf{x} = \mathbf{x}, \tag{8.22}$$

so that

$$P_2 \circ P_1 = \mathbf{I} \tag{8.23}$$

where $\mathbf{I}$ is an identity mapping.

8.2.2. Model II motion

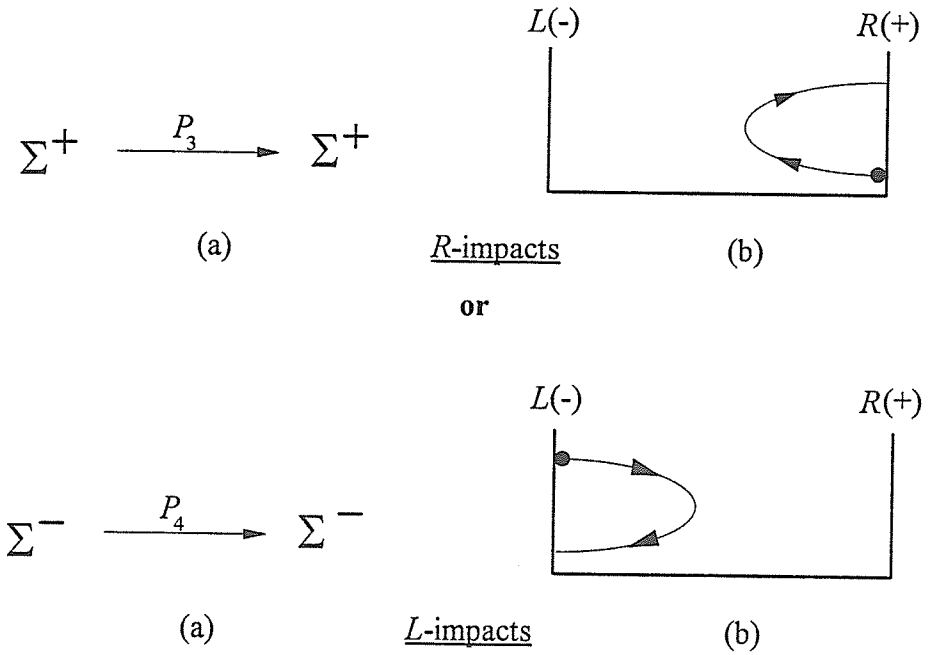

Figure 8.4 Model II motion: (a) commutative diagram and (b) physical model.

For this model, the commutative diagram is given in *Figure* 8.4(a) and the corresponding physical model in *Figure* 8.4(b). Physically, the impact process is that of one impact per side, per cycle. Since the impact can be one the right side (R) or on the lift side (L), we

again have two possibilities. Since these two situations are identical, just one case is considered. As before, the motion is described by

$$P\mathbf{x} = \mathbf{x} = P_3\mathbf{x}, \tag{8.24}$$

and its periodic solution is characterized by

$$\left.\begin{aligned} t_1 &= nT + t_0, \\ \omega t_0 + \varphi &= \frac{\pi}{2}, \\ \dot{y}_1 &= \dot{y}_0 = 0, \end{aligned}\right\} \tag{8.25}$$

where $T = 2\pi / \omega$ is the period. From the result of Mapping P_3 is enlisted in *Appendix* C.2 for $t \in (t_0, t_1)$, the solution simplifies to,

$$\dot{y} = A\omega\cos(\omega t + \varphi), \quad |y| = \left|-A\sin(\omega t + \varphi) + A + \frac{d}{2}\right| \le \frac{d}{2}. \tag{8.26}$$

That is

$$A \le 0. \tag{8.27}$$

However, $E = A\sin(\omega t + \varphi)$ where A is always positive. This conflicting result implies that this model is physically unattainable, and thus, the solution non-viable. The ball actually stops before reaching the sides. Similarly, for the period-doubling bifurcation motion, we have

$$P^{(2)}\mathbf{x} = P_3^{(2)}\mathbf{x} = P_2 \circ P_3\mathbf{x} = \mathbf{x}, \tag{8.28}$$

where from *Appendix* C.2.1, for mapping P_3, we have

$$\left.\begin{aligned} (1+e)(\dot{y}_1 + \dot{y}_0) &= 0, \\ t_1 &= \frac{n}{2}T + t_0, \\ t_2 &= nT + t_0. \end{aligned}\right\} \tag{8.29}$$

Since $\dot{y}_1, \dot{y}_0 \in \Sigma^+$ and $e > 0$, we get $\dot{y}_1 = \dot{y}_0 = \dot{y}_2 = 0$. Once again, this constitutes a non-viable solution and therefore the motion is physically unattainable.

8.2.3 Model III motion

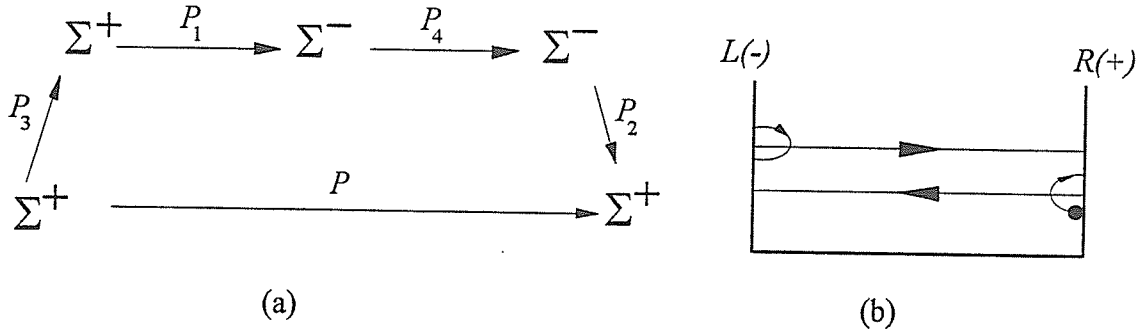

Figure 8.5 Model III motion: (a) commutative diagram and (b) physical model.

Figure 8.5 shows Model III motion: its commutative diagram in *Figure* 8.5(a) and the corresponding physical interpretation in *Figure* 8.5(b). The impact process as represented here contains four impacts per cycle, comprising of either a *RLLR* or a *LRRL* impact sequence. Since these two cases are the same, the discussion here will be limited to just the *RLLR* sequence. The mapping is

$$P = P_2 \circ P_4 \circ P_1 \circ P_3. \tag{8.30}$$

Since this model is the same as Model I motion, no further discussion is necessary.

8.2.4 Model IV motion

It should be mentioned that in going from a *LR* sequence (Model I motion) to a *RLLR* sequence (Model III motion), it is possible to generate two intermediate impact models: a *LLR* impact sequence and a *RRL* impact sequence. These are sketched in *Figure* 8.6 and

their mappings are $P = P_2 \circ P_4 \circ P_1$ and $P = P_1 \circ P_3 \circ P_2$ respectively. In going from this model to chaos via period-doubling bifurcation, the general mapping for the *LLR* motion is

$$P^{(k)} = \underbrace{(P_2 \circ P_4 \circ P_1)\circ\cdots\circ(P_2 \circ P_4 \circ P_1)}_{k \text{ terms}}, \qquad k = 1,2,3,\ldots, \tag{8.31}$$

and for the *RRL* motion we have

$$P^{(k)} = \underbrace{(P_1 \circ P_3 \circ P_2)\circ\cdots\circ(P_1 \circ P_3 \circ P_2)}_{k \text{ terms}}, \qquad k = 1,2,3,\ldots. \tag{8.32}$$

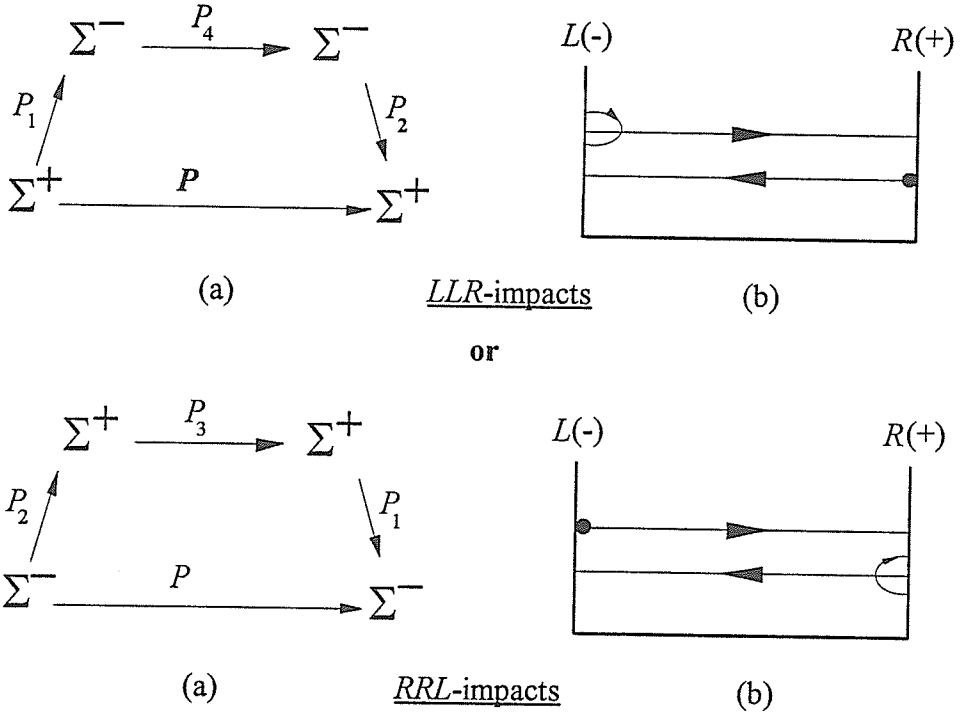

Figure 8.6 Model IV motion: (a) commutative diagram and (b) physical model.

8.2.5 Model V motion

It is desirable to generalize Model III motion, to handle the situation of uneven multiple impacts per side. This is shown in *Figure* 8.7 where we have m-impacts on the right side m_R) and n-impact on the left(n_L), resulting in an impact sequence described by

$\underbrace{R\cdots R}_{m_R}\underbrace{L\cdots L}_{n_L}R$. The motion is defined by

$$P = P_2 \circ P_4^{(n_L)} \circ P_1 \circ P_3^{(m_R)}. \tag{8.33}$$

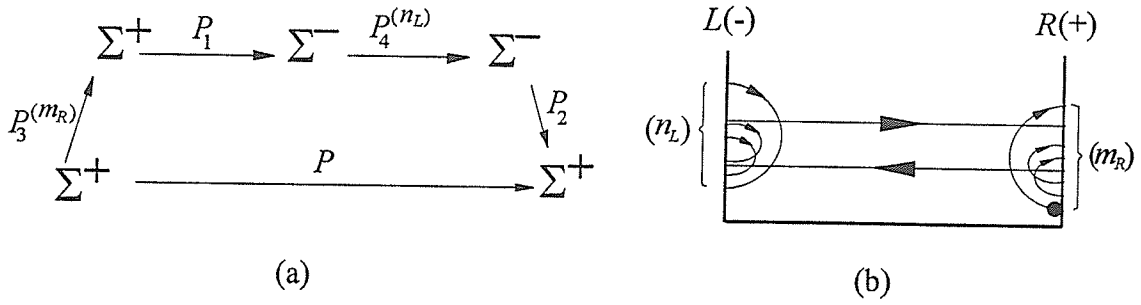

Figure 8.7 Model V motion: (a) commutative diagram and (b) physical model.

This model could have also been equally described by a $\underbrace{L\cdots L}_{m_L}\underbrace{R\cdots R}_{n_R}L$ impact sequence. The total number of impacts per cycle of the base motion for either description is $(m+n+1)$. The mapping is given by

$$P^{(k)} = \underbrace{(P_2 \circ P_4^{(n_L)} \circ P_1 \circ P_3^{(m_R)})\circ\cdots\circ(P_2 \circ P_4^{(n_L)} \circ P_1 \circ P_3^{(m_R)})}_{k \text{ terms}}, \qquad k = 1,2,3, \quad . \tag{8.34}$$

For the most general case of a varying, uneven multiple impacts per side, we have

$$P^{(k)} = (P_2 \circ P_4^{(n_{L1})} \circ P_1 \circ P_3^{(m_{R1})})\circ\cdots\circ(P_2 \circ P_4^{(n_{Lk})} \circ P_1 \circ P_3^{(m_{Rk})}) \tag{8.35}$$

in which m_{Ri}, n_{Li} consist of a set of positive integers, $i = 1,2,\ldots,k$, that can be randomly selected.

8.3 Non-Equispaced Periodic Motion

To determine the periodic motion of the five proposed impact models, a method similar to the one outlined in *Section* 7.2 is devised by introducing a new parameter pertaining to the impact time-interval for characterizing the motion. The formulation for the most general

situation of non-equispaced, periodic motion is presented. The details are as follows.

8.3.1 Non-equispaced period-1 motion for Model I

The periodic two-impacts in exactly n-cycles of base motion for Model I is discussed here. This model is very popular since its motion is easily observed during physical experimentations. A considerable amount of research for this type of motion exist, particularly for the case of symmetric two equispaced impacts per cycle motion (i.e., n=1). Note the term *symmetric* as used here implies that n is an odd integer. Choosing the initial Poincare section to be defined by Σ^- which implies $\dot{y}_i \le 0$, we have, from *Equation* (8.22) for periodic motion:

$$\left.\begin{aligned} t_{i+2} &= \frac{2n\pi}{\omega} + t_i; \\ \dot{y}_{i+2} &= \dot{y}_i; \qquad \dot{y}_{i+2},\ \dot{y}_i \le 0. \end{aligned}\right\} \tag{8.36}$$

From the results shown in the *Appendix* C.2, the solutions for $t = t_{i+1}$ are

$$\dot{y}_{i+1} = -A\omega\cos(\omega t_i + \varphi) + \left[-e\dot{y}_i + A\omega\cos(\omega t_i + \varphi)\right], \tag{8.37}$$

$$d = -A\left[\sin(\omega t_{i+1} + \varphi) - \sin(\omega t_i + \varphi)\right] + \left[-e\dot{y}_i + A\omega\cos(\omega t_i + \varphi)\right](t_{i+1} - t_i), \tag{8.38}$$

and for $t = t_{i+2}$, they are,

$$\dot{y}_{i+2} = -A\omega\cos(\omega t_{i+2} + \varphi) + \left[-e\dot{y}_{i+1} + A\omega\cos(\omega t_{i+1} + \varphi)\right], \tag{8.39}$$

$$-d = -A\left[\sin(\omega t_{i+2} + \varphi) - \sin(\omega t_{i+1} + \varphi)\right] + \left[-e\dot{y}_{i+1} + A\omega\cos(\omega t_{i+1} + \varphi)\right](t_{i+2} - t_{i+1}). \tag{8.40}$$

Two methods of manipulating *Equations* (8.37)-(8.40) for quantities of interest (such as $\dot{y}_i$, A, etc.) are provided: Method 1 is more direct and obvious, and Method 2 is more general and can be easily extended to handle the analysis of the five impact models.

Method 1

Adding *Equations* (8.37) and (8.39) and simplifying via *Equation* (8.36) yields

$$(1+e)(\dot{y}_i + \dot{y}_{i+1}) = 0 \quad \Rightarrow \quad \dot{y}_i = -\dot{y}_{i+1}. \tag{8.41}$$

Substituting *Equation* (8.41) into *Equation* (8.37) and for $e \neq 1$, we get

$$\dot{y}_i = \frac{A\omega}{1-e}\left[\cos(\omega t_{i+1} + \varphi) - \cos(\omega t_i + \varphi)\right]. \tag{8.42}$$

Similarly adding *Equations* (8.38) and (8.40) leads to

$$\left[-e\dot{y}_i + A\omega\cos(\omega t_i + \varphi)\right](t_{i+1} - t_i) + \left[-e\dot{y}_{i+1} + A\omega\cos(\omega t_{i+1} + \varphi)\right]\left(\frac{2n\pi}{\omega} + t_i - t_{i+1}\right) = 0. \tag{8.43}$$

Next, we introduce a new parameter such that $0 \leq q \leq 1$. Then, the time interval between two consecutive impacts is given by,

$$t_{i+1} - t_i = q\frac{2n\pi}{\omega}. \tag{8.44}$$

Observe from *Equation* (8.44) for Model I motion, q can be interpreted as follows: no impacts for q=0 and q=1; and equispaced impacts for $q = 1/2$. Therefore, q can be interpreted as the impact time-interval parameter. Substituting *Equations* (8.41) and (8.44) into *Equations* (8.42)-(8.43) yields

$$\dot{y}_i = -\frac{A\omega}{1-q(1+e)}\cos(\omega t_i + \varphi). \tag{8.45}$$

From *Equation* (8.45) we can compute the initial velocity for a given q. Eliminating $\cos(\omega t_i + \varphi)$ from *Equations* (8.42) and (8.45), we have

$$\cos(\omega t_{i+1} + \varphi) = -\frac{e - q(1+e)}{A\omega}\dot{y}_i. \tag{8.46}$$

Substituting *Equations* (8.44) and (8.45) into *Equation* (8.38), we obtain

$$\frac{1}{A}\left[d+\frac{2(1+e)(1-q)qn\pi\dot{y}_i}{\omega}\right]=\sin(\omega t_{i+1}+\varphi)-\sin(\omega t_i+\varphi). \tag{8.47}$$

Combining *Equations* (8.42) and (8.47) and eliminating the sine and cosine terms we get:

$$A=\frac{1}{2\left|\sin(qn\pi)\right|}\sqrt{\left[\frac{(1-e)\dot{y}_i}{\omega}\right]^2+\left[d+\frac{2(1+e)(1-q)qn\pi\dot{y}_i}{\omega}\right]^2};\quad \dot{y}_i\le 0,\quad n=1,2,3,\quad . \tag{8.48}$$

Equation (8.48) describes the parameter manifold of Model I motion for prescribed values of q. It yields the amplitude of the excitation A. Note that from its denominator, it is obvious that A will not exist for $q=l/n$ where l is an integer less than n. Physically, it implies the motion is non-attainable.

Method 2

Applying the procedure outlined in *Section* 7.2 for non-equispaced impacts, namely, by substituting *Equation* (8.44) into *Equations* (8.37)-(8.38), we obtained the following equations governing the periodic motion of Model I motion:

$$\left.\begin{aligned}\cos(\omega t_i+\varphi)&=\frac{K_1^q+eK_2^q\dot{y}_i+K_3^q\dot{y}_{i+1}}{A\omega K^q}\\ \sin(\omega t_i+\varphi)&=\frac{K_4^q+eK_5^q\dot{y}_i+K_6^q\dot{y}_{i+1}}{A\omega K^q}\end{aligned}\right\}, \tag{8.49}$$

where the various coefficients $K^q, K_1^q, \cdots, K_6^q$ are defined in *Appendix* C.2. Substituting *Equation* (8.49) into *Equation* (8.37) leads to

$$\dot{y}_{i+1}=\frac{L_1^q+L_2^q\dot{y}_i}{L^q}, \tag{8.50}$$

where the coefficients L^q, L_1^q, L_2^q are also listed in *Appendix* C.2. Once again, following the same procedure as in deriving *Equation* (8.49), but now, from *Equations* (8.39)-(8.40) we get,

$$\dot{y}_{i+2} = \dot{y}_i = \frac{L_1^{1-q} + L_2^{1-q}\dot{y}_{i+1}}{L^{1-q}} \tag{8.51}$$

In view of *Equation* (8.50), we have from *Equation* (8.51), after eliminating $\dot{y}_{i+1}$:

$$\dot{y}_i = \frac{L_1^{1-q}L^q + L_1^q L_2^{1-q}}{L^q L^{1-q} - L_2^q L_2^{1-q}}, \tag{8.52}$$

It can be shown from *Equations* (8.50)-(8.52) that $\dot{y}_i = -\dot{y}_{i+1}$. Also, eliminating the trigonometric terms in *Equation* (8.49) by squaring and adding, leads to

$$A = \frac{1}{\omega K^q}\sqrt{\left[K_1^q + \left(eK_2^q - K_3^q\right)\dot{y}_i\right]^2 + \left[K_4^q + \left(eK_5^q - K_6^q\right)\dot{y}_i\right]^2}; \quad \dot{y}_i \le 0, \quad n = 1,2,3,\cdots. \tag{8.53}$$

Observe that *Equations* (8.52) and (8.53) are expressed in terms of coefficients L^q, L_1^q, L_2^q $K^q, K_1^q, \cdots, K_6^q$ which are defined in *Appendix* C.2. Expressing them in this form makes the task of extending the formulation to handle the analysis of the non-equispaced *k*-impacts periodic motion for all the five proposed impact motion models more intuitive and thus, easier. It can be shown that *Equations* (8.52) and (8.53) are identical respectively, to *Equations* (8.45) and (8.48) derived in Method 1.

Equispaced period-1 motion

For this motion, $q = 1/2$. We can use equations from either Method 1 or Method 2 to derive the simplified equations governing this equispaced period-1 motion. Choosing Method 2, we have from *Equations* (8.49) and (8.53) for odd *n*:

$$\cos(\omega t_i + \varphi) = -\frac{(1-e)\dot{y}_i}{2A\omega}, \tag{8.54}$$

$$\sin(\omega t_i + \varphi) = \frac{1}{2A}\left(d + \frac{(1+e)n\pi}{2\omega}\dot{y}_i\right). \tag{8.55}$$

and *Equation* (8.53) reduces to,

$$A = \frac{1}{2}\sqrt{\left[\frac{(1-e)\dot{y}_i}{\omega}\right]^2 + \left[d + \frac{(1+e)n\pi\dot{y}_i}{2\omega}\right]^2}; \qquad \dot{y}_i \le 0, \quad n = 1,3,5,\cdots. \tag{8.56}$$

As shown in Han, Luo and Deng (1995), *Equation* (8.56) constitutes only a necessary condition for stability of equispaced motion. We will defer the derivation for the sufficient condition to the next section where the stability and bifurcation of periodic motion are formally introduced. If Σ^+ is chosen as the initial Poincare section which implies $\dot{y}_i \ge 0$, then *Equation* (8.56) modifies to:

$$A = \frac{1}{2}\sqrt{\left[\frac{(1-e)\dot{y}_i}{\omega}\right]^2 + \left[-d + \frac{(1+e)n\pi\dot{y}_i}{2\omega}\right]^2}; \qquad \dot{y}_i \ge 0, \quad n = 1,3,5,\cdots. \tag{8.57}$$

Generalizing *Equations* (8.56) and (8.57) we have,

$$A = \frac{1}{2}\sqrt{\left[\frac{(1-e)\dot{y}_i}{\omega}\right]^2 + \left[d - \frac{(1+e)n\pi|\dot{y}_i|}{2\omega}\right]^2}; \qquad |\dot{y}_i| \ge 0, \quad n = 1,3,5,\cdots. \tag{8.58}$$

For the case of two alternating impacts per cycle, that is n=1, we have from *Equation* (8.58),

$$A = \frac{1}{2}\sqrt{\left[\frac{(1-e)\dot{y}_i}{\omega}\right]^2 + \left[d - \frac{(1+e)\pi|\dot{y}_i|}{2\omega}\right]^2}; \qquad |\dot{y}_i| \ge 0. \tag{8.59}$$

For perfectly elastic impacts, i.e. e=1 we have,

$$\left.\begin{aligned} \dot{y}_i &= -\dot{y}_{i+1} \\ d &= \pm 2A - \frac{n\pi|\dot{y}_i|}{\omega} \end{aligned}\right\}; \qquad n = 1,3,5,\cdots. \tag{8.60}$$

8.3.2 Non-equispaced *k*-impacts periodic motion for Models I-V

The equations derived previously are valid only for the non-equispaced period-1 motion of Model I. In this section, we will formulate the equations for the most general situation, namely, that of the non-equispaced *k*-impacts periodic motion for Models I-V. Consider a model exhibiting *k*-impacts over nT period. Following the procedures of Method 2, we introduce a series of impact time-interval parameter q_j, satisfying,

$$t_{i+j} - t_{i+j-1} = q_j nT, \tag{8.61}$$

where $0 \le q_j \le 1$ and $\sum_{j=1}^{k} q_j =$. Note that it is necessary to introduce a series of q_j, instead of a single q in the previous section, since we are now dealing with motion consisting of *k*-impact time intervals. The governing equations for the motion pertaining to the q_j, impact time-interval are,

$$\dot{y}_{i+j} = -A\omega\cos(\omega t_{i+j} + \varphi) + \left[-e\dot{y}_{i+j-1} + A\omega\cos(\omega t_{i+j-1} + \varphi)\right], \tag{8.62}$$

$$\Delta = -A\sin(\omega t_{i+j+1} + \varphi) + A\sin(\omega t_{i+j} + \varphi) + \left[-e\dot{y}_{i+j-1} + A\omega\cos(\omega t_{i+j-1} + \varphi)\right](t_{i+j} - t_{i+j-1}), \tag{8.63}$$

where

$$\Delta = \begin{cases} -d & \text{for mapping } P_1, \\ d & \text{for mapping } P_2, \\ 0 & \text{for mappings } P_3 \text{ and } P_4. \end{cases} \tag{8.64}$$

Substituting *Equation* (8.61) into *Equations* (8.62)-(8.63) yields

$$\left.\begin{aligned}\cos\left(\omega t_{i+j-1}+\varphi\right)&=\frac{K_1^{q_j}+eK_2^{q_j}\dot{y}_{i+j-1}+K_3^{q_j}\dot{y}_{i+j}}{A\omega K^{q_j}}\\ \sin\left(\omega t_{i+j-1}+\varphi\right)&=\frac{K_4^{q_j}+eK_5^{q_j}\dot{y}_{i+j-1}+K_6^{q_j}\dot{y}_{i+j}}{A\omega K^{q_j}}\end{aligned}\right\}, \tag{8.65}$$

where the coefficients $K^{q_j}, K_1^{q_j}, \cdots, K_6^{q_j}$ are defined in *Appendix* C.2. Substituting *Equations* (8.61) and (8.65) back into *Equation* (8.62), we obtain

$$\dot{y}_{i+j}=\frac{L_1^{q_j}+L_2^{q_j}\dot{y}_{i+j-1}}{L^{q_j}}. \tag{8.66}$$

where the coefficients $L^{q_j}, L_1^{q_j}, L_2^{q_j}$ are defined in *Appendix* C.2. Repeating this process for all the k-time intervals and back substituting to recover the $(i+k)$th impact leads to

$$\dot{y}_{i+k}=\dot{y}_i=\frac{H_k}{1-H}, \tag{8.67}$$

where

$$\left.\begin{aligned}H_k&=\frac{L_1^{q_k}}{L^{q_k}}+\frac{L_2^{q_k}}{L^{q_k}}H_{k-1},\\ H&=\prod_{j=1}^{k}\frac{L_2^{q_j}}{L^{q_j}}.\end{aligned}\right\} \tag{8.68}$$

As shown in the previous section, the necessary condition for the existence of the k-impacts periodic model is given by,

$$A=\frac{1}{\omega K^{q_1}}\sqrt{\left(K_1^{q_1}+eK_2^{q_1}\dot{y}_i+K_3^{q_1}\dot{y}_{i+1}\right)^2+\left(K_4^{q_1}+eK_5^{q_1}\dot{y}_i+K_6^{q_1}\dot{y}_{i+1}\right)^2}. \tag{8.69}$$

To obtain the sufficient condition, we have to carry out a stability analysis and this is presented in the next section.

8.4 Stability and Bifurcation

Similar to the procedures outlined in *Chapter* 7, the sufficient condition for the k-impacts periodic motion will be formulated here via a linearization of the periodic solutions.

8.4.1 Period-1 motion for Model I

Non-equispaced periodic motion

We first linearize $\boldsymbol{x}_{i+1} = P\boldsymbol{x}_i$ and then compute its eigenvalues using the expressions given in *Appendix* C.2.1. Therefore, the Jacobian of the linearized mapping $DP = DP_1 \cdot DP_2$ is,

$$DP = DP_1 \cdot DP_2 = \left[\frac{\partial P_1(t_{i+2}, \dot{y}_{i+2})}{\partial(t_{i+1}, \dot{y}_{i+1})}\right]\left[\frac{\partial P_2(t_{i+1}, \dot{y}_{i+1})}{\partial(t_i, \dot{y}_i)}\right]_{\begin{pmatrix} t_{i+2} \\ \dot{y}_{i+2}\end{pmatrix}=\begin{pmatrix} t_i+2n\pi/\omega \\ \dot{y}_i\end{pmatrix}} \tag{8.70}$$

in which

$$\frac{\partial t_{i+1}}{\partial t_i} = \frac{1}{\dot{y}_{i+1}}\left[-e\dot{y}_i + A\omega^2(t_{i+1} - t_i)\sin(\omega t_{i+1} + \varphi)\right], \tag{8.71}$$

$$\frac{\partial t_{i+1}}{\partial \dot{y}_i} = \frac{e}{\dot{y}_{i+1}}(t_{i+1} - t_i), \tag{8.72}$$

$$\frac{\partial \dot{y}_{i+1}}{\partial t_i} = A\omega^2 \sin(\omega t_{i+1} + \varphi)\frac{\partial t_{i+1}}{\partial t_i} - A\omega^2 \sin(\omega t_i + \varphi), \tag{8.73}$$

$$\frac{\partial \dot{y}_{i+1}}{\partial \dot{y}_i} = A\omega^2 \sin(\omega t_{i+1} + \varphi)\frac{\partial t_{i+1}}{\partial \dot{y}_i} - e; \tag{8.74}$$

and

$$\frac{\partial t_{i+2}}{\partial t_{i+1}} = \frac{1}{\dot{y}_i}\left[-e\dot{y}_{i+1} + A\omega^2\left(t_i + \frac{2n\pi}{\omega} - t_{i+1}\right)\sin(\omega t_i + \varphi)\right], \tag{8.75}$$

$$\frac{\partial t_{i+2}}{\partial \dot{y}_{i+1}} = \frac{e}{\dot{y}_i}\left(t_i + \frac{2n\pi}{\omega} - t_{i+1}\right), \tag{8.76}$$

$$\frac{\partial \dot{y}_{i+2}}{\partial t_{i+1}} = A\omega^2 \sin(\omega t_i + \varphi)\frac{\partial t_{i+2}}{\partial t_{i+1}} - A\omega^2 \sin(\omega t_{i+1} + \varphi), \tag{8.77}$$

$$\frac{\partial \dot{y}_{i+2}}{\partial \dot{y}_{i+1}} = A\omega^2 \sin(\omega t_i + \varphi)\frac{\partial t_{i+2}}{\partial \dot{y}_{i+1}} - e. \tag{8.78}$$

Substituting the solutions in *Section* 8.3.1 into *Equations* (8.71)-(8.78), the parameterized matrix DP of *Equation* (8.70) is determined, from which its trace $Tr(DP)$ and determinant $Det(DP)$ can be easily calculated. The result for the eigenvalues of DP is

$$\lambda_{1,2} = \frac{Tr(DP) \pm \sqrt{Tr(DP)^2 - 4Det(DP)}}{2}. \tag{8.79}$$

Equispaced periodic motion

Specializing the formulas for the well-known equispaced periodic motion, i.e. $q = 1/2$, the computed trace and determinant of the linearized matrix are respectively given by,

$$\left.\begin{aligned} Tr(DP) &= 2e^2 + (1-e)^2\left(\frac{A\omega n\pi \sin(\omega t_i + \varphi)}{\dot{y}_i}\right)^2, \\ Det(DP) &= e^4. \end{aligned}\right\} \tag{8.80}$$

Substituting the results of *Equation* (8.80) into *Equation* (8.79) yields the eigenvalues, and from the subsequent eigenanalysis, the following conclusions can be derived.

(i) Stability conditions

(a) For *stable* motion (stable node (+)) we have,

$$\frac{|\dot{y}_i|}{\omega}\left(\frac{1-e}{2}\right) \le A \le \frac{|\dot{y}_i|}{\omega}\sqrt{\left(\frac{1-e}{2}\right)^2 + \left(\frac{1+e}{n\pi}\right)^2}; \quad n = 1,3,5,\cdots. \tag{8.81}$$

Since no fixed points exist below the lower limit, there is no period-1

equispaced motion below this limit. This observation can also be confirmed by examining *Equation* (8.54) and imposing $\left|\cos(\omega t_i + \varphi)\right| \le 1$. This implies that $A \ge d(1-e)/[n\pi(1+e)]$, which can also be derived by manipulating *Equations* (8.54)-(8.55). The equality at the upper limit is a bifurcation condition and will be discussed later.

(b) For *unstable* motion (saddle of the first kind) we have,

$$A > \frac{|\dot{y}_i|}{\omega}\sqrt{\left(\frac{1-e}{2}\right)^2 + \left(\frac{1+e}{N\pi}\right)^2}; \quad n = 1,3,5,\cdots. \tag{8.82}$$

(ii) Bifurcation condition

Instead of period-doubling bifurcations, we have only the saddle-node bifurcation. The condition is,

$$A = \frac{|\dot{y}_i|}{\omega}\sqrt{\left(\frac{1-e}{2}\right)^2 + \left(\frac{1+e}{n\pi}\right)^2}; \quad n = 1,3,5,\cdots. \tag{8.83}$$

If $e = 1$, we have $Tr(DP) = 2$ and $Det(DP) = 1$ and thus, its eigenvalues are always +1. This implies that a saddle-node always exists for the case of perfectly elastic impacts.

Stability plots

In this section, we are interested in generating stability plots of the period-1 motion for Model I. For equispaced motion, we employed the analytical results obtained previously and for non-equispaced motion, we generated the results numerically by computing its eigenvalues using *Equation* (8.79). To judge the stability and bifurcations of the motion, we adopted the method given in *Section* 7.3.1. The input parameters for the numerical simulations are $\omega = \pi$, $e = 0.5$ and $d = 10$. The results are plotted in *Figures* 8.8 and 8.9.

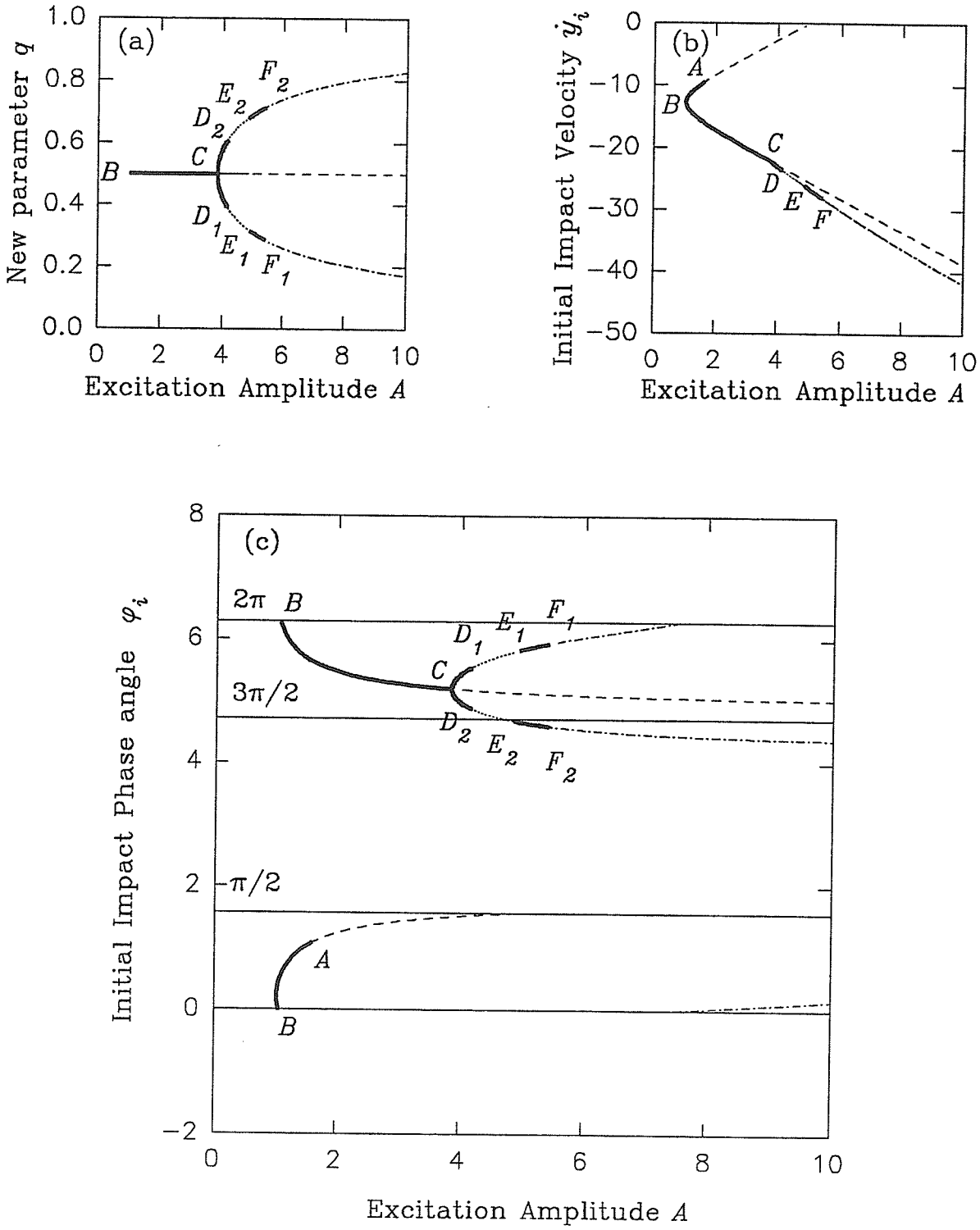

Figure 8.8 Stability and bifurcation of the Model I motion, left-side starting (—— stable node, ---- stable focus, — — 1st saddle, — - 2nd saddle).

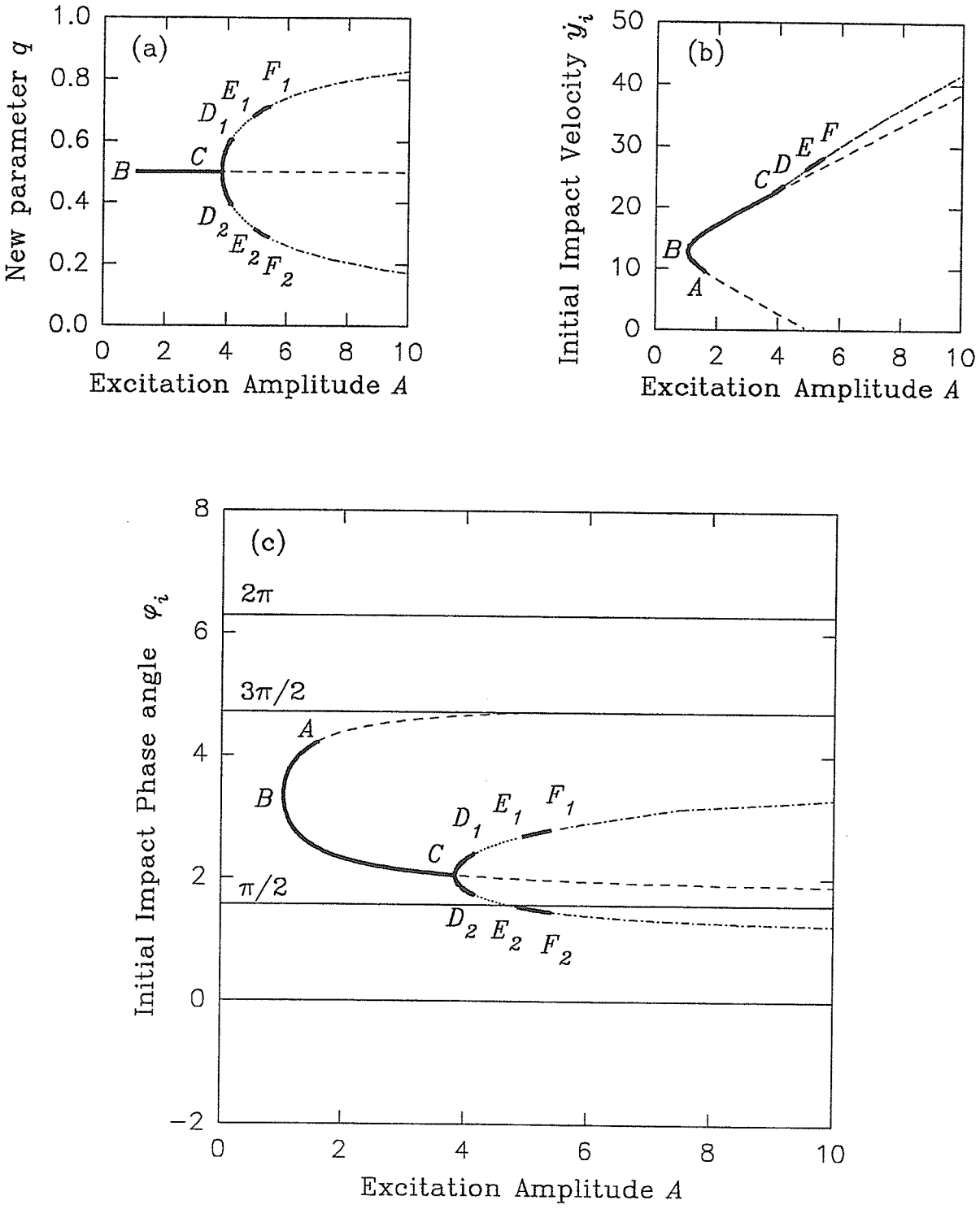

Figure 8.9 Stability and bifurcation of the Model I motion, right-side.starting (—— stable node, ---- stable focus, — — 1st saddle, — - 2nd saddle).

Note that *Figure* 8.8 depicts the motion starting on the left-side and *Figure* 8.9 for motion starting on the right-side. As shown in both figures, the curve ABC represents the stable period-1 equispaced motion, and the points A and C are its saddle-node bifurcation. The dash lines starting at A and C denote the unstable motion pertaining to the saddle of the first kind for equispaced motion.

Observe from graph (a) of the two figures, we have equispaced motion (i.e. q=0.5) for curve BC and non-equispaced motion once past the bifurcation point C. That is, the period-1 non-equispaced motion are represented by the two branches $CD_1E_1F_1$ and $CD_2E_2F_2$. Therefore, it can be seen that equispaced impacts become non-equispaced after bifurcation at C.

From graph (b) of the two figures, the line DEF represents the merging of the two branches, namely, the points D_1, E_1, F_1 coincide with corresponding points D_2, E_2, F_2. Observe that *Figures* 8.8(b) and 8.9(b) are the mirror-image of each other about the horizontal axis.

From graph (c) of the two figures, we note that they are the same with the initial phase angle translated by π in *Figure* 8.9(c). Observe also that period-doubling bifurcations or more accurately, grazing bifurcations of the period-1 non-equispaced motion occurs at F_1 and F_2. The dot-dash lines denote the unstable motion pertaining to the saddle of the second kind.

8.4.2 *k*-impacts periodic motion for Models I-V

Results of the k-impacts periodic motion for all motion models are discussed here, with the exception of Model II motion since it does not exist. The Jacobian for each of the motion models is derived and using the method outlined in *Section* 7.3, the stability and bifurcation of the motion can be determined via numerical experimentations. However, due to the extremely large number of possible impact combinations, the problem very

rapidly becomes numerically very intensive. Therefore, we will only list the Jacobian of the linearized mappings for the motion models considered.

Model III motion

$$\left.\begin{aligned} DP &= DP_2 \cdot DP_4 \cdot DP_1 \cdot DP_3 \\ &\vdots \\ DP^{(k)} &= \underbrace{DP_2 \cdot DP_4 \cdot DP_1 \cdot DP_3 \cdots DP_2 \cdot DP_4 \cdot DP_1 \cdot DP_3}_{k \text{ terms}} \end{aligned}\right\}. \tag{8.84}$$

Model IV motion

$$\left.\begin{aligned} DP &= DP_2 \cdot DP_4 \cdot DP_1 \\ &\vdots \\ DP^{(k)} &= \underbrace{DP_2 \cdot DP_4 \cdot DP_1 \cdots DP_2 \cdot DP_4 \cdot DP_1}_{k \text{ terms}} \end{aligned}\right\}. \tag{8.85}$$

Model V motion

$$\left.\begin{aligned} DP &= DP_2 \cdot DP_4^{(n_L)} \cdot DP_1 \cdot DP_3^{(m_R)} \\ &\vdots \\ DP &= \underbrace{DP_2 \cdot DP_4^{(n_{L1})} \cdot DP_1 \cdot DP_3^{(m_{R1})} \cdots DP_2 \cdot DP_4^{(n_{Lk})} \cdot DP_1 \cdot DP_3^{(m_{Rk})}}_{k \text{ terms}} \end{aligned}\right\}. \tag{8.86}$$

8.5 Numerical Verifications

To verify the stability of the periodic motion and to observe the chaotic phenomena, numerical simulations in the form of displacement-time curves, phase planes, switch-planes and Poincare mapping sections are presented. To simulate the nature of the stability, the input parameters for the numerical experimentations are computed rather than prescribed. In particular, the excitation parameter A, initial impact velocity $\dot{y}_i$ and initial impact phase

angle φ_i are computed via appropriate analytical expressions for $\omega = \pi$, $e = 0.5$ and $d = 10.0$, by assuming the impact to start at the left side of the oscillator, i.e. $y_i = -d/2$. This information is summarized in *Table* 8.1.

Table 8.1 Computed input data for numerical simulations ($\omega = \pi$, $e = 0.5$, $d = 10.0$, $y_i = -d/2$ and $t_i = 0.0$).

Figure No.	A	$\dot{y}_i$	φ_i	q	Stability Status
Figure 8.10(a)	2.2620	-21.6127	4.5363	0.50	Stable node (+)*
Figure 8.10(b)	3.9140	-22.6736	5.3550	0.45	Stable Node (+)
Figure 8.10(c)	4.2860	-23.7000	5.5573	0.390	Stable Focus
Figure 8.10(d)	5.1900	-27.2962	5.8889	0.299	Stable Node (-)
Figure 8.11	8.2520	-36.7835	4.4228	0.80	Unstable 2nd Saddle (-)

* Equispaced motion

Note that due to the choice of the computed input parameters, the first four motions listed in *Table* 8.1 are stable. This is also evidently clear from the results of the numerical experimentations in *Figure* 8.10 which depicts the relative displacement-time and phase plane plots in the relative frame for the Model I motion. *Figure* 8.10(a) plots the simplest and the most studied case for the impact pairs, namely, the stable equispaced motion. As the forcing amplitude A is increased, the impact motion becomes nonequispaced and this is shown in *Figure* 8.10(b)-(d).

Further increase of A result in chaos and the relative displacement-time and the relative velocity-time plots are shown in *Figure* 8.11. For this situation, we have the second saddle of non-equispaced impacts of the Model I motion. To confirm that the motion is indeed chaotic, we have also presented its phase plane and the left-right switch plane Σ.

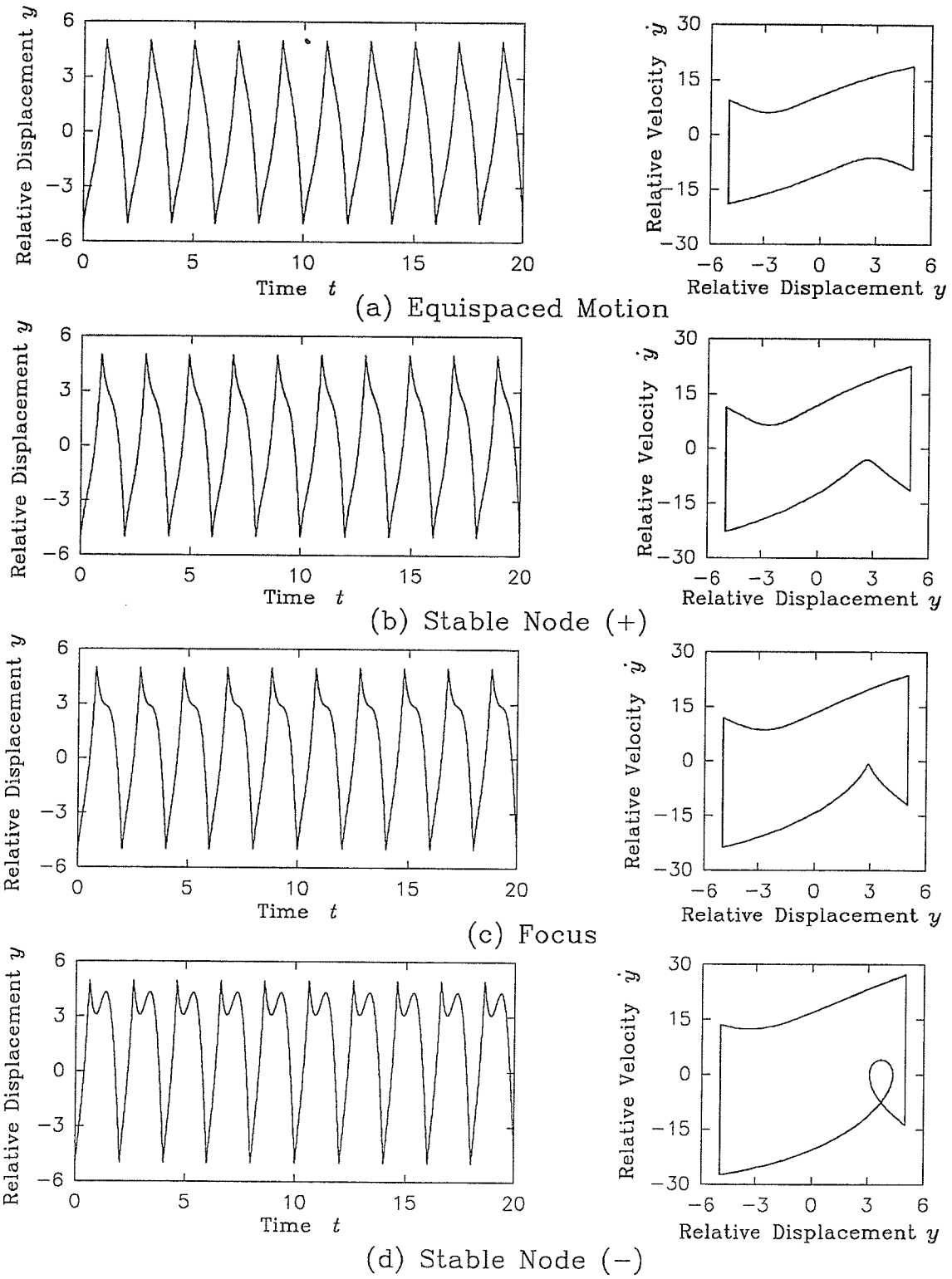

Figure 8.10 Period-1 solutions of the Model I motion for equispaced and non-equispaced impacts.

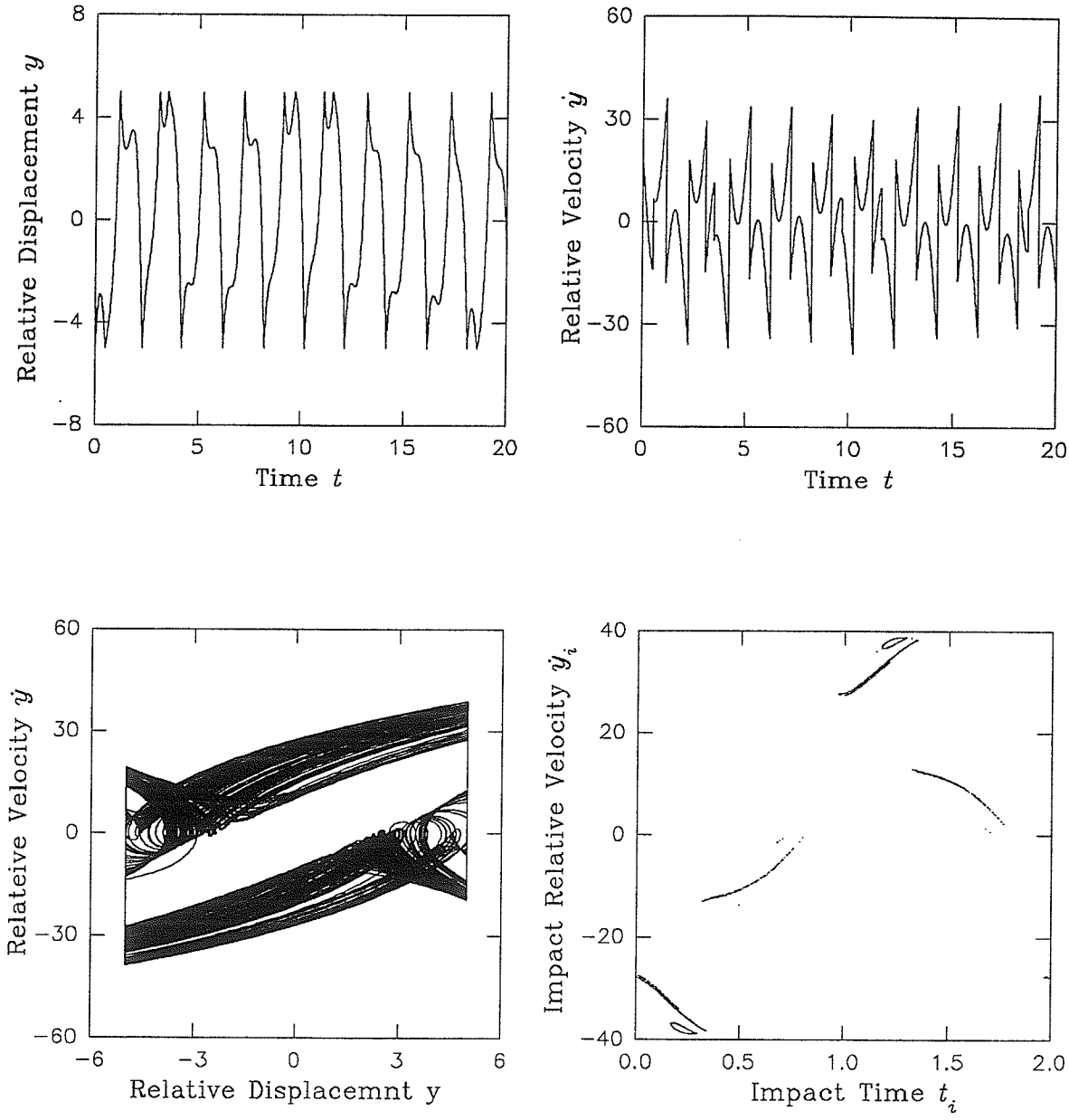

Figure 8.11 Chaotic Model I motion based on the 2nd saddle of non-equispaced impacts.

To get a feeling of the actual motion, we have also presented physical motion of the impact pair for all the cases listed in *Table* 8.1. This is given in the absolute displacement-time plots of *Figure* 8.12. The motion of the oscillator is denoted by the solid lines and the impact mass by the circles. Note that the first four plots (from the top) pertain to that of the stable motion and the last plot is that of the chaotic motion. Observe that there is no repeats in the chaotic motion.

8.6 Conclusions

A theory for a system with discontinuities as applied to the impact analysis of a horizontal impact pair is developed. Mappings for four switch planes are defined and from these, five impact motions; Model I, Model II, Model III, Model IV and Model V are derived. The simplest and most studied case, namely that of the equispaced impacts of the Model I motion, is scrutinized in detail. For this impact model, it is shown that period-doubling bifurcation cannot occur. Using computed instead of prescribed input parameters, numerical experimentations are performed and the analytically predicted stability is in excellent agreement with the numerically generated results. Both stable and unstable (chaotic) motions are generated. To get a sense of the impacts, plots of the physical motions are also provided.

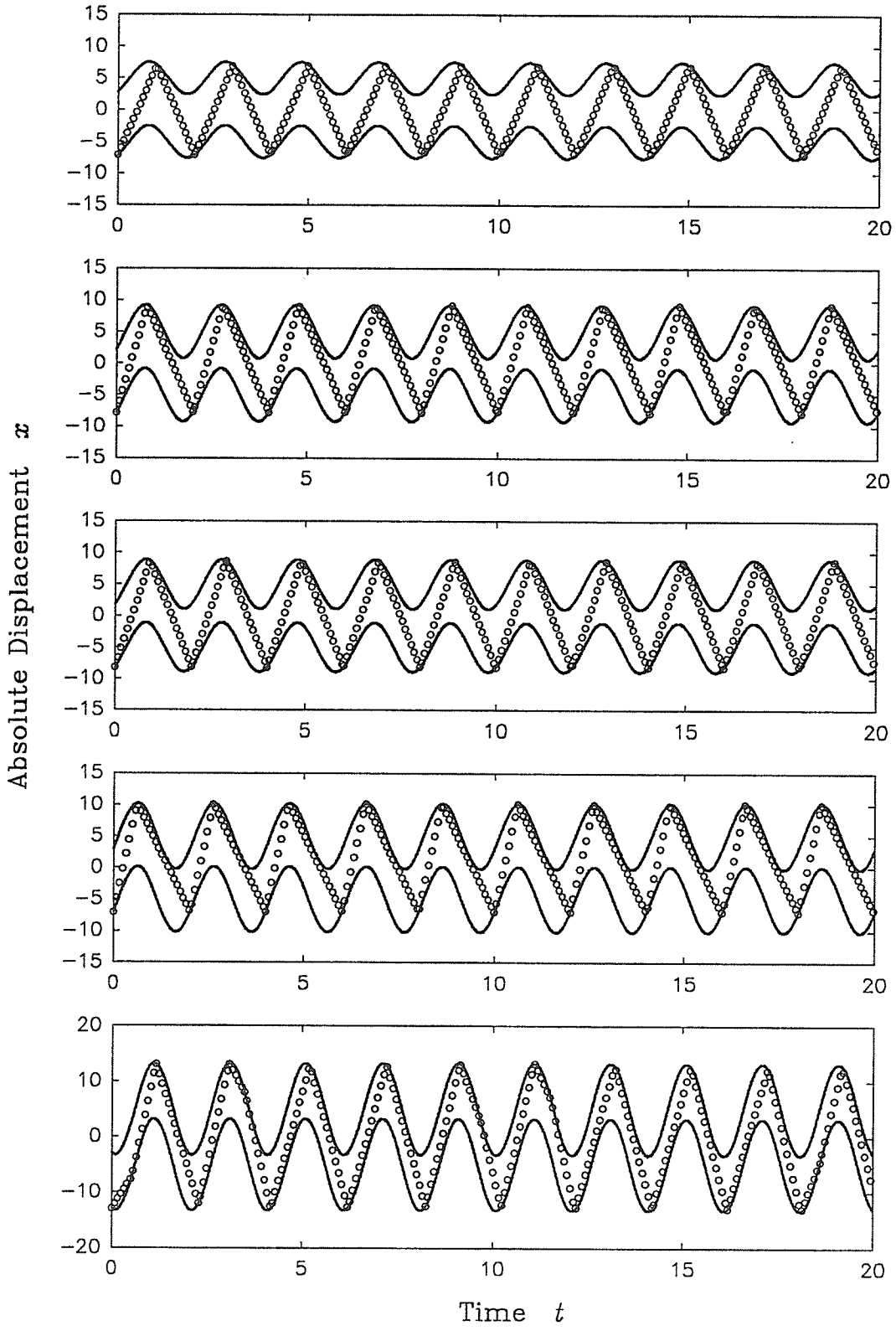

Figure 8.12 Physical motion for the stable and unstable Model I motion (∘ ∘ ∘ ball, —— wall).

PART III

MULTIFRACTALS IN CHAOTIC DYNAMICS

CHAPTER 9

PERIOD DOUBLING AND MULTIFRACTALS IN 1-D ITERATIVE MAPS

Consider the 1-D iterative map

$$x_{n+1} = f(x_n, \mu), \qquad n \in N; \tag{9.1}$$

where N is the natural number set. The nth iteration of $f(x_n)$ is denoted as

$$f^{(n)}(x, \mu) = f\left(f^{(n-1)}(x, \mu)\right), \qquad f^{(0)}(x, \mu) = x. \tag{9.2}$$

For 1-D discrete processes, it is the simplest nonlinear difference equation that has an extraordinary rich dynamical behavior, i.e. from stable point to chaos through cascades of stable cycles. Such a mathematical model has been extensively studied by several researchers. In particular, May (1976) gave an interesting account of this model for problems in the biological, economic and social sciences. The metric universality for this class of mapping is now a well-established phenomenon (Derrida, Gervois and Pomeau (1979)). Among the early investigators, Feigenbaum (1978, 1980a) studied the universal behavior of 1-D systems and quantitatively determined the universal numbers. These numbers present the threshold values from period doubling bifurcation to chaos. Nauenberg and Rudnick (1981) discussed the universality and the power spectrum at the onset of chaos for 1-D iterative maps. Collet, Eckman and Koch (1981) generalized the period doubling theory to higher dimensions. Zisook (1981) studied the universal effects of dissipation in the 2-D mapping. The computation of the universal rescaling factors for both 1 and 2-D maps has been carried to a very high precision by Hu and Mao (1985).

Halsey et al. (1986) provided fractal measures and their singularities, and applied them to characterize strange sets. They studied the fractal of the 2^{∞}-cycle of period doubling by choosing fractal scales $l_1 = 1/\alpha_{\mathrm{PD}}, l_2 = 1/\alpha_{\mathrm{PD}}^2$ where $\alpha_{\mathrm{PD}} = 2.502\ 907\ 875$ is the factor in the period doubling for the iterate map $x_{n+1} = \lambda x_n(1-x_n)$. They obtained the following dimensions:

$$D_0 = 0.537\cdots, \quad D_{-\infty} = \frac{\ln 2}{\ln \alpha_{\mathrm{PD}}} = 0.755\ 51\cdots, \quad D_{+\infty} = \frac{\ln 2}{2\ln \alpha_{\mathrm{PD}}} = 0.377\ 75\cdots, \quad (9.3)$$

where D_0 is the Hausdorff dimension and $D_{-\infty}, D_{+\infty}$ are the limit dimensions. A more accurate Hausdorff dimension was given by Rasband (1989):

$$D_0 = -\frac{\ln 2}{\ln\left[\frac{1}{2}\left(\frac{1}{\alpha_{\mathrm{PD}}} + \frac{1}{\alpha_{\mathrm{PD}}^2}\right)\right]} = 0.543\ 87\cdots, \quad (9.4)$$

In this chapter, a highly accurate method to compute the period doubling solutions of a general 1-D iterative map is presented. The technique consists of constructing similar structures of the period doubling solutions and then applying a renormalization procedure to evaluate the appropriate length scaling factors. For period-doubling solutions leading to chaos, this approach yields multifractal results of very high precision compared to the usual multifractal analysis alone. If the critical parameter associated with the Feigenbaum number is employed, the fractal characteristic parameters calculated will be exact. The stability status of the computed solutions can also be easily determined. An example is solved to demonstrate and to assess the accuracy of the procedure.

9.1 Similar Structures in Period Doubling

Consider a dynamical system represented by a family of 1-D maps of one parameter and which passed through a sequence of period doubling to chaos

$$x_{n+1} = f(x_n, \mu), \quad (9.5)$$

where μ is the parameter. The fixed point x^* can be easily determined from *Equation* (9.5) by setting $x_{n+1} = x_n$. If

$$\frac{dx_{n+1}}{dx_n} = \left.\frac{df}{dx_n}\right|_{x_n = x^*} = -1, \tag{9.6}$$

then this fixed point is the critical point of bifurcation. Suppose this solution of *Equation* (9.5) satisfies the condition under which it exists, i.e., $x_{A_0^0} \le x_{n+1} \le x_{A_1^0}$, we can find the minimum value μ_0^* at the onset of the fixed point. The maximum value of μ prior to the first bifurcation is μ_1^* and thus, stable solution of *Equation* (9.5) can be easily determined for $\mu \in [\mu_0^*, \mu_1^*]$. For $\mu > \mu_1^*$, *Equation* (9.5) exists period-2 bifurcations,

$$x_{n+2} = f^{(2)}(x_n, \mu). \tag{9.7}$$

If *Equation* (9.7) has a critical condition of bifurcation at $x_{n+2} = x_n$, similar to *Equation* (9.6), i.e.,

$$\frac{dx_{n+2}}{dx_n} = \left.\frac{df^{(2)}(x_n, \mu)}{dx_n}\right|_{x_n = x^*} = \left.\frac{dx_{n+2}}{dx_{n+1}}\frac{dx_{n+1}}{dx_n}\right|_{x_n = x^*} = -1, \tag{9.8}$$

then the critical parameter for the bifurcation of *Equation* (9.7) is μ_2^*. In a similar fashion, the stable solutions are evaluated at $\mu \in [\mu_1^*, \mu_2^*]$. The period-2 bifurcation of *Equation* (9.5) for $\mu > \mu_2^*$ is given by

$$x_{n+4} = f^{(4)}(x_n, \mu). \tag{9.9}$$

In general, this process can be represented by

$$x_{n+2^m} = f^{(2^m)}(x_n, \mu). \tag{9.10}$$

To analyze this process, we consider the various graphs for the period doubling bifurcation as depicted in *Figure* 9.1(a)-(d). It is clear from the squares in the plot there

exist similar structures in period doubling, in the iterative map *Equation* (9.5). From the x-axis of the plot, we can extract the similar structures and these results are summarized in *Figure* 9.2. Note that it is easier to compute the parameters μ, μ_1, μ_2 etc. via a renormalization group method rather than using numerical techniques. From the similar structure construction in *Figure* 9.2, *Equation* (9.7) can be renormalized by rescaling its map. That is, move the origin to the fixed point in *Equation* (9.5), by letting $\bar{z} = x - x^*$, and $z = a\bar{z}$, where a is the scaling factor of renormalization. *Equation* (9.7) then becomes

$$z_{n+1} = f(z_n, \mu_1), \tag{9.11}$$

where the new parameter μ_1 is given by the function

$$\mu_1 = g(\mu). \tag{9.12}$$

Equation (9.11) is similar to *Equation* (9.5). If it generates period doubling bifurcation, we get

$$\mu_2 = g(\mu_1) = g(g(\mu)), \tag{9.13}$$

and after m-cycle period doubling bifurcations, we have

$$\mu_m = g(\mu_{m-1}) = g^{(m)}(\mu). \tag{9.14}$$

If $\mu_m = \mu_{n-1} = \mu_\infty$, the period-doubling process approaches chaos. For $\mu_m < \mu_\infty$, the iterative map, $x_{n+1} = f(x_n, \mu)$, will have m-cycles period doubling bifurcations. The period doubling length scaling factors are defined as follows:

$$I^i_{s_i} = \left| z^*_{i-1} - z_{A_{s_0 s_1 \cdots s_l}} \right|, \quad I^i = \left| z^*_i - z_{A_{s_0 s_1 \cdots s_l}} \right|; \tag{9.15}$$

in which the index $i \in \{1,2,\cdots,m\}$ refers to the ith bifurcation of the iterative map and $s_i \in \{0,1\}$. The terms z^*_{i-1}, $z_{A_{s_0 s_1 \cdots s_l}}$ are computed respectively from:

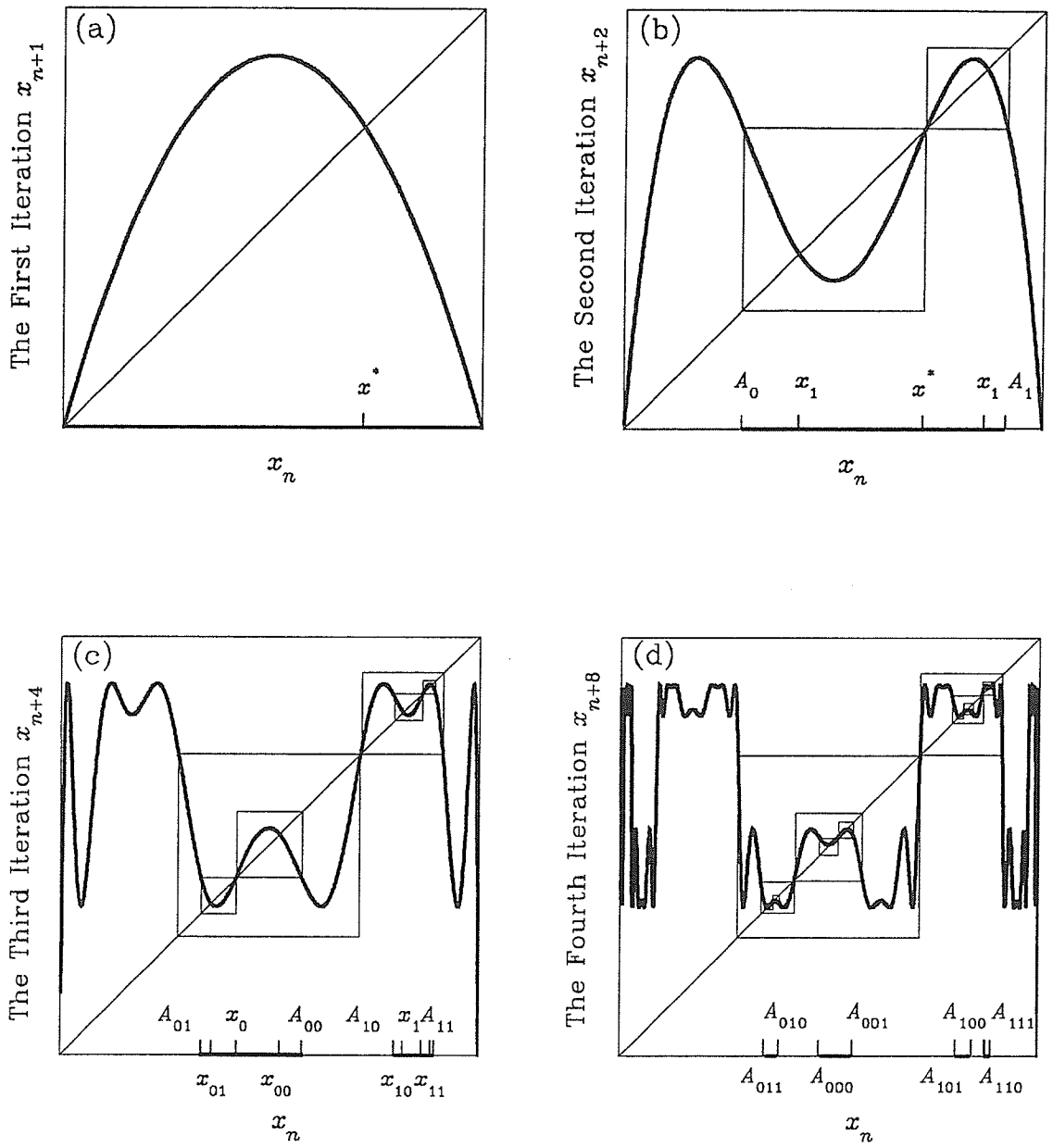

Figure 9.1 Iterative map $x_{n+1} = f(x_n, \mu)$

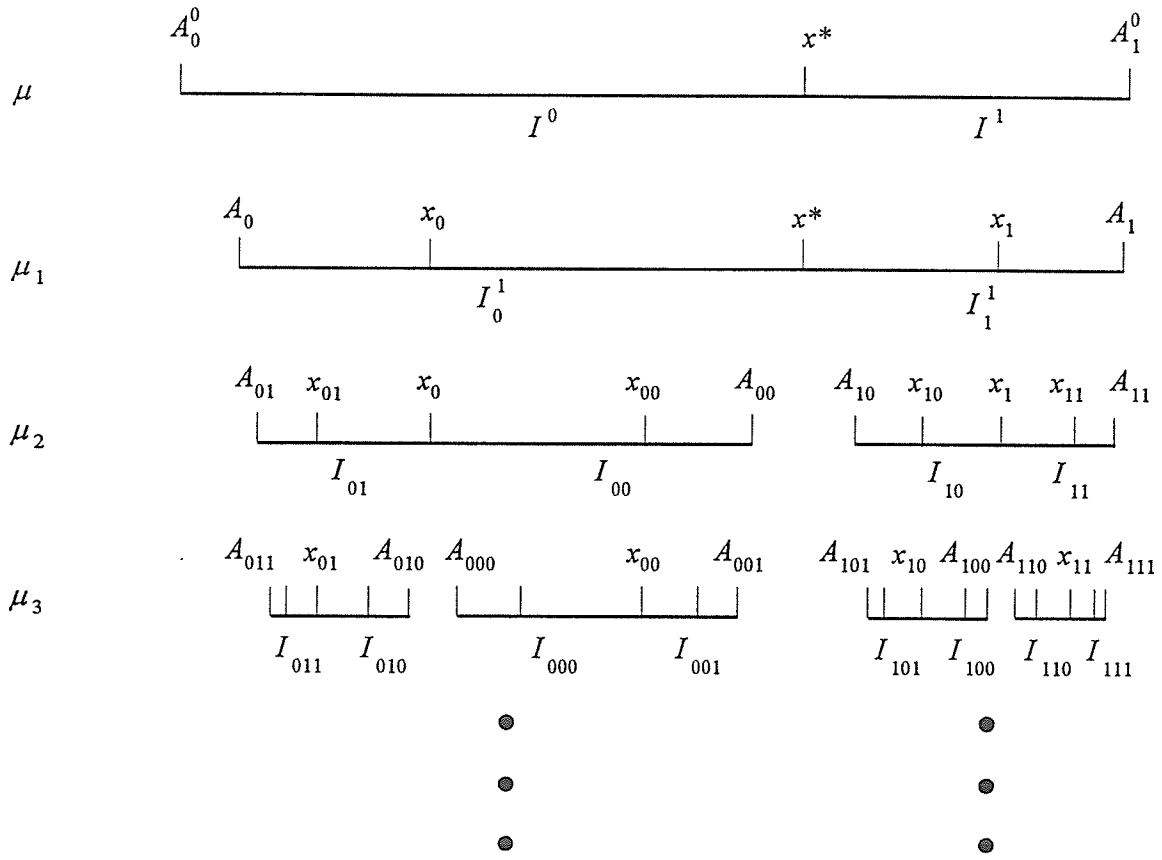

Figure 9.2 Period doubling construction of the 1-D iterative map $x_{n+1} = f(x_n, \mu)$

$$z_{i-1}^* = f\left(z_{i-1}^*, \mu_{i-1}\right), \quad z_{i-1}^* = f^{(2)}\left(z_{i-1}, \mu_{i-1}\right). \tag{9.16}$$

Note that in determining $z_{A_{s_0 s_1 \cdots s_i}}$, only two of its three nonzero z_{i-1} which results in minimum $\left|z_{i-1}^* - z_{i-1}\right|$ are selected. In particular, the length scaling factors of the *first* period doubling bifurcation are given by

$$I_0^1 = x^* - x_{A_0}, \quad I_1^1 = x_{A_1} - x^*, \quad I^0 = x^* - x_{A_0^0}; \tag{9.17}$$

where as shown in *Figure* 9.2, x_{A_0} and x_{A_1} can be calculated from

$$x^* = f^{(2)}(x, \mu). \tag{9.18}$$

In general, for the *m*th-cycle period-doubling bifurcations, the associated length scaling factor of the similar structure is defined as

$$I_{s_1 s_2 \cdots s_m} = I_{s_1 s_2 \cdots s_{m-1}} I_{s_m}^m = \prod_{i=1}^{m} I_{s_i}^i . \tag{9.19}$$

The solution of the period doubling for the iterative map *Equation* (9.5) is given by

$$x_{s_1 s_2 \cdots s_m} = x_{s_1 s_2 \cdots s_{m-1}} + (-1)^{\left(m - \sum_{i=1}^{m} s_i\right)} I_{s_1 s_2 \cdots s_m} I^m, \tag{9.20}$$

where $x_{s_0} = x^*$ is its fixed point. *Equation* (9.20) may also be expressed as

$$x_{s_1 s_2 \cdots s_m} = x^* + \sum_{i=1}^{m} (-1)^{\left(i - \sum_{j=1}^{i} s_j\right)} I_{s_1 s_2 \cdots s_i} I^i , \tag{9.21}$$

or more compactly by

$$x_{s_1 s_2 \cdots s_m} = x^* + \sum_{i=1}^{m} (-1)^{\left(i - \sum_{j=1}^{i} s_j\right)} \prod_{j=1}^{i} I_{s_j}^j I^i . \tag{9.22}$$

Since *Equation* (9.22) gives all the solutions of the *m*th-cycle period doubling bifurcation of the iterative map, it is clear that of these *m*th-solutions, only the *m*th solutions, namely, $x_{s_1 s_2 \cdots s_m}$, are stable at *m*th cycle period doubling bifurcation. All other solutions up to the (*m*-1)-cycle period doubling bifurcation, i.e., x_{s_1}, $x_{s_1 s_2}$, $\cdots$, $x_{s_1 s_2 \cdots s_{m-1}}$, are unstable. The usefulness of this analytical form of the result which is currently unavailable in literature is that, it can be employed to check the numerically-computed solutions. In view of these stable and unstable results, the chaotic solutions of the period doubling bifurcation of the iterative map can be conveniently summarized as follows

$$x_{s_1 s_2 \cdots s_m} = x_{s_1 s_2 \cdots s_{m-1}} + (-1)^{(m-k)} \left(I_1^1\right)^k \left(I_0^1\right)^{(m-k)} I^0, \tag{9.23}$$

in which k is the total number of $s_i = 1$, $i \in \{1,2,3,\cdots,m\}$ as $m \to \infty$. Note that the length scaling factors $I_1^1 = I_1^i, I_0^1 = I_0^i$ and $I^i = I^0$ remain constant as shown. Alternatively, one could also express this equation as

$$x_{s_1 s_2 \cdots s_m} = x^* + \sum_{i=1}^{m} (-1)^{(i-k)} \left(I_1^1\right)^k \left(I_0^1\right)^{(i-k)} I^i, \tag{9.24}$$

where k now, is the number of $s_j = 1$, $j \in \{1,2,3,\cdots,i\}$ for every i, as $m \to \infty$. It should also be mentioned that this similar structure analysis can be just as easily studied by means of the symbolic dynamics approach.

9.2 Fractality of Chaos via Period Doubling Bifurcation

For the period doubling bifurcations of 1-D iterative map leading to chaos, the fractal is a multifractal as shown in *Figure* 9.2. From *Equation* (9.14), μ_m is constant at chaos, i.e., $\mu_m = \mu_\infty$, and the similar structure of iterative map will become the self-similar structure. Thus

$$I_{s_i}^i = I_{s_1}^1 = I_{s_1}, \quad i \in N, \quad s_i \in \{0,1\}. \tag{9.25}$$

The chaotic fractal scalings of period doubling are constant, i.e.,

$$l_1 = I_0, \quad l_2 = I_1. \tag{9.26}$$

From Halsey et al (1986) the multifractal partition sum function is

$$\Gamma = \sum_{i=1}^{n} \frac{p_i^q}{l_i^\tau} = 1, \tag{9.27}$$

where for the two-scale fractal, n=2, τ is a weight parameter and $p_i = 1/2$ is the action probability. For the same action in period-2 bifurcation similar structure, we have:

$$\frac{2^{-q}}{I_0^{\tau}}+\frac{2^{-q}}{I_1^{\tau}}=1. \tag{9.28}$$

The weight parameter is

$$\tau(q)=\frac{\ln\left[1+\left(I_0/I_1\right)^{\tau}\right]-q\ln 2}{\ln I_0}. \tag{9.29}$$

Since $\tau(q)=(q-1)D_q$, the generalized fractal dimension D_q becomes

$$D_q=\frac{\ln\left(1+\left(I_1/I_0\right)^{(q-1)D_q}\right)-q\ln 2}{(q-1)\ln I_0}. \tag{9.30}$$

Several special cases of the generalized fractal dimensions are given as follows. The Hausdorff dimension is

$$D_0=-\frac{\ln\left(1+\left(I_1/I_0\right)^{D_0}\right)}{\ln I_0}. \tag{9.31}$$

The information dimension is

$$D_1=-\frac{2\ln 2}{\ln I_0+\ln I_1}. \tag{9.32}$$

The two limit dimensions are

$$D_{-\infty}=-\frac{\ln 2}{\ln I_0},\qquad D_{+\infty}=-\frac{\ln 2}{\ln I_1}. \tag{9.33}$$

The scaling index is

$$\alpha=\frac{d\tau(q)}{dq}=\frac{-\ln 2\left[1+\left(I_1/I_0\right)^{\tau}\right]}{\left(I_1/I_0\right)^{\tau}\ln I_0+\ln I_1}. \tag{9.34}$$

The singular fractal spectrum function is

$$f(\alpha)=\alpha q-\tau(q). \tag{9.35}$$

For the correlation dimension D_2, we have

$$D_2 = 2\alpha(q) - f(\alpha(q))\big|_{q=2}. \tag{9.36}$$

The characteristic parameters of the multifractal can be determined using *Equations* (9.29)-(9.36). Note that these relationships are not quite the same as those given in Halsey et al. (1986) and Cosenza et al. (1989). Since the fractal is constructed from the similar structure of the period doubling solutions of the iterative map, the scaling factors derived here are based on a more meaningful approach. As shown in an example, the results obtained here are more accurate than the previously published solutions.

9.3 An Example

In order to explain the similar structure approach for computing the solutions of the iterative map at periodic doubling, the following example is considered:

$$x_{n+1} = \mu x_n(1 - x_n). \tag{9.37}$$

Renormalizing the *i*th-period doubling bifurcation equation of *Equation* (9.37) yields,

$$x^i_{n+1} = \mu_i x^i_n\left(1 - x^i_n\right), \tag{9.38}$$

where the parameter relation is given by

$$\mu_i = \mu^2_{i-1} - 2\mu_{i-1} - 2. \tag{9.39}$$

9.3.1 Period doubling solutions

Let $\mu = 3.5$ and from *Equation* (9.39), the renormalized parameter $\mu_1 = 3.25$. Since $\mu_1 > 3$ which is the threshold value (as determined by *Equation* (9.6)), the new iterative map of *Equation* (9.37) will also exhibit period doubling bifurcations. Invoking *Equation*

(9.39) once again but this time for $\mu_1 = 3.25$, yields the renormalized parameter associated with the period-2 doubling bifurcation $\mu_2 = 2.06$. However, since $\mu_2 < 3$, this map will not exhibit period doubling bifurcations, and thus for this case, its solutions are stable. The first fixed point of the iterative map, *Equation* (9.37), is $x^* = 1 - 1/\mu$ and its period doubling factor are

$$\left.\begin{aligned} I^i &= z_i^* = 1 - \frac{1}{\mu_i} \\ z^i_{A_{s_i s_2 s_{i-1} 0}} &= \frac{1}{\mu_{i-1}}, \qquad z^i_{A_{s_i s_2 s_{i-1} 0}} = \frac{\mu_{i-1} + \sqrt{\mu_{i-1}^2 - 4}}{2\mu_{i-1}}, \\ I_0^i &= 1 - \frac{2}{\mu_{i-1}}, \qquad I_0^i = \frac{2 - \mu_{i-1} + \sqrt{\mu_{i-1}^2 - 4}}{2\mu_{i-1}}. \end{aligned}\right\} \tag{9.40}$$

For $\mu = 3.5$, the solution of *Equation* (9.37) are

$$\left.\begin{aligned} x^* &= 1 - 1/\mu \\ x_0 &= x^* - I_0^1 I^1, \quad x_1 = x^* + I_1^1 I^1 \\ x_{01} = x_0 - I_0^1 I_1^2 I^2, &\quad x_{01} = x_0 + I_0^1 I_0^2 I^2, \quad x_{10} = x_1 - I_1^1 I_0^2 I^2, \quad x_{10} = x_1 - I_1^1 I_1^2 I^2. \end{aligned}\right\} \tag{9.41}$$

According to the above analysis, the solutions of iterative map x^*, x_0 and x_1 are unstable at $\mu = 3.5$ but the period-2 bifurcation solutions x_{01}, x_{00}, x_{10}, x_{11} are stable. These results are tabulated in *Table* 9.1. For the purpose of comparison, the exact period-1 bifurcation solutions of *Equation* (9.37) which are computed using

$$x_0 = \frac{1 + \mu - \sqrt{\mu^2 - 2\mu - 3}}{2\mu}, \qquad x_1 = \frac{1 + \mu + \sqrt{\mu^2 - 2\mu - 3}}{2\mu}; \tag{9.42}$$

are also listed. As shown in *Table* 9.1, the similar structure technique for computing the

Table 9.1 Solution of *Equation* (9.37) at $\mu = 3.5$

Sampling Point	Doubling Time	Stability Status	Similar Structure Solution	Exact Result	Relative Error
x^*	0	unstable	0.714 285 143	0.714 285 143	0.00%
x_0	1	unstable	0.417 582 417	0.428 571 428	2.56%
x_1	1	unstable	0.850 005 845	0.857 142 857	0.83%
x_{01}	2	stable	0.373 027 890	-	-
x_{00}	2	stable	0.502 497 502	-	-
x_{10}	2	stable	0.811 163 383	-	-
x_{11}	2	stable	0.870 386 293	-	-

period doubling solutions for the 1-D iterative map yields excellent agreement with the exact solutions. If the period doubling solutions are chaotic at $\mu = \mu_\infty$, this structure will be a similar structure, and its solutions can be determined from *Equation* (9.24). Note that the scaling factors of period doubling for these solutions are constant. *Figure* 9.3 lists the period doubling solutions of the iterative map at $\mu = \mu_\infty = 3.569\ 945\ 6$ in a binary tree format.

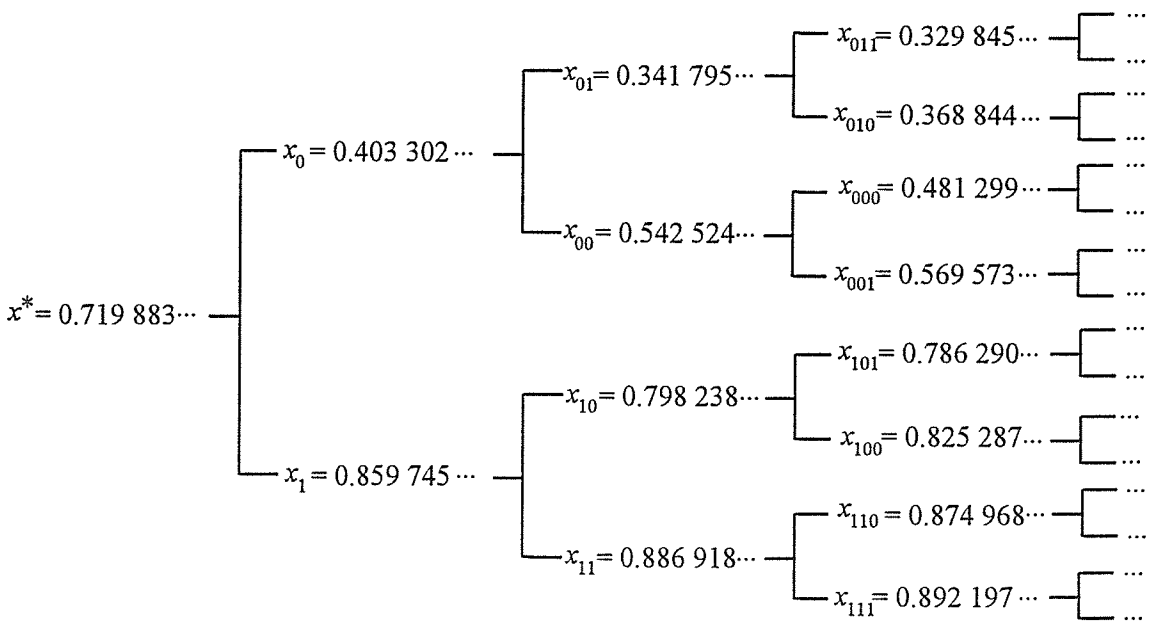

Figure 9.3 Binary tree for the chaotic solution at $\mu = \mu_\infty = 3.569\ 945\ 6 \cdots$.

9.3.2 Fractality

Taking $\mu_i = \mu_{i-1}$ in *Equation* (9.39), the critical chaos parameter of the period doubling solutions can be calculated to yield, $\mu = \mu_\infty = 3.561\ 552\ 8\cdots$ and the length scaling factors are:

$$I_0 = I_0^1 = 0.438\ 447\ 185\cdots,\ I_1 = I_1^1 = 0.194496\ 855\cdots,\ I_1/I_0 = 0.433\ 603\ 840\cdots. \quad (9.43)$$

Substituting these length scaling factors into *Equations* (9.31)-(9.33), several of the generalized fractal dimensions can be computed and the results are listed in the *Table* 9.2. To assess the accuracy of these results obtained through renormalization, the length scaling factors associated with the critical parameter of the chaos $\mu_\infty = 3.569\ 945\ 6$ are evaluated as follows

$$I_0 = I_0^1 = 0.439\ 767\ 373\cdots,\ I_1 = I_1^1 = 0.194\ 283\ 973\cdots,\ I_1/I_0 = 0.441\ 788\ 057\cdots. \quad (9.44)$$

Table 9.2 Comparison of the computed generalized fractal dimension D_q

D_q	Renormalization Results	Exact Solution	Halsey et al. (1986) Cosenza et al. (1989)	Rasband (1989)
D_0	0.585 286 432	0.586 670 729	0.537	0.543 87
D_1	0.563 109 625	0.563 547 168	-	-
$D_{-\infty}$	0.840 671 676	0.843 748 337	0.755 51	-
$D_{+\infty}$	0.423 337 537	0.423 054 580	0.377 75	-

These length scaling factors are exact and when substituted into *Equations* (9.31)-(9.33), yield the exact results of the generalized fractal dimensions. Observe that the solutions calculated via the renormalization technique agree very well with exact results. For the purpose of comparison, some of the available solutions of other researchers are also tabulated in *Table* 9.2. As shown, the results of Rasband (1989) are not only slightly larger than those of Halsey et al. (1986) and Cosenza et al. (1989), but also more

and this can be attributed to the rather crude approximations employed in these models.

The discussion here refers to the plots presented in the next four figures, namely, *Figures* 9.4-9.7. It will be of interest to compare the weight parameter function $\tau(q)$ given in *Equation* (9.29), using the two different sets of length scaling factors. This is shown in *Figure* 9.4. The generalized fractal dimension D_q is sketched in *Figure* 9.5, the scaling index $\alpha(q)$ in *Figure* 9.6 and the fractal spectrum function in *Figure* 9.7. In all cases, excellent agreement between the renormalized and exact solutions and those of Halsey et al. (1986) marked by the dash line are observed. Additionally, in *Figure* 9.7, we have provided an independent comparison in the form of the experimental results of Glazier et al. (1986) which are denoted by solid circles. Observe that our analytical solutions agree particularly well with the experimental results.

9.4 Conclusions

Through the construction of similar structures, a new method for the analysis of period doubling bifurcations in 1-D iterative maps is suggested. An example was solved to demonstrate and assess the accuracy of the procedure. The weight parameter function, several generalized fractal dimensions, the scaling index and the fractal spectrum functions are derived. Comparison with published solutions and that obatined via physical experiments showed that the proposed procedure yields very accurate results. In this sense, the method represents a significant improvement over the currently available techniques.

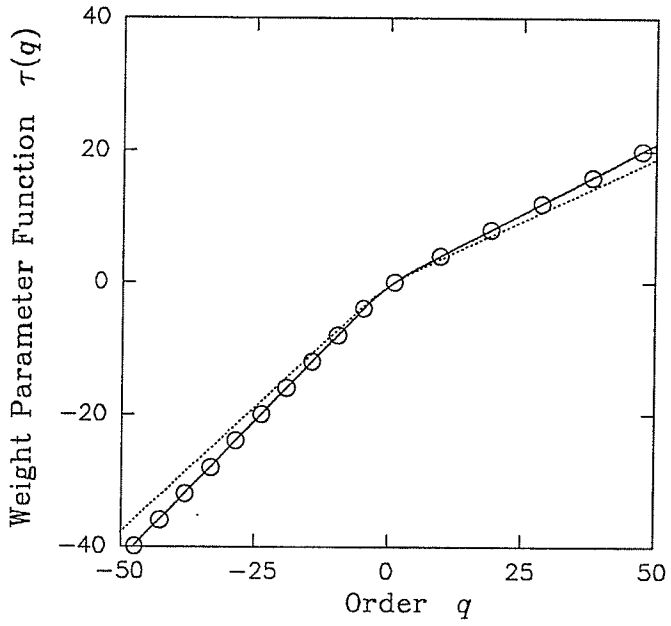

Figure 9.4 Weight parameter function τ_q for the iterative map of *Equation* (9.37) (—— exact solutions, ∘ ∘ ∘ renormalization solutions, ---- Halsey et al. (1986)).

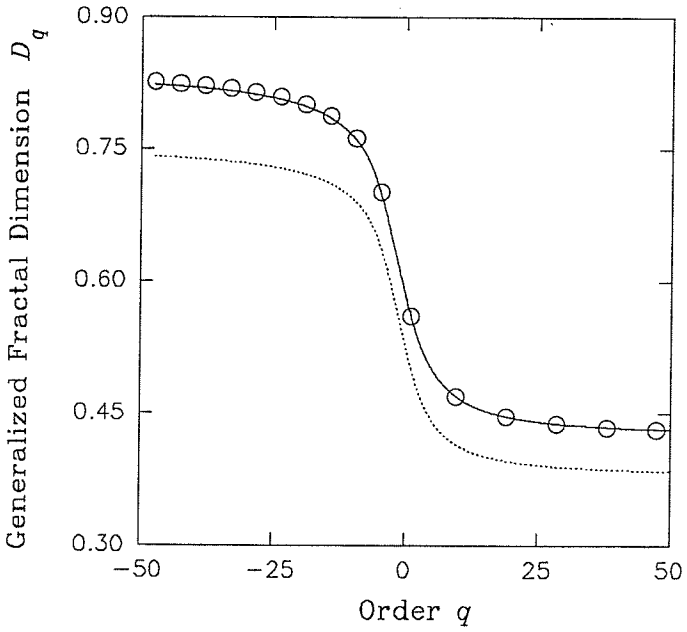

Figure 9.5 Generalized fractal dimensions D_q for the iterative map of *Equation* (9.37) (—— exact solutions, ∘ ∘ ∘ renormalization solutions, ---- Halsey et al. (1986)).

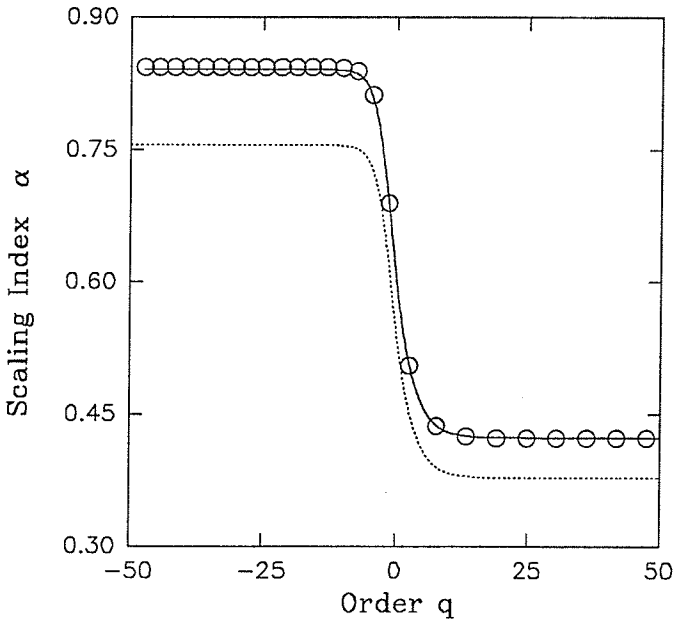

Figure 9.6 Scaling index $\alpha(q)$ for the iterative map of *Equation* (9.37)) (—— exact solutions, ∘ ∘ ∘ renormalization solutions, ---- Halsey et al. (1986).

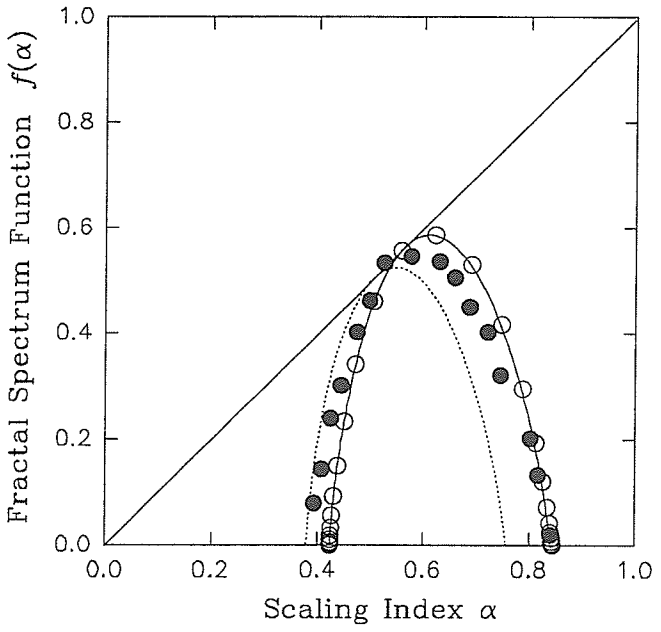

Figure 9.7 Fractal spectrum function $f(\alpha)$ for the iterative map of *Equation* (9.37) —— exact solutions, ∘ ∘ ∘ renormalization solutions, ---- Halsey et al. (1986), ● ● ● experimental results (Glazier et al. 1986)).

CHAPTER 10

MULTIFRACTALS IN CHAOTIC DYNAMICS VIA *m*-D HORSESHOE MAPS

In *Chapter* 9, we discussed the fractality of the chaotic attractor in 1-D iterative maps via period-doubling bifurcations. This chapter introduces multifractals in chaotic dynamics via *m*-D horseshoe maps. In chaotic dynamics, various methods are used for characterizing the complexity of chaos, such as Poincare mapping sections, power spectrum analysis, Lyapunov exponent and generalized Hausdorff dimension, statistical thermodynamic approach and ergodic theory, etc. (Renyi (1971), Ott (1981), Eckman and Ruelle (1985), Rasband (1989) and Shigmatsa (1990)). Fractal theory was formally introduced by Mandelbrot (1977). A detailed introduction to multifractals in dynamical systems was presented by McCauley (1990). Other studies involving the application of fractals in nonlinear dynamics include Grebogi, Ott and Yorke (1988), Bene and Szepfalusy (1988), Szepfalusy and Tel (1989), Romeiras, Grebogi and Ott (1990), Kovacs and Tel (1992), and Luo and Han (1992a). Our main work here is concerned with the development of a new fractal theory based on the *m*-D horseshoe maps and its application to hyperbolic invariant sets in chaotic dynamics.

10.1 A New Multifractal Theory in *n*-D Euclidean Space

In this section, a new theory for describing multifractals of the hyperbolic invariant sets is established.

10.1.1 Fractals

Mandelbrot (1977) presented the following definition of a 1-D fractal

$$Nr^D = 1, \tag{10.1}$$

by considering a 1-D nonfractal segment of unit interval which is divided into M parts, with each part having a scaling ratio of $r = 1/M$, and repeating this process ad infinitum for N non-empty parts (or non-tremas) yields a fractal. For further details, the reader is referred to *Appendix* A.3. The exponent D is called the Hausdorff dimension (or more accurately, Hausdorff-Besicovitch dimension) and is given from *Equation* (10.1) as,

$$D = \frac{\log N}{\log M} = -\frac{\log N}{\log r}, \tag{10.2}$$

where log(·) is natural logarithms. Extending the 1-D fractal concept to a 2-D Euclidean fractal body, we consider a nonfractal body of unit square which is divided into M parts in two directions: M_h and M_v pieces respectively in the *horizontal* and *vertical* directions. We assumed that $M = M_h \times M_v$ and their scaling ratios are $r_h = 1/M_h$ and $r_v = 1/M_v$. Assuming $N = N_h \times N_v$ non-empty parts and repeating the process ad infinitum, the 2-D fractal object shown in *Figure* 10.1 is realized. From *Equation* (10.1) and assuming that the fractals in each of the directions are generated independently, we get,

$$N_h N_v r_h^{D_h} r_v^{D_v} = 1. \tag{10.3}$$

Note that for each of the directions, $N_h r_h^{D_h} = 1$ and $N_v r_v^{D_v} = 1$ and this leads to

$$\left.\begin{aligned} D_h &= \frac{\log N_h}{\log M_h} = -\frac{\log N_h}{\log r_h}, \\ D_v &= \frac{\log N_v}{\log M_v} = -\frac{\log N_v}{\log r_v}. \end{aligned}\right\} \tag{10.4}$$

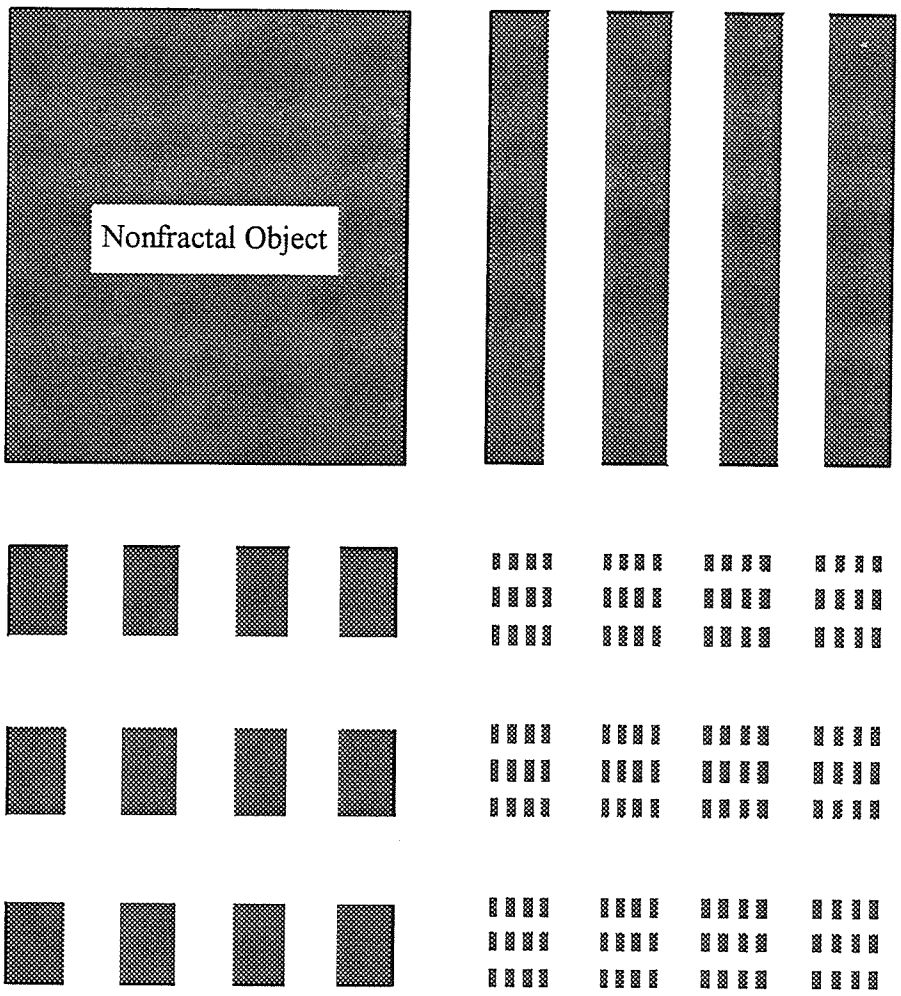

Figure 10.1 2-D fractal object.

Thus the fractal dimension of the 2-D fractal object is

$$D = D_h + D_v. \tag{10.5}$$

Generalizing the concept to handle the computation of the m-D fractal dimension of an m-D fractal body where $m \le n$, we conclude as follows.

Dividing an n-D unit nonfractal geometric object into M sub-objects in the m-D Euclidean space leads to $M = \prod_{i=1}^{m} M_i$, where we have the scaling ratio $r_i = 1/M_i$.. If

there are N nonempty sub-objects corresponding to the m-D Euclidean space, then we have $N = \prod_{i=1}^{m} N_i$. Assuming the fractals in each of the directions are generated independently, we have,

$$\left.\begin{aligned} N_i r_i^{D_i} &= 1, \\ D_i &= \frac{\log N_i}{\log M_i} = -\frac{\log N_i}{\log r_i}. \end{aligned}\right\} \tag{10.6}$$

The fractal dimension of the n-D objects is

$$D = (n-m) + \sum_{i=1}^{m} D_i. \tag{10.7}$$

To demonstrate and verify the suggested procedure, we will compute the fractal dimension of the triadic Koch surface depicted in *Figure* 10.2. From *Figure* 10.2(a), we have $n = 2, m = 1, N_1 = 4, M_1 = 3$ (or alternatively, $n = m = 2, N_1 = 4, M_1 = 3, N_2 = M_2$). From *Equations* (10.6)-(10.7) we get $D_1 = \log 4/\log 3$ and $D_2 = 1$ and thus, the fractal dimension of the triadic Koch surface is

$$D = 1 + \frac{\log 4}{\log 3} = 2.2618595\cdots. \tag{10.8}$$

Note that this fractal dimension is identical to that obtained using the traditional approach.

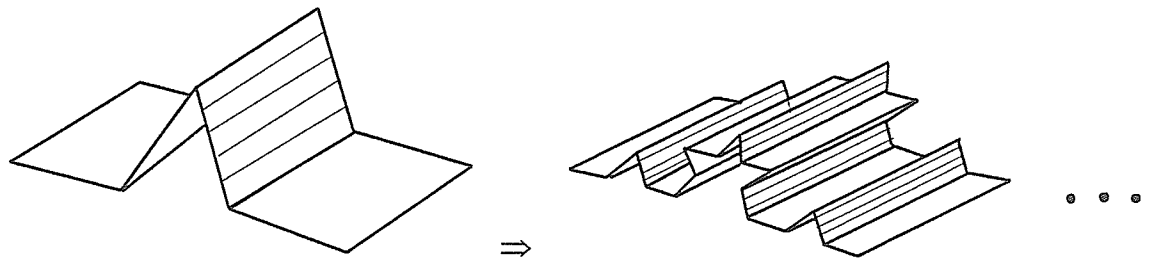

Figure 10.2 Triadic Koch surface

10.1.2 A Model for Multifractals

The formalism developed up to now, is valid only for uniform fractals. To extend the method to handle *m*-D *nonuniform* fractals (or simply, multifractals) in the *n*-D Euclidean space, we modify the models of Halsey et. al. (1986) and Leung and Luo (1992). We consider that there are N_i sub-objects having n_i scales in the *i*th direction, and the *j*th-scale has a measured length r_{ij}, scale probability weight p_{ij} and scale number n_{ij}. The multifractal partition function is given by,

$$\Gamma_i(\tau_i, q) = \sum_{j=1}^{n_i} n_{ij} \frac{p_{ij}^q}{l_{ij}^{\tau_i}} = 1, \tag{10.9}$$

where $\tau_i(q)$ is defined by introducing the following weight parameter for multifractals in the *i*th direction:

$$\tau_i(q) = (q-1)D_i(q), \tag{10.10}$$

and the partition function behaves as,

$$\Gamma_i(\tau_i, q) = \begin{cases} 0 & \text{at } \tau_i < \tau_i(q), \\ \infty & \text{at } \tau_i > \tau_i(q), \\ \text{constant} & \text{at } \tau_i = \tau_i(q). \end{cases} \tag{10.11}$$

Furthermore, from thermodynamics consideration, the scaling index in the *i*th direction is

$$\alpha_i = \frac{d\tau_i}{dq}, \tag{10.12}$$

and applying the Legendre transform yields,

$$\tau_i(q) = \alpha_i q - f_i(\alpha_i), \tag{10.13}$$

in which the $f_i(\alpha_i)$ is a fractal spectrum in the *i*th direction given by,

$$\frac{df_i}{d\alpha_i} = q; \tag{10.14}$$

Summarizing the results for all the directions, we arrive at the following equations for the m-D multifractal theory in n-D Euclidean space:

$$\tau(q) = (n-m)(q-1) + \sum_{i=1}^{m} \tau_i(q), \tag{10.15}$$

$$\alpha = \sum_{i=1}^{m} \alpha_i, \tag{10.16}$$

$$f(\alpha) = \sum_{i=1}^{m} f(\alpha_i). \tag{10.17}$$

10.2 Fractals Generated by a 1-D Horseshoe Iterative Map

In this section, fractals generated by a 1-D horseshoe iterative map in chaotic dynamics is studied. Luo and Han (1992a) analyzed the fractality of chaos caused by period doubling bifurcations for 1-D iterative maps. Tel and his co-workers (1989, 1992) studied the fractality of fully developed chaos. Beyond the fully developed chaos of 1-D iterative maps, we have the chaotic state produced by 1-D horseshoe maps, and it is proposed to discuss its fractality. Initially, we will look at the fractality of chaos generated by a uniform 1-D iterative map and then, we will investigate the multifractals produced by a nonuniform 1-D iterative map.

10.2.1 Fractals in a uniform 1-D Cantor-horseshoe

Consider a 1-D iterative map that possesses a uniform horseshoe structure, namely, a uniform cantor structure in the phase space $x_{n+1} = f(x_n, \mu)$ where $n \in N$ and μ is a

control parameter. Note that N expresses a natural number set. Consider for instance, the tent map f in the unit interval $I=[0,\ 1]$ given by,

$$f:\ \begin{cases} x_{n+1}=\mu x_n & \text{for } x_n \le \dfrac{1}{2}, \\ x_{n+1}=\mu(1-x_n) & \text{for } x_n \ge \dfrac{1}{2}. \end{cases} \tag{10.18}$$

where $\mu \ge 2$. The phase graph and fractal structure are procreated using *Equation* (10.18) for unit interval I as shown in *Figure* 10.3. The two sub-intervals, I_0 and I_1 in *Figure* 10.3(a) are obtained from the first iteration of *Equation* (10.18) with $x_{n+1} \le 1$. That is, $I_0 = I_1 = 1/\mu$. Therefore, for the first iteration of *Equation* (10.18), its invariant set is

$$f(I) = I_0 \cup I_1. \tag{10.19}$$

Similarly for the second iteration, we have $f^{(2)}(I)=\bigcup I_{\sigma_1\sigma_2}$, and $\sigma_i \in\{0,1\}$ for $i\in\{1,2\}$. Repeating this iteration ad infinitum leads to its invariant set as follows,

$$\Lambda=\bigcap_{n=0}^{\infty} f^{(n)}(I), \tag{10.20}$$

where $f^{(n)}(I)=\bigcup_{n} I_{\sigma_1\sigma_2\cdots\sigma_n}$, and $\sigma_i \in\{1,2\}$ for $i\in\{1,2,\cdots,n\}$. For any value n, the scale ratio and the number of the non-empty interval are

$$\left.\begin{aligned} r &= \left|I_{\sigma_1\sigma_2\cdots\sigma_n}\right| = \frac{1}{\mu^n}, \\ N &= 2^n. \end{aligned}\right\} \tag{10.21}$$

The Hausdorff dimension of the invariant set shown in *Equation* (10.20) is

$$D_0 = \lim_{n\to\infty}\frac{\log N}{\log r} = \frac{\log 2}{\log \mu}. \tag{10.22}$$

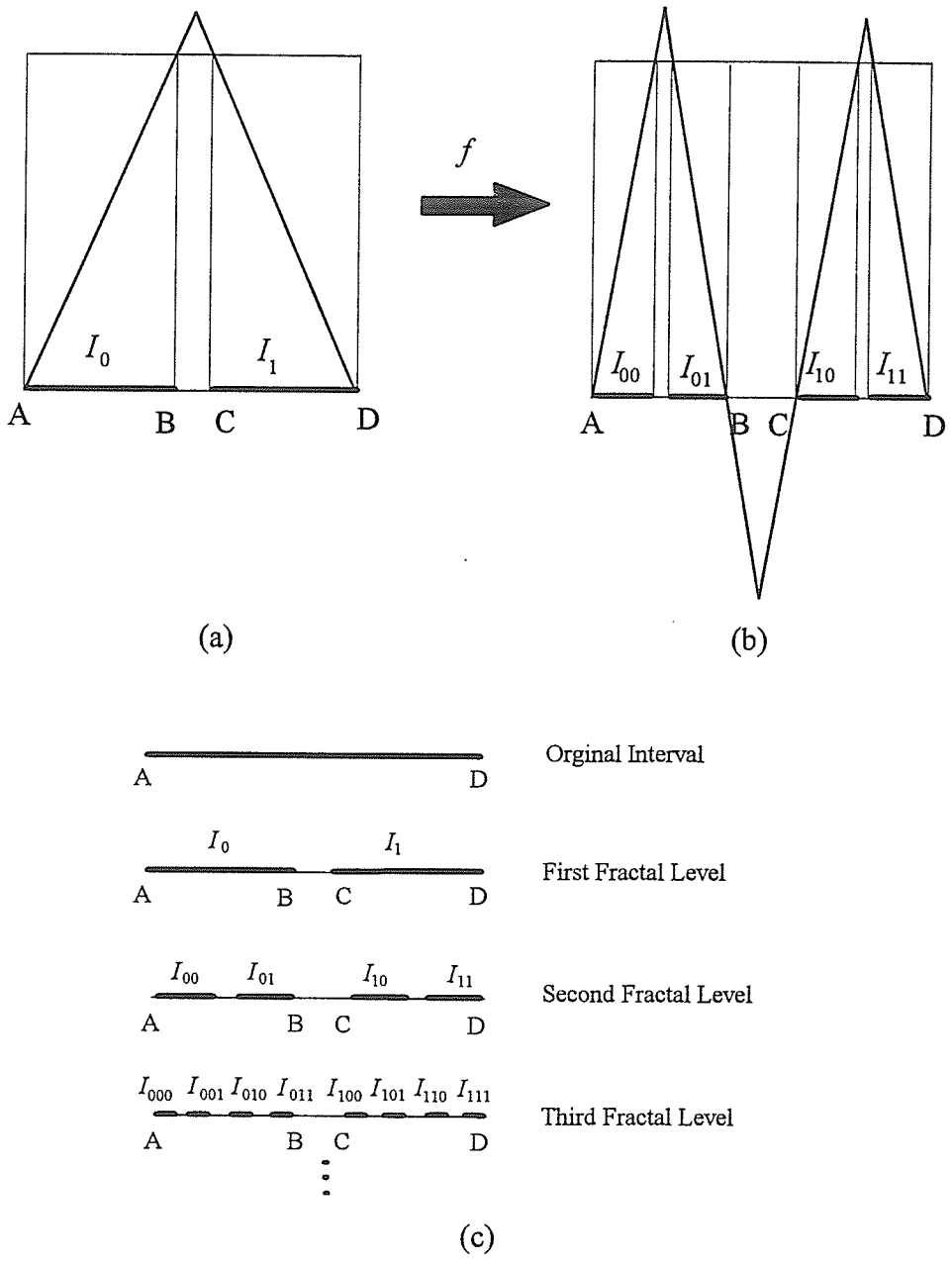

Figure 10.3 Phase graphs and fractal structures generated via *Equation* (10.18).

10.2.2 Fractals in a nonuniform 1-D Cantor-horseshoe

Consider a 1-D iterative map to have the multiscale Cantor-horseshoe structure, for instance, an asymmetric tent map as follows,

$$f:\begin{cases} x_{n+1}=\mu_1 x_n & \text{for } x_n \le \dfrac{\mu_2}{\mu_1+\mu_2}, \\ x_{n+1}=\mu_2(1-x_n) & \text{for } x_n \ge \dfrac{\mu_2}{\mu_1+\mu_2}. \end{cases} \tag{10.23}$$

where the control parameters μ_1, μ_2 satisfy $\mu_1\mu_2 \ge (\mu_1+\mu_2)$. *Figure* 10.4 shows the phase graph and fractal structure procreated using *Equation* (10.23). Observe that due to the nonuniform structure, we now have a two-scale multifractal. Therefore, after the first iteration of *Equation* (10.23) on the original interval $I=[0,1]$, i.e., $f(I)=I_0 \cup I_1$; we find that the lengths of two new sub-intervals are not identical, namely, $r_1=|I_0|=1/\mu_1$, $r_2=|I_1|=1/\mu_2$. Repeating this iterative process ad infinitum results in an invariant set,

$$\Lambda=\bigcap_{n=0}^{\infty} f^{(n)}(I). \tag{10.24}$$

where $f^{(n)}(I)=\bigcup_n I_{\sigma_1\sigma_2\cdots\sigma_n}$, and $\sigma_i \in \{1,2\}$ for $i \in \{1,2,\cdots,n\}$. From the iteration process, the probability of appearance for the two scales is

$$p_0=p_1=\frac{1}{2}. \tag{10.25}$$

Applying *Equation* (10.9), a partition function for the horseshoe invariant set of *Equation* (10.23) can be computed from

$$\Gamma=\left(\frac{\mu_1^{\tau}}{2^q}+\frac{\mu_2^{\tau}}{2^q}\right)^n=1, \tag{10.26}$$

from which, we get

$$q=\frac{\log\left(\mu_1^{\tau}+\mu_2^{\tau}\right)}{\log 2}. \tag{10.27}$$

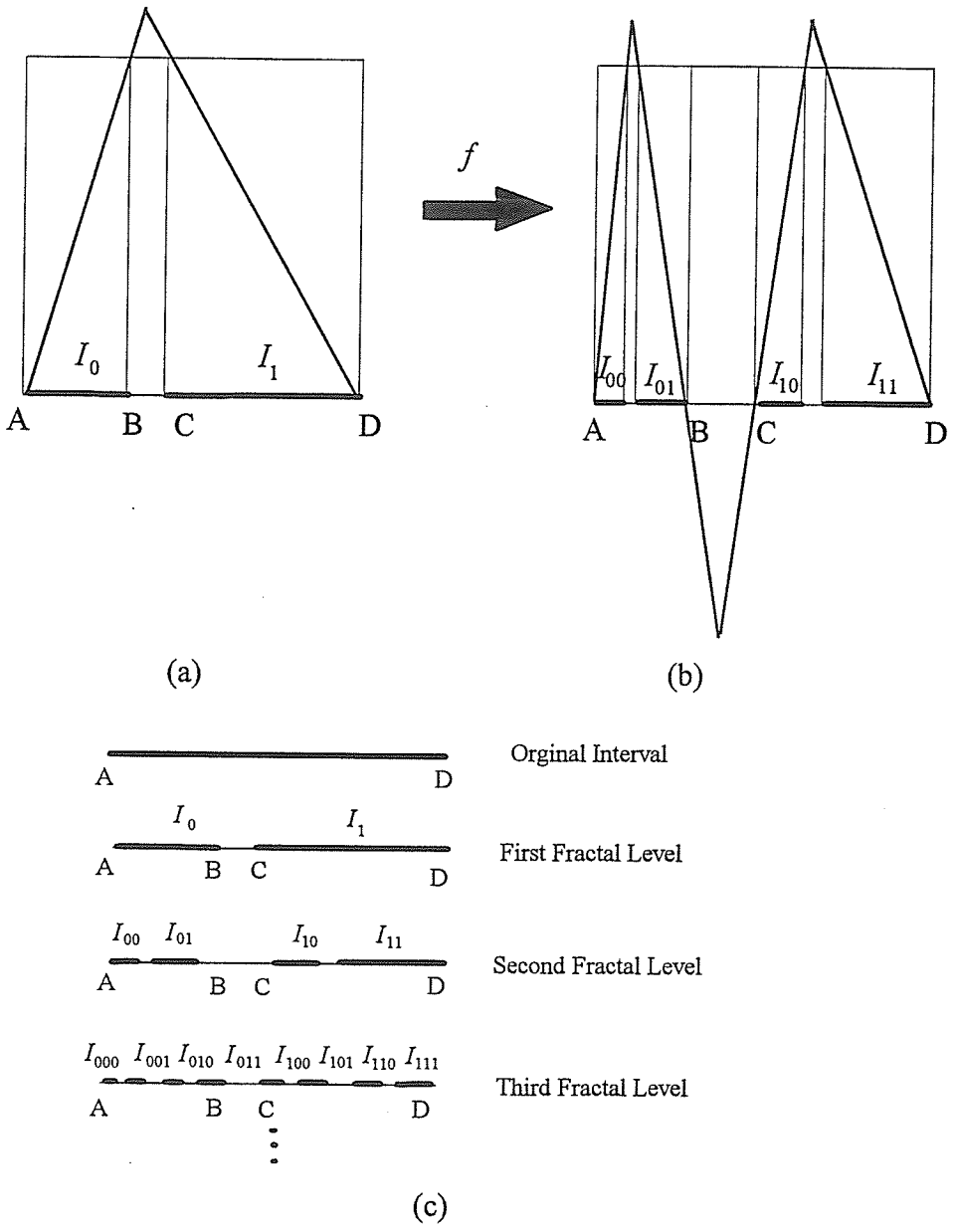

Figure 10.4 Phase graphs and fractal structures generated via *Equation* (10.23).

From *Equations* (10.10)-(10.13) and (10.26), the fractal dimension, scaling index and fractal spectrum are given respectively by:

$$D_q = \frac{\tau \log 2}{\log\left(\mu_1^\tau + \mu_2^\tau\right) - \log 2}, \tag{10.28}$$

$$\alpha = \frac{\left(\mu_1^\tau + \mu_1^\tau\right)\log 2}{\mu_1^\tau \log \mu_1 + \mu_2^\tau \log \mu_2}, \tag{10.29}$$

$$f(\alpha) = \alpha q - \tau(q). \tag{10.30}$$

Imposing $\mu_1 \le \mu_2$ in *Equations* (10.28)-(10.30), we get the following specific fractal dimensions,

$$D_1 = \alpha, \quad D_{-\infty} = \frac{\log 2}{\log \mu_1}, \quad D_\infty = \frac{\log 2}{\log \mu_2}, \tag{10.31}$$

and the Hausdorff dimension D_0 is determined using

$$\mu_1^{-D_0} + \mu_2^{-D_0} = 1. \tag{10.32}$$

Fractal characteristics of the nonuniform 1-D Cantor-horseshoe set are plotted in *Figure* 10.5. The following line notations are employed in the graph:

- solid line for $\mu_1 = 2,\ \mu_2 = 3$,
- dash line for $\mu_1 = 2,\ \mu_2 = 4$,
- dash-dot line for $\mu_1 = 3,\ \mu_2 = 4$.

Figure 10.5(a) shows the weight parameter τ versus the order of moment, q, *Figure* 10.5(b) the fractal dimension D_q versus q, *Figure* 10.5(c) the scaling index α versus q, and finally, *Figure* 10.5(d) the fractal spectrum $f(\alpha)$ versus α. Unlike *Figure* 9.7 where our theoretical solutions have been compared with those of physical experiments, here we can only provide theoretically computed limiting values such as the Hausdorff dimension, since experimental results are unavailable. From *Figure* 10.5(d), we see that the Hausdorff dimension $D_0 \approx 0.788,\ 0.674,\ 0.556$ for the three combinations of μ_1, μ_2. These values can also be directly computed from *Equation* (10.32), using a nonlinear solver.

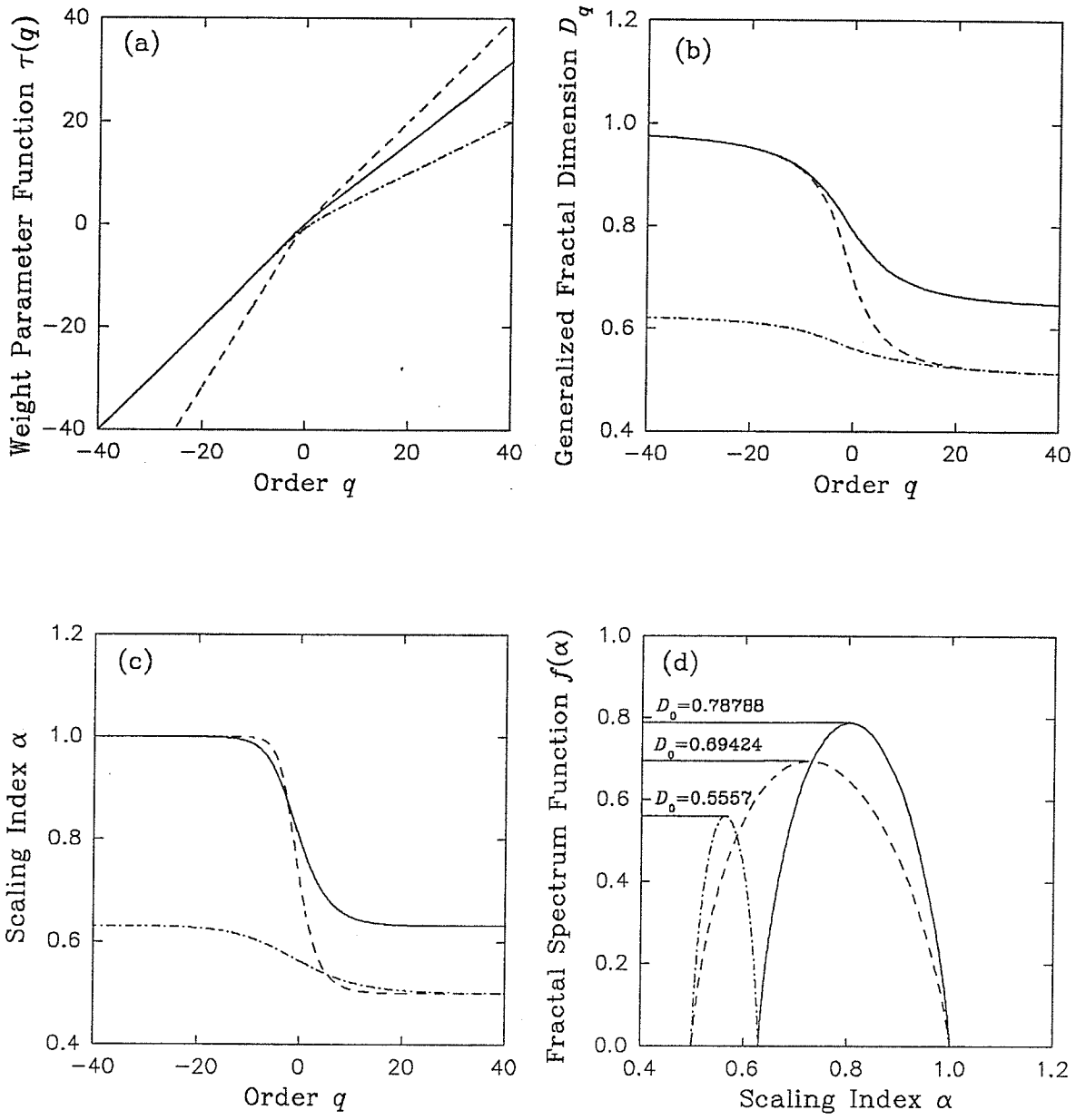

Figure 10.5 Fractal characteristics of the 1-D nonuniform Cantor set.

10.3 Fractals of the 2-D Horseshoe

In this section, we introduce 2-D fractals based on the Smale horseshoe map. As before, we will first consider fractals of the uniform horseshoe set, and then fractals of the nonuniform horseshoe set.

10.3.1 A uniform Smale horseshoe

The Smale horseshoe arising from the transversely homoclinic orbits via the Poincare map is very important essential for describing the dynamics in the neighborhood of the saddle. To analyze the fractality of this 2-D invariant set, we consider the original 2-D unit square $\boldsymbol{D}=\{(x,y)\in R^2 \mid 0\le x\le 1,\ 0\le y\le 1\}$ and define a mapping $f:\boldsymbol{D}\to R^2$. Therefore, we get (Wiggin (1988)),

$$f:\begin{cases}\begin{pmatrix}x_{n+1}\\ y_{n+1}\end{pmatrix}=\begin{pmatrix}\lambda & 0\\ 0 & \mu\end{pmatrix}\begin{pmatrix}x_n\\ y_n\end{pmatrix} & \text{on } H_0,\\ \begin{pmatrix}x_{n+1}\\ y_{n+1}\end{pmatrix}=\begin{pmatrix}-\lambda & 0\\ 0 & -\mu\end{pmatrix}\begin{pmatrix}x_n\\ y_n\end{pmatrix}+\begin{pmatrix}1\\ \mu\end{pmatrix} & \text{on } H_1.\end{cases} \tag{10.33}$$

where $0<\lambda\le 1/2,\ \mu\ge 2$. From *Equation* (10.33), we can define two rectangles in the horizontal direction:

$$\left.\begin{aligned}H_0&=\{(x,y)\in R^2 \mid 0\le x\le 1,\ 0\le y\le 1/\mu\},\\ H_1&=\{(x,y)\in R^2 \mid 0\le x\le 1,\ 1-1/\mu\le y\le 1\}.\end{aligned}\right\} \tag{10.34}$$

Applying f to these two horizontal rectangles produces two vertical rectangles. That is,

$$\left.\begin{aligned}f(H_0)\equiv V_0&=\{(x,y)\in R^2 \mid 0\le x\le \lambda,\ 0\le y\le 1\},\\ f(H_1)\equiv V_1&=\{(x,y)\in R^2 \mid 1-\lambda\le x\le 1,\ 0\le y\le 1\}.\end{aligned}\right\} \tag{10.35}$$

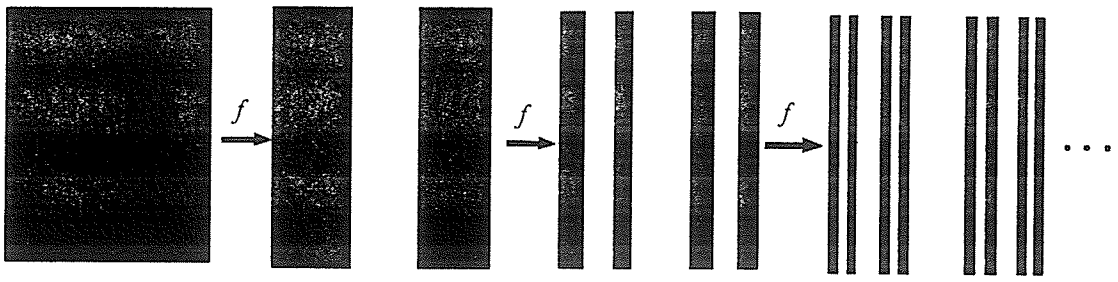

Figure 10.6 Vertical invariant set procreated via *Equation* (10.33).

To construct the Smale horseshoe that intersects between a vertical invariant set and a horizontal invariant set, we first apply f ad infinitum to the unit square S, namely,

$$\begin{aligned}\Lambda_V &= \bigcap_{n=1}^{\infty} f^{(n)}(\boldsymbol{D}) = \bigcup_{\substack{s_{-i}\in S \\ i=1,2,\cdots}} \left(f\left(V_{s_{-2}\cdots s_{-k}\cdots}\right)\cap V_{s_{-1}}\right) = \bigcup_{\substack{s_{-i}\in S \\ i=1,2,\cdots}} V_{s_{-1}\cdots s_{-k}\cdots} \\ &= \left\{p=(x,y)\in \boldsymbol{D}\middle| f^{(-i+1)}(p)\in V_{s_{-i}}, s_{-i}\in S, i=1,2,\cdots\right\},\end{aligned} \tag{10.36}$$

where $S=\{0,1\}$. This results in the vertical invariant set as shown in *Figure* 10.6. Note that the fractal has a scaling ratio $r_x = \lambda$ and its Hausdorff dimension can be computed by

$$D_{0x} = -\frac{\log 2}{\log \lambda}. \tag{10.37}$$

Since the vertical invariant set does not have fractals in the y-direction, $D_{0y}=1$. Therefore, the resultant Hausdorff dimension for the vertical invariant set is

$$D = D_{0x} + D_{0y} = 1 - \frac{\log 2}{\log \lambda}. \tag{10.38}$$

Note that *Equation* (10.38) is identical with the expression obtained by Guckenheimer and Holmes (1983) using a different approach.

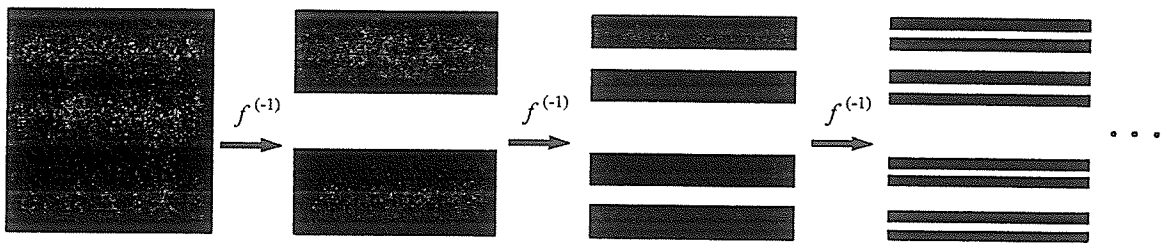

Figure 10.7 Horizontal invariant set procreated via an inverse map of *Equation* (10.33).

In a similar manner, the horizontal invariant set can be reprocreated via the inverse map $f^{(-1)}$ acting on the unit square S, that is,

$$\begin{aligned}\Lambda_H &= \bigcap_{n=1}^{\infty} f^{(-n)}(\boldsymbol{D}) = \bigcup_{\substack{s_{-i}\in S \\ i=1,2,\cdots}} \left(f\left(H_{s_1\cdots s_k\cdots}\right)\cap H_{s_0}\right) = \bigcup_{\substack{s_{-i}\in S \\ i=1,2,\cdots}} H_{s_0\cdots s_k\cdots} \\ &= \left\{p=(x,y)\in \boldsymbol{D}\middle| f^{(i)}(p)\in H_{s_i}, s_i \in S, i=0,1,2,\cdots\right\}.\end{aligned} \tag{10.39}$$

The result is sketched in *Figure* 10.7 where its scaling ratio $r_y = 1/\mu$. The fractal of the horizontal invariant set in the y-direction has a Hausdorff dimension of,

$$D_{0y} = \frac{\log 2}{\log \mu}. \tag{10.40}$$

The resultant Hausdorff dimension of the horizontal invariant set is thus given by,

$$D_0 = 1 + \frac{\log 2}{\log \mu}. \tag{10.41}$$

The intersection of the vertical and the horizontal invariant sets yields the Smale horseshoe which is shown in *Figure* 10.8. That is, we have:

$$\Lambda = \Lambda_V \cap \Lambda_H = \bigcap_{n=-\infty}^{\infty} f^{(n)}(\boldsymbol{D}). \tag{10.42}$$

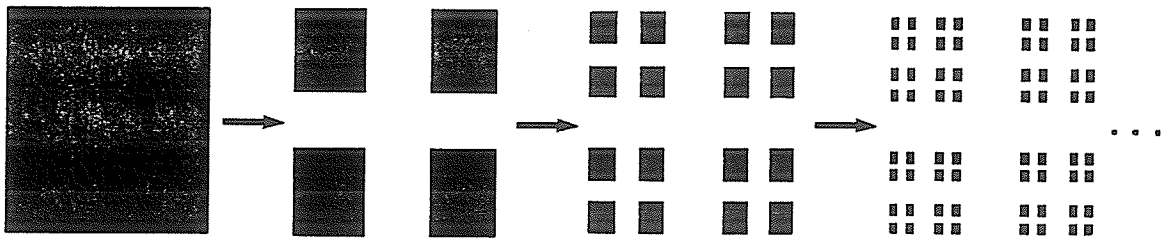

Figure 10.8 Smale horseshoe generated by iteration of *Equation* (10.33).

The Hausdorff dimension of the Smale horseshoe procreated via ad infinitum n iterations of the 2-D map f on the unit square S is:

$$D = D_{0x} + D_{0y} = \log 2\left(\frac{1}{\log \mu} - \frac{1}{\log \lambda}\right). \tag{10.43}$$

Figure 10.9(a)-(c) shows respectively the Hausdorff dimensions for the vertical and horizontal invariant sets, and the Smale horseshoe.

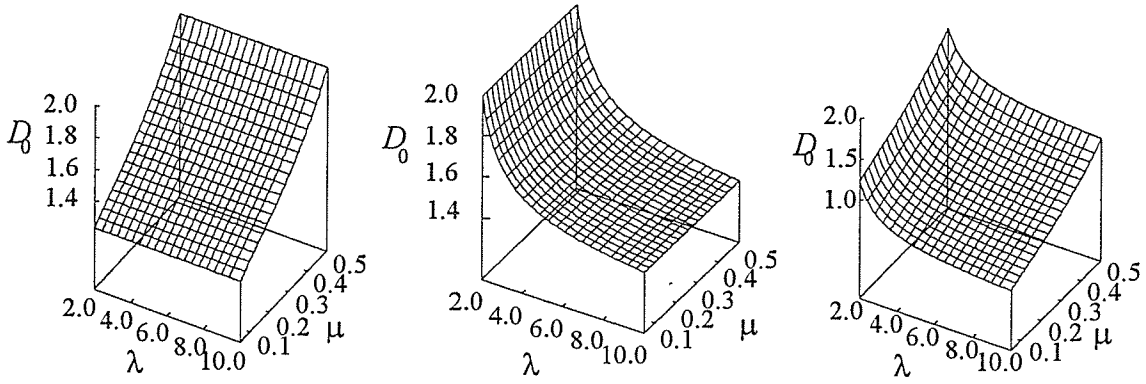

Figure 10.9 Hausdorff dimension for the uniform Smale horseshoe.

10.3.2 A nonuniform Smale horseshoe

In this section, we discuss the multifractality of the nonuniform Smale horseshoe. Consider a map for nonuniform Smale horseshoe given by

$$f:\begin{cases}\begin{pmatrix}x_{n+1}\\ y_{n+1}\end{pmatrix}=\begin{pmatrix}\lambda_1 & 0\\ 0 & \mu_1\end{pmatrix}\begin{pmatrix}x_n\\ y_n\end{pmatrix} & \text{on } H_0,\\ \begin{pmatrix}x_{n+1}\\ y_{n+1}\end{pmatrix}=\begin{pmatrix}-\lambda_2 & 0\\ 0 & -\mu_2\end{pmatrix}\begin{pmatrix}x_n\\ y_n\end{pmatrix}+\begin{pmatrix}1\\ \mu_2\end{pmatrix} & \text{on } H_1.\end{cases} \tag{10.44}$$

where $0<\lambda_i\le 1/2$ and $\mu_i\ge 2$ and $i=\{1,2\}$. Note that from *Equation* (10.44), two separate rectangles in the horizontal direction can be defined:

$$\left.\begin{aligned}H_0&=\left\{(x,y)\in R^2 \mid 0\le x\le 1,\ 0\le y\le 1/\mu_1\right\},\\ H_1&=\left\{(x,y)\in R^2 \mid 0\le x\le 1,\ 1-1/\mu_2\le y\le 1\right\}.\end{aligned}\right\} \tag{10.45}$$

Applying f in *Equation* (10.44) to these two horizontal rectangles produces two vertical rectangles,

$$\left.\begin{aligned}f(H_0)\equiv V_0&=\left\{(x,y)\in R^2 \mid 0\le x\le \lambda_1,\ 0\le y\le 1\right\},\\ f(H_1)\equiv V_1&=\left\{(x,y)\in R^2 \mid 1-\lambda_2\le x\le 1,\ 0\le y\le 1\right\}.\end{aligned}\right\} \tag{10.46}$$

Applying maps f and $f^{(-1)}$ ad infinitum to the unit square S yields the Smale horseshoe, that is,

$$\Lambda=\Lambda_V\cap\Lambda_H=\bigcap_{n=-\infty}^{\infty}f^{(n)}(\boldsymbol{D})=\left[\bigcap_{n=0}^{\infty}f^{(-n)}(\boldsymbol{D})\right]\cap\left[\bigcap_{n=1}^{\infty}f^{(n)}(\boldsymbol{D})\right]. \tag{10.47}$$

We will first present multifractal results for the vertical rectangle invariant set, followed by the horizontal invariant set. Then we will add these two sets of results to get the multifractal characteristics for the nonuniform Smale horseshoe.

Observe that the vertical invariant set of *Equation* (10.44) has two scaling ratios $r_{1x} = \lambda_1$ and $r_{2x} = \lambda_2$ and probability weight $p_{1x} = p_{1x} = 1/2$. Therefore, from the 1-D multifractal theory, its partition function in x-direction is

$$\Gamma_x = \left(\frac{\lambda_1^{-\tau_x}}{2^q} + \frac{\lambda_2^{-\tau_x}}{2^q} \right)^n = 1. \tag{10.48}$$

Re-expressing *Equation* (10.48), we have

$$q = \frac{\log\left(\lambda_1^{-\tau_x} + \lambda_2^{-\tau_x}\right)}{\log 2}. \tag{10.49}$$

The multifractal dimension, scaling index and fractal spectrum for the vertical invariant set in the x-direction are

$$D_{qx} = \frac{\tau_x \log 2}{\log\left(\lambda_1^{-\tau_x} + \lambda_2^{-\tau_x}\right) - \log 2}, \tag{10.50}$$

$$\alpha_x = \frac{\left(\lambda_1^{-\tau_x} + \lambda_1^{-\tau_x}\right)\log 2}{\lambda_1^{-\tau_x} \log \lambda_1 + \lambda_2^{-\tau_x} \log \lambda_2}, \tag{10.51}$$

$$f_x(\alpha_x) = \alpha_x q - \tau_x(q). \tag{10.52}$$

Next, we consider the multifractality of the horizontal invariant set of *Equation* (10.44) in the y-direction and the results are,

$$q = \frac{\log\left(\mu_1^{\tau_y} + \mu_2^{\tau_y}\right)}{\log 2}. \tag{10.53}$$

$$D_{q_y} = \frac{\tau_y \log 2}{\log\left(\mu_1^{\tau_y} + \mu_2^{\tau_y}\right) - \log 2}; \tag{10.54}$$

$$\alpha_y = \frac{\left(\mu_1^{\tau_y} + \mu_2^{\tau_y}\right)\log 2}{\mu_1^{\tau_y} \log \mu_1 + \mu_2^{\tau_y} \log \mu_2}; \tag{10.55}$$

$$f(\alpha_y) = \alpha_y q - \tau_y(q). \tag{10.56}$$

We can now summarize the multifractal characteristics for the vertical invariant set, the horizontal invariant set and the non-uniform Smale horseshoe in *Table* 10.1.

Table 10.1 Multifractal characteristics for 2-D nonuniform invariant sets

Vertical Invariant Set		Horizontal Invariant Set		Smale horseshoe	
$\tau_q = q-1+\tau_{qx},$ $D_q = 1+D_{qx},$ $\alpha = 1+\alpha_x,$ $f(\alpha) = 1+f(\alpha_x).$	(10.57)	$\tau_q = q-1+\tau_{qy},$ $D_q = 1+D_{qy},$ $\alpha = 1+\alpha_y,$ $f(\alpha) = 1+f(\alpha_y).$	(10.58)	$\tau = \tau_x + \tau_y,$ $D_q = D_{qx} + D_{qy},$ $\alpha = \alpha_x + \alpha_y,$ $f(\alpha) = f(\alpha_x) + f(\alpha_y).$	(10.59)

The multifractal characteristics of the Smale horseshoe in *Equation* (10.59) are plotted in *Figure* 10.10 using $\mu_1 = 4$ and $\mu_2 = 5, \lambda_1 = 1/2$ and $\lambda_2 = 1/3$.

10.4 Conclusions

A theory for investigating multifractals in chaotic dynamics is developed via m-D horseshoe maps in this chapter. We first examined and derived the results for 1-D uniform and nonuniform Cantor sets, and then followed by the 2-D uniform and nonuniform Smale horseshoes. The various fractal characteristics are studied. Plots of these results are also provided.

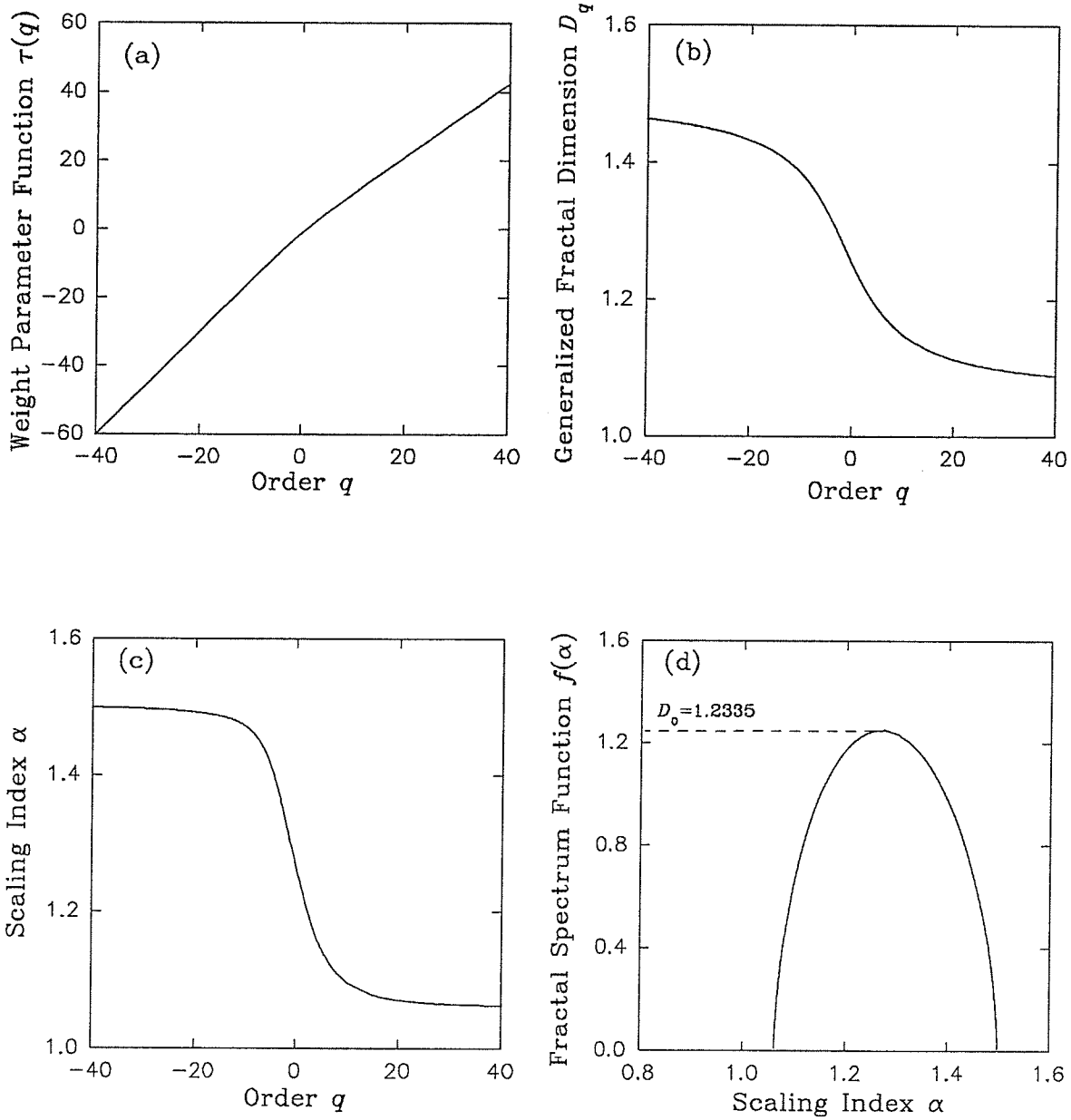

Figure 10.10 Multifractal characteristics of the 2-D nonuniform Smale horseshoe.

CHAPTER 11
CONCLUSIONS

This thesis is concerned with the analytical modeling of bifurcations, chaos and multifractals. The objective was to carry out theoretical studies of these areas for nonlinear dynamic problems arising from engineering applications. To verify and assess the performance of these analytical models, comparisons with published solutions and those obtained via numerical simulations are performed. In all cases, good to excellent agreements are observed. One of the notable achievements of this doctoral research is the demonstration of the ability to analytically predict bifurcations and the onset of chaos by employing computed instead of prescribed input parameters in numerical simulations. This ability is very beneficial as it can significantly reduce the amount of numerical experimentation required to simulate the desired nonlinear dynamics phenomena. From an engineering point of view, this would be a very useful tool for nonlinear analysis.

The chapter is organized by first presenting a summary of the achievements and conclusions of the three main parts of the research, followed by a brief discussion on some unsolved problems and future work.

11.1 Achievements and Conclusions

In *Part* I, we focused our investigation on the modeling of bifurcations and chaos in continuous systems by solving the Duffing oscillator. The main achievements are as follows.

- An improved method of harmonic balance for handling stability and bifurcation of periodic solutions of damped Duffing oscillators is presented. In order to substantially reduce the amount of numerical experimentation, the input data are computed rather than prescribed as is done traditionally. The number of numerically determined stable and unstable solutions agree exactly with the analytical predictions.

- Chirikov overlap criterion and renormalization group technique are used for the first time to independently derive the chaotic condition near a subharmonic resonant orbit for the undamped Duffing oscillator. The analytically predicted chaos by these two methods is confirmed numerically and perfect agreement in their numbers of subharmonic resonances is observed. Chaotic motion of a weakly damped oscillator is studied using the Melnikov method. Plots of the Poincare mapping section indicate the presence of strange attractors in the damped system.

- A new method based on the incremental energy approach is developed for the modeling of stochastic layers near the separatrix. Analytical expressions for the outer and inner strengths of the stochastic layer for the Duffing and forced planar-pendulum oscillators are obtained. Good agreement between the analytical results computed using the Chirikov overlap criterion and the renormalization group technique on one hand, with our proposed incremental energy method on the other, is observed, particularly at the lower-order resonances. Numerical simulations confirm the number of analytically predicted resonances generated for both the oscillators.

- A new method based on the incremental energy approach is developed for the modeling of resonant layers in nonlinear dynamics via an investigation of the Duffing oscillator. The appearance, disappearance and accumulated disappearance strengths of the resonant layers are derived. Comparisons between the proposed procedure with the Chirikov overlap criterion, the renormalization group technique and numerical simulations are performed, and good quantitative and qualitative agreements are observed for all four types of Duffing oscillator.

- Based on its discrete mapping, the universal character of the Duffing oscillator is studied for the first time. The approach involves a Naive discretization of the differential equation of motion and the subsequent application of the cubic renormalization on its discrete equation. Very good agreement is observed between the analytical predictions and the numerically simulated results of the mapping. The jump phenomenon and the strange attractor are clearly seen in the cascades of bifurcations of the damped oscillator.

In *Part* II, the stability and bifurcation of periodic solutions of a discrete system are investigated. A bouncing ball and a horizontal impact pair subjected to harmonic excitation is prescribed. The following are the main achievements.

- Based on the differential equation of motion of a ball bouncing on a massive vibrating table, the stability and bifurcation conditions are derived for the first time. Mappings for up to period-k motion are obtained. Three types of stable motion are found: stable node (+), stable focus and stable node (-); and two types of unstable motion are observed: saddle of the first kind and saddle of the second kind. From the Poincare mappings of the unstable period-1 motion, the two saddles are shown to possess identical Smale horseshoe structures. This is not necessarily true for the higher periodic solutions. Plots of the physical motion are also provided.

- A theory for a system with discontinuities as applied to the impact analysis of a horizontal impact pair is developed. Mappings for four switch planes are defined and from these, five impact motions; Model I, Model II, Model III, Model IV and Model V are derived. From a detailed scrutiny of the equispaced impacts of the Model I motion, it is shown that period-doubling bifurcation cannot occur. Using computed instead of prescribed input parameters, numerical experimentations are performed and the analytically predicted stability is in excellent agreement with the numerically generated results. Both stable and unstable (chaotic) motions are generated. To get a sense of the impacts, plots of the physical motions are also provided.

Part III presents our research in the area of multifractals in chaotic dynamics. New models for the construction of multifractals and analysis of their fractal characteristics are developed. The primary achievements are described as follows.

- Through the construction of similar structures, a new method for the analysis of period doubling bifurcations in 1-D iterative maps is suggested. An example was solved to demonstrate and assess the accuracy of the procedure. The weight parameter function, several generalized fractal dimensions, the scaling index and the fractal spectrum functions are derived. Comparison with published solutions and that obtained via physical experiments showed that the proposed procedure yields very accurate results. In this sense, the method represents a significant improvement over the currently available techniques.

- A theory for investigating multifractals in chaotic dynamics is developed via m-D horseshoe maps. We first examined and derived the results for 1-D uniform and nonuniform Cantor sets, and then followed by the 2-D uniform and nonuniform Smale horseshoes. The various fractal characteristics are studied. Plots of these results are also provided.

11.2 Unsolved Problems and Future Work

During the course of carrying out this research, several unsolved problems have been identified and are summarized in this section. Some of these unsolved problems can be treated as future work. Additionally, there is a conspicuous lack of actual physical experiments to verify the modeling of chaos and other nonlinear dynamics phenomena.

- One of the key unsolved problem in this work (and also, for that matter, in nonlinear dynamics) is the ability to model multi-degrees of freedom systems. Since such systems are more realistic, the solutions obtained are not only more useful, but also, more accurate. However, this is an extremely difficult and complex undertaking.

- Much of the work described in this thesis pertains to the Duffing oscillator. It would be interesting (and not necessarily difficult) to extend the analytical methods to other types of common engineering systems such as the van der Pol oscillator.

- For strongly damped systems, there are no analytical methods for the prediction of bifurcation and the onset of chaos

- Well established methods such as the Chirikov overlap criterion and the renormalization group technique are able to capture approximately the primary resonance, whereas our proposed incremental energy approach is able to exactly model the primary resonance. However, our incremental energy method suffers from one minor drawback, namely, the effects of secondary resonance have not been adequately considered.

- The analytical prediction of chaos in discrete oscillators is an area that needs addressing. Currently, the most popular approach is to treat such systems by solving their equivalent mappings. However, it is not necessarily clear if the mappings actually represent the physical systems. A better approach is to employ the differential equations governing the discrete systems, but this method can be mathematically intractable.

- It can be very challenging to simulate the analytically determined higher periodic solutions of discrete systems. This is due to the extremely large number of possible combinations of their motion models. Not only an efficient book-keeping technique needs to be developed to keep track of each of the motion models, but it is necessary to address the requirement for very intensive computer memory consumption.

- It is also extremely difficult to model multi-discrete variables even in single degree of freedom discontinual systems.

- Multifractals generated at the onset of chaos for m-D iterative maps (non-horseshoes) have not been investigated due to the extreme difficulty in their construction.

- A theory for constructing multifractals for chaotic and strange attractors in continuous systems is still unavailable.

- Further identification and application of fractals in engineering problems need to be addressed. Currently, some of the most popular usage of fractals in engineering include strength characterization, fracture propagation and fluid turbulence modeling.

APPENDICES

APPENDIX A

BASIC THEORIES IN BIFURCATION, CHAOS AND FRACTALS

In this chapter, the basic theories of bifurcation, chaos and fractal for engineering applications are presented. Several main types of bifurcation models in continuous and discrete dynamical systems are described. For continuous dynamical systems in *Section* A.1, bifurcations in 1-D and 2-D systems are introduced . An attempt to define chaos in terms of the KS entropy and a means of characterizing it are also provided. Several analytical methods for predicting the appearance of chaos are described. These include the Chirikov resonance overlap criterion, renormalization techniques and Melnikov method. For the discrete dynamical systems in *Section* A.2, bifurcations in 1-D and 2-D maps are discussed. The various routes to chaos for 1-D and 2-D maps are mentioned. Finally, in *Section* A.3, multifractals in chaotic dynamics are presented. The basic concepts of fractals and their generation by multigenerators are introduced. The section ends by a discussion of the measures of multifractals.

A.1 Continuous Dynamic Systems

A.1.1 Bifurcations

Poincare first coined the term *bifurcation* to describe the branching of equilibrium solutions derived from a family of differential equations. Since bifurcation solutions are asymptotic solutions of the nonlinear equations, the bifurcation theory is thus, concerned with the theory of steady, periodic, subharmonic and quasi-periodic solutions for both

autonomous and non-autonomous systems. Note that the vice-versa is not necessarily true. That is, not all asymptotic solutions are due to bifurcation. Consider a n-D system of differential equations with m-D parameter μ

$$\dot{x} = f(x, \mu), \tag{A.1}$$

where $x \in \mathscr{R}^n$, $\mu \in \mathscr{R}^m$. The equilibrium solutions of *Equation* (A.1) are determined by $f(x, \mu) = 0$. If $Df(x, \mu) = \partial f(x, \mu)/\partial x$ at an equilibrium point (x_0, μ_0) has a zero eigenvalue, several branches of equilibrium may be ensue; and this point (x_0, μ_0) is called the bifurcation point. We will now consider bifurcation of continuous dynamical systems in one- and two-dimensions.

A.1.1(a) One-dimensional systems

Several typical bifurcations of 1-D dynamical systems are presented here. Note that stable solutions are marked with the solid line, while unstable solutions are indicated by the dash line. *Figure* A.1 depicts the bifurcation condition $Df(x_0, \mu_0) = 0$ in the complex plane.

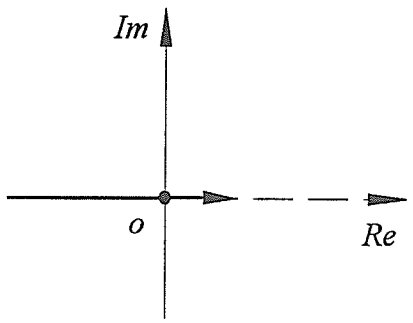

Figure A.1 Eigenvalues of $Df(x_0, \mu_0)$ in the complex plane.

(i) Saddle-node bifurcation

Consider the following example of saddle-node bifurcation,

$$\dot{x} = \mu - x^2, \tag{A.2}$$

which describes for instance, the dynamics of snap-through buckling of an arch. Its bifurcation diagram is illustrated in *Figure* A.2(a).

(ii) Transcritical bifurcation

Consider an example depicting transcritical bifurcation, that is,

$$\dot{x} = \mu x - x^2, \tag{A.3}$$

Equation (A.3) can be used to describe the dynamics of buckling of a frame. The bifurcation diagram for this case is sketched in *Figure* A.2(b).

(iii) Pitchfork bifurcation for stable-symmetry

Consider the following equation

$$\dot{x} = \mu x - x^3 \tag{A.4}$$

representing for example, the dynamical Euler buckling problem in structural engineering. Its bifurcation diagram is given in *Figure* A.2(c).

(iv) Pitchfork bifurcation for unstable-symmetry

The following equation governs the dynamical buckling of beams, plates, shells, etc.,

$$\dot{x} = \mu x + x^3. \tag{A.5}$$

Its bifurcation diagram shown in *Figure* A.2(d). Note that other bifurcations for 1-D systems, such as the symmetric break, are not covered here.

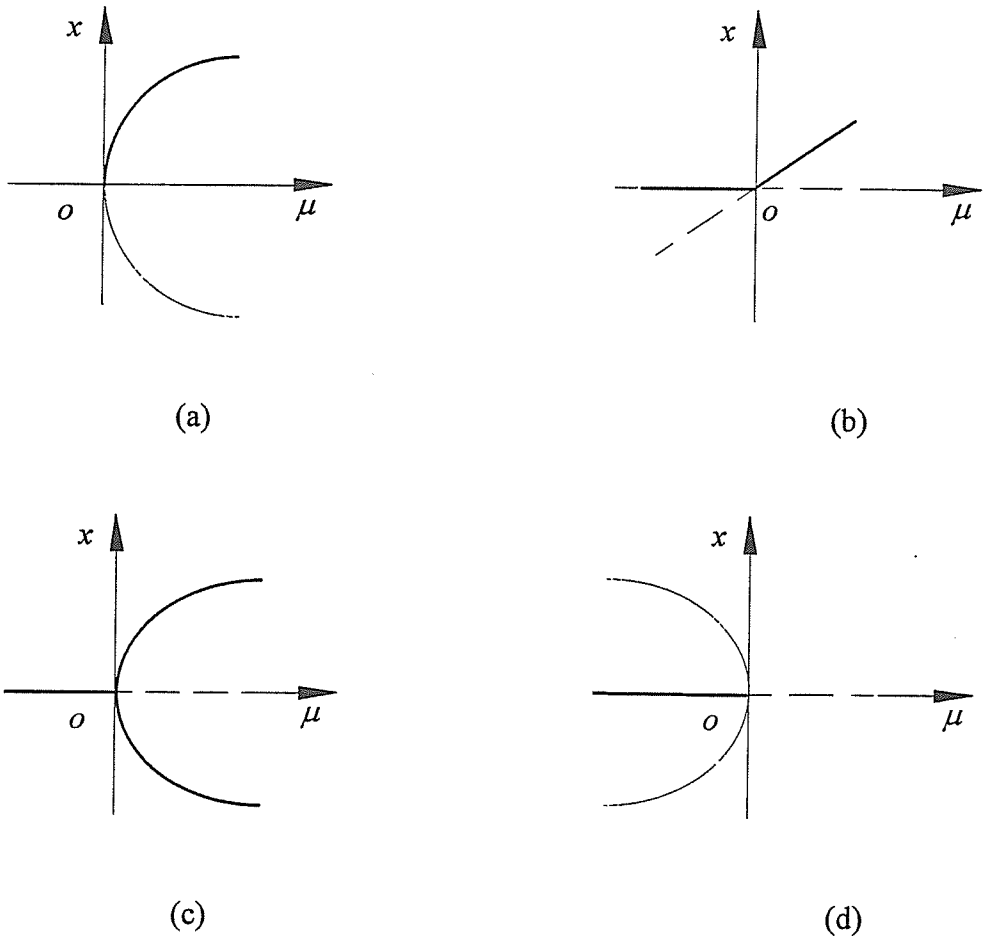

Figure A.2 Bifurcation diagrams: (a) saddle-node bifurcation, (b) transcritical bifurcation, (c) pitchfork bifurcation for stable-symmetry and (d) pitchfork bifurcation for unstable-symmetry.

A.1.1(b) Two-dimensional systems

Next we consider 2-D systems. Once again, several typical bifurcations are outlined.

Bifurcations at nonhyperbolic equilibrium solutions

Consider the $n \times n$ matrix $Df(x_0, \mu_0)$ of *Equation* (A.1) at the nonhyperbolic equilibrium solution. Assume it has a zero eigenvalue corresponding to eigenvector v, and similarly, its transpose, namely, $Df(x_0, \mu_0)^T$ has a zero eigenvalue corresponding to eigenvector w.

Furthermore, suppose that $Df(x_0,\mu_0)$ has k eigenvalues with negative part and $(n-k-1)$ eigenvalues with positive real part, then we say that *Equation* (A.1) exhibits:

(i) saddle-node bifurcation if

$$w^T f_\mu(x_0,\mu_0)\neq 0,\quad w^T\left[D^2 f(x_0,\mu_0)(v,v)\right]\neq 0, \tag{A.6}$$

(ii) transcritical bifurcation if

$$w^T f_\mu(x_0,\mu_0)=0,\ w^T\left[Df(x_0,\mu_0)v\right]\neq 0,\quad \text{and}\quad w^T\left[D^2 f(x_0,\mu_0)(v,v)\right]\neq 0, \tag{A.7}$$

(iii) pitchfork bifurcation if

$$\left.\begin{aligned}&\mathbf{w}^T f_\mu(\mathbf{x}_0,\mu_0)=0,\quad \mathbf{w}^T\left[Df(\mathbf{x}_0,\mu_0)\mathbf{v}\right]\neq 0\\ &\mathbf{w}^T\left[D^2 f(\mathbf{x}_0,\mu_0)(\mathbf{v},\mathbf{v})\right]=0,\quad \mathbf{w}^T\left[D^3 f(\mathbf{x}_0,\mu_0)(\mathbf{v},\mathbf{v},\mathbf{v})\right]\neq 0\end{aligned}\right\}. \tag{A.8}$$

Note that the bifurcations at the nonhyperbolic periodic orbits are quite similar to the bifurcations at the nonhyperbolic equilibrium solutions.

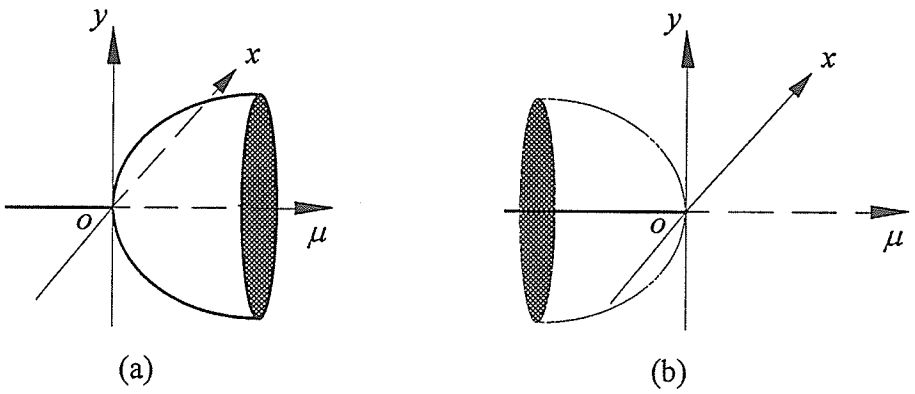

Figure A.3 Hopf bifurcations: (a) supercritical and (b) subcritical.

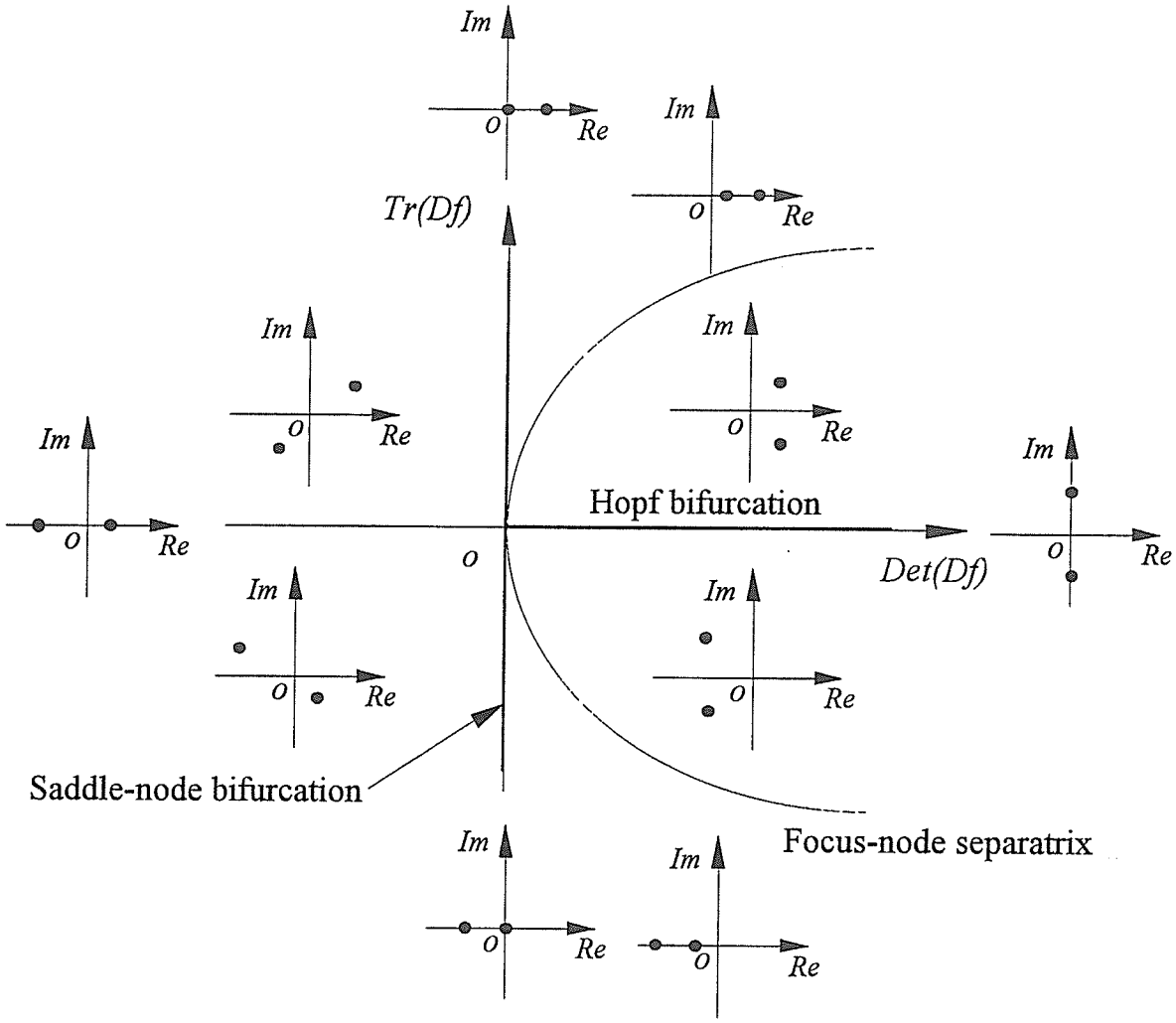

Figure A.4 Stability and bifurcation diagrams for a 2-D system.

Hopf bifurcations at equilibrium solutions

If the $n \times n$ matrix $Df(\boldsymbol{x}_0, \mu_0)$ of *Equation* (A.1) at the equilibrium solution has a simple pair of pure imaginary eigenvalues and all other eigenvalues have non-zero real part, *Equation* (A.1) will exhibit Hopf bifurcation at μ_0. Hopf bifurcations are of two kinds: supercritical Hopf bifurcation which has a stable limit cycle and subcritical Hopf bifurcation which has an unstable limit cycle. For a 2-D dynamical system, Hopf bifurcation is sketched in *Figure* A.3. Engineering examples of this type of bifurcation

includes, the galloping vibration of a fluid-structure problem and the dynamics of a spinning shaft system.

Taking a 2-D dynamic system as an example the bifurcation conditions and stability condition are summarized in *Figure* A.4. Note that we have, $Det(Df) = Det(Df(x_0, \mu_0))$ and $Tr(Df) = Tr(Df(x_0, \mu_0))$

Global bifurcations (homoclinic bifurcations)

Global bifurcations at equilibrium solutions are characterized by the lost of transversality between the stable and unstable trajectories. Using Melnikov method, homoclinic bifurcations can be investigated. For many continuous systems, their nonlinear characteristics can be qualitatively studied via discrete maps, such as Poincare mapping and energy iterative map. We will present bifurcation and chaos analyses of discrete dynamical systems in a later section.

A.1.2 Chaos

Here we look at some basic concepts of chaos and also, examine some analytical methods for predicting its onset in continuous systems. We will first classify chaos and then we will attempt to define it. Traditionally, chaos is divided into two types: chaos in a conservative system and chaos in a dissipative system, as depicted in *Figure* A.5.

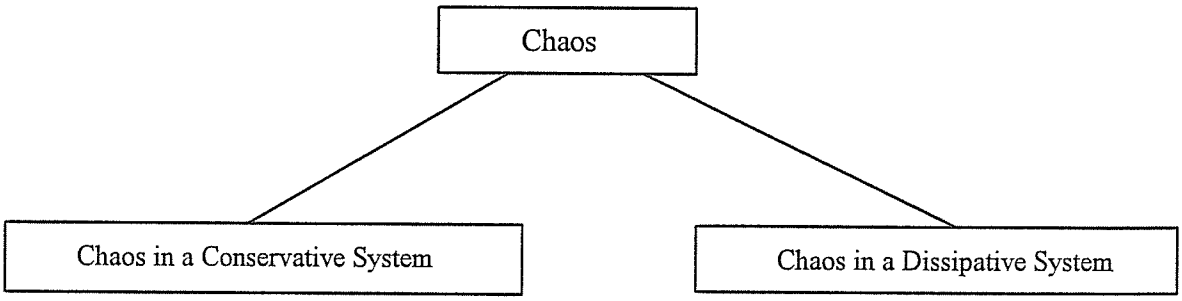

Figure A.5 Classifications of chaos.

Some methods of chaos analysis are valid only for conservative systems (e. g. Chirikov overlap criterion) and some for both conservative and dissipative systems (Melnikov method). Intuitively, chaos can be defined in terms of the dynamical behavior of orbit pairs in the phase space. If these initially close together orbits move apart exponentially, we have a chaotic flow. Mathematically, we say that the *flow of trajectories in a given region of phase space exhibits deterministic chaos if its KS entropy*** *is positive* (Krylov (1950), Kolmogorov (1958), Sinai (1959, 1963)). That is, the flow of trajectories (in the phase space) intersected in the neighborhood of a hyperbolic fixed point. For regular motion, the KS entropy is zero and for random motion, it is infinite. Adler, Konheim and McAndrew (1965) introduced the notion of *T-entropy* (topological entropy) which is not dependent on metric scales as in KS entropy. Shaw (1981) proposed a new characterization of chaos based on information via the information production rate. Unlike the KS and T-entropies which can only be zero or positive, this information production rate can take positive and negative values.

Many researchers believed that horseshoe maps are fundamental to chaos models of dynamical systems. One prototypical map in nonlinear dynamics is the Smale horseshoe which can be constructed via a linearized map in the neighborhood of the hyperbolic fixed point. That is, a map f. from a unit square of phase space defined by,

$$f: \begin{cases} H_0 : \begin{pmatrix} x_{n+1} \\ y_{n+1} \end{pmatrix} = \begin{pmatrix} \lambda & 0 \\ 0 & \mu \end{pmatrix} \begin{pmatrix} x_n \\ y_n \end{pmatrix} \\ \\ H_1 : \begin{pmatrix} x_{n+1} \\ y_{n+1} \end{pmatrix} = \begin{pmatrix} -\lambda & 0 \\ 0 & -\mu \end{pmatrix} \begin{pmatrix} x_n \\ y_n \end{pmatrix} + \begin{pmatrix} 1 \\ \mu \end{pmatrix} \end{cases} \tag{A.9}$$

with $0 < \lambda < 0.5$, $\mu > 2$. At the hyperbolic fixed point, a dynamical system displaying such behavior is said to exhibit sensitive dependence on initial conditions. Also, from a fractal

** We shall discuss more about this KS entropy in a later section.

point of view, the complicated geometrical structures can be characterized as having fractional dimensions (Luo and Han (1994b)). They are termed as strange attractors and the motion on them is chaotic.

A.1.2(a) Determination of chaos

Criteria for determining chaos are basically of two types: empirical and theoretical, and some of the principal ones are Lyapunov characteristic exponent, fractal dimension characterization, Poincare mapping and Fourier spectra of trajectories. These criteria can be verified through either physical experimentation or numerical simulation. In this paper, we will concentrate on the most popular technique; namely, the Lyapunov characteristic exponent method.

Lyapunov Characteristic Exponent

As explained earlier, chaos is said to occur when the orbit pairs diverges exponentially, and the Lyapunov characteristic exponent measures the rate of this exponential divergence. A positive exponent implies chaos, while a zero or negative exponent indicates the motion is regular. For a detailed derivation, we consider the following map,

$$x_{n+1} = f(x_n), \tag{A.10}$$

which will result in a chaotic motion. The Lyapunov exponent $\lambda(x_0)$ measures exponent divergence as sketched in *Figure* A.6.

Consider the neighborhood of the point x_0 in the phase space which is acted on by *Equation* (A.10). Setting $\varepsilon = \|\Delta x_0\|$, we have

$$\|\Delta x_0\| e^{N\lambda(x_0)} = \left\| f^N(x_0 + \Delta x_0) - f^N(x_0) \right\|, \tag{A.11}$$

where $\|(\ )\|$ denotes norm. In the limits $\varepsilon = \|\Delta x_0\| \to 0$ and $N \to \infty$, *Equation* (A.11) leads to the correct formal expression for $\lambda(x_0)$:

$$\begin{aligned}\lambda(x_0) &= \lim_{N\to\infty}\lim_{\|\Delta x_0\|\to 0}\frac{1}{N}\log\frac{\left\|f^N(x_0+\Delta x_0)-f^N(x_0)\right\|}{\|\Delta x_0\|} \\ &= \lim_{N\to\infty}\frac{1}{N}\log\left\|\frac{df^N(x_0)}{dx_0}\right\|\end{aligned} \tag{A.12}$$

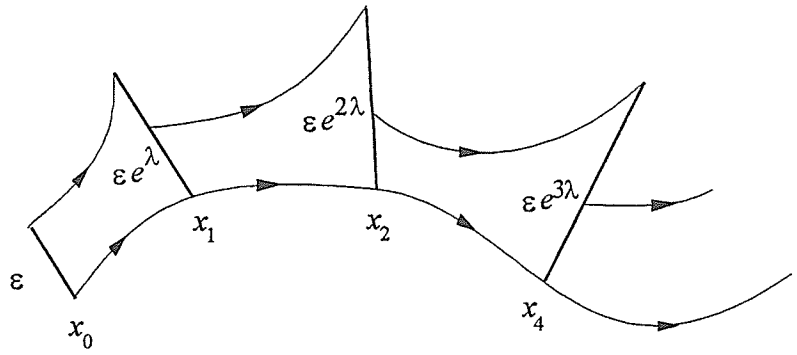

Figure A.6 Definition of the Lyapunov characteristic exponent.

Note that the Lyapunov exponent measures the average loss of the information after one iteration. Using the chain rule in *Equation* (A.12), we have

$$\begin{aligned}\lambda(x_0) &= \lim_{N\to\infty}\frac{1}{N}\log\left\|\frac{df^N(x_0)}{dx_0}\right\| = \lim_{N\to\infty}\frac{1}{N}\log\left\|\prod_{i=0}^{N-1}\frac{df(x_i)}{dx_i}\right\| \\ &= \lim_{N\to\infty}\frac{1}{N}\sum_{i=0}^{N-1}\log\left\|\frac{df(x_i)}{dx_i}\right\|\end{aligned} \tag{A.13}$$

Thus, base on the Lyapunov exponent, the criterion for chaos is

$$\lambda(x_0) > 0, \qquad \text{chaotic;} \tag{A.14}$$

$$\lambda(x_0) \le 0, \qquad \text{regular motion.} \tag{A.15}$$

The Kolmogorov-Sinai (KS) Entropy

The KS-entropy is perhaps the most important measure for characterizing the chaotic motion in an arbitrary dimensional phase space. Therefore, we would like to introduce this concept here. For a more detailed discussion, the reader is referred to Reichl (1992). Consider in *Figure* A.7(a) the phase space of a unit square that is partitioned into a set $\{A_i(0)\}$ of cells, where $A_i(0)$, I=1,2. A new set of cells $\{A_i(-1)\}$ is generated by allowing the original set to evolve backwards for a unit time. Let us next introduce the partition B(-1) which consists of the intersection of these two sets, that is, $B(-1) = \{A_i(0) \cap A_j(-1)\}$ as shown in *Figure* A.7(b). We can continue to generate the next partition B(-2) such that $B(-2) = \{A_i(0) \cap A_j(-1) \cap A_k(-2)\}$ and so on (in *Figure* A.7(c)). It can be shown that (Lichtenberg and Lieberman (1992)),

$$k_R(\{A_i(0)\}) = -\lim_{t\to\infty} \frac{1}{t} \sum_{i=1}^{R_t} \alpha[B_i(-t)] \ln \alpha[B_i(-t)] > 0 \tag{A.16}$$

is required if the $B(-t)$ decreases exponentially as $t \to \infty$ where R_t, $\alpha[B_i(-t)]$ are the number of elements of $B(-t)$ and the measure of each element respectively. The maximum of k_R as the initial cell size tends to zero, is the KS entropy, K. Note that K>0 when the average measure of an element of B decreases exponentially, that is, chaos occurs when this happens. Pesin (1977) derived the relationship between the KS-entropy and the Lyapunov exponents as follows

$$K = \int_{\Gamma} \left[\sum_{\lambda_i(x)>0} \lambda_i(x) \right] d\alpha, \tag{A.17}$$

where the integral is over a prescribed portion of the phase space and the sum is over all positive Lyapunov exponents.

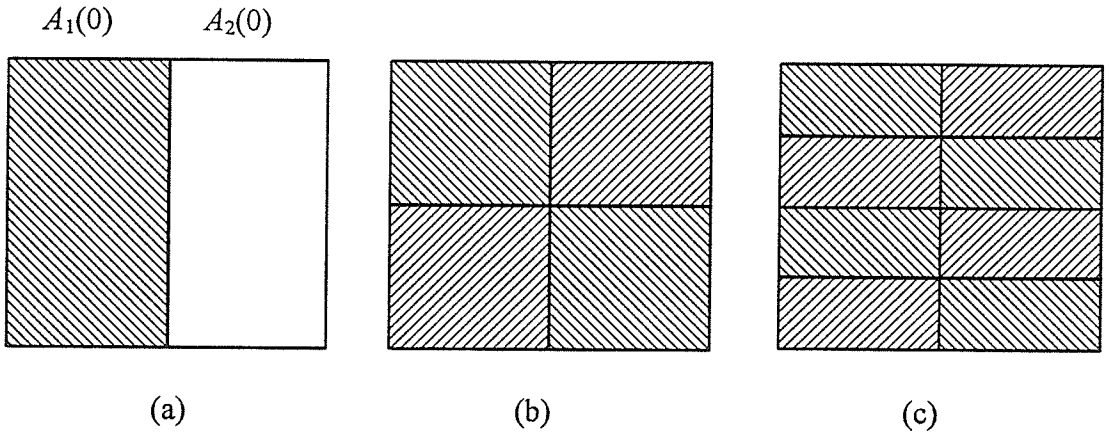

Figure A.7 Partitions of the phase space of a unit square: (a) 2-element, (b) 4-element and (c) 8-element.

A.1.2(b) Analytical methods

We will now describe some more recent analytical methods for predicting the appearance of chaos in continuous systems.

Chirikov resonance overlap criterion

To estimate the critical condition for the transition of local stochasticity to chaos (or global stochasticity), the work of Chirikov (1979) can be employed. He postulated that the critical condition required to destroy the last KAM tori between the two lowest-order primary resonances occurs when the sum of the half-widths of the two island separatrices is equal to the distance between these two resonances. Consider the following Hamiltonian,

$$H = \frac{y^2}{2} + K\cos\theta + 2K\cos\theta\cos(\Omega t), \tag{A.18}$$

where $y = \dot{\theta}$. It is assumed that third term of *Equation* (A.18) is a perturbation, therefore, the unperturbed Hamiltonian of *Equation* (A.18) is

$$H_0 = \frac{y^2}{2} + K\cos\theta. \tag{A.19}$$

From an undamped pendulum, the fixed points are at $(y = 0,\ \cos\theta = \pm 1)$. The centers of the ellipse are at $(y = 0,\ \cos\theta = -1)$ and the hyperbolic fixed points on the separatrix are at $(y = 0,\ \cos\theta = 1)$. Hence, the half-width of the island separatrix at $\cos\theta = -1$ is calculated by

$$\Delta y_{\max} = 2\sqrt{K}. \tag{A.20}$$

Three kinds of resonance overlap condition can be obtained and they are,

(i) *simple overlap condition*

$$2\Delta y_{\max} = 2\pi \ \Rightarrow\ K = \left(\frac{\pi}{2}\right)^2 \approx 2.46740; \tag{A.21}$$

(ii) *overlap condition of the first and second-order resonances*

$$2\sqrt{K} + \frac{1}{2}K = \pi, \tag{A.22}$$

which yields $K \approx 1.46$;

(iii) *the improved overlap condition*

Here, Chirikov considered the thickness of the separatrix layer based on the overlap condition of the first and second-order resonances. The critical condition is therefore,

$$\left(2+\frac{w_1}{2}\right)\sqrt{K}+\frac{K}{2}=\pi \tag{A.23}$$

in which

$$w_1=\frac{4(2\pi)^2}{K^{5/2}}\exp\left(-\frac{\pi^2}{\sqrt{K}}\right). \tag{A.24}$$

From *Equation* (A.23), we can compute $K\approx 1.2$.

(iv) *Stochastic layers of a physical problem.*

We consider the Hamiltonian of system to be given by

$$H(x,y)=H_0(y)+\varepsilon V(x,y,t), \tag{A.25}$$

where H_0 is an integrable part and, εV is a perturbation, dependent on the time t. Analyzing the resonance condition of *Equation* (A.25) and we get after rescaling the energy, the following simplified expression:

$$H=\frac{y^2}{2}-M\cos\theta-P\cos\nu(\theta-\Omega t). \tag{A.26}$$

Setting $P=0$ in *Equation* (A.26), we can calculate the half-width of the resonance due to the cosine wave of amplitude M at $y=0$ to be $\Delta y_{\max}=2\sqrt{M}$. Similarly, setting $M=0$ in *Equation* (A.26), we can also calculate the half-width of the resonance due to the cosine wave of amplitude P at $y=1$ to be $\Delta y_{\max}=2\sqrt{P}$. Applying Chirikov overlap criterion, we get

$$2\sqrt{M}+2\sqrt{P}=1. \tag{A.27}$$

Renormalization techniques

Escande and Doveil (1981), Doveil and Escande (1981) and Escande (1985) discussed the paradigm Hamiltonian and presented the renormalization procedure for *Equation* (A.26). We will adopt Escande and Doveil methodology to derive the renormalization procedure. In so doing, it is assumed that $M > P$. Consider *Equation* (A.26) to consist of two parts: H_0 and H_1, namely,

$$H_0 = \frac{y^2}{2} - M\cos\theta = E_0, \tag{A.28}$$

where E_0 denotes a constant energy term. Then, we have

$$H_1 = -P\cos\nu(\theta - \Omega t). \tag{A.29}$$

From *Equation* (A.28), we have as its solution

$$\theta = 2\mathrm{am}\left(\frac{K(k)\varphi}{\pi}, k\right), \tag{A.30}$$

$$y = \pm 2k\sqrt{M}\,\mathrm{cn}\left(\frac{2K(k)\varphi}{\pi}, k\right), \tag{A.31}$$

where am and cn are respectively, the elliptic amplitude and the Jacobi elliptic functions; and k is the modulus of elliptic function given by

$$k^2 = \frac{2M}{E_0 + M}. \tag{A.32}$$

Using *Equations* (A.30) and (A.31), the action variable J can be calculated as

$$J = \frac{4\sqrt{M}}{\pi k}K(k). \tag{A.33}$$

Substituting *Equations* (A.30)-(A.31) and (A.33) into *Equation* (A.26) yields

$$H = H_0(J) - P\sum_{-\infty}^{\infty} V_n(J)\cos\left[(\nu+n)\varphi - \nu\Omega t\right], \tag{A.34}$$

where $V_n(J)$ is coefficient of Fourier series of $\cos k(\varphi - \Omega t)$. Invoking *Equation* (A.34), the resonant condition is obtained,

$$\dot{\varphi} = \left(\frac{\partial E_0}{\partial J}\right) = \frac{\nu\Omega}{\nu+n+\delta} = \frac{\pi\sqrt{M}}{kK(k)} \tag{A.35}$$

in which $\delta = \{0,\ 1\}$. Renormalizing the energy in *Equation* (A.34) for the *n*th resonance yields,

$$\overline{H} = \frac{\overline{y}^2}{2} - \overline{M}\cos\overline{\theta} - \overline{P}\cos\overline{\nu}\left(\overline{\theta} - \overline{\Omega}t\right), \tag{A.36}$$

where

$$\overline{M} = \frac{PV_{n+\delta}\omega(\nu+n)^2(\nu+n+)^2}{\nu^2}, \tag{A.37}$$

$$\overline{P} = \frac{PV_{n+1-\delta}\omega(\nu+n)^2(\nu+n+)^2}{\nu^2}, \tag{A.38}$$

$$\overline{\nu} = \frac{(\nu+n+1-\delta)}{\nu+n+\delta}, \tag{A.39}$$

$$\overline{\Omega} = \frac{(2\delta-1)\nu\Omega}{\nu+n+1-\delta}, \tag{A.40}$$

$$\overline{\theta} = (\nu+n+\delta)\varphi - \nu\Omega t, \tag{A.41}$$

Solving *Equations* (A.37)-(A.39) numerically as self-similar structures, we have

$$2\sqrt{M}+2\sqrt{P}\approx 0.7\,. \tag{A.42}$$

Observe that *Equation* (A.37) and *Equation* (A.42) have similar form.

Melnikov method

For a conservative system, we have introduced two methods, the Chirikov overlap criterion and the renormalization technique, to predict the chaos. For a dissipative system, the motion near the separatrix is not necessarily chaotic, as it may be in either transient or steady states. It is important to determine the critical condition under which the transverse intersection of the stable and unstable manifolds will appear. Melnikov (1963) devised a method to analyze the motion near the separatrices of near-integrable systems. Applying this method to a near-integrable system yields a critical condition for the onset of a homoclinic intersection near the separatrix. This procedure is valid even for a system with a dissipative perturbation. Morosov (1973), McLaughlin (1979) and Holmes (1979, 1980) applied the Melnikov method to look at the perturbed dynamics of non-Hamiltonian systems. Guckenheimer and Holmes (1983) generalized the method to study subharmonic bifurcations. Wiggins (1989, 1990) applied this method to investigate the critical condition of higher-dimensional dynamical systems. In this paper, we will emphasize the method to determine approximately, the chaotic conditions of some selected engineering problems. Consider a 2-D dynamical system which has homoclinic or heteroclinic orbits and is perturbed by a periodic function of time. The governing equations for this system are,

$$\begin{cases}\dot{x}=f_1(x,y)+\varepsilon g_1(x,y,t)\\ \dot{y}=f_2(x,y)+\varepsilon g_2(x,y,t)\end{cases}. \tag{A.43}$$

The Melnikov function is defined as,

$$M(t_0)=\int_{-\infty}^{\infty}\left[f_1(x_0,y_0)g_2(x_0,y_0,t-t_0)-f_1(x_0,y_0)g_2(x_0,y_0,t-t_0)\right]dt \tag{A.44}$$

where (x_0, y_0) is the homoclinic orbit of the conservative system. If $M(t_0) = 0$ is independent of perturbation parameter ε, then for $\varepsilon > 0$ sufficiently small, the stable and unstable trajectories in phase space intersect transversely. Similarly, (x_α, y_α) yields the subharmonic resonant orbits of the conservative system under a periodic function. That is,

$$M^{m/n}(t_0) = \int_0^{mT} \left[f_1(x_\alpha, y_\alpha) g_2(x_\alpha, y_\alpha, t - t_0) - f_1(x_\alpha, y_\alpha) g_2(x_\alpha, y_\alpha, t - t_0) \right] dt \quad \text{(A.45)}$$

If $M^{m/n}(t_0) = 0$ is independent of perturbation parameter ε, and in *Equation* (A.43), for $\varepsilon > 0$ sufficiently small, then *Equation* (A.43) has a subharmonic orbit of period mT. Other methods for handling dissipative systems include the methods of harmonic balance and averaging.

A.2 Discrete Dynamical System

For many continuous systems, their nonlinear characteristics can be qualitatively investigated via discrete maps, such as Poincare mapping and energy iterative maps. At the same time, for discontinuous systems, their iterative maps can be easily setup on the basis of appropriate physical laws. Therefore, the methods of discrete mapping constitute very important tools in a nonlinear dynamics analysis. Once again, we have divided the presentation here into 1-D and 2-D maps.

A.2.1 Bifurcations

A.2.1(a) One-dimensional maps

Consider a 1-D map,

$$x_{n+1} = f(x_n, \mu), \quad \text{(A.46)}$$

where μ is a unknown parameter. To determine the period-1 solution of *Equation* (A.46), we substitute $x_{n+1} = x_n$ into *Equation* (A.46), and this yields the periodic solution

$x_n = x^*$. We can then investigate the stability of the solution and compute the critical bifurcation parameters for the following conditions:

(i) Pitchfork bifurcation

$$\frac{dx_{n+1}}{dx_n} = \left.\frac{df(x_n,\mu)}{dx_n}\right|_{x_n=x^*} = -1. \tag{A.47}$$

(ii) Tangent (saddle-node) bifurcation

$$\frac{dx_{n+1}}{dx_n} = \left.\frac{df(x_n,\mu)}{dx_n}\right|_{x_n=x^*} = 1. \tag{A.48}$$

These two kinds of bifurcation for 1-D iterative maps are depicted in *Figure* A.8. Note that the most common pitchfork bifurcation involves an infinite cascades of period doubling bifurcations with universal scalings. An exact renormalization theory for period doubling bifurcation was developed in terms of a functional equation by Feigenbaum (1978), and Collet and Eckmann (1980). Helleman (1980) employed an *algebraic* renormalization procedure to determine the rescaling constants. It is assumed that $f(x,\mu)$ has a quadratic maximum at $x = x_0$. If chaotic motion ensues at μ_∞ through the period-doubling bifurcation, the function $x_{n+1} = f(x_n, \mu_\infty)$ is rescaled by a scale factor α and it has self-similar structure near $x = x_0$.

Under the transition to chaos, we will first introduce the period doubling bifurcation where we will discuss two renormalization procedures, namely, the renormalization group approach via the functional equation method as outlined by Feigenbaum (1978) (see also, Schuster (1988), and Lichtenberg and Lieberman (1992)), and the algebraic renormalization technique as described by Helleman (1980). Then we will discuss the quasiperiodicity route to chaos and also, the intermittency route to chaos.

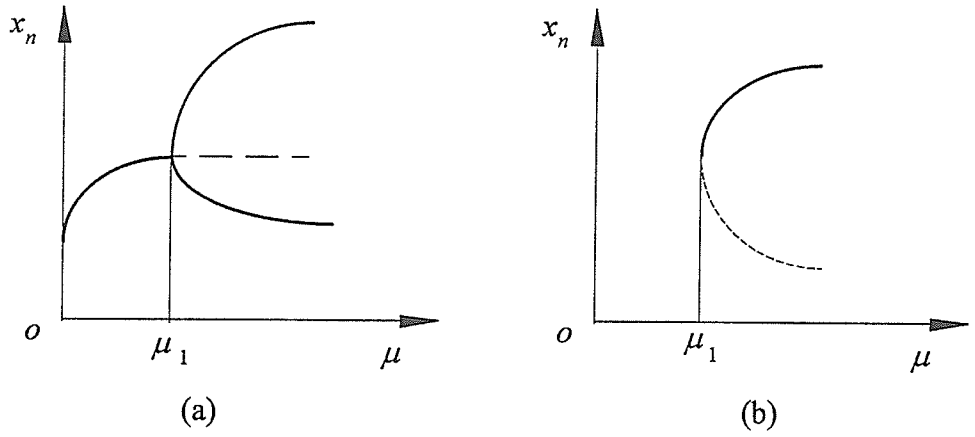

Figure A.8 Bifurcation types: (a) Period-doubling and (b) saddle-node.

A.1.2(b) Two-dimensional maps

Bifurcation and stability for 2-D discrete maps

Consider a 2-D map defined by,

$$P: \begin{cases} x_{n+1} = f(x_n, y_n, \mu) \\ y_{n+1} = g(x_n, y_n, \mu) \end{cases} \tag{A.49}$$

where μ is an unknown parameter. The period-n fixed point for *Equation* (A.49) is (x_n^*, y_n^*, μ_n^*), i.e., $P^{(n)}\begin{pmatrix} x_n^* \\ y_n^* \end{pmatrix} = \begin{pmatrix} x_n^* \\ y_n^* \end{pmatrix}$ where $P^{(n)} = P \circ P^{(n-1)}$ and $P^{(0)} = 1$, and its stability and bifurcation conditions are given as follows.

(i) period-doubling (flip or pitchfork) bifurcation

$$Tr(DP^{(n)}) + Det\left(DP^{(n)}\right) + 1 = 0, \tag{A.50}$$

(ii) saddle-node bifurcation

$$Tr\left(DP^{(n)}\right)+Det\left(DP^{(n)}\right)=1, \tag{A.51}$$

(iii) Neimark bifurcation

$$Det\left(DP^{(n)}\right)=1, \tag{A.52}$$

where
$$DP^{(n)}=\underbrace{\left[\frac{\partial P(x_n,y_n)}{\partial P(x_{x-1},y_{n-1})}\right]\cdots\left[\frac{\partial P(x_1,y_1)}{\partial P(x_0,y_0)}\right]}_{n}. \tag{A.53}$$

Note that
$$DP=\left[\frac{\partial P(x,y)}{\partial(x,y)}\right]=\begin{pmatrix}D_xf & D_yf\\ D_xg & D_yg\end{pmatrix}, \tag{A.54}$$

$$Tr(DP)=D_xf+D_yg,\ Det(DP)=D_xf\cdot D_yg-D_yf\cdot D_xg; \tag{A.55}$$

and
$$\left.\begin{aligned}&D_xf=\partial f(x,y,\mu)/\partial x\big|_{x=x^*,y=y^*},\ D_yf=\partial f(x,y,\mu)/\partial y\big|_{x=x^*,y=y^*}\\ &D_xg=\partial g(x,y,\mu)/\partial x\big|_{x=x^*,y=y^*},\ D_yg=\partial g(x,y,\mu)/\partial y\big|_{x=x^*,y=y^*}\end{aligned}\right\}. \tag{A.56}$$

The bifurcation and stability conditions for the solution of period-n for *Equation* (A.49) are summarized in *Figure* A.9.

A.2.2 Routes to chaos

Next, we consider routes to chaos. We will first present the 1-D discrete system, then we will discuss the 2-D discrete systems.

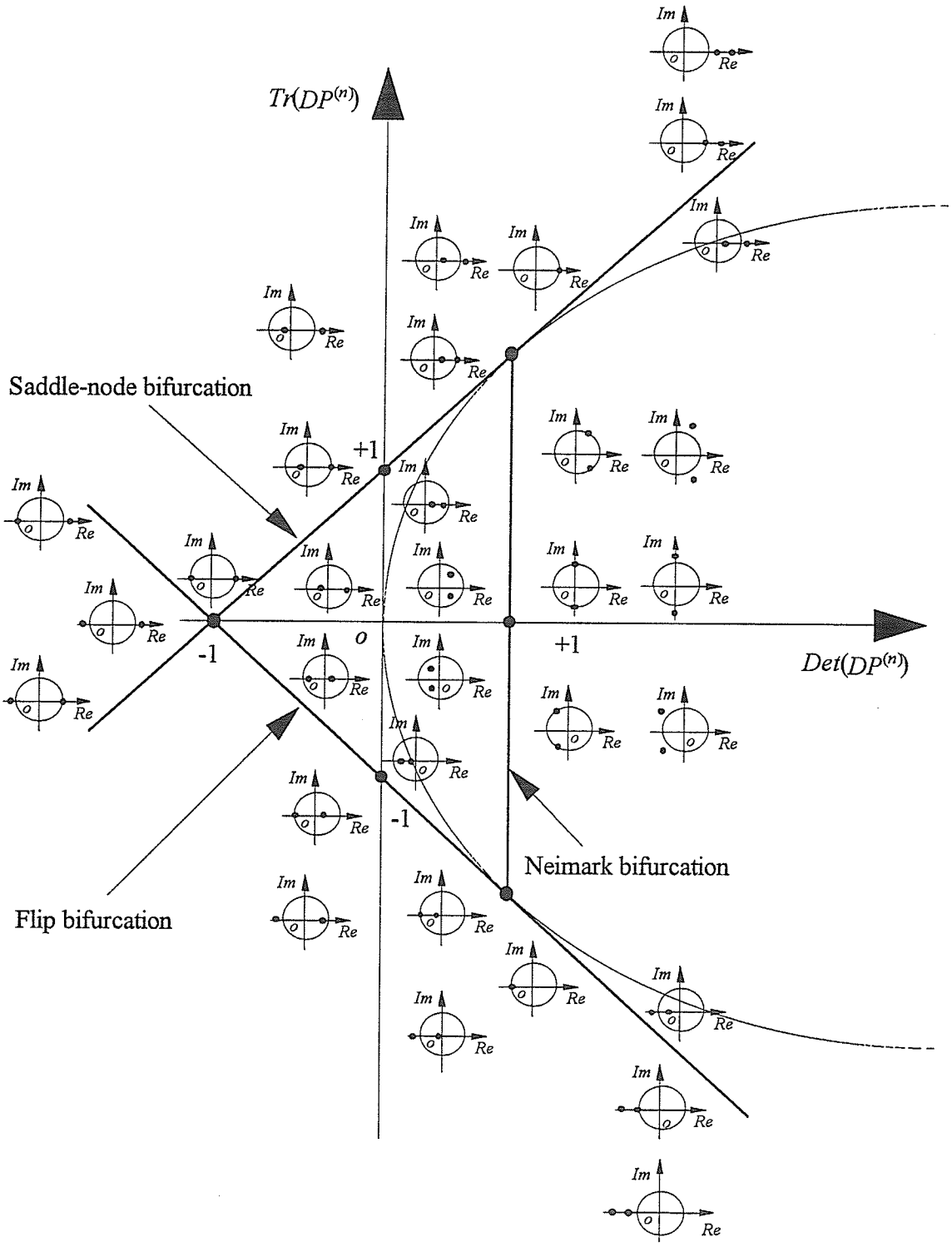

Figure A.9 Stability and bifurcation conditions for period-*n* solutions of *Equation* (A.49).

A.2.2(a) One-dimensional maps

Period doubling route to chaos

(i) *Functional renormalization theory*

The universal function is

$$g^*(x) = \lim_{n\to\infty} \alpha^n f^{(2^n)}\left(\frac{x}{\alpha^n}, \mu_\infty\right), \tag{A.57}$$

where g^* must satisfy the rescaling equation of the geometry, that is,

$$g^* = \alpha g^*\left(g^*\left(\frac{x}{\alpha}\right)\right) = Tg^* \tag{A.58}$$

in which T is a period-doubling operator. From *Equation* (A.58), we can determine the universality of the scale factor α. To obtain the universal constant δ, we first linearize $f(x,\mu_n)$ at $\mu_n = \mu_\infty$

$$f(x,\mu_n) = f(x,\mu_\infty) + \left.\frac{\partial f(x,\mu)}{\partial \mu}\right|_{\mu_n=\mu_\infty} (\mu_n - \mu_\infty). \tag{A.59}$$

Applying the period-doubling operator n times to *Equation* (A.59) yields,

$$\lim_{n\to\infty} T^n f(x,\mu_n) = g^*(x) + L^n_{g^*}\left(\frac{\partial f(x,\mu)}{\partial \mu}\right)\Bigg|_{\mu_n=\mu_\infty} (\mu_n - \mu_\infty). \tag{A.60}$$

Substituting the unstable eigenvalue of L_{g^*} into *Equation* (A.60), we get

$$\lim_{n\to\infty} T^n f(x,\mu_n) = g^*(x) + \delta^n\left(\frac{\partial f(x,\mu)}{\partial \mu}\right)\Bigg|_{\mu_n=\mu_\infty} (\mu_n - \mu_\infty). \tag{A.61}$$

Transforming the point of origin to $x = x_0$ and normalizing *Equation* (A.46) by setting $g^*(0) = 1$, we arrived at the condition as follows,

$$f^{(2^n)}(\mu_n, 0) = 0. \tag{A.62}$$

From *Equations* (A.61-A.62), the universal constant is proportional to

$$\mu_n - \mu_\infty \sim \delta^{-n}. \tag{A.63}$$

(ii) *Algebraic renormalization theory*

Taking into account the period-2 solutions of *Equation* (A.46), we can solve for $x_{1\pm}, x_{2\pm}$ at $x_n = x_{n+2}$:

$$f(x_n, \mu) = x_{n+1} \text{ and } f(x_{n+1}, \mu) = x_{n+2}. \tag{A.64}$$

Using a Taylor series expansion, we can apply a perturbation to *Equation* (64) at $x_n = x_{2\pm} + \Delta x_n$, $x_{n+1} = x_{1\pm} + \Delta x_{n+1}$ and $x_{n+2} = x_{2\pm} + \Delta x_{n+2}$, that is,

$$\Delta x_{n+1} = f_1(\Delta x_n, \mu), \tag{A.65}$$

$$\Delta x_{n+2} = f_2(\Delta x_{n+1}, \mu). \tag{A.66}$$

Substituting *Equation* (A.65) into *Equation* (A.66), we obtain

$$\Delta x_{n+2} = f_2(f_1(\Delta x_n, \mu), \mu) = f(\Delta x_n, \overline{\mu}). \tag{A.67}$$

Re-scale *Equation* (67) by putting

$$x' = \alpha \Delta x, \tag{A.68}$$

into *Equation* (A.67), the renormalized *Equation* (A.46) is

$$x'_{n+2} = f\left(x'_n, \overline{\mu}_{2^{n+1}}\right), \tag{A.69}$$

where

$$\overline{\mu}_{2^{n+1}} = g\left(\overline{\mu}_{2^n}\right). \tag{A.70}$$

Equation (A.70) presents a relationship of the bifurcation values between two period doubling bifurcations. The rescaling factor α is determined by comparing *Equation* (A.69) with *Equation* (A.46). If chaos appears via the period-doubling cascade, i. e. , $\overline{\mu}_{2^{n+1}} = \overline{\mu}_{2^n} = \mu_\infty$, we can determine the universal parameter manifolds.

Quasiperiodicity route to chaos

Consider a mapping defined on the unit interval $0 \le x \le 1$, that is,

$$x_{n+1} = x_n + \Omega + f(x_n, \mu) = F(x_n, \Omega, \mu), \tag{A.71}$$

where $f(x_n, \mu)$ is a periodic modulo, i. e. , $f(x_n + 1, \mu) = f(x_n, \mu)$; and Ω is a prescribed parameter defined in the interval $0 \le \Omega \le 1$. Note in *Equation* (A.71) we have to adjust two parameters Ω, μ to generate a transition from quasiperiodicity to chaos. We can increase say, μ and to keep the rational winding number $w = p/q$ fixed to a selected value, we will have to increase Ω as well. The winding number w is an important quantity for describing the dynamics and is given by,

$$w(\Omega, \mu) = \lim_{n\to\infty} \frac{x_n - x_0}{n}, \tag{A.72}$$

Define a quantity $\Omega_{p,q}(\mu)$ which belongs to a q-cycle of the map $f(x, \mu)$ and shifted by p. This quantity generates a rational winding number $w = p/q$ and for a fixed value of μ, it can be determined from

$$F^{(q)}\left(0, \Omega_{p,q}, \mu\right) = p, \tag{A.73}$$

where $F^{(q)} = F\left(F^{(q-1)}\right)$. Choosing the winding number equal to the golden mean $w^* = \left(\sqrt{5}-1\right)/2$, we get the ensuing motion to be chaotic and the universal constants can be computed.

Intermittency route to chaos

There are three types of intermittencies, Type I, II and III. In this section, we will present only Types I and III intermittencies. The Type II intermittency is discussed in a later section under 2-D maps.

(i) Type I intermittency

Consider an iterative map with a small perturbation defined by

$$x_{n+1} = \varepsilon + x_n + \eta x_n^2, \tag{A.74}$$

where ε is a control parameter and η is a prescribed parameter. This mapping results in the Type I intermittency and is caused by the tangent bifurcation which occurs when a real eigenvalue of *Equation* (A.74) crosses the unit circle at +1. *Figure* A.10 shows the tangent bifurcation and iterative map for the Type I intermittency. Examples of this situation include the Poincare map for the Lorenz model and the iterative map for the window of period-3 solution in the chaotic band. The renormalization procedure of *Equation* (A.74) has been presented in Hu and Rudnick (1982). Also, an interested reader can refer to Guckenheimer and Holmes (1983), and Schuster (1988) for additional details.

(ii) Type III intermittency

Consider the following iterative map,

$$x_{n+1} = -(1+\varepsilon)x_n - \eta x_n^3, \tag{A.75}$$

which produces the Type III intermittency and is caused by the inverse pitchfork bifurcation. Here, we know that a real eigenvalue equals to -1 at bifurcation. *Figure* A.11 depicts the bifurcation diagram and the iterative map for the Type III intermittency.

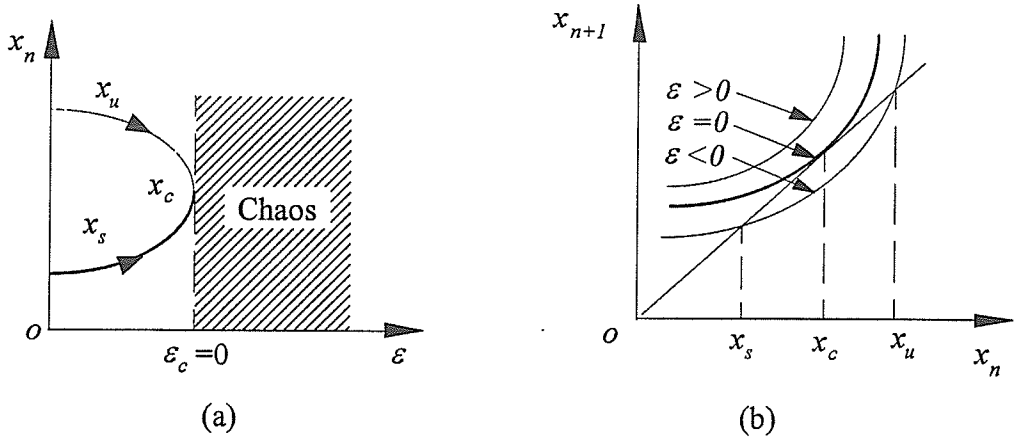

Figure A.10 *Equation* (A.74): (a) bifurcation and (b) iterative map.

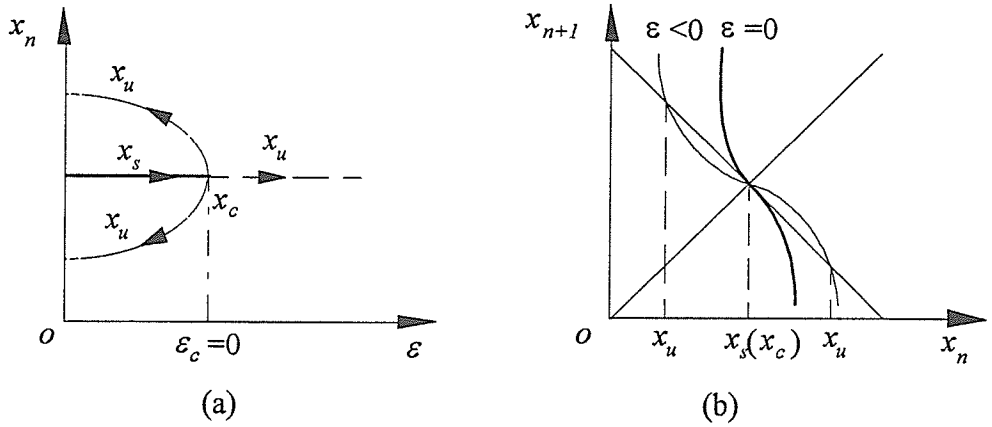

Figure A.11 *Equation* (A.75): (a) bifurcation and (b) iterative map.

A.2.2(b) Two-dimensional systems

Period doubling route to chaos

For 2-D invertible maps, the transition from regular motion to chaos takes place via a series of cascades of period-doubling bifurcations. Collect and Eckmann (1980)

introduced an exact renormalization method for this situation. However, this exact method is not convenient to use for solving the practical problems, therefore, Mackay (1983) and Helleman (1980, 1983) have developed a simpler analytical approach to renormalize the period doubling bifurcation sequences of the 2-D iterative map. This method is similar to the algebraic renormalization technique of 1-D iterative map presented earlier and will not be pursued here. For additional details, the reader can refer to the work of Eckmann and his co-workers. Eckmann et. al. (1981) developed for a conservative system, an exact renormalization procedure (see also Collet, Eckmann and Koch (1981)). Greene et. al. (1981) carried out a more complete study of 2-D Hamiltonian maps.

Quasiperiodic transition to chaos

This route to chaos is best studied via the standard map. Here, we will introduce the map and the chaotic conditions. The standard map is defined by,

$$\left.\begin{aligned} x_{n+1} &= x_n + K\sin(\theta_n) \\ \theta_{n+1} &= \theta_n + x_{n+1} \end{aligned}\right\}. \tag{A.76}$$

The critical condition of *Equation* (A.76) for transition from local to global stochasticity is $K_{cr} \approx 0.9716\cdots$. For a dissipative standard map, we have

$$\left.\begin{aligned} x_{n+1} &= (1-\delta)x_n + K\sin(\theta_n) \\ \theta_{n+1} &= \theta_n + x_{n+1} \end{aligned}\right\}, \tag{A.77}$$

where δ is the dissipative coefficient. Note that some results are given in Lichtenberg and Lieberman (1983).

Type II intermittency to chaos

Consider the following mapping which represents Type II intermittency to chaos,

$$\left.\begin{aligned} x_{n+1} &= (1+\varepsilon)x_n + \eta x_n^3 \\ \theta_{n+1} &= \theta_n + \Omega \end{aligned}\right\} \tag{A.78}$$

When a pair of complex eigenvalues of *Equation* (A.78) passes the unit circle, the subcritical Neimark bifurcation occurs. Hence, Type II intermittency results from the subcritical Neimark bifurcation as shown in *Figure* A.12.

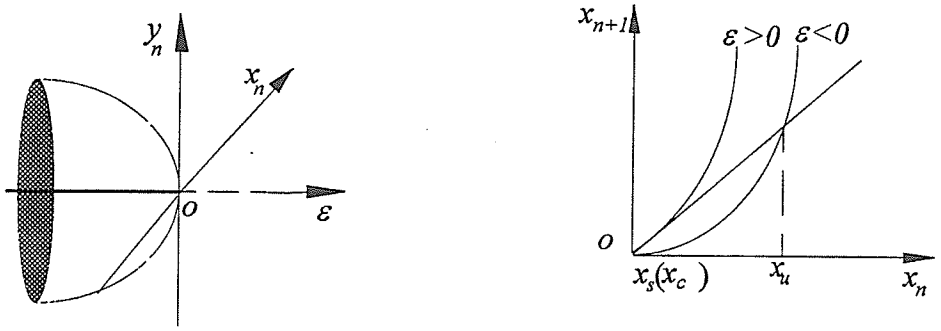

(a) (b)

Figure A.12 *Equation* (A.78): (a) Neimark bifurcation and (b) iterative map.

A.3 Fractals in Chaotic dynamics

Chaos possesses self-similar structures which imply the presence of fractals. By self-similarity, we mean that no matter how much the view is zoomed, the same basic shape is retained. Therefore, whether an object is viewed globally or locally, the same basic structure is observed. It is also possible to use fractal dimension measurements to describe chaotic or strange attractors in a dissipative dynamical system. Most fractals in chaotic dynamics have multiscales and multimeasures, and thus, they are nonuniform fractals or multifractals. Unlike fractals which are geometrically self-similar, multifractals are statistically self-similar. Some basic concepts of fractals necessary to study their characteristics in chaos will be presented next.

A.3.1 Basic concepts

What are fractals? Simply speaking, fractals are objects that possess non-integer dimension and self-similarity. They do not necessarily have characteristic sizes, namely, we cannot measure dimensional quantities such as length, area, and volume. Their geometry can only be realized using a recursion of the iterative map.

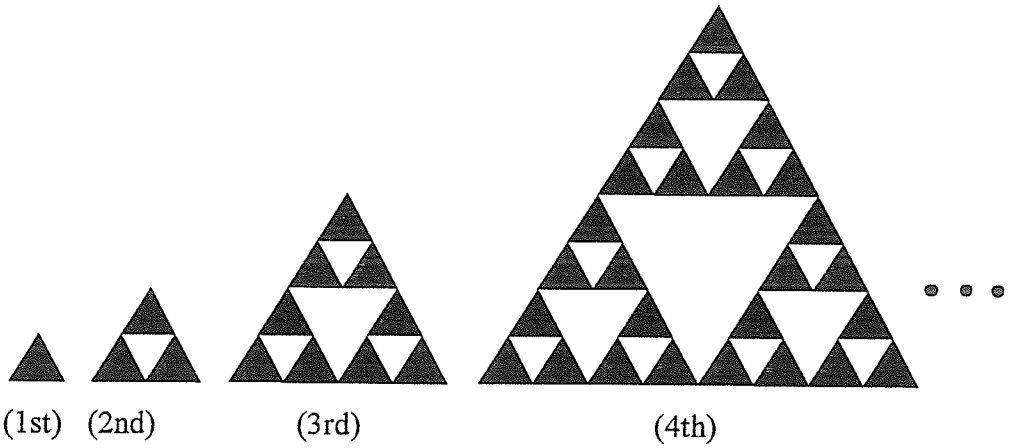

Figure A.13 The first four generations of the Sierpinski gasket fractals based on a aggregation rule.

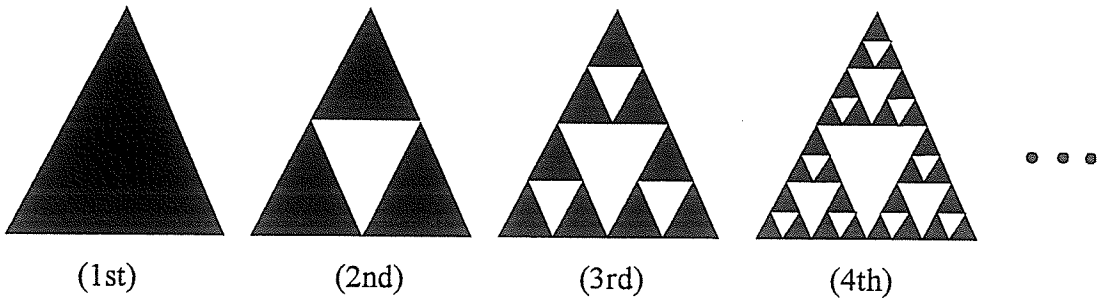

Figure A.14 The first four generations of the Sierpinski gasket fractals based on a reduction rule.

Before formally defining fractals, we would like to present the following two examples known as the Sierpinski gasket fractals. In *Figure* A.13, the fractals are generated by

addition (aggregation rule), whereas in *Figure* A.14, they are produced by subtraction (reduction rule). They possess the characteristics of self-similarity and as will be shown later, they have a non-integer dimension of 1.58. Therefore, the Sierpinski gasket is a fractal.

Table A.1 Fractal distribution of the Sierpinski gasket in *Figure* A.13

Generation No.	Scaling Size L	No. of Self-Similar Structure $N(L)$
1st	$2^0 r_0$	3^0
2nd	$2^1 r_0$	3^1
3rd	$2^2 r_0$	3^2
4th	$2^3 r_0$	3^3
⋮	⋮	⋮
*n*th	$2^n r_0$	3^n

Table A.2 Fractal distribution of the Sierpinski gasket in *Figure* A.14

Generation No.	Scaling Size L	No. of Self-Similar Structure $N(L)$
1st	$(1/2)^0 r_0$	3^0
2nd	$(1/2)^1 r_0$	3^1
3rd	$(1/2)^2 r_0$	3^2
4th	$(1/2)^3 r_0$	3^3
⋮	⋮	⋮
*n*th	$(1/2)^n r_0$	3^n

From *Figures* A.13-14, the scaling size L and number of self-similar structures $N(L)$ can be summarized in *Tables* 1 and A.

The self-similar law in *Figure* A.13, based on *Table* A.1 and the aggregation rule, is:

$$N(L) = \left(\frac{L}{r_0}\right)^D, \tag{A.79}$$

whereas, in *Figure* A.14, the self-similar law, based on *Table* A.2 and the reduction rule, is:

$$N(L) = \left(\frac{r_0}{L}\right)^D. \tag{A.80}$$

Observed that in *Equation* (A.79), the scaling size L 'grows' rapidly as would be expected under the aggregation rule. On the other hand, it is obvious from *Equation* (A.80), the scaling size L 'shrink' rapidly as would be expected under the reduction rule. To characterize a fractal, we will work with the simplest dimension, namely, the Hausdorff dimension based on a uniform formula.

Definition: For any objects with non-empty N parts which are scaled by a ratio r in the m-D Euclidean space, we have, assuming self-similarity,

$$N(L)r^D = 1. \tag{A.81}$$

Solving for the Hausdorff dimension D in *Equation* (A.81), we get

$$D = -\frac{\log N}{\log r}, \tag{A.82}$$

To formally derive *Equations* (A.81)-(A.82), we can pursue the following mathematical approach (see for example, Falconer (1990)). Define a mapping S: $E \to E$ in R^n, where

$E \in R^n$ is a closed set. Assuming a number r with $0 < r < 1$ such that $|S(x) - S(y)| = r|x - y|$ for all $x, y \in E$, we termed the mapping S a similarity since it transforms sets into geometrically similar ones. We consider a self-similar set F of E to be invariant under the mapping S if $F = \bigcup_{i=1}^{N(E)} S(F)$, where we have assumed that after mapping S has acted on F, it produced $N(E)$ similar sets. The Hausdorff dimension measure $H^D(F)$ is defined for any $\delta > 0$:

$$\mathrm{H}^D(F) = \lim_{\delta \to 0} \inf \left\{ \sum_{j=1}^{\infty} |U_j|^D : F \subset \bigcup_{i=1}^{\infty} U_j \in R^n \text{ and } 0 < |U_j| \le \delta \text{ for all } j \right\}, \qquad \text{(A.83)}$$

where $\{U_j\}$ is any non-empty $\delta-$cover of F in R^n. Applying $H^D(F)$ in *Equation* (A.83) to the self-similar set F, we get:

$$\mathrm{H}^D(F) = \sum_{i=1}^{N(E)} \mathrm{H}^D(S(F)) = N(E) r^D \mathrm{H}^D(F). \qquad \text{(A.84)}$$

In *Equation* (A.84), if the linear scale of the closed set E is now the scaling size L, we recover back *Equation* (A.81).

To compute the Hausdorff dimension for the Sierpinski gasket fractals of *Figures* A.13-A.14, we can use *Equation* (A.82) and get the scaling ratio $r = r_0/(2^n r_0) = 2^{-n}$ for *Figure* A.13, and $r = (2^{-n} r_0)/r_0 = 2^{-n}$ for *Figure* A.14 to yield:

$$D = \frac{\log(3^n)}{\log(2^n)} = \frac{\log(3)}{\log(2)} = 1.58\cdots. \qquad \text{(A.85)}$$

Another interesting point about fractals is that different fractals can have the same fractal dimension as for example, the Sierpinski gasket fractals. Take for instance, the fractals in

Figure A.15. Using *Equation* (A.82), we can calculate their Hausdorff dimension $D = 1.58\cdots$.

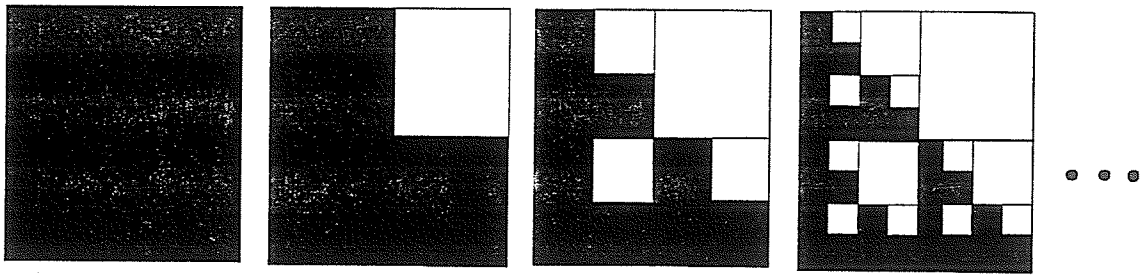

Figure A.15 Fractals generated by an iterative map in 2-D space.

Fractals can be classified as *nonrandom* and *random*, and also, depending on their scales and measures, they can be uniform or non-uniform. Uniform fractals are called simply as 'fractals' whereas nonuniform fractals are known as 'multifractals'. As expected, a nonrandom fractal is generated by a deterministic rule, such as a given iterative map and a random fractal by a stochastic rule. Random fractals whether uniform or otherwise, are always statistically self-similar. That is, they cannot be geometrically self-similar. Thus, random fractals can represent natural phenomena such as coastlines, land surfaces, roughness, cloud boundaries, etc. much better than nonrandom fractals.

A.3.2 Computer generation of fractals

Next we discussed the generation of fractals via a multigenerator (see Luo(1991) and, Leung and Luo (1992)). We will first present the generation of nonrandom fractals using a single-scale single generator, then we will generate random fractals using a single-scale multigenerator.

Nonrandom Fractals

If there are K generators in the fractal structure, and the ith generator has N_i non-empty sets with a linear scaling ratio r_i in R^n, then for all K generators, we have respectively, the equivalent nonempty sets N and linear scaling ratio r given by:

$$N = \prod_{i=1}^{K} N_i \quad \text{and} \quad r = \prod_{i=1}^{K} r_i . \tag{A.86}$$

From *Equation* (A.82), the Hausdorff dimension of this fractal is

$$D = -\frac{\sum_{i=1}^{K} \log N_i}{\sum_{i=1}^{K} \log r_i}. \tag{A.87}$$

Generalizing, if the ith generator has m_i-time action on the fractal, the Hausdorff dimension is defined by

$$D = -\frac{\sum_{i=1}^{K} m_i \log N_i}{\sum_{i=1}^{K} m_i \log r_i} \tag{A.88}$$

However, from *Equation* (A.86), it is obvious that the Hausdorff dimension is independent of the action order of the generators. This implies that the different fractals can have the same Hausdorff dimension.

Random Fractals

Basically, there are 3 possible methods of generation: random action, random generators and, combined random action and generators.

(i) Random action

From *Equation* (A.88), we can set $M = \sum_{i=1}^{K} m_i$, and manipulating, we get,

$$D = -\frac{\sum_{i=1}^{K} \frac{m_i}{M} \log N_i}{\sum_{i=1}^{K} \frac{m_i}{M} \log r_i} = -\frac{\sum_{i=1}^{K} p_i \log N_i}{\sum_{i=1}^{K} p_i \log r_i}, \tag{A.89}$$

where p_i is the action probability of the ith generator and possesses the following properties: $\sum_{i=1}^{K} p_i = 1$ and $p_i = m_i / M$.

(ii) Random generator

If the ith generator has L_i sub-generators with action probabilities p_{ij} ($\sum_{j=1}^{L_i} p_{ij} = 1$), linear scaling ratio r_{ij} and, non-empty subsets N_{ij} ($j = 1,2,\cdots L_i$), we have

$$\langle N_i \rangle = \sum_{j=1}^{L_i} p_{ij} N_{ij} \quad \text{and} \quad \langle r_i \rangle = \sum_{j=1}^{L_i} p_{ij} r_{ij}, \tag{A.90}$$

and

$$D = -\frac{\sum_{i=1}^{K} m_i \log\langle N_i \rangle}{\sum_{i=1}^{K} m_i \log\langle r_i \rangle} = -\frac{\sum_{i=1}^{K} m_i \log\left(\sum_{j=1}^{L_i} p_{ij} N_{ij}\right)}{\sum_{i=1}^{K} m_i \log\left(\sum_{j=1}^{L_i} p_{ij} r_{ij}\right)}. \tag{A.91}$$

(iii) Combined random action and random generator

Combining the previous two cases, we get the most general approach, that is, the combined random action and random generator. The Hausdorff dimension is given by,

$$D = -\frac{\sum_{i=1}^{K} p_i \log\langle N_i \rangle}{\sum_{i=1}^{K} p_i \log\langle r_i \rangle} = -\frac{\sum_{i=1}^{K} p_i \log\left(\sum_{j=1}^{L_i} p_{ij} N_{ij}\right)}{\sum_{i=1}^{K} p_i \log\left(\sum_{j=1}^{L_i} p_{ij} r_{ij}\right)} \tag{A.92}$$

A.3.3 Multifractals

Next, we turn our attention to multifractals which are fractals with nonuniform scales and measures. First, we introduce the concept of fractal measures and then fractal scales.

A.3.3 (a) Single multifractal measure

One scaling multifractal

Multifractal distributions can be described using the scaling properties of the coarse-grained measures. For example, consider $p_r(x_i)$ to be the probability measure in a box of size l_i centered at the point x_i, and that this box has a scaling ratio $r_i = l_i/L$, where L denotes its largest scale. We can define the scaling index α as a local singularity strength at position x_i (Halsey et al. (1986)):

$$p_{r_i}(x_i) \sim r_i^{\alpha}. \tag{A.93}$$

Consider the scaling of the qth order moment of $p_{r_i}(x_i)$ with box size l_i. A new auxiliary parameters $\tau(q)$ is now introduced via the following equation,

$$\sum_i \left[p_{r_i}(x_i)\right]^q = r_i^{\tau(q)}. \tag{A.94}$$

Solving *Equation* (A.94) for $\tau(q)$ we get

$$\tau(q) = \lim_{r_i \to \infty} \frac{\log\left(\sum_i \left[p_{r_i}(x_i)\right]^q\right)}{\log(r_i)}. \tag{A.95}$$

Next another dimension is introduced, namely, the generalized dimension which is given by

$$D_q = \frac{\tau(q)}{q-1}. \tag{A.96}$$

Consider a number $N_{r_i}(\alpha)$ of a box of size r_i, which has a value of α in the band $d\alpha$. The fractal spectrum $f(\alpha)$ is defined as

$$N_{r_i}(x_i) = \rho(\alpha) r_i^{-f(\alpha)}\, d\alpha, \tag{A.97}$$

where $\rho(\alpha)$ is a nonsingular weighting function. In view of *Equations* (A.93)-(A.94), *Equation* (A.97) when summed for all α we get:

$$\sum_i \left[p_{r_i}(x_i)\right]^q = \int_0^\alpha \rho(\xi) r_i^{q\xi - f(\xi)}\, d\xi \sim r_i^{\tau(q)}. \tag{A.98}$$

Consider $r = \max_i(r_i) \to 0$, we obtain

$$\tau(q) = q\alpha - f(\alpha). \tag{A.99}$$

Differentiating *Equation* (A.99) with respect to q yields

$$\alpha = \frac{d\tau(q)}{dq} \quad \text{and} \quad q = \frac{df(\alpha)}{d\alpha}. \tag{A.100}$$

Multiscaling fractals

Before presenting a discussion of the multiscaling-fractals, it is necessary to introduce Hausdorff dimension for fractals with multiscales. Deriving in the same fashion a was done in *Section* A.3.1, we can define a group of mappings S_i: $E \to E$ in R^n, which $E \in R^n$ is a closed set. Assuming a number r_i with $0 < r_i < 1$ such as $|S_i(x) - S_i(y)| = r_i|x - y|$ for all $x, y \in E$, we termed the mapping S_i similarities. Next, we consider a self-similar set F of E to be invariant under the mapping S_i if $F = \bigcup_{i=1}^{N(E)} S_i(F)$ where we have assumed that after mapping S_i has acted on F, it produced $N(E)$ similar sets. We can apply in an analogous fashion, $H^D(F)$ in *Equation* (A.83) to the self-similar set F, and get:

$$\mathrm{H}^D(F) = \sum_{i=1}^{N(E)} \mathrm{H}^D(S_i(F)) = \sum_{i=1}^{N(E)} r_i^D \mathrm{H}^D(F). \tag{A.101}$$

Simplifying *Equation* (A.101) leads to the following expression for calculating the Hausdorff dimension of multifractals:

$$\sum_{i=1}^{N(E)} r_i^D = 1. \tag{A.102}$$

Next we look at the measure of a multifractal. Considering a multiscaling box as a measure of fractals, Grassberger (1983a, b, c), and Halsey et al. (1986) introduced a general spectrum of fractal dimensions. If the scaling ratio $r_i = l_i/L$ of every box is variable, a partition sum can be similarly defined as

$$\Gamma(q,\tau,r_i) = \sum_i \frac{p_i^q}{r_i^{\tau(q)}}, \tag{A.103}$$

where the auxiliary parameter τ is now given by,

$$\tau(q) = (q-1)D_q. \tag{A.104}$$

For a chosen value of q, for $r = \max_i(r_i) \to 0$, the partition sum goes from zero to infinity, and we get:

$$\Gamma(q,\tau(q),r_i) = \begin{cases} 0 & \tau < \tau(\mathrm{q}) \\ \infty & \tau > \tau(\mathrm{q}). \\ \text{constant} & \tau = \tau(\mathrm{q}) \end{cases} \tag{A.105}$$

Note *Equations* (A.99)-(A.100) are still available for use in the computation of the scaling index and fractal spectrum.

A.3.3 (b) Joint multifractal measure

Assume $p_{ij}(x_i)$ denotes the jth measure in the total m-probability measures, for a box of size l_i, centered at the point x_i where $j = 1,2,\cdots,m$. Assume also, this box has a scaling

ratio $r_i = l_i/L$, where L is the largest scale. The scaling index $\alpha_j(q_1, q_2 \cdots q_m)$ is defined as a local singularity strength at position x_i for probability $p_{ij}(x_i)$. That is,

$$p_{ij}(x_i) \sim r_i^{\alpha_j}. \tag{A.106}$$

Similarly, we can define a partition sum:

$$\Gamma\left(\{q_1, q_2, \cdots q_m\}, \tau(q_1, q_2, \cdots q_m), \{r_1, r_2, \cdots r_m\}\right) = \sum_i \frac{\prod_{j=1}^{m} p_{ij}^{q_j}}{r_i^{\tau(q_1, q_2, \cdots q_m)}}, \tag{A.107}$$

where the auxiliary parameter $\tau(q_1, q_2, \cdots q_m)$ is now given by

$$\tau(0, \cdots, q_j, \cdots, 0) = (q_j - 1) D_{q_j}. \tag{A.108}$$

Choosing a q and for $r = \max_i(r_i) \to 0$, the partition sum goes from zero to infinity, and we get:

$$\Gamma\left(\{q_1, q_2, \cdots q_m\}, \tau(q_1, q_2, \cdots q_m), \{r_1, r_2, \cdots r_m\}\right) = \begin{cases} 0 & \tau < \tau(q_1, q_2, \cdots q_m) \\ \infty & \tau > \tau(q_1, q_2, \cdots q_m) \\ \text{constant} & \tau = \tau(q_1, q_2, \cdots q_m) \end{cases}. \tag{A.109}$$

Consider a number $N_{r_i}(\alpha_1, \alpha_2, \cdots, \alpha_m)$ of the boxes of size r_i, which have values of $(\alpha_1, \alpha_2, \cdots \alpha_m)$ in a volume $\prod_{i=1}^{m} d\alpha_j$,, the fractal spectrum $f(\alpha_1, \alpha_2, \cdots \alpha_m)$ is defined by:

$$N_{r_i}(\alpha_1, \alpha_2, \cdots, \alpha_m) = \rho(\alpha_1, \alpha_2, \cdots, \alpha_m) r_i^{-f(\alpha_1, \alpha_2, \cdots, \alpha_m)} \prod_{i=1}^{m} d\alpha_j. \tag{A.110}$$

For all $(\alpha_1, \alpha_2, \cdots \alpha_m)$, and in view of *Equations* (A.106) and (A.109), *Equation* (A.107) becomes

$$\sum_i \frac{\prod_{j=1}^{m}\left[p_{ij}(x_i)\right]^{q_j}}{r_i^{\tau(\alpha_1,\alpha_2,\cdots,\alpha_m)}} = \int \rho(\alpha_1,\alpha_2,\cdots,\alpha_m)\left(\prod_{j=1}^{m} d\alpha_j\right) r_i^{-\tau(q_1,q_2,\cdots,q_m)+\sum_{j=1}^{m} q_j\alpha_j - f(\alpha_1,\alpha_2,\cdots,\alpha_m)} . \quad \text{(A.111)}$$

For $r = \max_i(r_i) \to 0$, we get

$$\tau(q_1,q_2,\cdots,q_m) = \sum_{j=1}^{m} q_j\alpha_j - f(\alpha_1,\alpha_2,\cdots,\alpha_m). \quad \text{(A.112)}$$

Differentiating *Equation* (A.112) with respect to q_i and α_i yields

$$\alpha_j(q_1,q_2,\cdots,q_m) = \frac{\partial\tau(q_1,q_2,\cdots,q_m)}{\partial q_j} \text{ and } q_j = \frac{\partial f(\alpha_1,\alpha_2,\cdots,\alpha_m)}{\partial\alpha_j}. \quad \text{(A.113)}$$

APPENDIX B

DUFFING OSCILLATOR

B.1 Results for the Undamped Duffing oscillator

Since the solutions for Cases I and IV(c) Duffing oscillators are already given in *Chapter* 3, we only list the corresponding results for Cases II-IV(b) oscillators in this appendix. These results are obtained in the same manner as for the Case I oscillator.

Case II The results are:

$$E_0 = \frac{k^2 {\alpha_1}^2}{\left(1+k^2\right)^2 \alpha_2}, \quad e^2 = \frac{2k^2\alpha_1}{\left(1+k^2\right)\alpha_2}, \quad \omega = \frac{\sqrt{\alpha_2}e\pi}{2\sqrt{2}kK(k)}, \tag{B.1}$$

$$\Omega = (2n-1)\omega_{2n-1}, \tag{B.2}$$

$$2Q_0\Omega\pi\sqrt{\frac{2}{\alpha_2}}\operatorname{csch}\left[\left(n-\frac{1}{2}\right)\pi\frac{K'\left(k_{2n-1}\right)}{K\left(k_{2n-1}\right)}\right]|G_1| = 0.9716354, \tag{B.3}$$

$$2Q_0\pi\Omega\sqrt{\frac{2}{\alpha_2}}\operatorname{csch}\left[\left(n-\frac{1}{2}\right)\pi\frac{K'\left(k_{2n-1}\right)}{K\left(k_{2n-1}\right)}\right] = \left|E_0^{2n+1} - E_0^{2n-1}\right|; \tag{B.4}$$

$$\mathrm{G}_0 = \frac{\pi^2}{4e^2\left(k'_{2n-1}\right)^2 K\left(k_{2n-1}\right)^3}\left[K\left(k_{2n-1}\right) - \frac{1+\left(k_{2n-1}\right)^2}{1-\left(k_{2n-1}\right)^2}E\left(k_{2n-1}\right)\right], \tag{B.5}$$

$$G_1 = -\frac{2\Omega\alpha_2}{k_{2n-1}\left(k'_{2n-1}\right)^2}\left(\frac{1+\left(k_{2n-1}\right)^2}{\alpha_1}\right)^{\frac{5}{2}}\left[K\left(k_{2n-1}\right)-\frac{1+\left(k_{2n-1}\right)^2}{1-\left(k_{2n-1}\right)^2}E\left(k_{2n-1}\right)\right], \tag{B.6}$$

$$Q_{2n-1} = \frac{\sqrt{2}\Omega}{\sqrt{\alpha_2}(2n-1)}\operatorname{sech}\left[\pi\left(n-\frac{1}{2}\right)\frac{K'\left(k_{2n-1}\right)}{K\left(k_{2n-1}\right)}\right], \tag{B.7}$$

$$Q_{2n+1} = \frac{\sqrt{2}\Omega}{\sqrt{\alpha_2}(2n+1)}\operatorname{sech}\left[\pi\left(n+\frac{1}{2}\right)\frac{K'\left(k_{2n+1}\right)}{K\left(k_{2n+1}\right)}\right]. \tag{B.8}$$

The chaotic conditions obtained using the Chirikov overlap criterion and the renormalization group methods are respectively, of the same form as given by *Equations* (3.33) and (3.35).

Case III The results are:

$$k = \frac{1}{\sqrt{2}},\ h = \left(\frac{4E_0}{\alpha_2}\right)^{1/4},\ K(k) \approx 1.8541,\ \omega = \frac{\sqrt{\alpha_2}h\pi}{2K(k)}, \tag{B.9}$$

$$2Q_0\Omega\pi\sqrt{\frac{2}{\alpha_2}}\operatorname{sech}\left[\left(n-\frac{1}{2}\right)\pi\right]\left|G_1\right| = 0.9716354, \tag{B.10}$$

$$2Q_0\pi\Omega\sqrt{\frac{2}{\alpha_2}}\operatorname{sech}\left[\left(n-\frac{1}{2}\right)\pi\right] = \left|E_0^{2n+1} - E_0^{2n-1}\right|, \tag{B.11}$$

$$G_0 = \frac{\pi^2}{2h^2K\left(k_{2n-1}^c\right)^2}, \tag{B.12}$$

$$G_1 = -\frac{8\Omega K\left(k_{2n-1}^c\right)}{\alpha_2^{3/2}h^5}. \tag{B.13}$$

$$Q_{2n-1}=\frac{\sqrt{2}\Omega}{\sqrt{\alpha_2}(2n-1)\cosh\left[\pi\left(n-\frac{1}{2}\right)\right]}, \tag{B.14}$$

$$Q_{2n+1}=\frac{\sqrt{2}\Omega}{\sqrt{\alpha_2}(2n+1)\cosh\left[\pi\left(n+\frac{1}{2}\right)\right]}. \tag{B.15}$$

To derive the chaotic conditions we substitute *Equations* (B.14)-(B.15) into *Equations* (3.33) and (3.35) and the following explicit formulas derived based on the Chirikov overlap criterion and the renormalization group technique respectively are:

$$Q_0=\frac{K\left(k_{2n-1}^c\right)^3\Omega^3\left\{\sqrt{(2n-1)\,\mathrm{sech}\left[\pi(\mathrm{n}-1/2)\right]}+\sqrt{(2n+1)\,\mathrm{sech}\left[\pi(\mathrm{n}+1/2)\right]}\right\}^{-2}}{(2n-1)^3(2n+1)\pi^3\sqrt{\alpha_2}}, \tag{B.16}$$

$$Q_0=\frac{0.49K\left(k_{2n-1}^c\right)^3\Omega^3\left\{\sqrt{(2n-1)\,\mathrm{sech}\left[\pi(\mathrm{n}-1/2)\right]}+\sqrt{(2n+1)\,\mathrm{sech}\left[\pi(\mathrm{n}+1/2)\right]}\right\}^{-2}}{(2n-1)^3(2n+1)\pi^3\sqrt{\alpha_2}}. \tag{B.17}$$

Case IV(a) The results are:

$$E_0=\frac{\left(1-k^2\right)k^2\alpha_1^2}{\left(2k^2-1\right)^2\alpha_2},\quad e^2=\frac{2k^2\alpha_1}{\left(2k^2-1\right)\alpha_2},\quad \omega=\frac{\sqrt{\alpha_2}e\pi}{2\sqrt{2}kK(k)}, \tag{B.18}$$

$$\Omega=(2n-1)\omega_{2n-1}, \tag{B.19}$$

$$2Q_0\Omega\pi\sqrt{\frac{2}{\alpha_2}}\mathrm{sech}\left[\left(n-\frac{1}{2}\right)\pi\frac{K'\left(k_{2n-1}\right)}{K\left(k_{2n-1}\right)}\right]|G_1|=0.9716354, \tag{B.20}$$

$$2Q_0\Omega\pi\sqrt{\frac{2}{\alpha_2}}\mathrm{sech}\left[\left(n-\frac{1}{2}\right)\pi\frac{K'\left(k_{2n-1}\right)}{K\left(k_{2n-1}\right)}\right]=\left|E_0^{2n+1}-E_0^{2n-1}\right|, \tag{B.21}$$

$$G_0 = \frac{\pi^2}{4e^2 K(k_{2n-1})^3}\left[K(k_{2n-1}) - \frac{1-2(k_{2n-1})^2}{1-(k_{2n-1})^2}E(k_{2n-1})\right], \tag{B.22}$$

$$G_1 = -\frac{2\Omega\alpha_2}{(k_{2n-1})^2}\left(\frac{2(k_{2n-1})^2-1}{\alpha_1}\right)^{\frac{5}{2}}\left[K(k_{2n-1}) - \frac{1-2(k_{2n-1})^2}{1-(k_{2n-1})^2}E(k_{2n-1})\right], \tag{B.23}$$

$$Q_{2n-1} = \frac{\sqrt{2}\Omega}{\sqrt{\alpha_2}(2n-1)}\operatorname{sech}\left[\pi\left(n-\frac{1}{2}\right)\frac{K'(k_{2n-1})}{K(k_{2n-1})}\right], \tag{B.24}$$

$$Q_{2n+1} = \frac{\sqrt{2}\Omega}{\sqrt{\alpha_2}(2n+1)}\operatorname{sech}\left[\pi\left(n+\frac{1}{2}\right)\frac{K'(k_{2n+1})}{K(k_{2n+1})}\right]. \tag{B.25}$$

The chaotic conditions computed via the Chirikov overlap criterion and the renormalization group technique are respectively, of the same form as listed in *Equation* (3.33) and (3.35).

Case IV(b) The results are:

$$E_0 = \frac{(k^2-1)\alpha_1^2}{(2-k^2)^2\alpha_2}, \quad e^2 = \frac{2\alpha_1}{(2-k^2)\alpha_2}, \quad \omega = \frac{\sqrt{\alpha_2}e\pi}{\sqrt{2}K(k)}; \tag{B.26}$$

$$\Omega = n\omega_n, \tag{B.27}$$

$$Q_0\pi\Omega\sqrt{\frac{2}{\alpha_2}}\operatorname{sech}\left[n\pi\frac{K'(k_n)}{K(k_n)}\right]|G_1| = 0.9716354, \tag{B.28}$$

$$Q_0\pi\Omega\sqrt{\frac{2}{\alpha_2}}\operatorname{sech}\left[n\pi\frac{K'(k_n)}{K(k_n)}\right] = \left|E_0^{n+1} - E_0^n\right|, \tag{B.29}$$

where we have,

$$G_1 = -\frac{\Omega\alpha_2}{(k_n)^4}\left(\frac{2-(k_n)^2}{\alpha_1}\right)^{\frac{5}{2}}\left[2K(k_n)-\frac{2-(k_n)^2}{1-(k_n)^2}E(k_n)\right]. \tag{B.30}$$

The chaotic conditions for this oscillator based on the Chirikov overlap criterion and the renormalization group technique respectively are:

$$Q_0 = \frac{\Omega^2}{4n^2(n+1)^2 G_0}\left(\frac{1}{\sqrt{Q_n}+\sqrt{Q_{n+1}}}\right)^2, \tag{B.31}$$

$$Q_0 = \frac{0.49\Omega^2}{4n^2(n+1)^2 G_0}\left(\frac{1}{\sqrt{Q_n}+\sqrt{Q_{n+1}}}\right)^2, \tag{B.32}$$

in which

$$G_0 = \frac{\pi^2}{e^2 k_n^4 K(k_n)^3}\left[2K(k_n)-\frac{2-(k_n)^2}{1-(k_n)^2}E(k_n)\right], \tag{B.33}$$

$$Q_n = \frac{\sqrt{2}\Omega}{\sqrt{\alpha_2 n}}\operatorname{sech}\left[\pi n\frac{K'(k_n)}{K(k_n)}\right], \tag{B.34}$$

$$Q_{n+1} = \frac{\sqrt{2}\Omega}{\sqrt{\alpha_2 (n+1)}}\operatorname{sech}\left[\pi (n+1)\frac{K'(k_{n+1})}{K(k_{n+1})}\right]. \tag{B.35}$$

B.2 Results for the Weakly Damped Duffing Oscillator

The results for Cases I and IV(c) oscillators are already presented in *Chapter* 3 and in this appendix, we list only the solutions for Cases II, III, IV(a) and IV(b) oscillators.

Case II $P_{mcr} > P,\ 2P_{mcr} > EA$

$$I_1 = \frac{8\alpha_1^{\frac{3}{2}}}{3\left(1+k^2\right)^{\frac{3}{2}}\alpha_2}\left[\left(1+k^2\right)E(k)-(1-k^2)K(k)\right], \tag{B.36}$$

$$I_2 = 2\pi\Omega\sqrt{\frac{2}{\alpha_2}}\operatorname{csch}\left[\left(n-\frac{1}{2}\right)\pi\right]\sin(\Omega t_0). \tag{B.37}$$

Case III $P_{mcr} = P,\ 2P_{mcr} > EA$

$$I_1 = \frac{16}{3\left((2n-1)\right)^3\alpha_2}K(k)^4\Omega^3, \tag{B.38}$$

$$I_2 = 2\pi\Omega\sqrt{\frac{2}{\alpha_2}}\operatorname{sech}\left[\left(n-\frac{1}{2}\right)\pi\right]\sin(\Omega t_0). \tag{B.39}$$

Case IV(a) $P_{mcr} < P,\ 2P_{mcr} < EA,\ E_0 > 0$

$$I_1 = \frac{8\alpha_1^{\frac{3}{2}}}{3\left(1-k^2\right)^{\frac{3}{2}}\alpha_2}\left[\left(2k^2-1\right)E(k)+(1-k^2)K(k)\right], \tag{B.40}$$

$$I_2 = 2\pi\Omega\sqrt{\frac{2}{\alpha_2}}\operatorname{sech}\left[\left(n-\frac{1}{2}\right)\pi\frac{K'}{K}\right]\sin(\Omega t_0). \tag{B.41}$$

Case IV(b) $P_{mcr} < P,\ 2P_{mcr} < EA,\ E_0 < 0$

$$I_1 = \frac{4\alpha_1^{\frac{3}{2}}}{3\left(2-k^2\right)^{\frac{3}{2}}\alpha_2}\left[\left(2-k^2\right)E(k)-2(1-k^2)K(k)\right], \tag{B.42}$$

$$I_2 = \frac{\pi\sqrt{2}\Omega}{\sqrt{\alpha_2}}\operatorname{sech}\left[n\pi\frac{K'}{K}\right]\sin(\Omega t_0). \tag{B.43}$$

B.3 A STOCHASTIC LAYER

Invoking the three assumptions for a conservative system stated in *Section* 4.1, we can introduce the following definition pertaining to the stochastic layer near either a homoclinic or heteroclinic orbit.

Definition:

Considering the conservative part of *Equation* (4.1), there exist $\delta > 0$ in the energy space for all $\varepsilon_1 > 0$ in the phase space. That is, for the separatrix energy E_0, we have

$$\left|E_\alpha - E_0\right| < \delta \text{ (or } \left|E_\beta - E_0\right| < \delta \text{).} \tag{B.44}$$

The sets $\Gamma^\alpha = \left\{q^\alpha(t) \middle| \left|q^\alpha(t) - q^0(t)\right| \le \varepsilon_1, t \in R\right\}$ and $\Gamma^\beta = \left\{q^\beta(t) \middle| \left|q^\beta(t) - q^0(t)\right| \le \varepsilon_1, t \in R\right\}$ are respectively termed as the *domains* of the α-orbit and β-orbit near Γ^0 (see *Figure* 4.1). The union of the α-orbit and β-orbit domains with Γ^0, namely, $\Gamma = \Gamma^\alpha \cup \Gamma^\beta \cup \Gamma^0$ produces a larger domain covering both the α and β-orbits. If the phase trajectory of *Equation* (4.1) exists in this domain, then this enlarged domain is defined as the *stochastic layer* of *Equation* (4.1).

Proof of Theorem 4.1:

From assumption (iii) in *Section* 4.1, all the α-orbit (or β-orbit) are periodic and elliptic (Lichtenberg and Lieberman (1992), Abraham and Marsden (1978)), therefore the nonlinear period of the α-orbit (or β-orbit) is

$$T = \frac{2\pi}{\omega} = 2\pi\left(\frac{\partial H_0}{\partial J}\right)^{-1} = F(K(k)), \tag{B.45}$$

where the action variable $J = \frac{1}{2\pi}\oint_{q^\alpha} y dx$ for the given energy E_α of a closed orbit q^α, the modulus $k = F_1(E_\alpha)$ and the functions F and F_1 is all differentiable in E_α. Expanding the

kernel $K(k)$ of F (Cayley 1895), we have:

$$K(k)=\ln\left(\frac{4}{k'}\right)+\frac{1^2}{2^2}\left(\ln\left(\frac{4}{k'}\right)-1\right)(k')^2+\text{h.o.t.}, \tag{B.46}$$

where $k'=\sqrt{1-k^2}$. Note that this series is rapidly convergent as $k\to 1$. That is, for small $\varepsilon>0$, we have

$$\frac{\frac{1}{4}\left[\ln\left(\frac{4}{k'}\right)-1\right](k')^2}{\ln\left(\frac{4}{k'}\right)}=\frac{1-k^2}{4}\left[1-\frac{2}{\ln\left(\frac{16}{1-k^2}\right)}\right]\equiv o(\varepsilon), \tag{B.47}$$

which is identical to *Equation* (4.6). Note that *Equation* (B.47) indicates the orbit q^α approaches its separatrix q^0 as $k\to 1$. From *Equations* (B.45) and (B.47), the energy band $|E_\alpha-E_0|<\delta$ near the separatrix q^0 can be determined and invoking the definition, this band is the stochastic layer. Likewise, we can carry out the same process for the β-orbit.

Proof of Theorem 4.2:

If the elliptic orbits of the Hamiltonian vector field $f(x)$ in *Equation* (4.1) satisfy *Equation* (B.47), there exists a neighborhood $N(E_0)$ of the separatrix energy E_0 given by

$$N(E_0)=\left\{E_\alpha\cup E_\beta \;\middle|\; |E_\alpha-E_0|<\delta \text{ and } |E_\beta-E_0|<\delta\right\}. \tag{B.48}$$

If the phase trajectory of *Equation* (4.1) is located at the energy orbits of the unperturbed Hamiltonian and these orbits satisfy *Equation* (B.48), then this neighborhood is a stochastic layer. In this neighborhood, the energy increment of *Equation* (4.1) ΔH is exactly determined by

$$|\Delta H|=\left\{\left|\tilde{E}_\alpha-E_0\right| \text{ or } \left|\tilde{E}_\beta-E_0\right|\right\}\le\delta, \tag{B.49}$$

where $\widetilde{E}_\alpha$ (or $\widetilde{E}_\beta$) is the energy of the α-orbit (or β-orbit) of the unperturbed Hamiltonian for one cycle of the separatrix. Since the stochastic layer of *Equation* (4.1) is composed of resonance overlap, different structures of stochastic layer are subjected to different resonance overlaps. If the resonance of the α-orbit (or β-orbit) in the stochastic layer is governed by $\omega = m\Omega/n$, this resonant orbit energy satisfies *Equation* (B.48). Therefore using *Equation* (B.45) and invoking $\omega = m\Omega/n$ and $k = F_1\left(E_\alpha^{m/n}\right)$ yields the resonant energy of the α-orbit. That is,

$$E_\alpha^{m/n} = F_1^{(-1)}\left(K^{(-1)}\left(F^{(-1)}\left(\frac{2n\pi}{m\Omega}\right)\right)\right). \tag{B.50}$$

Likewise, the resonant energy of the β-orbit $E_\beta^{m/n}$ can also be similarly determined. Setting $\widetilde{E}_\alpha = E_\alpha^{m/n} = E_1^i$ (or $\widetilde{E}_\beta = E_\beta^{m/n} = E_2^j$) in *Equation* (B.49), we have

$$|\Delta H| = \left\{\left|E_1^i - E_0\right| \text{ or } \left|E_2^j - E_0\right|\right\} \le \delta, \tag{B.51}$$

where *Equation* (B.50) can be used for evaluating the resonant energy. Observe that *Equation* (B.51) is identical to *Equation* (4.7).

To determine the disappearance of a stochastic layer, we must set the minimum condition to the largest energy of the resonant orbit in the stochastic layer. That is,

$$|\Delta H| = \min_{i,j}\max\left\{\left|E_1^i - E_0\right|,\ \left|E_2^j - E_0\right|\right\} \le \delta. \tag{B.52}$$

Proof of *Theorem* 4.3:

This proof is similar to the proof of *Theorem* 4.2. For disappearance of a stochastic layer, the global stochastic layer must satisfy $|E_\alpha - E_0| > \delta$ (or $|E_\beta - E_0| > \delta$), i.e.,

$$|\Delta H| = \left\{\left|E_\alpha^i - E_0\right| \text{ or } \left|E_\beta^j - E_0\right|\right\} > \delta. \tag{B.53}$$

APPENDIX C

IMPACT OSCILLATOR

C.1 Bouncing Ball

The various equations pertinent to the bouncing ball of *Chapter* 7 are presented here.

C.1.1 Periodic motion

Since the results of the period-1 motion are already given in *Chapter* 7, we will only list the corresponding results for period-k motion where $k \geq 2$ here.

Period-2 motion:

The coefficients for the period-2 motion are:

$$m_1^q = 1 - \cos(\omega qnT), \tag{C.1}$$

$$m_2^q = \sin(\omega qnT), \tag{C.2}$$

$$m_3^q = qgnT, \tag{C.3}$$

$$K^q = \left[2 - 2\cos(\omega qnT) - \omega qnT \sin(\omega qnT)\right], \tag{C.4}$$

$$K_1^q = gqnT\left[1 - \cos(\omega qnT) - \frac{1}{2} qnT\omega \sin(\omega qnT)\right], \tag{C.5}$$

$$K_2^q = 1 - \cos(\omega qnT) + qnT\omega \sin(\omega qnT), \tag{C.6}$$

$$K_3^q = 1-\cos(q\omega nT), \tag{C.7}$$

$$K_4^q = qnTg\left\{-\frac{\omega qnT}{2}\left[1+\cos(\omega qnT)\right]+\sin(\omega qnT)\right\}, \tag{C.8}$$

$$K_5^q = -\omega qnT\cos(\omega qnT)+\sin(\omega qnT), \tag{C.9}$$

$$K_6^q = -\omega qnT+\sin(q\omega nT), \tag{C.10}$$

$$L^q = K^q - m_1^q K_3^q - m_2^q K_6^q, \tag{C.11}$$

$$L_1^q = -m_3^q K^q + m_1^q K_1^q + m_2^q K_4^q, \tag{C.12}$$

$$L_2^q = -K^q + m_1^q K_2^q + m_2^q K_5^q. \tag{C.13}$$

Period-k motion:

Similarly, the coefficients for the period-k motion are:

$$m_1^{q_j} = 1-\cos\left(\omega q_j nT\right), \tag{C.14}$$

$$m_2^{q_j} = \sin\left(\omega q_j nT\right), \tag{C.15}$$

$$m_3^{q_j} = q_j gnT, \tag{C.16}$$

$$K^{q_j} = 2-2\cos\left(\omega q_j nT\right)-\omega q_j nT\sin\left(\omega q_j nT\right), \tag{C.17}$$

$$K_1^{q_j} = gq_j nT\left[1-\cos\left(\omega q_j nT\right)-\frac{1}{2}q_j nT\omega\sin\left(\omega q_j nT\right)\right], \tag{C.18}$$

$$K_2^{q_j} = 1-\cos\left(\omega q_j nT\right)-q_j nT\omega\sin\left(\omega q_j nT\right), \tag{C.19}$$

$$K_3^{q_j} = 1-\cos\left(\omega q_j nT\right), \tag{C.20}$$

$$K_4^{q_j} = q_j nTg\left\{-\frac{\omega q_j nT}{2}\left[1+\cos\left(\omega q_j nT\right)\right]+\sin\left(\omega q_j nT\right)\right\}, \tag{C.21}$$

$$K_5^{q_j} = -q_j nT\cos\left(\omega q_j nT\right)+\sin\left(\omega q_j nT\right), \tag{C.22}$$

$$K_6^{q_j} = -q_j nT+\sin\left(\omega q_j nT\right), \tag{C.23}$$

$$L^{q_j} = K^{q_j} - m_1^{q_j} K_3^{q_j} - m_2^{q_j} K_6^{q_j}, \tag{C.24}$$

$$L_1^{q_j} = -m_3^{q_j} K^{q_j} + m_1^{q_j} K_1^{q_j} + m_2^{q_j} K_4^{q_j}, \tag{C.25}$$

$$L_2^{q_j} = -K^{q_j} + m_1^{q_j} K_2^{q_j} + m_2^{q_j} K_5^{q_j}. \tag{C.26}$$

C.1.2 Stability and bifurcation

The Jacobian of the mapping P at the ith impact of the bouncing ball, DP is defined by

$$DP = \left[\frac{\partial P\left(t_{i+1},\dot{y}_{i+1}\right)}{\partial\left(t_i,\dot{y}_i\right)}\right] = \begin{pmatrix} \dfrac{\partial t_{i+1}}{\partial t_i} & \dfrac{\partial t_{i+1}}{\partial \dot{y}_i} \\ \dfrac{\partial \dot{y}_{i+1}}{\partial t_i} & \dfrac{\partial \dot{y}_{i+1}}{\partial \dot{y}_i} \end{pmatrix}_{\left(t_i,\dot{y}_i\right)}, \tag{C.27}$$

where

$$\frac{\partial t_{i+1}}{\partial t_i} = \frac{1}{\dot{y}_{i+1}}\left\{-e\dot{y}_i+\left[A\omega^2\sin\left(\omega t_{i+1}+\varphi\right)-g\right]\left(t_{i+1}-t_i\right)\right\}, \tag{C.28}$$

$$\frac{\partial t_{i+1}}{\partial \dot{y}_i} = \frac{e}{\dot{y}_{i+1}}\left(t_{i+1}-t_i\right), \tag{C.29}$$

$$\frac{\partial \dot{y}_{i+1}}{\partial t_i} = \left[A\omega^2\sin\left(t_{i+1}+\varphi\right)-g\right]\frac{\partial t_{i+1}}{\partial t_i} - \left[A\omega^2\sin\left(t_i+\varphi\right)-g\right], \tag{C.30}$$

$$\frac{\partial \dot{y}_{i+1}}{\partial \dot{y}_i} = \left[A\omega^2\sin\left(\omega t_{i+1}+\varphi\right)-g\right]\frac{\partial t_{i+1}}{\partial \dot{y}_i} - e. \tag{C.31}$$

For period-k motion of the bouncing ball we have $\boldsymbol{x}_{i+k} = P^{(k)}\boldsymbol{x}_i$, where $P^{(k)} = \underbrace{P \circ P \circ \cdots \circ P}_{k}$.

Its Jacobian at its fixed point is

$$DP^{(k)} = \underbrace{DP \cdots DP}_{k} = \left[\frac{\partial P(t_{i+k}, \dot{y}_{i+k})}{\partial(t_{i+k-1}, \dot{y}_{i+k-1})}\right] \cdots \left[\frac{\partial P(t_{i+1}, \dot{y}_{i+1})}{\partial(t_i, \dot{y}_i)}\right]_{\begin{pmatrix} t_{i+k} \\ \dot{y}_{i+k} \end{pmatrix} = \begin{pmatrix} t_i + 2n\pi/\omega \\ \dot{y}_i \end{pmatrix}}, \tag{C.32}$$

from which the trace $Tr\left(DP^{(k)}\right)$ and the determinant $Det\left(DP^{(k)}\right)$ of *Equation* (C.32) can be easily evaluated. Its eigenvalues are then computed from,

$$\lambda_{1,2} = \frac{Tr\left(DP^{(k)}\right) \pm \sqrt{Tr\left(DP^{(k)}\right)^2 - 4Det\left(DP^{(k)}\right)}}{2}. \tag{C.33}$$

Setting one of eigenvalues of (C.33) to -1 we get the condition for the period doubling bifurcation of the period k motion, that is,

$$Tr\left(DP^{(k)}\right) + Det\left(DP^{(k)}\right) + 1 = 0. \tag{C.34}$$

On the other hand, setting one of eigenvalues of (C.33) to +1, we get the condition for the saddle node bifurcation of the period k motion, namely,

$$Tr\left(DP^{(k)}\right) = 1 + Det\left(DP^{(k)}\right). \tag{C.35}$$

C.2 An Impact Pair

The various equations pertinent to the horizontal impact pair of *Chapter* 8 are presented here.

C.2.1 Basic mappings and their Jacobian matrix

Basic mappings:

The solutions for the four mappings and the evaluation of their Jacobian are listed here.

Mapping P_1:

$$\dot{y}_{i+1} = -A\omega\cos(\omega t_{i+1} + \varphi) + [-e\dot{y}_i + A\omega\cos(\omega t_i + \varphi)], \tag{C.36}$$

$$-d = -A\sin(\omega t_i + \varphi) + [-e\dot{y}_i + A\omega\cos(\omega t_i + \varphi)](t_{i+1} - t_i) + A\sin(\omega t_i + \varphi). \tag{C.37}$$

Mapping P_2:

$$\dot{y}_{i+1} = -A\omega\cos(\omega t_{i+1} + \varphi) + [-e\dot{y}_i + A\omega\cos(\omega t_i + \varphi)], \tag{C.38}$$

$$d = -A\sin(\omega t_i + \varphi) + [-e\dot{y}_i + A\omega\cos(\omega t_i + \varphi)](t_{i+1} - t_i) + A\sin(\omega t_i + \varphi). \tag{C.39}$$

Mapping P_3 and P_4:

$$\dot{y}_{i+1} = -A\omega\cos(\omega t_{i+1} + \varphi) + [-e\dot{y}_i + A\omega\cos(\omega t_i + \varphi)], \tag{C.40}$$

$$0 = -A\sin(\omega t_i + \varphi) + [-e\dot{y}_i + A\omega\cos(\omega t_i + \varphi)](t_{i+1} - t_i) + A\sin(\omega t_i + \varphi). \tag{C.41}$$

Jacobian matrix:

The Jacobian of mapping P_1, DP_1 is defined by

$$DP_1 = \left[\frac{\partial(t_{i+1}, \dot{y}_{i+1})}{\partial(t_i, \dot{y}_i)}\right]_{(t_i, \dot{y}_i)} = \begin{bmatrix} \frac{\partial t_{i+1}}{\partial t_i} & \frac{\partial t_{i+1}}{\partial \dot{y}_i} \\ \frac{\partial \dot{y}_{i+1}}{\partial t_i} & \frac{\partial \dot{y}_{i+1}}{\partial \dot{y}_i} \end{bmatrix}_{(t_i, \dot{y}_i)}, \tag{C.42}$$

where

$$\left.\begin{aligned}
&\frac{\partial t_{i+1}}{\partial t_i} = \frac{1}{\dot{y}_{i+1}}\left[-e\dot{y}_i + A\omega^2(t_{i+1}-t_i)\sin(\omega t_i+\varphi)\right],\\
&\frac{\partial t_{i+1}}{\partial t_i} = \frac{e}{\dot{y}_{i+1}}(t_{i+1}-t_i),\\
&\frac{\partial \dot{y}_{i+1}}{\partial t_i} = \frac{1}{\dot{y}_{i+1}}A\omega^2\sin(\omega t_i+\varphi)\left[-e\dot{y}_i + A\omega^2(t_{i+1}-t_i)\sin(\omega t_i+\varphi)\right] - A\omega^2\sin(\omega t_i+\varphi),\\
&\frac{\partial \dot{y}_{i+1}}{\partial y_i} = \frac{e}{\dot{y}_{i+1}}A\omega^2(t_{i+1}-t_i)\sin(\omega t_i+\varphi) - e.
\end{aligned}\right\} \quad \text{(C.43)}$$

The Jacobians for the remaining mappings, that is, P_2 to P_4 can be defined in the same manner. However, it is necessary to first obtain the impact times. This is described as follows. The times of ith and the $(i+1)$th impacts for mapping P_1, t_i and t_{i+1} can be computed using *Equations* (C.36)-(C.37). Similarly, the impact times t_i and t_{i+1} for mapping P_2, and for mapping P_3 and P_4 can be determined from *Equations* (C.38)-(C.39) and *Equations* (C.40)-(C.41), respectively.

C.2.2 Periodic motion

Non-equispaced period-1 motion:

The coefficients for the non-equispaced period-1 motion are:

$$m_1^q = 1-\cos(\omega qnT), \quad \text{(C.44)}$$

$$m_2^q = \sin(\omega qnT), \quad \text{(C.45)}$$

$$K^q = 2-2\cos(\omega qnT)-\omega qnT\sin(\omega qnT), \quad \text{(C.46)}$$

$$K_1^q = \Delta\omega\sin(q\omega nT), \quad \text{(C.47)}$$

$$K_2^q = 1-\cos(\omega qnT)+qnT\omega\sin(\omega qnT), \tag{C.48}$$

$$K_3^q = 1-\cos(q\omega nT), \tag{C.49}$$

$$K_4^q = \Delta\omega\left[1-\cos(q\omega nT)\right], \tag{C.50}$$

$$K_5^q = -\omega qnT\cos(\omega qnT)+\sin(\omega qnT), \tag{C.51}$$

$$K_6^q = -\omega qnT+\sin(q\omega nT), \tag{C.52}$$

$$L^q = K^q - m_1^q K_3^q - m_2^q K_6^q, \tag{C.53}$$

$$L_1^q = m_1^q K_1^q + m_2^q K_4^q, \tag{C.54}$$

$$L_2^q = e\left(-K_1^q + m_1^q K_2^q + m_2^q K_5^q\right), \tag{C.55}$$

where $\Delta = \begin{cases} -d & \text{for mapping } P_1 \\ d & \text{for mapping } P_2 \end{cases}$ in *Equations* (C.48) and (C.51).

k-impact periodic motion:

Similarly, the coefficients for the non-equispaced *k*-impact periodic motion are:

$$m_1^{q_j} = 1-\cos\left(\omega q_j nT\right), \tag{C.56}$$

$$m_2^{q_j} = \sin(\omega qnT), \tag{C.57}$$

$$K^{q_j} = 2-2\cos\left(\omega q_j nT\right)-\omega q_j nT\sin\left(\omega q_j nT\right), \tag{C.58}$$

$$K_1^{q_j} = -\Delta\omega\sin(qn\omega T), \tag{C.59}$$

$$K_2^{q_j} = 1-\cos\left(\omega q_j nT\right)-q_j nT\omega\sin\left(\omega q_j nT\right), \tag{C.60}$$

$$K_3^{q_j} = 1 - \cos\left(\omega q_j nT\right), \tag{C.61}$$

$$K_4^{q_j} = \Delta\omega\left(1 - \cos\left(q_j \omega NT\right)\right), \tag{C.62}$$

$$K_5^{q_j} = -q_j nT\cos\left(\omega q_j nT\right) + \sin\left(\omega q_j nT\right), \tag{C.63}$$

$$K_6^{q_j} = -q_j nT + \sin\left(\omega q_j nT\right), \tag{C.64}$$

$$L^{q_j} = K^{q_j} - m_1^{q_j} K_3^{q_j} - m_2^{q_j} K_6^{q_j}, \tag{C.65}$$

$$L_1^{q_j} = m_1^{q_j} K_1^{q_j} + m_2^{q_j} K_4^{q_j}, \tag{C.66}$$

$$L_2^{q_j} = -K^{q_j} + m_1^{q_j} K_2^{q_j} + m_2^{q_j} K_5^{q_j}, \tag{C.67}$$

where $$\Delta = \begin{cases} -d & \text{for mapping } P_1 \\ d & \text{for mapping } P_2 \\ 0 & \text{for mappings } P_3 \text{ and } P_4 \end{cases}.$$

REFERENCES

ABRAHAM, R. AND J. E. MARSDEN (1978), *Foundations of Mechanics*, The Benjamin / Cummings Publishing Company: London.

ADLER, R. L., A. G. KONHEIM AND M. H. MCANDREW (1965), "Topological Entropy", *Trans. Amer. Math. Soc.*, **114**, 309-319.

ARNOLD, V. I. (1963), "Proof of A. N. Kolmogorov's Theorem on the Preservation of Quasiperiodic Motions under Small Perturbations of the Hamiltonian", *Russ. Math. Surv.*, **18**, 9-36.

AWREJCEWICZ, J. AND J. MROZOWSKI (1989), "Bifurcation and Chaos of a Particular Van del Pol-Duffing Oscillator", *J. of Sound and Vibr.*, **132**, 89-100.

BABARBANEL, H. D. I., R. BROWN, J. J. SIDOROWICH AND L. S. TSIMRING (1993), "The Analysis of Observed Chaotic Data in Physical Systems", *Rev. Mod. Phys.*, **65**, 1331-1392.

BAPAT, C. N., N. POPPLEWELL AND K. MCLACHLAN (1983), "Stable Periodic Motions of an Impact-Pair", *J. of Sound and Vibr.*, **87**, 19-40.

BAPAT, C. N. AND C. BAPAT (1988), "Impact-Pair Under Periodic Excitation", *J. of Sound and Vibr.*, **120**, 53-61.

BAPAT, C. N. AND S. SANKAR (1985), "Single Unit Impact Damper in Free and Forced Vibrations", *J. of Sound and Vibr.*, **99**, 85-94.

BARKHAM, P. G. D. AND A. C. SOUDACK (1969), "An Extension to the Method of Kryloff and Bogoliuboff", *Int. J. of Control*, **10**, 377-392.

BAYLY, P. V. AND L. N. VIRGIN (1993), "An Experimental Study of an Impacting Pendulum, *J. of Sound and Vibr.*, **164**, 364-374.

BENE, J. AND P. SZEPFALUSY (1988), "Multifractal Properties in the One-Dimensional Random-Field Ising Model", *Phys. Rev.*, **37A**, 1703-1707.

BENEDICKS, M. (1994), "New Developments in the Ergodic Theory of Nonlinear Dynamical Systems", *Phil. Trans. Roy. Soc. Lond.*, **346A**, 145-157.

BISHOP, S. R. (Ed.) (1994), "Impact Oscillator", *Phil. Trans. R. Soc. Lond.*, **347A**, 345-448.

BORGAS, M. S. (1993), "The Multifractal Lagrangian Nature of Turbulence", *Phil. Tans. Roy. Soc. Lond.*, **342A**, 374-411.

BRESSLOFF, P C. AND J. STARK (1991), "Neural Networks, Learning Automata and Iterated Function Systems", *Fractals and Chaos*, A. J. Crilly, R. A. Earnshaw and H. Jones (eds.), Springer-Verlag: New York.

BRINDLEY, J., M. D. SAVAGE AND C. M. TAYLOR (1990), "The Nonlinear Dynamics of Journal Bearings", *Phil. Trans. R. Soc. Land.*, **332A**,107-119.

BRUNSDEN, V., J. CORTELL AND P. J. HOLMES (1989), "Power Spectra of Chaotic Vibrations of a Buckled Beam, *J. of Sound and Vibr.*, **130**, 1-25.

BUNDE , A. AND S. HAVLIN (1991), *Fractals and Disordered Systems*, Springer-Verlag: Berlin.

BURTON, T. D. AND Z. RAHMAN (1986), "On the Multiscale Analysis of Strongly Nonlinear forced oscillators", *Int. J. of Nonlinear Mech.*, **21**, 135-146.

CHIRIKOV, B. V. (1979), "A Universal Instability of Many-Dimensional Oscillator System", *Phys. Rep.*, **52**, 263-3114.

CARR, J. (1981), *Applications of Center Manifold Theory*, Springer-Verlag: New York

CAYLEY, A. (1895), *Elliptic Functions*, Bell and Sons: London.

COLLET, P. AND J. P. ECKMANN (1980), *Iterated Maps on the Interval as Dynamical Systems*, Progress on Physics, **I**, Birkhauser, Boston.

COLLET, P., J. P. ECKMANN AND H. KOCH (1981), "Period Doubling Bifurcations for Families of Maps on R^n", *J. of Stat. Phys.*, **25**, 1-14.

COLLET, P., J. P. ECKMANN AND O. E. LANFORD (1980), "Universal Properties of Maps on an Interval", *Comm. in Math. Phys.*, **76**, 211-254.

COSENZA, M. G., W. D. MCCORMICK AND J. B. SWIFT (1989), "Finite-Size Effects on the Fractal Spectrum of the Period-Doubling Attractor", *Phys. Rev.*, **39A**, 2734-2737.

DAVIES, H. G. (1980), "Random Vibrations of a Beam Impacting Stops", *J. of Sound and Vibr.*, **68**, 479-487.

DEBNATH, M. AND A. R. CHOWDHURY (1991), "Period Doubling and Hysteresis in a Periodically Forced, Damped Anharmonic Oscillator", *Phys. Rev.*, **44A**, 1049-1060.

DERRIDA, B., A. GERVOIS AND Y. POMEAU (1979), "Universal Metric Properties of Bifurcations and Endomorphisms", *J. of Phys.*, **12A**, 269-296

DENG, W. (1964), "Action of the Impact Damper and Determination of its Basic Parameters", *Chinese J. of Mech. Eng.*, **12**, 83-93.

DERRIDA D., A. GERVOIS AND Y. POMEAU (1979), "Universal Metric Properties of Bifurcations of Endomorphisms", *J. of Phys.*, **12A**, 269-296.

DEVANEY, R. L. (1986), *An Introduction to Chaotic Dynamical Systems*, Benjamin Cummings: Menlo Park, CA.

DOOREN, R. V. (1988), "On the Transition from Regular to Chaotic Behavior in the Duffing Oscillator", *J. of Sound and Vibr.*, **123**, 327-339.

DOVEIL, F. AND D. F. ESCANDE (1981), "Destabilization of an Enumerable Set of Cycles in a Hamiltonian System", *Phys. Lett.*, **84A**, 399-403.

DOWELL, E. H. (1982), "Flutter of a Buckled Plate as an Example of Chaotic motion of a Deterministic Autonomous System", *J. of Sound and Vibr.*, **85**, 333-344.

DOWELL, E. H. (1984), "Observation and Evolution of Chaos for an Autonomous System", *ASME J. of Appl. Mech.* **51**, 664-673.

DOWELL, E. H. AND C. PEZESHKI (1986), "On the Understanding of Chaos in Duffing's Equation Including a Comparison with Experiment", *ASME J. of Appl. Mech.*, **53**, 5-9.

DUBOWSKY, S. AND F. FREUDENSTEIN (1971), "Dynamic Analysis of Mechanical Systems with Clearances", *Trans. Am. Soc. Mech. Engrs*, **93B**, 305-316.

DUBOWSKY, S. AND M. F. MOENING (1978), "An Experimental and Analytical Study of Impact Forces in Elastic Mechanical Systems with Clearances", *Mechanism and Machine Theory*, **13**, 451-465.

DUFFING, G. (1918), *Erzwungene Schwinggungen bei Veranderlicher Eigenfrequenz.* Vieweg: Braunchweig.

ECKMANN, J.-P. (1981), "Roads to Turbulence in Dissipative Dynamical Systems", *Rev. Mod. Phys.*, **53**, 643-654.

ECKMANN, J.-P. AND D. RUELLE (1985), "Ergodic Theory of Chaos and Strange Attractors", *Rev. Mod. Phys.*, **57**, 617-656.

ERIKSSON, A. B., T. EINARSSON AND S. OSTLUND (1992), "Circle Maps with Symmetry-Breaking Perturbations", *Physica* **57D**, 58-84.

EVERSON, R. M. (1986), "Chaotic Dynamics of a Bouncing Ball", *Physica* **19D**, 355-383.

ESCANDE, D. F. (1985), "Stochasticity in Classical Hamiltonian Systems: Universal Aspects", *Phys. Rep.*, **121**, 165-261.

ESCANDE, D. F. AND F. DOVEIL (1981), "Renormalization Method for the Onset of Stochasticity in a Hamiltonian System", *Phys. Lett.*, **83A**, 307-310.

FALCONER, K. (1990), *Fractal Geometry: Mathematical Foundations and Applications*, John Wiley and Sons: Chichester.

FEDER, J. (1988), *Fractals.* Plenum: New York.

FEIGENBAUM, M. J. (1978), "Quantitative Universality for a Class of Nonlinear Transformations", *J. Stat. Phys.*, **19**, 25-52.

FEIGENBAUM, M. J. (1979), "The Universal Metric Properties of Nonlinear Transformations", *J. of Stat. Phys.*, **21**, 669-706.

FEIGENBAUM, M. J. (1980a), "Universal Behavior in Nonlinear Systems", *Los Alamos*

Science, **1**, 4-27.

FEIGENBAUM, M. J. (1980b), "The Transition to Aperiodic Behavior in Turbulent Systems, *Comm. in Math. Phys.*, 77, 65-86.

FEIGENBAUM, M. J. (1983), "Universal Behavior in Nonlinear Systems", *Physica*, **7D**, 16-39

FOALE, S. AND S. R. BISHOP (1992), "Dynamical Complexities of Forced Impacting Systems", *Phil. Trans. R. Soc. Lond.*, **338A**, 547-556.

FRANASZEK, M. AND H. M. ISOMAKI (1991), "Anomalous Chaotic Transients and Repellors of the Bouncing Ball Dynamics", *Phys. Rev.*, **33A**, 1134-1140.

FRANCESCHINI, V. AND R. TEBALDI (1979), "Sequences of Infinite Bifurcations and Turbulence in a Five Truncation of the Navier-Stokes Equations", *J. of Stat. Phys.*, **21**, 707-726.

FRESCHET, M. (1938), *Methods des Fonctions Arbitraires. Theorie des Evenements en Chaine dans le Cas d'un Nombre Fini d'Etats Possibles*, Gauthier-Villars: Paris.

GARCIA-MARGALLO, J. AND J. D. BEJARANO (1987), "A Generalization of the Method of Harmonic Balance", *J. of Sound and Vibr.*, **116**, 591-595.

GLAZIER, J. A., M. H. JENSEN, A. LIBCHABER AND J. STAVENS (1986), " Structure of Arnold Tongues and $f(\alpha)$ Spectrum for Period Doubling: Experimental Results", *Phys. Rev.*, **34A**, 1621-1625.

GOUYET, J. F., M. ROSSO AND B. SAPOVAL (1991), "Fractal Surfaces and Interfaces", *Fractals and Disordered Systems*, A. Bunde and S. Havlin (eds.), 229-261.

GRASSBERGER, P. AND I. PROCACCIA (1983a), "On the Characterization of Strange Attractors", *Phys. Rev. Lett.*, **50**, 346-349.

GRASSBERGER, P. AND I. PROCACCIA (1983b) "Estimation of the Kolmogorov Entropy from a Chaotic Signal", *Phys. Rev.*, **29A**, 2591-2593.

GRASSBERGER, P. AND I. PROCACCIA (1983c), "Measuring the Strangeness of Strange Attractors", *Physica*, **9D**,189-208.

GREBOGI, C., E. OTT AND J. A. YORKE (1988), "Unstable Periodic Orbits and the Dimensions of Multifractal Chaotic Attractors", *Phys. Rev.*, **37A**, 1711-1724.

GREENE, J. M. (1968), "Two-Dimensional Measure-Preserving Mappings", *J. of Math. Phys.*, **9**, 760-768.

GREENE, J. M. (1979), "A Method for Computing the Stochastic Transition", *J. of Math. Phys.*, **20**, 1183-1201.

GREENE, J. M., R. S. MACKAY, F. VIVALDI AND M. J. FEIGENBAUM (1981), "Universal Behavior in Families of Area-Preserving Maps", *Physica*, **3D**, 468-486.

GRUBIN, P. (1956), "On the Theory of the Acceleration Damper", *ASME J. of Appl. Mech.*, **23**, 373-378

GUCKENHEIMER, J. AND P. HOLMES (1983), *Nonlinear Oscillations, Dynamical Systems, and Bifurcations of Vector Fields*, Springer-Verlag: New York

HADAMARD, J. (1901), "Sur l'iteration et les Solutions Asymptotiques des Equations Differentielles", *Bull. Soc. Math. France*, **29**, 224-228.

HAINES, R. S. (1979), "Survey: 2-Dimensional Motion and Impact at Revolute Joint", *Mechanism and Machine Theory*, **15**, 361-370.

HALSEY, T. C., M. H. JENSEN, L. P. KADANOFF, I. PROCACCIA AND B. I. SHRAIMAN (1986), "Fractal Measures and their Singularities: the Characterization of Stranger Sets", *Phys. Rev.*, **33A**, 1141-1151.

HAO, B. L. (1989), *Elementary Symbolic Dynamics and Chaos in Dissipative Systems*, World Scientific: Singapore.

HAN, RAY P. S. AND A. C. J. LUO (1993), "Multiparameter Bifurcation of a Generalized Duffing Oscillator", *Proc. 2nd Int. Conf. Nonlinear Mech.*, Beijing, August 23-26.

HAN, RAY P. S. AND A. C. J. LUO (1994), "Analytical Predictions of Chaos in a Nonlinear Rod", *Int. J. Nonlinear Dynamics*, submitted.

HAN, RAY P. S. AND A. C. J. LUO (1995a), "Comments on the Subharmonic resonances and Criteria for Escape and Chaos in a Driven oscillator", *J. of Sound and Vibr.*, submitted.

HAN, RAY P. S. AND A. C. J. LUO (1995b), "Resonant Layers in Nonlinear Dynamics", in preparation.

HAN, RAY P. S., A. C. J. LUO (1995c) "The Science of Nonlinear Dynamics in Engineering", *J. of Appl. Mech. Rev.*, invited review paper, in preparation.

HAN, RAY P. S. AND A. C. J. LUO (1995d), "Period-k motion of a Bouncing Ball with a Harmonically Excited Table", in preparation.

HAN, RAY P. S., A. C. J. LUO AND W. DENG (1995), "Chaotic Motion of a Horizontal Impact Pair", *J. of Sound and Vibr.*, **181**, 231-250.

HAYASHI (1964), *Nonlinear Oscillators in Physical Systems*, McGraw-Hill,: New York

HEIMAN, S., P. J. SHERMAN AND A. K. BAJAJ (1987), "On the Dynamics and Stability of an Inclined Impact Pair", *J. of Sound and Vibr.*, **114**, 535-547.

HEIMAN, S., A. K. BAJAJ AND P. J. SHERMAN (1988), "Periodic Motions and Bifurcation in Dyanmics of an Inclined Impact Pair", *J. of Sound and Vibr.*, **124**, 55-78.

HERRMANN, H. J. (1991), "Fractures", *Fractals and Disordered Systems*, A. Bunde and S. Havlin (eds.), 175-204, Springer-Verlag: New York.

HELLEMAN, R. H. G. (1980a), "Self-Generated Chaotic Behavior in Nonlinear Mechanics", *Fundamental Problems in Statistical Mechanics*, E. G. D. Cohen (ed.), **5**, 165-233 North-Holland: Amsterdam.

HELLEMAN, R. H. G.(ed.) (1980b), *Nonlinear Dynamics*, (Annals of the New York Academy of Science) **357**, New York Academy of Sciences: New York.

HELLEMAN, R. H. G. (1983), "One Mechanism for the Onsets of Large Scale Chaos in Conservative and Dissipative Systems", *Long-Time Prediction in Dynamics*, C. W. Hotrod, L. E. Reichl and V. Szebehely (eds.), 95-126. John Wiley and Sons: New York.

HENDRICKS, F. (1983), "Bounce and Chaotic Motion in Impact Print Hammers" *IBM J.*, **27**, 273-280.

HENON, M. AND C. HEILES (1964), "The Applicability of the Third Integral of Motion: Some Numerical Experiments", *Astron. J.*, **69**, 73-79.

HOLMES, P. J. (1979), "A Nonlinear Oscillator with a Strange Attractor", *Phil. Trans. Roy. Soc. A*, **292**, 419-448.

HOLMES, P. J. (1980), "Averaging and Chaotic Motions in Forced Oscillations", *SIAM J. of Appl. Math.*, **38**, 65-115; Errata and Addenda, *SIAM J. of Appl. Math.*, **40**, 167-168.

HOLMES, P. J. (1982), "The Dynamics of Repeated Impacts with a Sinusoidally Vibrating Table", *J. of Sound and Vibr.*, **84**, 173-189.

HOLMES, P.J. AND F. C. MOON (1983), "Strange Attractors and Chaos in Nonlinear Dynamics", *ASME J. of Appl. Mech.*, **50**, 1021-1032.

HOUSNER, G. W. (1963), "The Behaviour of Inverted Pendulum Structures during Earthquakes", *Bull. Seism. Soc. Amer.*, **53**, 403-417.

HSU, C. S. (1981), "A Generalized Theory of Cell-to-Cell Mapping for Nonlinear Dynamical Systems", ASME *J. of Appl. Mech.*, **48**, 634-642.

HU, B. AND J. MAO (1985), "The Eigenvalue Matching Renormalization Group", *Phys. Lett.*, **108A**, 305-307.

HU, B. AND J. RUDNICK (1982), "Exact Solutions of the Feigenbaum Renormalization Group Equations for Intermittence", *Phys. Rev. Lett.*, **48**, 1645-1648.

JOHSON, R. C. (1958), "Impact Forces in Mechanisms", *Machine Design*, **30**, 138-146.

KLUIVING, R., H. W. CAPEL AND R. A. PASMANTER (1990), "Phase-Transition-like Phenomenon in a Piecewise Linear Map", *Physica* **A 164**, 93-642.

KLUIVING, R., H. W. CAPEL AND R. A. PASMANTER (1992a), "Symbolic Dynamics of Fully Developed Chaos, Part I", *Physica A*, **183**, 67-95.

KLUIVING, R., H. W. CAPEL AND R. A. PASMANTER (1992b), "Symbolic Dynamics of Fully Developed Chaos, Part II", *Physica A*, **183**, 96-129.

KOBAYASHI, T., N. MORI, H. HATA, T. HORITA, T. YOSHIDA AND H. MORI (1989), "Critical Scaling Laws of Dynamics Structure Functions for Type I Intermittent Chaos", *Progr. of Theor. Phys.*, **82**,1-6.

KOBRINSKII, A. E. (1969), *Dynamics of Mechanisms with Elastic Connections and Impact Systems*. Iliffe Books: London.

KOLMOGOROV, A. N. (1954), "On Conservation of Conditionally Periodic Motions Under Small Perturbations of the Hamiltonian", *Dokl. Acad. Nauk. SSSR*, **98**, 527-530.

KOLMOGOROV, A. N. (1958), "A New Invariant of Transitive Dynamical Systems", *Dokl. Acad. Nauk. SSSR*, **119**, 861-865.

KOVACS, Z. AND T. TEL (1992), "Bivariate Thermodynamics of Multifractals as an Eigenvalue Problem", *Phys. Rev.*, **45A**, 2770-2285.

KRYLOV, N. (1950), *Studies on the Foundation of Statistical Physics, Akad. Nauk. SSSR* M.-L.

LEAN, G. H. (1971), "Subharmonic Motion of Moored Ships Subjected to Wave Action", *Trans. R. Naval Architects*, **113**, 387-399.

LEUNG, A. Y. T.(1991), "Rigorous Studies of a Duffing Oscillator", *J. of Sound and Vibr.*, **149**, 147-149.

LEUNG, A. Y. T. AND A. C. J. LUO (1992), "Fractals by Multigenerator", *Microcomputer in Civil Eng.*, **7**, 257-264.

LICHTENBERG, A. J. AND M. A. LIEBERMAN (1992), *Regular and Chaotic Dynamics*, 2nd ed., Springer-Verlag: New York.

LIEBER, P. AND D. P. JENSEN (1945), " An Acceleration Damper: Development, Design and some Applications", *Trans. of ASME*, **67**, 523-324.

LIN, W. A. AND REICHL, L. E. (1986), "External Field Induced Chaos in an Infinite Square Well Potential", *Physica*, **19D**, 145-152.

LORENZ, E. N. (1963), "Deterministic Non-Periodic Flow", *J. Atmos. Sc.*, **20**, 130-141.

LUO, A. C. J. (1991), "Generalized Fractal Theory", *Proc. on Chinese Conf. Turb. and Stability*, Tianjing, P. R. China.

LUO, A. C. J. (1993a), "Stochastic Layer of Duffing's Equation near its Homoclinic Orbit under a Periodic Excitation", *Proc. of 2nd Int. Conf. on Nonlinear Mech.*, Beijing, China, August 23-26.

LUO, A. C. J. (1993b), "Stochastic Layer of Duffing's Equation near its Subharmonic Orbit", *Int. Symp. on Nonlinear Dynamics and Stoch. Mech.*, Waterloo, Aug. 28-Sept. 1.

LUO, A. C. J. (1994), "A Stochastic Layer of Duffing's Equation near its Subharmonic Orbits", *J. of Hydrodynamics*, Ser. B, **6**(2), 91-110.

LUO, A. C. J. (1995), "Criterion of Stochastic Layer near a Planar Homoclinic Orbit in Nonlinear Dynamical System", *J. of Hydrodynamics, Ser. B.*,**7(2)**, 35-50.

LUO, A. C. J. and W. DENG (1990), "Motion Behavior of an Impact Ball in the Impact Damper", *Proc. of the ICVPE'90*, Wuhan, P.R.China, 447-452.

LUO, A. C. J. AND RAY P. S. HAN (1992a), "Period Doubling and Multifractal in 1-D Iterative Maps", *J. Chaos, Solitons & Fractals*, **2**, 335-348.

LUO, A. C. J. AND RAY P. S. HAN (1992b), "Fractal Analysis of a Multidimensional Horseshoe Map", *Symp. on Fractals in Engineering*, Montreal. Canada, June 3-5.

LUO, A. C. J. AND RAY P. S. HAN (1994), "Dynamics of a Bouncing Ball with a Periodic Vibrating Table Revisited", in press: *Int. J. Nonlinear Dynamics.*

LUO, A. C. J. AND RAY P.S. HAN (1995a), "Universality of Duffing Equation via its Discrete Mapping", *PACAM IV, 4th Pan-American Congr. Appl. Mech.*, Buenos Aires, Argentina, Jan. 3-6.

LUO, A. C. J. AND RAY P. S. HAN (1995b) "An Analytical Approach for Predicting Bifurcation and Stability of Periodic Solutions via a Damped Driven Duffing Oscillator", *ASME J. of Sound and Acous.*, submitted.

LUO, A. C. J. AND RAY P. S. HAN (1995c), "Universal Properties of Duffing Equation", in preparation.

LUO, A. C. J. AND RAY P. S. HAN (1995d), "Multifractals in Chaotic Dynamics via Horseshoe Maps", in preparation.

LUO, A. C. J. AND RAY P.S. HAN (1995e), "An Accurate Determination of Periodic Solutions for a Driven Oscillator with Strong Nonlinearity, Damping and Excitation", in preparation.

LUO, A. C. J. AND RAY P. S. HAN (1995f), "Stochastic Layers in Nonlinear Dynamics", in preparation.

LUO, A. C. J., RAY P. S. HAN AND Y. M. XIANG (1995), "Chaotic Analysis of Subharmonic Resonant Waves in Undamped and Damped String", *J. of Hydrodynamics*, Ser. B, 7(2), 92-104.

MACKAY, R. S. (1983), "Period Doubling as a Universal Route to Stochasticity", *Long-Time Prediction in Dynamics, Long-Time Prediction in Dynamics*, C. W. Hotrod, L. E. Reichl and V. Szebehely (eds.), John Wiley and Sons: New York, 127-134.

MANDELBROT, B. B. (1977), *Fractals: Form, Chance and Dimension*, W. H. Freeman and Company: San Francisco.

MANDELBROT, B. B. (1982), *The Fractal Geometry of Nature,* W. H. Freeman and Company: San Francisco.

MASRI, S.F. AND T.D. CAUGHEY (1966), "On the Stability of the Impact Damper", *ASME J. of Appl. Mech.*, **33**, 586-592.

MASRI, S. F., A. G. CHASSIAKOS AND T. K. CAUGHEY (1993), "Identification of Nonlinear Dynamic Systems Using Neural Networks", *ASME J. of Appl. Mech.*, **60**, 123-133.

MAY, R. M. (1976), "Simple Mathematical Models with very Complicated Dynamics",

Nature, **261**, 459-467.

MCLAUGHLIN, J. B. (1979), "Stochastic Behavior in Slightly Dissipative Systems", *Phys. Rev.*, **20A**, 2114-2119.

MCCAULEY, J. L. (1990), "Introduction to Multifractals in Dynamics Systems Theory and Fully Developed Fluid Turbulence", *Phys. Rep.*, **189**, 225-266.

MEISS, J. D.(1992), "Symplectic Maps, Variational Principles and Transport", *Rev. of Mod. Phys.*, **64**, 793-848

MELNIKOV, V. K. (1963), "On the Stability of the Center for Time Periodic Perturbations", *Trans. Moscow Math. Soc.*, **12**, 1-57.

MENEVEAU, C., K. R. SREENIVASAN, P. KAILSANATH AND M. S. FAN (1990), "Joint Multifractal Measures: Theory and Applications to Turbulence", *Phys. Rev.*, **41A**, 894-912.

METROPOLIS, N., STEIN, M. L. AND STEIN, P. R. (1973), "On Finite Limit Sets for Transformations on the Unit Interval", *J. of Comb. Theory*, **15**, 25-44.

MOON, F. C. (1980a), "Experiments on Chaotic Motions of a Forced Nonlinear Oscillator: Strange Attractors", *ASME J. of Appl. Mech.*, **47**, 638-644.

MOON, F. C. (1980b), "Experimental Models for Strange Attractor Vibration in Elastic Systems", *New Approaches to Nonlinear Problems in Dynamics*, P. J. Holmes (ed.), 487-495. SIAM: Philadelphia.

MOON, F. C. (1987), *Chaotic Vibrations: An Introduction for Applied Scientists and Engineers*, John Wiley and Sons: New York.

MOON, F. C. AND P. J. HOLMES (1979), "A Magnetoelactic Strange Attractor", *J. of Sound and Vibr.*, **65**, 285-296.

MOON, F. C. AND G. X. LI (1985a), "The Fractal Dimension of the Two-Well Potential Strange Attractor", *Physica*, **17D**, 99-108.

MOON, F. C. AND G. X. LI (1985b), "Fractal Basin Boundaries and Homoclinic Orbits for Periodic Motion in a Two-Well Potential", *Phys. Rev. Lett.*, **55**, 1439-1442.

MOON, F. C. AND S. W. SHAW (1983), "Chaotic Vibrations of a Beam with Nonlinear Boundary Conditions", *Int. J. of Nonlinear Mech.*, **18**, 465-477.

MOORE, D. B. AND S. W. SHAW (1990), "The Experimental Response of an Impacting Pendulum System", *Int. J. of Nonlinear Mech.*, **18**, 465-477.

MORI, N., T. KOBAYASHI, H. HATA, T. MORITA, T. HORITA and H. MORI (1989), "Scaling Structures and Statistical Mechanics of Type I Intermittent Chaos", *Progr. of Theor. Phys.*, **81**, 60-77.

MOROSOV, A. D. (1973), "Approach to a Complete Qualitative Study of Duffing Equation", *USSR J. Comp. Math. and Math. Phys.*, **13**, 1134-1152.

MOSER, J. (1962), "On Invariant Curves of Area-Preserving Mappings of an Annulus", *Nachr. Akad. Wiss. Gottingen Math. Phys. Kl.*, **2**, 1-20.

NAUENBERG M. AND J. RUDNICK (1981), "Universality and Power Spectrum at the Onset of Chaos", *Phys. Rev.*, **24B**, 493-495.

NAYFEH, A. H. (1973), "Nonlinear Transverse Vibrations of Beams with Properties that Vary along the Length", *J. of Acous. Soc. Amer.*, **53**, 766-770.

NAYFEH, A. H. (1973), *Perturbation Methods*, John Wiley and Sons: New York.

NAYFEH, A. H. AND D. T. MOOK (1979), *Nonlinear Oscillations*, John Wiley and Sons: New York.

NORDMARK, A. B. (1991), "Non-Periodic Motion Caused by Grazing Incidence in an Impact Oscillator, *J. of Sound and Vibr.*, **145**, 279-297.

OLEMSKOI, A. I. AND A.YA. FLAT (1993) "Applications of Fractals in Condensed-Matter Physics", *Physics-Uspekhi*, **36**, 1087-1128.

OTT, E. (1981), "Strange Attractors and Chaotic Motions of Dynamical System", *Rev. of Mod. Phys.*, **64**, 655-671.

PAIDOUSSIS, M. P. AND G. X. Li (1992), "Cross-Flow Induced Chaotic Vibrations of Heat Exchanger Tubes Impacting on Loose Supports", *J. of Sound and Vibr.*, **152**, 305-326.

PERKO, L. (1991), *Differential Equation and Dynamical System*, Text in Applied Mathematics 7, Springer-Verlag: New York.

PESIN, J. B. (1977), "Characteristics Lyapunov Exponents and Smooth Ergodic Theory", *Russ. Math. Surv.*, **32**, 55-114.

PETERKA, F. AND J. VACIK (1992), "Transition to Chaotic Motion in Mechanical Systems with Impacts", *J. of Sound and Vibr.*, **154**, 95-115.

PFEIFFER, F. AND A. KUNERT (1990), "Rattling Models from Deterministic to Stochastic Processes", *Int. J. of Nonlinear Dynamics*, **1**, 63-74.

POINCARE, H. (1899) *Les Methodes Nouvelles de la Mecanique Celeste*, 3 Volumes, Gauthier-Villars: Paris.

POMEAU, Y. AND P. MANNEVILLE (1980), "Intermittent Transition to Turbulence in Dissipative Dynamical Systems, *Comm. in Math. Phys.*, **74**, 189-197.

RASBAND, S. N. (1989), *Chaotic Dynamics of Nonlinear System*, John Wiley and Sons: New York.

REICHL, L. E. (1992), *The Transition to Chaos in Conservative Classic System: Quantum Manifestations*, Spring -Verlag: New York.

REICHL, L. E. AND W. M. ZHENG (1984a), "Field-Induced Barrier Penetration in the Quadratic Potential", *Phys. Rev.*, **29A**, 2186-2193.

REICHL, L. E. AND W. M. ZHENG (1984b), "Perturbed Double-Well System: The Pendulum Approximation and Low-Frequency Effect", *Phys. Rev.*, **30A**, 1068-1077.

REITHMEIER E. (1989), "Periodic Solutions on Nonlinear Dynamical Systems with Discontinuities", *Proc. of IUTAM Symp. on Nonlinear Dynamics in Engineering*

Systems, Stuggart, German, 249-256.

RENYI, A. (1971), *Probability Theory*, North-Holland: Amsterdam.

ROMEIRAS, F. J., C. GREBOGI AND E. OTT (1990), "Multifractal Properties of Snapshot Attractor of Random Maps", *Phys. Rev.*, **41A**, 784-799.

RUELLE, D. AND F. TAKENS (1971) "On the Nature of Turbulence", *Comm. in Math. Phys.*, **20**, 167-192.

SCHROEDER, M. (1990), *Fractals, Chaos, Power Laws: Minutes from an Infinite Paradise*, W. H. Freeman and Company: New York.

SCHUSTER, H. G. (1989), *Deterministic Chaos, An Introduction*, 2nd Ed., VCH Verlagsgesellschaft MBH: Weinheim, Germany.

SENATOR M. (1970), "Existence and Stability of Periodic Motions of a Harmonically Forced Impacting System", *J. of Acoust. Soc. Amer.*, **47**, 1390-1397.

SHAW, J. AND S. W. SHAW (1989), "The Onset of Chaos in a Two Degree-of-Freedom Impact System", *ASME J. of Appl. Mech.*, **56**, 168-174.

SHAW, R. (1981), "Strange Attractors, Chaotic Behavior and Information Flow", *Z. Naturforsch*, **36A**, 80-112.

SHAW, S. W. (1985a), "Dynamics of Harmonically Excited Systems having Rigid Amplitude Constraints, Part I-Subharmonic Motions and Local Bifurcations", *ASME J. of Appl. Mech.*, **52**, 453-458.

Shaw, S. W. (1985b), "Dynamics of Harmonically Excited Systems having Rigid Amplitude Constraints, Part II-Chaotic motions and Global Bifurcations", *ASME J. of Appl. Mech.*, **52**, 459-464.

SHAW, S. W. (1985c), "Forced Vibrations of a Beam with One-Sided Amplitude Constraint: Theory and Experiment", *J. of Sound and Vibr.*, **99**, 199-212.

SHAW, S. W. AND P. J. HOLMES (1983a), "A Periodically Forced Piecewise Linear Oscillator", *J. of Sound and Vibr.*, **90,** 123-155.

SHAW, S. W. AND P. J. HOLMES (1983b), "Periodically Forced Impact Oscillator", *Phys. Rev. Lett.*, **51**, 623-625.

SHAW, S. W. AND H. R. RAND (1989), "The Transition to Chaos in a Simple Mechanical System", *Int. J. of Nonlinear Mech.*, **24**, 41-56.

SHENKER, S. J.(1982) "Scaling Behavior in a Map of a Circle onto Itself: Empirical Results", *Physica*, **5D**, 405-411.

SHIGMATSA, H. (1990) "Statistical-Thermodynamic Approach to a Chaotic Dynamical System: Exactly Solvable Examples", *J. of Stat. Phys.*, **59**, 259-297.

SINAI, YA. G. (1959) "On the Concept of Entropy of a Dynamical System", *Dokl. Akad. Nauk. SSSR* **124**, 768-776.

SINAI, YA. G. (1963) "On the Foundation of the Ergodic Hypothesis for a Dynamical

System of Statistical Mechanics ", *Sov. Math. Dokl.* **4**, 1818-1822.

Smale, S. (1963), "Diffeomorphisms with many Periodic Points", *Differential and Combinatorial Topology*, S.S. Cairns (ed.), 63-80, Princeton University Press: Princeton, NJ.

SMALE, S. (1967) "Differentiable Dynamical Systems", *Bull. Amer. Math. Soc.*, **73**, 747-817.

STOKER, J. J. (1968), *Nonlinear Elasticity*, Gordon and Breach: New york.

SZEPFALUSY, P. and T. Tel (1989) "Dynamical Fractal Properties of One-Dimensional Maps", *Phys. Rev.*, **35A**, 477-480.

THOMPSON, J. M. T. AND R. GHAFFARI (1982), "Chaos after Period Doubling Bifurcation in the Resonance of an Impact Oscillator", *Phys. Lett.*, **91A**, 5-8.

THOMPSON J. M. T. AND H. B. STEWART (1986), *Nonlinear Dynamics and Chaos: Geometrical Methods for Engineer and Scientists*, John Wiley and Sons: Chichester.

TUFILLARO, N. B. AND A. M. ALBANO (1986), "Chaotic Dynamics of a Bouncing Ball", *Amer. J. of Phys.*, **54**, 939-944.

UEDA, Y. (1979), "Randomly Transitional Phenomena in the System Governed by Duffing's Equation", *J. of Stat. Phys.*, **20,** 187-196.

UEDA, Y. (1980a), "Steady Motions Exhibited by Duffing's Equation: A Picture Book of Regular and Chaotic Motions", *New Approaches to Nonlinear Problems in Dynamics*, P. J. Holmes (ed.), 311-322. SIAM: Philadelphia.

UEDA, Y. (1980b), "Explosion of Strange Attractors Exhibited by Duffing's Equation", in *Nonlinear Dynamics*, R. H. G. Helleman (ed.), pp. 422-434. New York Academy of Sciences: New York.

UEDA,Y., N. AKAMATSU AND C. HAYASHI (1973), Computer Simulation of Nonlinear ordinary differential equations and non-periodic oscillations. *Trans. IECE JAP.*, **56A**, 218-225.

WANG, C. S., Y. H. KAO, J. C. HUANG AND Y. S. GOU (1992), "Potential Dependence of the Bifurcation Structure in General Duffing Oscillator", *Phys. Rev.* **45A**, 3471-3485.

WARBUTON, G. B. (1957), "Discussion of on the Theory of the Acceleration Damper", *ASME J. of Appl. Mech.*, **24,** 322-324.

WHITTAKER, W. T. AND G. N. WATSON (1946), *A Course in Modern Analysis*, Cambridge University Press: New York.

WHISTON, G. S.(1992), "Singularities in Vibro-Impact Dynamics", *J. of Sound and Vibr.*, **152**, 427-460.

WIGGINS, S. (1988) *Global Bifurcations and Chaos*, Springer-Verlag: New York.

WIGGINS, S. (1990) *Introduction to Applied Nonlinear Dynamical Systems and Chaos*, Springer-Verlag: New York.

WOOD, L. A. and K. P. BYRNE (1981), Analysis of a Random Repeated Impact Process,

J. of Sound and Vibr., **81**, 329-325.

XU, Z. AND Y.K. CHEUNG (1994), "Averaging Method using Generalized Harmonic Functions for Strongly Nonlinear Oscillators", *J. of Sound and Vibr.*, **174**, 563-573.

Yuste, S.B. and J. D. Bejarano (1989), "Extension and Improvement to the Krylov-Bogoliubov Method Using Elliptic Functions", *Int. J. of Control*, **49**, 1127-1141.

Yuste, S.B. and J. D. Bejarano (1990), "Improvement to the Krylov-Bogoliubov Method that use Elliptic Functions", *J. of Sound and Vibr.*, **139**, 151-163.

ZISOOK, A. Z. (1981), "Universal Effects of Dissipation in Two-Dimensional Mappings", *Phys. Rev.*, **24A**, 1640-1642.

INDEX